COOLING THE PV PANEL

Hasan Ahmed Ibrahim Al-Asadi

Submitted in accordance with the requirements for the degree of

Doctor of Philosophy

The University of Leeds

School of Mechanical Engineering

July, 2020

The candidate confirms that the work submitted is his own and that appropriate credit has been given where reference has been made to the work of others.

Abstract

Photovoltaic (PV) panels are becoming increasing popular and are proving to be very successful to fulfil the energy demand in the future. However, these PV panels still have some challenges, including the decrease in efficiency with increasing temperature, and non-uniform temperature of the PV panels. It would be worthwhile to assess the cooling impact on the annual electrical PV panel output and to present a new cooling system to overcome these problems. The main aim of this work is to implement an accurate numerical method to predict the annual impact of phase change material (PCM) on the PV panel electric output. In addition, new systems of PV panels incorporated with PCM- metal foam, will be designed to reduce the temperature of the PV panels.

This research includes five contributions. Firstly, a novel one dimensional PV-PCM model has been presented to investigate the annual impact of the PCM on performance of the PV panels with high accuracy and stable solutions based on lumped-distributed parameter model. Secondly, the distributed parameter model, has been developed to include a thermal contact conductance with the explicit and implicit discretization. These models have considered the volume change when the phase change from solid to liquid and vice versa. Thirdly, the lumped-distributed parameter model has been used to investigate the impact of the composite paraffin-PCM on the annual electrical output of the PV panel for Baghdad and Milan. Fourthly, the thermosphysical properties of 29 PCMs have been collected and their impacts with different thicknesses have been investigated. Finally, the impacts of different PCMs with different thicknesses and different aluminium (Al) foam percentages on the annual electrical output of the PV panel have been investigated to find the best PCM, the optimal thickness and the best Al foam percentage for each city.

A novel one-dimensional, lumped-distributed parameter model with time and space discretization for the PV-PCM system has been presented and the time independency investigated. The results indicate that the maximum difference between the one second time step and four second time step is 0.7838^{o}C. The results of the lumped-distributed parameter model have been validated against the literature and the maximum relative error is 6.47 percent.

Secondly, an improvement was implemented by adding the thermal contact conductance in lumped-numerical model. Then, three scenarios were studied to assess the impact on the PV panel efficiency of different technical contacts between the PV panel and aluminium container of the PCM. In the first scenario, the PCM is inside an aluminium box attached to the PV panel with thermal contact adhesive. The second scenario is without thermal contact adhesive. In the third scenario, a 0.5 mm air gap is created between the aluminium box and PV panel. The highest electric efficiency difference found is 3.493 percent between the first with third scenarios.

Thirdly, the lumped-distributed parameter model considers the volume change during phase change from solid to liquid. The results of considering the volume change have been compared with not considering it, and the maximum difference was 4.1 percent.

Next, the explicit and implicit methods for the distributed parameter model, have been implemented using the MATLAB software, and the computer runtimes for these methods have been compared with that solution of the lumped-distributed parameter model. The results indicate that the runtimes required for the implicit method of lumped-distributed parameter model and the distributed parameter model to study a transient 18,000 seconds for the PV-PVM system are 16.813 and 525.045 seconds respectively. The computer runtime for the explicit method for the distributed parameter model to study a one second is 51,391.431 seconds. Therefore, the lumped-distributed parameter model presented in this work is proven to be better able to simulate the PV-PCM module, with faster computer runtime compared with implicit and explicit method for the distributed parameter model.

Finally, this lumped-distributed parameter model for the PV-PCM system has been used to investigate the impact of different PCMs, different thicknesses, and different Al foam percentages on the annual electrical output of PV panels in Baghdad and Milan. The results indicate the maximum enhancements for the annual electrical output of PV panel for Baghdad and Milan are 3.19 and 4.11 percent respectively.

List of contain

List of figures

List of tables

Nomenclature for physical quantities their symbols and SI units		
Symbol	**Quantity**	**SI Unit**
T	Absolute temperature	K
T	Celsius temperature = T - 273.15 K	°C
ΔT	Difference or interval	K
T_{ref}	Reference temperature	°C
T_m	Melting temperature	°C
$\bar{T}$	Mean temperature	
G	Solar radiation	W m^{-2}
η	The efficiency of the solar panel	
$\eta_{T\ ref}$	Reference efficiency of the PV cells at the reference temperature	
β_{ref}	Temperature coefficient	
λ	Thermal conductivity	W m^{-1} K^{-1}
α	Absorptivity [radiation]	-
σ	Stefan–Boltzmann constant equals to $5.67 * 10^{-8}$	W. m-2. K -4
ρ	density	kg m^{-3}
β	Absorptivity, volumetric expansion coefficient, tilted angle of a PV panel with a horizontal surface	K^{-1}
ε	Emissivity [radiation]	-
E	Energy, function of time	J
H	Enthalpy [=U+pv]	J
Q	Quantity of heat	J
$\dot{Q}$	Rate of heat	W
$\dot{q}$	Flux [$\dot{Q}$ A^{-1}]	W m^{-2}
C	Heat capacity, light speed	J K^{-1} , m s^{-1}
c_p	Specific heat [constant *pressure*]	J kg^{-1} K^{-1}
h	Heat transfer coefficient, Planck's constant	W m^{-2} K^{-1}
z	Height	m
w	Width	m
δ [$\Delta\ell$]	Thickness	m
x	Distance along path	m
t	Time	s
V	Volume	m^3
$\dot{V}$	Flow rate	m^3 s^{-1}
q	Rate [power]	W = kg m^2 s^{-3}

λ	Wavelength	m
$\boldsymbol{\nu}$	frequency	s^{-1}
I_L	Generated current	A
I_o	Diode reverse saturation current	A
R_s	Series resistance	
R_{sh}	Shunt resistance	
V_{oc}	Open circuit voltage	
P_{mp}	Maximum power	W
I_{mp}	Current at maximum power	
V_{mp}	Voltage at maximum power	
h_{fg}	Heat of fusion	J/kg
$\emptyset$	The percentage of the liquid phase	
μ	Viscosity	
u	Velocity in x direction	m/s
v	Velocity in y direction	m/s
PV	Photovoltaic	
PCM	Phase change material	
m-Si	Mono crystalline silicon	
CN	Crank-Nicolson	
FIB	fully implicit backward	
p-Si	Poly crystalline silicon	
a-S	Amorphous silicon	
CIS	Copper indium sulphide	
CdTe	Cadmium telluride	
C–L	Capric–lauric acid	
C–P	Capric–palmitic acid	
SP22	Commercial blend	
CaCl2.6H2O	Calcium chloride hexahydrate	
EVA	ethylene vinyl acetate	
TED	thermo-electric device	
1D	One dimensional	
nm	Nano meter	$M*10^{-9}$
NOTC	Nominal Operating Cell Temperature	
CFD	Computational fluid dynamics	
td	Tedlar	
Al	Aluminium	
Ra		
g	Gravity acceleration	m s^{-2}
Ra	Rayleigh number	m2 s^{-1}
α	thermal diffusivity	m s^{-1}
u_∞	Wind velosity	m s^{-1}
Pr	Prandtl number	

Re	Reynolds number	
x	Distance along path	m
A, B, C and D	Matrix coefficients	
DNI	Direct normal irradiation	W m^{-2}
GHI	Global horizontal irradiation	W m^{-2}
DHI	diffuse horizontal irradiation	W m^{-2}
NSRDB	National Solar Radiation Database	radius
SRB	Surface Radiation Budget	radius
L_{st}	longitude on which the local time is based	radius
L_{loc}	longitude of the observer	radius
n	Number of discretization, day number	radius
ω	degree of the sun moving across the sky	radius
Z_s	surface azimuth angle	radius
Z	the solar azimuth angle	radius
θ	angle of the incidence	radius
Φ	zenith angle	radius
δ	declination angle	radius
G_b	Direct beam irradiation	W m^{-2}
G_d	Global diffuse irradiation	W m^{-2}
G_{Bt}	Direct beam radiation on a tilted surface	W m^{-2}
G_{Dt}	Diffuse radiation on a tilted surface	W m^{-2}
G_{Gt}	Ground-reflected solar radiation on a tilted surface	W m^{-2}
Ai	Transmittance of the atmosphere for direct solar radiation	W m^{-2}
ρ_g	Reflectance of the ground	
ρ_{comp}	Density of the PCM-foam composite	*kg* m^{-3}
ρ_F	Density of the foam material	*kg* m^{-3}
C_{comp}	Specific heat capacity of the PCM-foam composite	*J* Kg^{-1} $^0C^{-1}$
C_F	Specific heat capacity of the foam	*J* Kg^{-1} $^0C^{-1}$
Subscripts		
i	The node space number, in	
j	*PV, Al and s*	
p	Time step	

o	Out
a	Ambient
s	Solid
L	Liquid
cond	Conduction
conv	Convection
rad	Radiation
ε	Emissivity [radiation]
sky	Sky
Al	Aluminium
PCS	Solid phase
PCL	Liquid phase
g	Glass
in	Inlet
gap	The gap between the PV panel and the aluminium container
ref	The reference temperature 298 K
n	Number of discretization
m	Time step
e	Effective

Chapter One Introduction

1.1 Background of problem

In order to employ the available renewable power resources, many sustainable energy technology developments are in progress to meet future energy demands. This global energy demand may increase by up to 148% from 2012 to 2040 as a result of overall population growth and technology development (Conti et al., 2016). Solar energy is one of the most important types of renewable energy that can help overcome this problem during this period. Figure 1-1 compares the immense amount of solar energy available yearly to the other energy resources available (Perspectives, 2011). The harvest of this energy has rapidly developed, especially using photovoltaic (PV)f cells (Green et al., 2015).

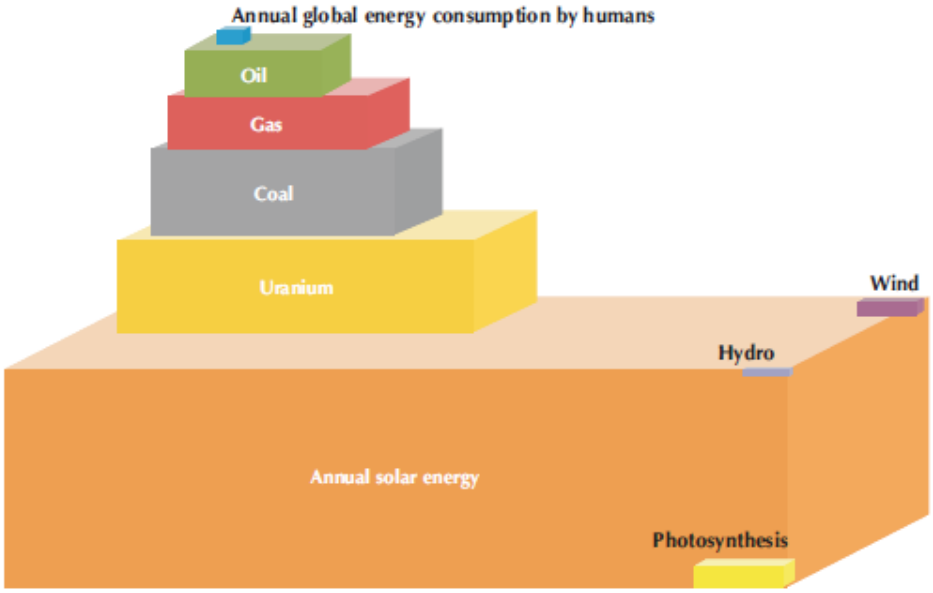

Figure 1-1: Annual sun energy and all possible fossil resources (Perspectives, 2011).

The global installation of solar photovoltaic panels reached 98.9 GW in 2017 alone (Osborne, 2018) with most of this capacity is of monosilicon- and polysilicon-type panels. However, PV panels still present some obstacles. PV cells are devices that convert sunlight directly into electricity; the first one was made by William Becquerel in 1839 using the semiconductor material mentioned in (Allan, 2015). The semiconductor material consists of three main layers: the

gab band, the valence band, and the conduction band. If the photon knocks the electron in the valence band with enough energy, the electron passes through the band gab and generates electricity, while if the photon's energy is not sufficient, the energy converts to heat (Kalogirou, 2009). This heat leads to an increase in the temperature of the PV panel and in turn decreases the efficiency. In addition, this increasing temperature could generate hot spots, which lead to both low-quality voltage output and damage the PV panel due to thermal stress (Bahaidarah et al., 2016). The loss of electrical power output is 0.45% for each 1 °C increase in PV cell temperature above 25 °C (Alami, 2014). Therefore, in order to reduce the problem of high temperatures in the PV panel, active or passive cooling is performed using air, phase-change material (Products), or water as a cooling fluid (Ho et al., 2015).

One promising passive cooling technique used to reduce PV cell temperature is a PCM, which is incorporated into the back surface of a PV panel. The most important feature of a PCM is that it can absorb a large amount of heat when the solid phase changes to a liquid phase at a constant temperature. This feature can be used to manage PV cells at a uniform and desired temperature without having to consume extra power to circulate coolants. Initially, a PCM absorbs heat energy sensibly until reaching the melting temperature (Browne et al., 2015), and the temperature remains constant within the melting boundary. This melting boundary moves in the opposite direction of the PV cell. The absorbed heat rate is represented by the speed of this movement, which is a function of the thermo-physical properties of the PCM and its latent heat capacity. Finally, the stored heat inside the PCM is released into the air at night. These processes lead to a decrease in PV panel temperatures and an increase in the efficiency of PV panels.

Based on the literature review, several research techniques have been developed. These include one-dimensional models to investigate the impact of the PCM on the performance of PV panels. These studies have used either implicit or explicit methods, which consume computing time. In addition, the literature models have not considered the thermal-contact conductance of the PV panel with the PCM container. In addition, these models have not considered the volume change that occurs when the phase changes from solid to liquid or vice

versa. Furthermore, the low thermal conductivity of the PCM is one of the most significant drawbacks in that it reduces the cooling effectiveness of the PCM.

In summary, although PV-PCM panel systems have been developed in the last few years to be used worldwide, this system could be further developed to work more efficiently. The temperature of stand-alone PV panels can reach in excess of 80 °C. This high temperature could decrease the efficiency of the panel by 0.4 to 0.5% with each 1 °C above 25 °C (Huang, 2011a). In addition, the quality of the electricity output decreases with the temperature differences. Therefore, this study will develop a mathematical and numerical PV-PCM model. A new one-dimensional numerical method will be used to study the temperature distribution of both the PV-PCM system and a novel combination of the PV-PCM system with Al metal foam will be studied.

1.2 Aim and objectives

The aim of this study is to investigate the impact of the PCM on the annual electric output of the PV panel. The main objectives include:

1. A new model for the PV-PCM will be presented based on the lumped-distributed parameter model. The results will be compared to the distributed parameter model.
2. These two models for the PV-PCM will be developed to include thermal contact conductance.
3. These two models will be developed to consider the change in volume of the PCM during the phase change.
4. These two models will be solved based on the explicit and implicit numerical methods. The time computing time consumption for these three solutions will be compared.
5. The stability analysis for these three solutions will be implemented using von Neumann's method.
6. The impact of a composite paraffin PCM on the annual electrical output of PV panels in Baghdad and Milan will be investigated.

7. The impact of using different aluminium foam percentages with different PCMs of different thicknesses on the annual electrical output of PV panels in Baghdad and Milan will be investigated.

1.3 Thesis structure

1.3.1 Chapter one

This chapter highlights the main research problem and introduces the aim and the objectives.

1.3.2 Chapter two

In this chapter, the physics of PV cells, namely heat generation and its negative impact on PV cells' performance, will be discussed in detail. Furthermore, the literature on passive air cooling, floating PV panel cooling, the incorporation of the PCM, and thermo-electric device (TED) with PV panels has been reviewed. Finally, this chapter will launch the motivation for this PhD work.

1.3.3 Chapter three

This chapter presents four contributions. First, 1D thermal analysis of the PV-PCM system has been introduced. A lumped-distributed parameter model and a fully distributed model for the PV-PCM have been introduced. Second, these two models have been developed to include the thermal contact conductance between the PV panel and the PCM container. Also, the volume change during the phase change has been considered for the both models. Finally, a lumped model for the stand-alone PV panel has been introduced.

1.3.4 Chapter four

This chapter introduces the space and the time discretization for the three mathematical models. Then, the von Neumann method used to investigate the stability of the numerical solution methods.

1.3.5 Chapter five

This chapter presents the results of the mathematical models, including the validation work for the implicit and lumped-numerical models for the PV-PCM module and for the stand-alone PV panel. In addition, the impact of different thermal contact conductance will be investigated. Moreover, the impact of the volume change during the phase change will be studied. Finally, a comparison of the run time taken of the explicit, implicit, and lumped-numerical models for the PV-PCM module will be illustrated.

1.3.6 Chapter six

This chapter presents the sources of solar radiation and how to calculate solar radiation on an inclined surface using the measured solar radiation of a horizontal surface. Then, the yearly solar radiation will be used to study the impact of the PCM on the electrical power and temperature of PV panels in Baghdad and Milan.

1.3.7 Chapter seven

In order to determine the best PCM types with optimal thicknesses to produce maximum electrical power from the PV panel, first a range of the PCMs with thermophysical properties will be collected. Then, the impact of PCMs with different thicknesses on the electrical output of the PV panel will be investigated. Next, a model to predict the thermophysical properties of PCMs with metal foam will be implemented. Finally, this chapter presents the impact of the different PCMs with different Al foam percentages and different thicknesses on the annual performance of PV panels in Baghdad and Milan.

1.3.8 Chapter eight

This chapter will state the conclusions and recommendations for future work.

Chapter Two Literature Review

2.1 Outline

In this chapter, the physics of PV cells, namely heat generation and its negative impact on PV cells' performance, will be discussed in detail. Furthermore, the literature on passive air cooling, floating PV panel cooling, incorporation of the PCM, and TED with PV panels will be reviewed. Finally, this chapter will explain the motivation for this PhD work.

2.2 Solar panel

2.2.1 Solar panel physics

In order to demonstrate the principle of the PV cell, general and specific information about the materials and semiconductor are required. This basic information, such as the conductivity of the materials, the recombination, the p-n junction, and the PV effect, will lead to an understanding of electric and heat generation. In addition, the precise part of the PV cell in which heat and electricity are generated will be described.

2.2.1.1 The semiconductor material and recombination phenomenon

Generally, the materials are divided into three groups: conductive, insulator, and semi-conductive materials. All the materials consist of atoms, each of which contains a nucleus and electrons. The electrons rotate around the nucleus in different orbitals depending on the energy bands (Kalogirou, 2009). As depicted in Figure 2-1, the insulator materials only have electrons in the filled band, which is nearest to the atom, and require very high energy in order to exit to other energy bands. Second, the conducting materials have electrons in the conduction band. Here, these electrons are responsible for heat and electrical conductivity (Kalogirou, 2009). Third, the semiconductor materials have valence electrons in the valance band from which these electrons can exit and move to the conduction band. The energy that is needed to move an electron from the valence band to the conduction bands is called the energy gap. When the incident light is

absorbed by the semiconductor, if the photon energy is insufficient, this energy converts to heat. However, if the energy is sufficient, the electron passes through the band gap and moves to the conduction band (Kalogirou, 2009). This photon energy (E) (watts) depends on the frequency where the light speed (C) (m/s) is the frequency (v) (s^{-1}) multiplied by the wavelength (λ) (m):

$$\boldsymbol{C = \lambda . \nu} \qquad 2\text{-}1$$

$$\boldsymbol{E = h . \nu} \qquad 2\text{-}2$$

where h is the Planck's constant. However, after a short time and before producing an electrical current, this electron wastes its energy and goes back to its valance band, producing heat and photon. This phenomenon is called recombination, which prohibits the electric power production (Duffie and Beckman, 2013a, Hersch and Zweibel, 1982). Therefore, to overcome this problem of recombination, the p-n junction is introduced. The p-n junction is explained in the next section.

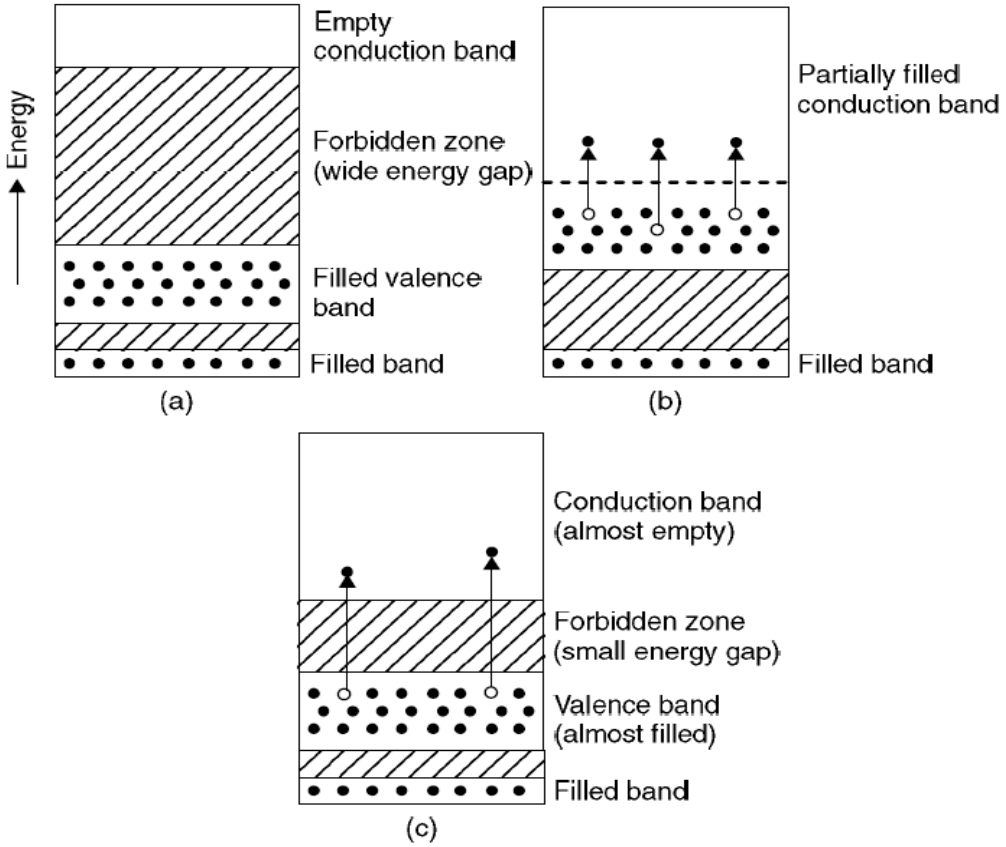

Figure 2-1: The different bands of energy for the a. insulator, b. conductor, and c. semiconductor materials (Kalogirou, 2009).

2.2.1.2 The p-n junction

In order to prevent the recombination of the electron with a hole in the semiconductor, a potential barrier has been introduced using the p-n junction (Duffie and Beckman, 2013a). This p-n junction consists of two different layers of doping silicon. The first layer, called n-type silicon, has a high intensity of electrons, while the second layer, referred to as p-type silicon, has a high intensity of holes, which is the result of doping these layers with phosphor and boron, respectively (Duffie and Beckman, 2013a). When n-type silicon, with an excess of electrons, connects to p-type silicon, which has a deficiency of electrons, a number of the electrons diffuse from the n-type silicon to the p-type silicon, and a number of holes diffuse in the opposite direction. The diffusing transporter currents combine to form the diffusion current , which drifts from the p-type side to the n-type side. The holes that drift to the n-type silicon rapidly re-associate with the electrons along the junction, while, similarly, electrons diffused to the p-type side will rapidly recombine with the holes there. Thus, there will be a depletion region formed on both sides of the junction, with the p-type side being negatively charged and the n-type side being positively charged (Gray, 2003). The charges will establish an electrical field across the depletion region, resulting in built-in potential across the region. In the classical silicon PV cell, the thickness of the n-type side is approximately $0.5*10^{-6}$ m, while the thickness of the p-type side is approximately $0.25*10^{-3}$ m (Kalogirou, 2009).

2.2.1.3 The electric and heat generation in the PV panel

An electrical current is produced when the incident light with sufficient energy within an appropriate wavelength range impinges on a semiconductor PV cell. However, if the photon does not have enough energy, heat will be generated in the local position of the atom, which is known as thermalisation. In contrast, if the photon has very high energy, part of this energy will be used to generate free electrons, and the rest will be converted to heat (Hersch and Zweibel, 1982).The electrical generation process is explained in more detail in Figure 2-2. As previously mentioned, each p-type side and n-type side is formed from semiconductor material; when a photon with enough energy hits the electron in the valence band, the electron will move to the conducting band and produce the

electron and hole. The electrons will then move to the n-type side and accumulate there, while the holes accumulate on the p-type side (Markvarta and Castañerb, 2011). This will lead to voltage differences between the n and p sides. As depicted in Figure 2-2, the metal grid above the n-type side is used to collect electrons, while the metal sheet is used underneath the p-type side (Gray, 2003).

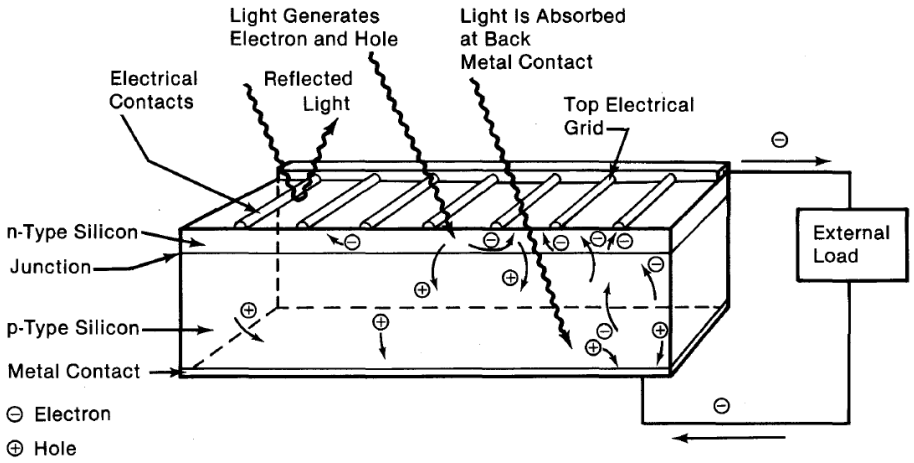

Figure 2-2: A schematic of the solar cell operation process (Hersch and Zweibel, 1982).

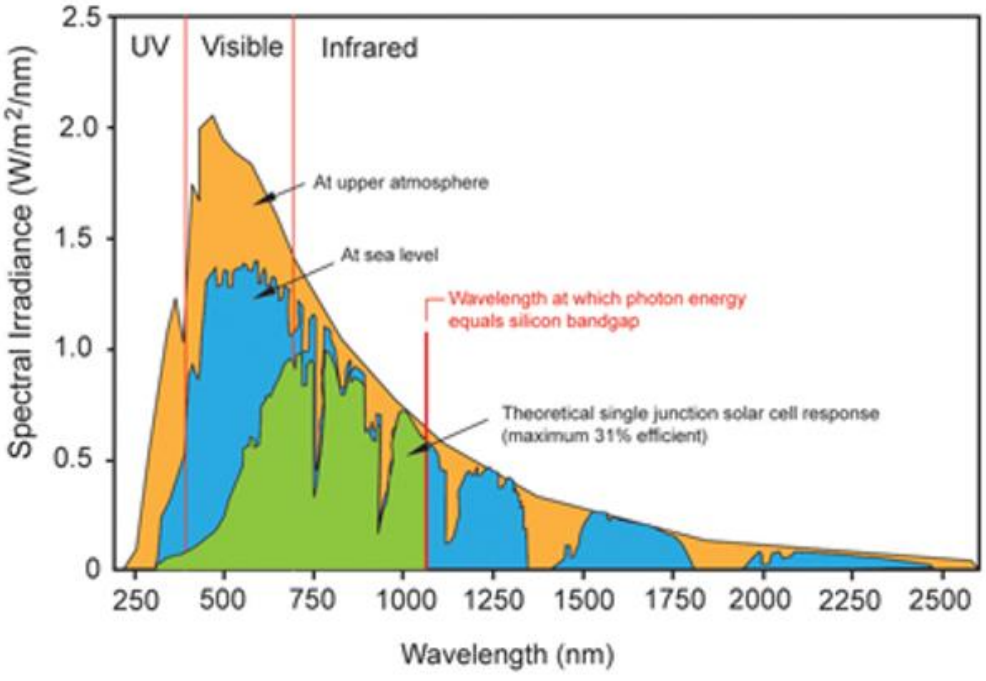

Figure 2-3: The reflected and absorbed incident light by the crystalline silicon PV cell (Santbergen and van Zolingen, 2008).

Figure 2-3 depicts the total spectral irradiance, which reaches to the upper atmosphere and to sea level corresponding with wavelengths of sunlight. In

addition, the useful theoretical spectral irradiance for the PV cell (31% efficiency) corresponding with wavelength bands. It can be seen that the useful wavelength is limited to between 300 nm and 1150 nm. Therefore, the remaining wavelengths are converted to heat energy inside the PV cell.

However, the different PV cell types have different band gaps depending on the material used in each type. These differences in band gaps lead to the harvest of various ranges of sunlight wavelengths (Haller et al., 2013). Figure 2-4 illustrates the useful range of wavelength for each type of PV cell. The x-axis represents the wavelength in nanometres, while the y-axis represents the quantum efficiency, that is, the proportion of the collected carriers to the photon number by the PV cells with specific wavelengths of sunlight (Haller et al., 2013). The symbols m-Si, a-Si, CdTe, and CIs represent the different types of PV cells, namely, monocrystalline silicon, amorphous silicon, cadmium telluride, and copper indium selenide, respectively. Comparing Figure 2-3 and Figure 2-4, it can be seen that there is a massive percentage of sunlight, which is absorbed by the semiconductor and is not converted to electricity; instead, it is converted to heat.

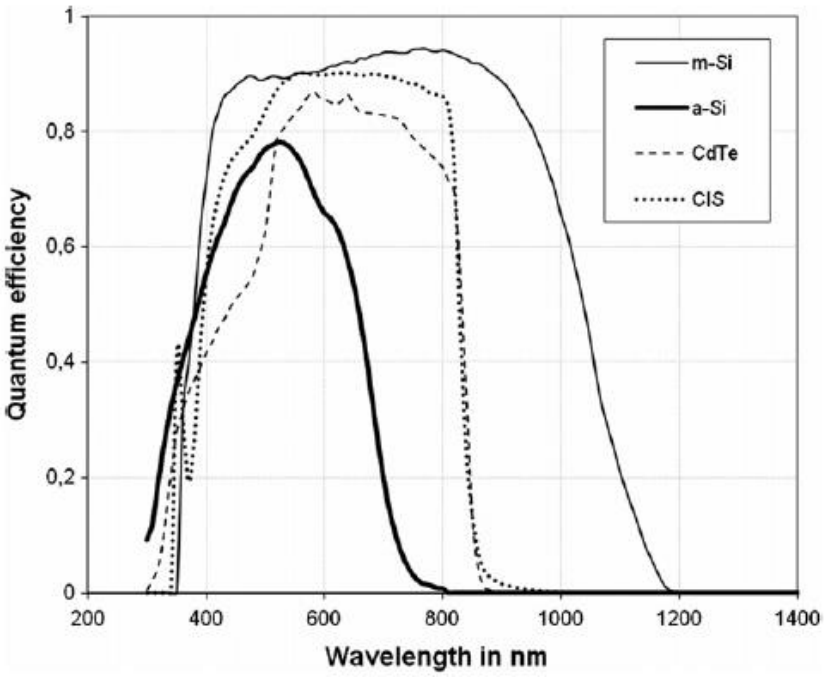

Figure 2-4: A plot of quantum efficiency against solar wavelength for a types of PV cells: m-Si, a-Si, CdTe, and CIs (Haller et al., 2013).

Table 2-1 can be used to calculate the percentage of power that is converted to heat from the detrimental wavelength bands of sunlight. This table depicts the energy percentages corresponding to the wavelength bands of terrestrial sunlight.

Table 2-1 The energy band percentage corresponding with wavelength for the solar irradiation (Duffie and Beckman, 2013a).

Energy Band (%)	Wavelength Range (Nanometers)	Midpoint Wavelength (Nanometers)
0–5	280–416	385
5–10	416–458	439
10–15	458–492	475
15–20	492–525	508
20–25	525–559	542
25–30	559–592	575
30–35	592–627	609
35–40	627–662	644
40–45	662–700	680
45–50	700–741	719
50–55	741–786	764
55–60	786–835	808
60–65	835–885	859
65–70	885–970	917
70–75	970–1038	100
75–80	1038–1140	107
80–85	1140–1257	120
85–90	1257–1541	131
90–95	1541–1750	163
95–100	1750–4000	219

2.2.2 Types of PV cells

Several types of PV cells have been developed using various materials, such as crystalline silicon, thin film, organic (polymer), hybrid PV cells, and dye-sensitised cells, as depicted in Figure 2-5 (Bahrami et al., 2013). The overall worldwide production capacity of PV cells reached approximately 40 GW in 2013 (Pandey et al., 2016). In the 1950s, the highest efficiency of solar cells (10%) was achieved using silicon cells (Bahrami et al., 2013). Other types have rapidly developed, for example, the multi-junction solar cell, which has achieved maximum efficiency, reaching 46% in 2016. This section will describe several materials that are used in PV cells.

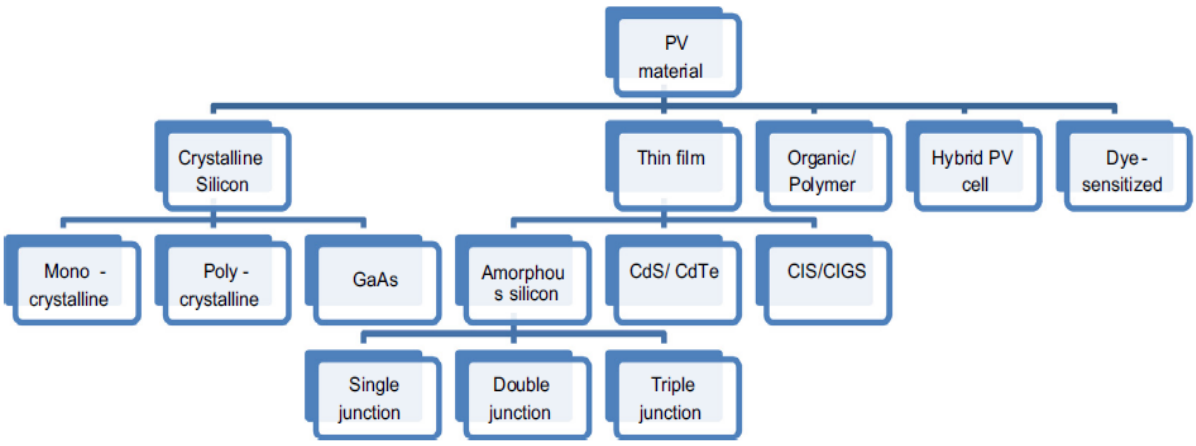

Figure 2-5: The classification of PV cells (Pandey et al., 2016).

Crystalline silicon cells are categorised into three main types: polycrystalline, monocrystalline, and gallium arsenide cells. Polycrystalline silicon cells are produced by casting high pure molten silicon. This cast is then sliced into the appropriate sizes, and the slices are used to produce PV cells (Bagher et al., 2015). Monocrystalline cells are produced from very high pure silicon to achieve the crystal lattice, which extends to the edge. Monocrystalline cells have a high efficiency and low cost compared to polycrystalline cells; the reported efficiencies of monocrystalline and polycrystalline cells are 25.6% and 20.8%, respectively (Pandey et al., 2016). Both types consist of six main layers – glass, ethylene vinyl acetate (Li et al., 2014), cell, EVA (ethylene vinyl acetate), back sheet (some also produce Tedler, which is a polymer sheet), and the frame (PVeducation.org, 2017) (see Figure 2-6). The dimensions of these layers along with the thermos-physical properties are listed in Table 2-2.

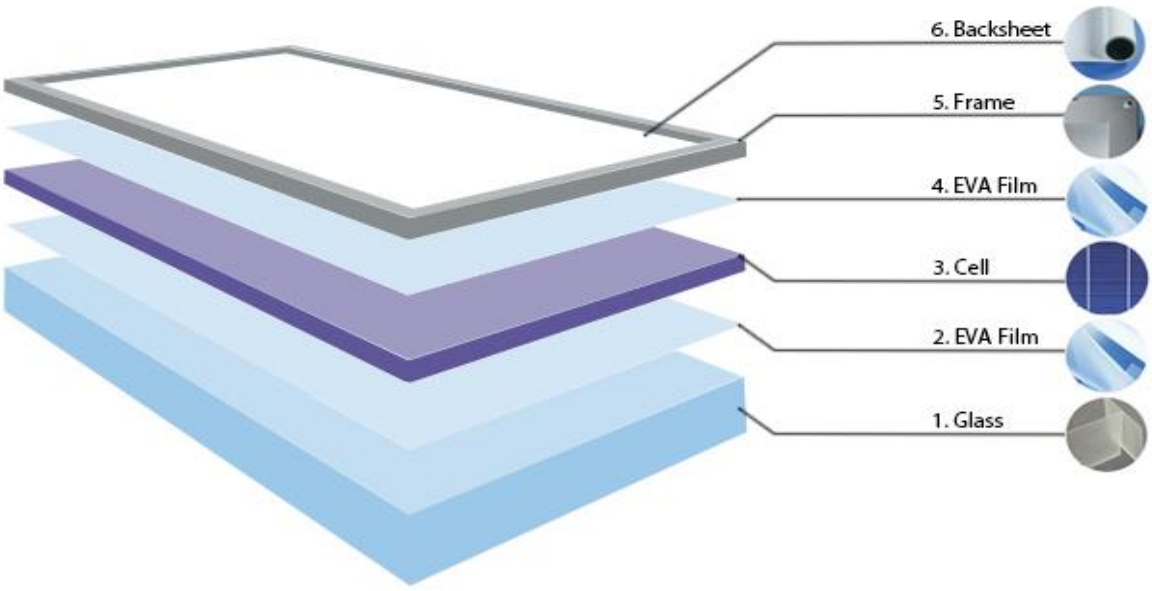

Figure 2-6: The layers of monocrystalline and polycrystalline cells (Renogy, 2016).

Table 2-2: The thicknesses and the thermos-physical properties of silicon PV cell layers (Kant et al., 2016).

PV layers	Density kg/m^3	Specific heat Jkg^{-1}K^{-1}	Thickness m	Thermal conductivity W m^{-1}K^{-1}
Glass face	3000	500	0.003	1.8
EVA	960	2090	0.0005	0.35
Silicon cells	2330	677	0.0003	148
Polyester/ Tedler Trilamiate	1200	1250	0.0005	0.2

The thin film cell is different from the crystalline silicon cells, where a thin layer of the semiconductor deposits on a substrate. This substrate can be metal, plastic, or glass. The light thickness layer ranges from between nanometres to ten micrometres (Bagher et al., 2015). This type is classified into three groups: amorphous silicon, cadmium telluride CdTe, and copper indium gallium diselenide CIGS. The silicon is non-crystalline, and the thickness is very thin (5–

20 micrometres). This kind of PV cell is promising because it is cheaper than crystalline cells, but the efficiency is lower. This type has been developed to produce CdTe and CIGS, which have higher efficiencies (21% and 20.5%, respectively) (Pandey et al., 2016). The primary layers of CdTe and CIGS cells are depicted in Figure 2-7.

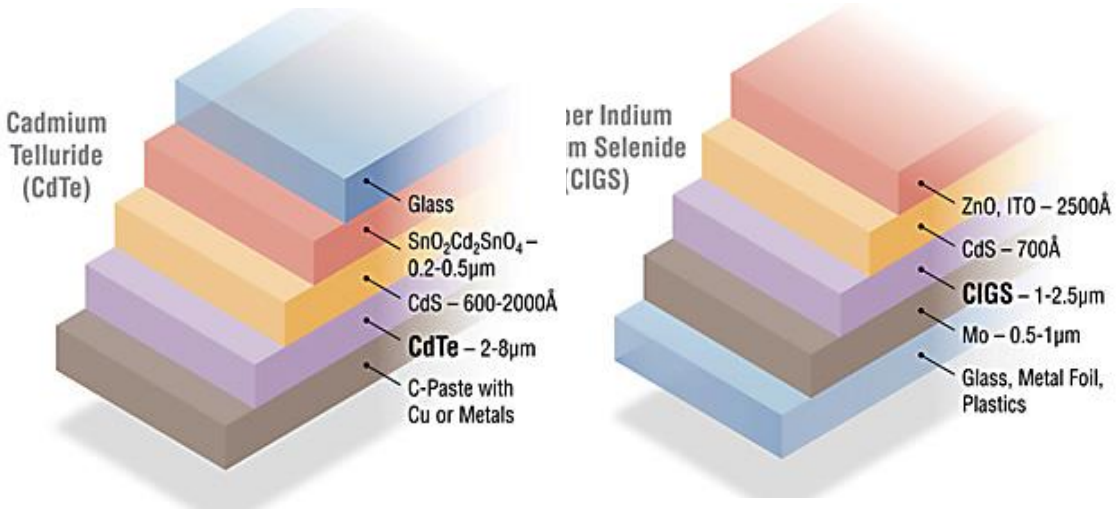

Figure 2-7: The layers of CdTe and CIGS cells (NERL, 2016).

Polymer cells are constructed from a conjugated polymer, which works as a semiconductor. The electron can be moved when it receives energy from the photon to achieve the photovoltaic effect (Bagher et al., 2015). Polymer cells have potential advantages owing to their favourable properties, such as their low cost of production, flexibility, and low weight. In addition, polymer cells can be produced by printing or coating because they can be produced from the solution (Bagher et al., 2015). However, the reported efficiency of 11% is still low.

The hybrid PV cell has high performance compared to the silicon solar panel. However, the cost of this type of cell is still high compared to that of the organic solar panel. Therefore, organic and non-organic cells are combined to produce a low-cost and high-efficiency hybrid PV cell (Pandey et al., 2016). The combination is explained in Figure 2-8.

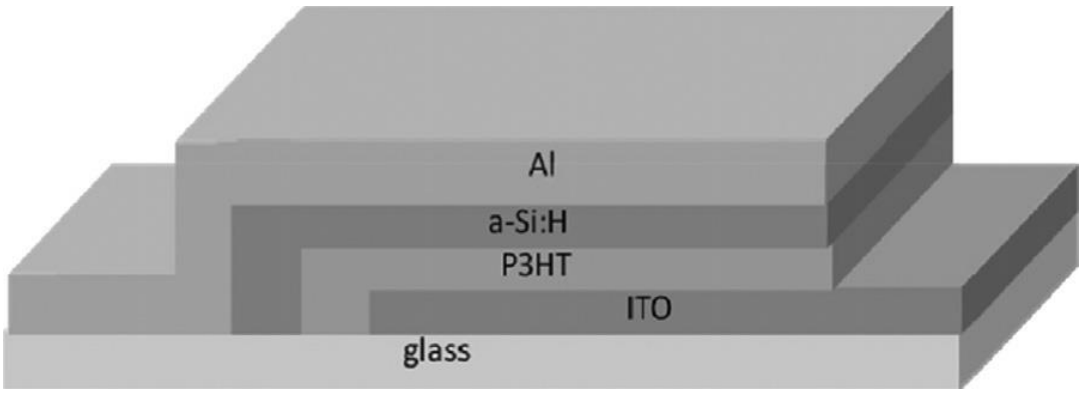

Figure 2-8: The layers of the hybrid solar cell (Zhang et al., 2014).

Finally, the dye-sensitised cell was discovered by Graetzel and O'Regan in 1991. This type of cell has several advantages, one of which is that it can be produced by conventional roll-printing, making it cost-effective. In addition, the dye-sensitised cells are semi-transparent and semi-flexible, thus there are more possible applications for and opportunities to use this type of cell. However, there are developments underway to eliminate obstacles to chemical stability (Bagher et al., 2015).

2.2.3 The electrical and temperature parameters

2.2.3.1 The physics behind the effect of high temperatures on the PV cell output

It is relatively complex to physically demonstrate the impact of temperature on the performance of the PV cell. There are two main drawbacks when the temperature of the PV cell is increased. First, the silicon semiconductor will degrade as a result of lattice vibration (Hersch and Zweibel, 1982). Second, the voltage produced will decrease, leading to decreased power output. The voltage decreases as a result of a decrease in the charge of the depletion region, which appears on both sides of the p-n junction. If the temperature of the PV cell increases, a number of the electron-hole pairs will be separated on both the p-type side and n-type side. On the n-type side, the holes will cross to the p-type side, and the free electrons will accumulate on the n-type side. In contrast, on the

p-type side, the electrons cross to the n-type side. This phenomenon leads to a decrease in the charge of the p-n junction and in turn decreases the voltage and power output. In addition, at high temperatures, the silicon p-n junction loses its function completely for the silicon cell type, and no voltage is produced, as depicted in Figure 2-9 (Hersch and Zweibel, 1982).

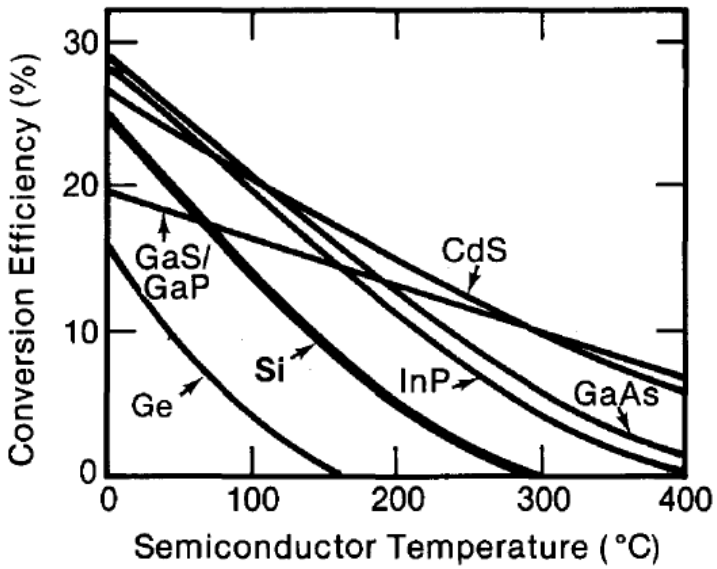

Figure 2-9: The effect of temperature increases on PV cell efficiency (Hersch and Zweibel, 1982).

2.2.4 The electric parameters

The voltage-current (I-V) curve can be calculated under different solar intensities and different PV cell temperatures to evaluate the performance of solar panels. A simple module to describe the I-V relationship can be used to accurately predict the PV cell output (Kalogirou, 2009). The equivalent circuit for the solar panel is depicted in **Figure 2-10**, and the model is (Fu and Tong, 2010):

$$I = I_L - I_D - I_{sh} = I_L - I_o \left[exp[\frac{q[V + IR_s]}{nkT}] - 1\right]$$

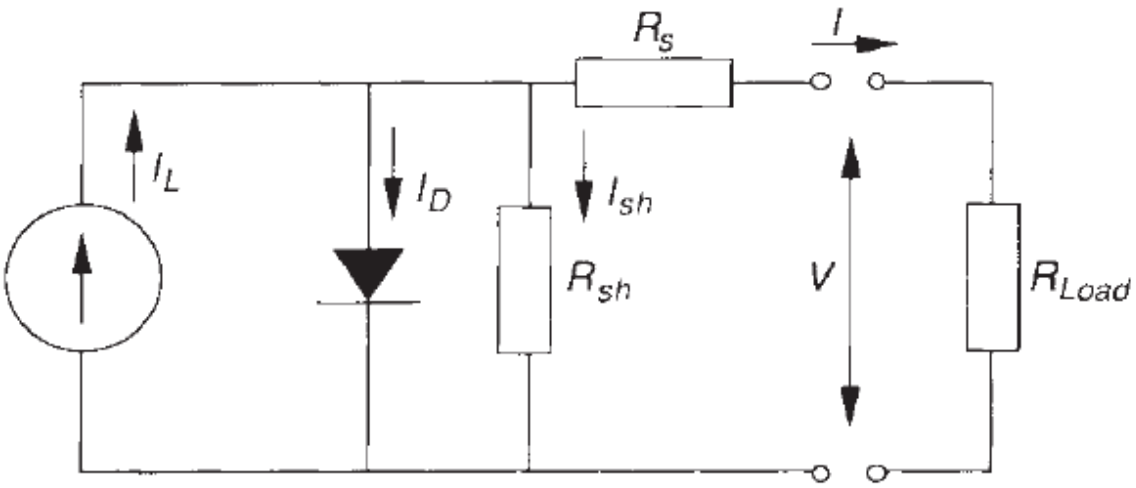

Figure 2-10: The equivalent circuit of the PV cell (Kalogirou, 2009)

Where I_L is the generated current, I_o is the diode reverse saturation current, R_s is the series resistance, and R_{sh} is the shunt resistance. All five parameters depend on the temperature and solar intensity; therefore, the efficiency of the PV cell depends on the temperature as well as solar radiation. These parameters are usually measured by the factory according to the reference conditions, which are 1000 W/m^2 and 25 °C. Figure 2-11 depicts the relationship between the voltage and the current where the x-axis is the voltage and the y-axis is the current (Kalogirou, 2009). From Figure 2-11, it can be seen the current decrease slightly until the voltage is 15 V; then the current decreases dramatically until the voltage is 21.4 V, which represents the open circuit voltage (V_{oc}), while the maximum power (P_{mp}) can be obtained by determining the p-v relationship, which occurs at I_{mp} and V_{mp}. This optimal power depends on the load resistance (Kalogirou, 2009). Therefore, to obtain the desired voltage or desired current, the PV cells are connected in parallel or in series. While, if the five PV cells are connected in parallel or in series, the current increases by five times.

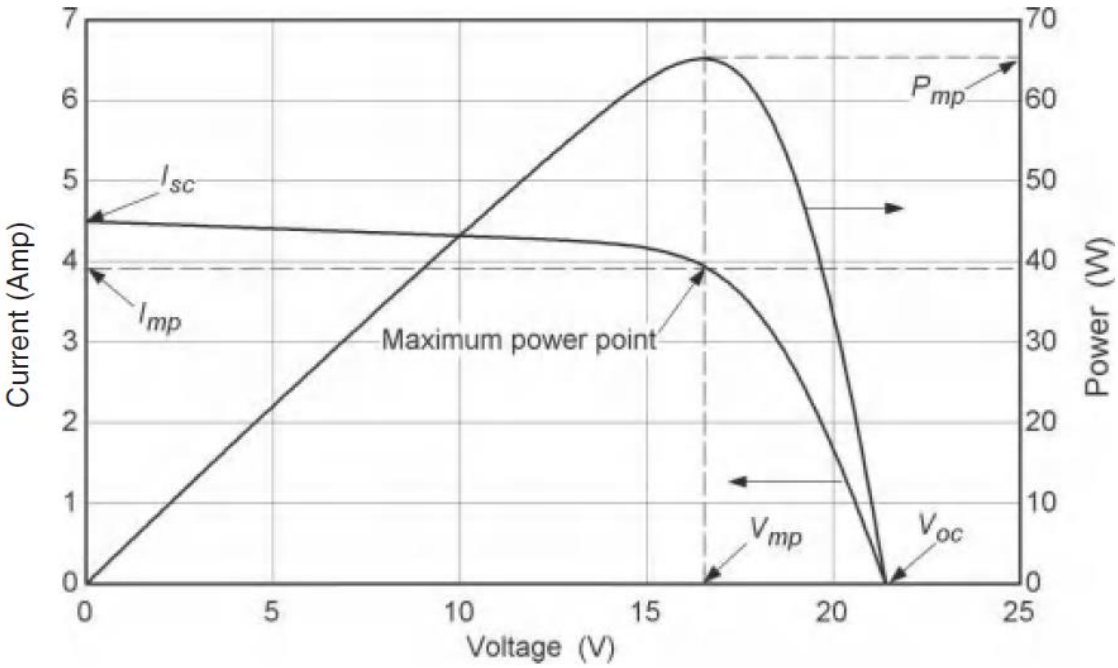

Figure 2-11: I-V and P-V relationship (Kalogirou, 2009).

2.2.5 The temperature parameter

Several studies have pointed out that temperature has a significant impact on the performance of PV cells (Fesharaki et al., 2011). To investigate the impact of temperature on the performance of the PV panel as a whole, Equ 2-3 can be used (Fesharaki et al., 2011):

$$\eta = \eta_{T\,ref}\left[1 - \mu_{ref}\left(T_{pv} - T_{ref}\right) + \gamma \log_{10} I(t)\right] \quad \textbf{2-3}$$

Where η is the efficiency of the solar panel, $\eta_{T\,ref}$ is the reference efficiency of the PV cells at the reference temperature T_{ref}, and μ_{ref} is the temperature coefficient, which is different for each type of PV cell. The $\eta_{T\,ref}$ and β_{ref} are given by the factory and are tested under specific conditions according to the ASTM where the solar radiation intensity and the T_{ref} are 1000 W/m^2 and 25 ℃, respectively (Singh and Ravindra, 2012). Fesharaki et al. (2011) have illustrated the relationship between temperature and PV cell efficiency. The results show that the efficiency increased when the temperature decreased from 75 °C to 0 °C, as depicted in Figure 2-12. Several studies have pointed out that temperature

has a significant impact on the performance of PV cells (Fesharaki et al., 2011). To investigate the impact of temperature on the performance of the PV panel as a whole, Equ 2-3 can be used (Fesharaki et al., 2011):

2-3. The efficiency of different types of PV cells has been tested with different temperatures by Hashim (2015). The types of PV cells tested are monocrystalline silicon (m-Si), polycrystalline silicon (p-Si), amorphous silicon (a-S), copper indium sulphide (CIS), cadmium telluride (CdTe), and dye-sensitised solar cells (DSC). The results indicate that the efficiency decreases as the temperature increases for most types of PV cells, while the DSC had different results, as shown in Figure 2-13.

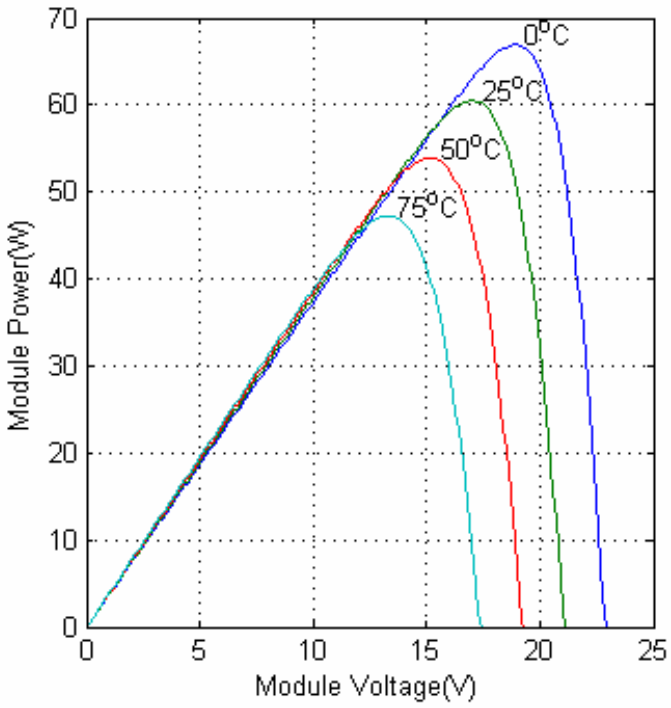

Figure 2-12: The relationship between the PV cells power, voltage and temperature (Hashim, 2015).

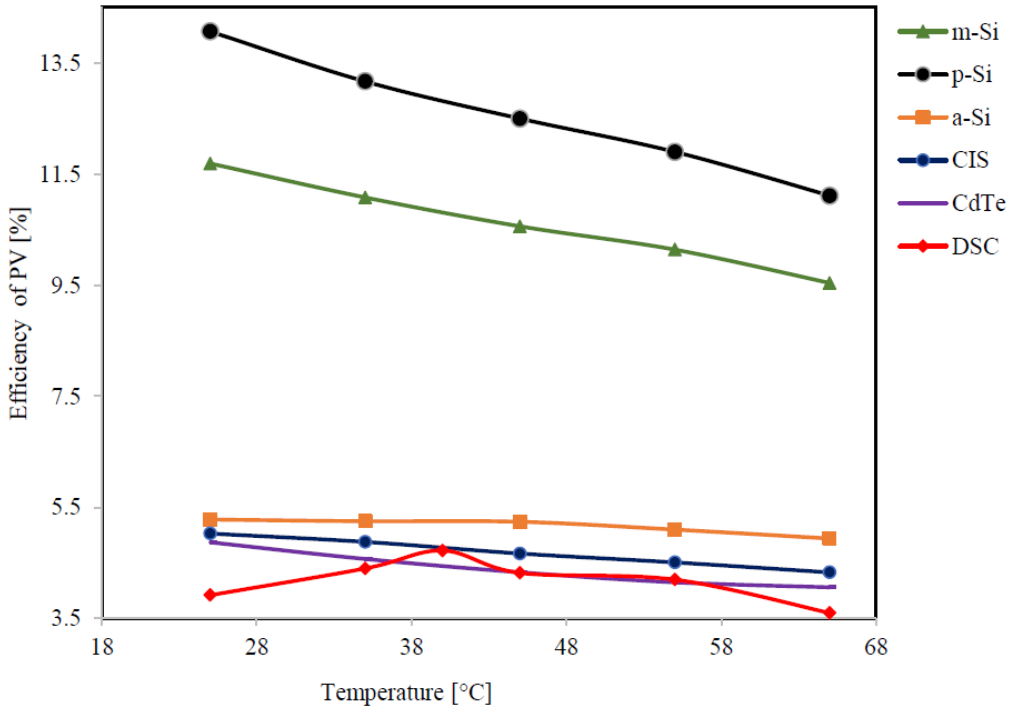

Figure 2-13: The relationship between different types of PV cell efficiency and the temperature.

Several empirical equations have been developed to predict solar panel temperature (T_{pv}), which depends on the ambient temperature (T_a), wind speed, Nominal Operating Cell Temperature (NOCT), reference efficiency, and the temperature coefficient. First, the standard formula describes the T_{pv} in Equation 2-4:

$$\boldsymbol{T_{pv} = T_a + \frac{I}{I_{NOCT}}(T_{NOCT} - T_{a,NOCT})} \qquad 2\text{-}4$$

where T_a and I are the ambient temperature and the solar radiation, respectively. T_{NOCT} is the NOTC at I_{NOCT}= 800 W m^{-2}, $T_{a,NOCT} = 20$ °C, and air velocity is 1 m/s. In addition, T_{NOCT} depends on the type of PV cell (Schwingshackl et al., 2013). Second, Skoplaki has developed a more accurate equation, which considers more parameters:

$$\boldsymbol{T_{pv} = T_a + \frac{I}{I_{NOCT}}\left(T_{NOCT} - T_{a,NOCT}\right).\frac{h_{w,NOCT}}{h_{w,v}}\left(1 - \frac{\eta_{T\,ref}}{\tau.\alpha}(1 - \beta_{ref}.\eta_{T\,ref})\right)} \qquad 2\text{-}5$$

where τ and α can be considered 0.9 and $h_{w,v}$ is the heat transfer coefficient, which depends on the air velocity, as expressed in Equation 2-6, while $h_{w,NOCT}$ is the heat transfer coefficient at a velocity of 1 m s^{-1} (Schwingshackl et al., 2013):

$$h_{w,v} = 8.91 + 2\,v_{air} \qquad 2\text{-}6$$

where v_{air} is the air velocity. Third, Koehl has suggested a simple equation to predict the temperature of the PV cell:

$$T_{pv} = T_a + \frac{I}{U_0 + U_1 v_{air}} \qquad 2\text{-}7$$

Where U_0 and U_1 are specified by Koehl. Using Equations 2-4, 2-5, 2-6, and 2-7, the temperature of the solar panel can be calculated using three methods. However, these methods do not accurately calculate the temperature of the PV cell because they do not consider the effect of natural convection.

In summary, first, some of the sunlight energy converts to heat inside the PV cells and increases the PV cell temperature. This temperature increase leads to a decreased PV cell efficiency and increased degradation of the PV cell. Second, the non-uniform temperatures of the PV panels lead to different voltage outputs. These differences in voltage output lead to complicated problems when connecting them electrically.

2.3 Cooling methods for the PV panel

In order to overcome the problems that result from an increased temperature in the PV panel, different PV panel cooling methods have been studied within the literature. The main cooling methods consist of air cooling, liquid cooling, thermoelectric cooling, and PCM cooling, as shown in Figure 2-14. Both the forced air and forced liquid cooling consume high levels of electrical power to circulate the fluid, and they require maintenance (Shukla et al., 2017). Therefore, this literature review will only discuss natural air cooling, floating cooling, thermoelectric cooling, and PCM cooling for PV panels.

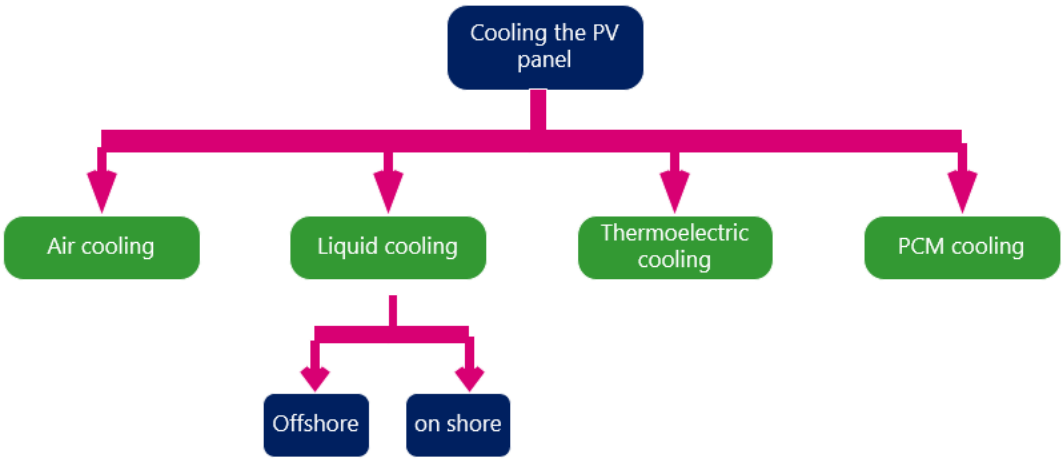

Figure 2-14: Main cooling methods for PV panels

2.3.1 Natural air cooling for PV panels

Usually, the air works as a natural coolant for PV panels due to wind and natural convection. Some studies, such as a study conducted by Mittelman et al. (2009), tried to increase natural air convection using an open air channel with PV panels. They used Fluent software to study the impact of the different depths of the channel. They assumed that the ambient wind speed was 1 m s^{-1}. The results indicate that the maximum air speed generated inside the channel was approximately 1.1 m s^{-1}. However, they claimed that the temperature of the PV panel with an open air channel was lower than that of the PV panel without an open air channel by 10–20 K.

2.3.2 Cooling floating PV panels

In order to improve the efficiency of floating PV cells, several projects and research studies have implemented different cooling methods.

The Aichi project (20 kW) compared two floating groups; the first one used the water spray cooling method, and the second one did not (Trapani and Redón Santafé, 2015). The efficiency of the first group increased by 9.6% (with the temperature dropping to 25 °C) compared to that of the second group. However, this system used extra power to circulate and spray the water, which meant extra costs and running power consumption.

Similarly, the efficiency of the Hapcheon 500 kW floating PV power plant, which was tilted to 33°, was compared to that of the Haman 1 MW land PV power plant, which was tilted to 30° (Choi, 2014). The distance between the two plants is 60 km. The results indicate that the efficiency of the floating system was 10.3% higher than that of the land power plant; Choi (2014) claimed that this efficiency was due to the cooling effect. However, no cooling system was used by the plant. In contrast, Sahu et al. (2016) stated that this efficiency improvement was the result of the transfer of heat from the PV panels to the water by the aluminium structure. However, it can be seen in Figure 2-15 that the temperature differences between the floating and land PV panels are not significant, while studies of PV cells have stated that their efficiency can improve by 0.4–0.5% for every 1 °C drop (Huang, 2011a). Figure 2-15 shows that the temperature differences are less than 10 °C, and sometimes the land PV power plant has a lower temperature than the floating PV power plant. This means this temperature difference is not enough to improve the PV cell efficiency by 10.3%. Therefore, this improvement could be the result of the different tilt angles of these power plants or other factors.

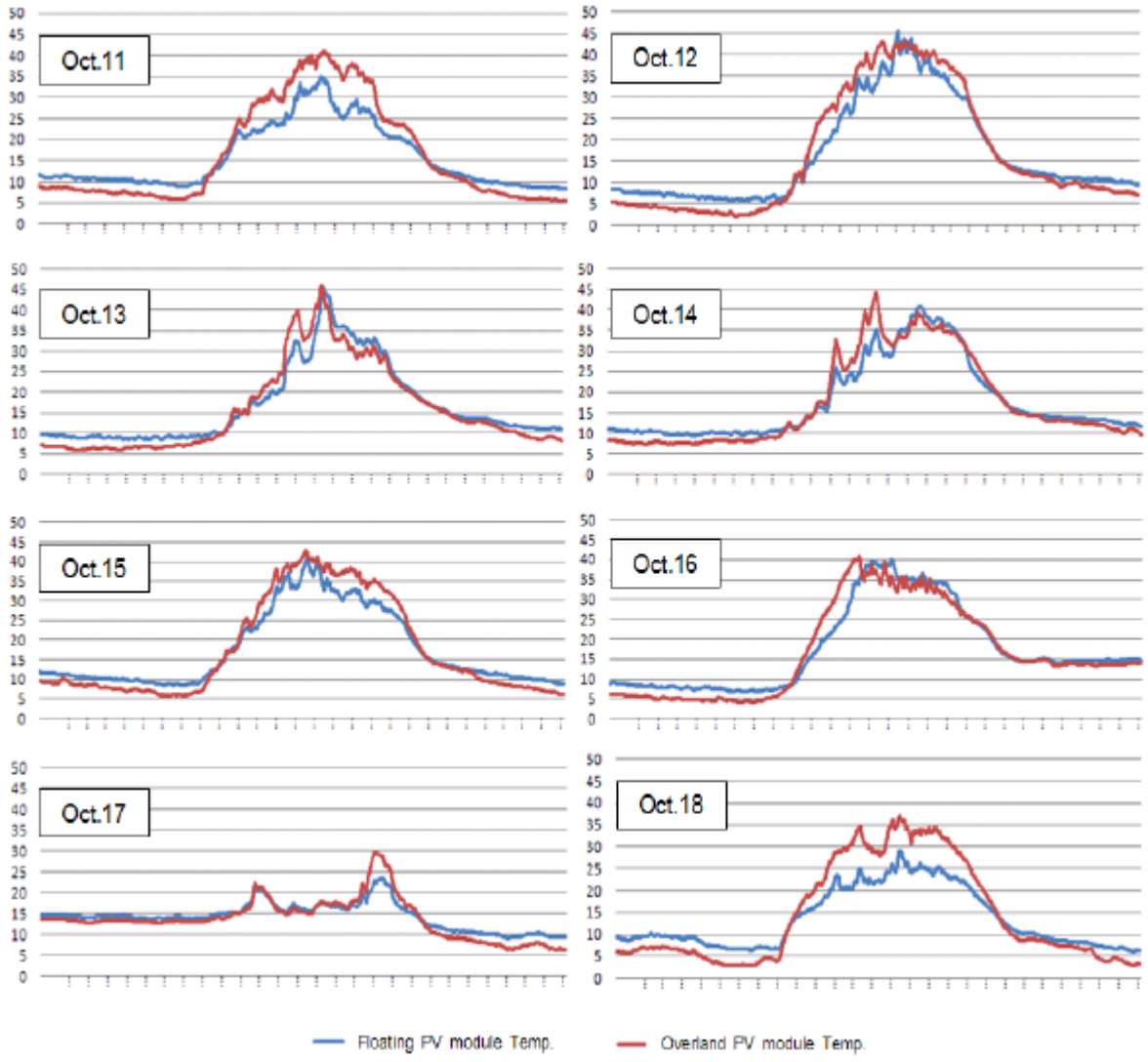

Figure 2-15: PV Cell temperature differences between the Hapcheon 500kW floating PV power plant and the Haman 1MW land PV power plant (Choi, 2014).

Furthermore, very few papers have discussed the cooling methods used for floating PV panels, such as the direct contact of PV panels with the water's surface and using a PCM with horizontal PV panels. Trapani and Millar (2014) presented a new concept for cooling floating PV cells; their concept involves direct contact between the water and the PV panels, as depicted in Figure 2-16. The results indicate that the efficiency of the PV cells increased by about 5% due to the water cooling. A variant of this cooling method was presented by Ho et al. (2016) where they combined a PCM with floating PV cells. The results illustrate that the efficiency of the floating PV-PCM system increased by 2.03% compared to that of the floating PV cells alone. However, the tilt angle in both these studies

was zero, which means that these systems do not work at the optimal angle. Consequently, the solar radiation received by this system would be less than that received by inclined floating PV cells. Therefore, it would be ideal to design new methods to cool inclined floating PV panels that do not consume power during the cooling process.

Figure 2-16: Floating PV panels (Trapani and Millar, 2014).

2.3.3 PV-TED

The thermo-electric devise (TED) is used as a cooling devise or TED is used convert some of the waste heat to electrical power. There are several materials of the TED depending on the operating temperature. The best type of TED for an operating temperature of less than 150 °C is Bi_2Te_3 (Twaha et al., 2016). TED performance depends on a number of parameters, such as the length of the thermoelement, the leg area ratio between n- and p-type legs, fill fraction, and load resistance (Twaha et al., 2016).

Cui et al. (2016) introduced a new concentrated PV-PCM-TED system, which is explained in **Figure 2-17**. They placed the PCM between the PV panel and the TED. In this system, they used a lens to concentrate the sun's radiation in-front the PV cell and pumped water to be used as a heat sink with specific dimensions. The aim of this integration was to ensure that the temperature of the PV panel

and TED did not fluctuation and remained close to the optimal temperature. Four kinds of the PV panels (c-Si, CIGS, single-junction GaAs, and GaInP/InGaAs/Ge [III–V]) were tested. They created a thermal network for the suggested system with a thermal basis analysis for the PCM and water heat sink, and they specified the governing energy equation. They discussed the assessment of PV panels, thermoelectric effects, PCM selection, the heat sink dimensions, and the optimisation of the system (Cui et al., 2016).

This study did not discuss the fins inside the PCM. Also, it did not discuss the different types of TED effects, which can significantly affect the thermal distribution and the overall output. In addition, this system used extra power to reject the waste heat as well as extra equipment.

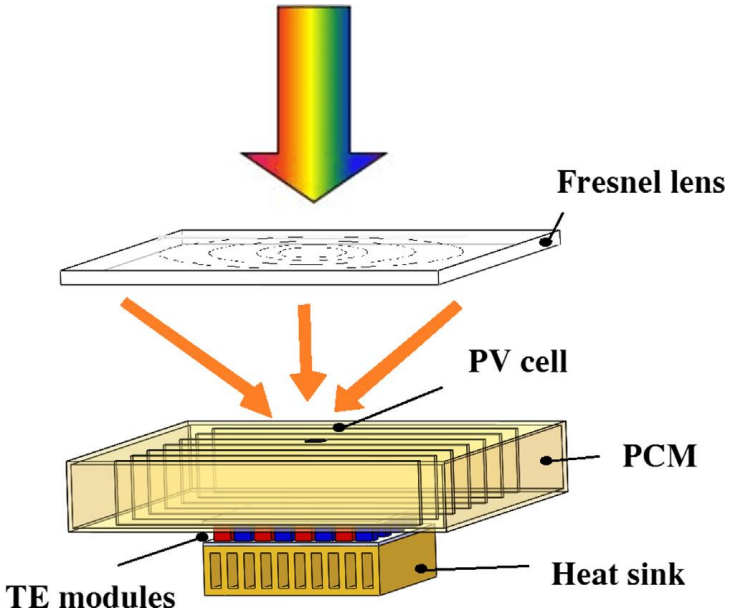

Figure 2-17: The concentrated PV-PCM-TED system (Cui et al., 2016).

Lamba and Kaushik (2016) carried out a theoretical study for the concentrated PV-TED system. The schematic of this system is shown in Figure 2-18. This study derived a theoretical model to estimate the temperatures of the PV cells as well as the cold and hot sides of the TED. These temperatures have been used with other parameters to calculate the electrical output of the concentrated PV-TED system using MATLAB software. Their research used one type of PV cell and a different number of legs for the TED. The results show that the power output of the PV-TED system is more than the PV alone, and the best concentrated ratio

of solar energy is three suns. The electrical output was reduced by 0.7%. However, it only considered Fourier's law relating to the TED regardless of the influence of the Seebeck effect on heat conduction. Moreover, this study did not consider the impact of natural convection on the PV cells' temperatures

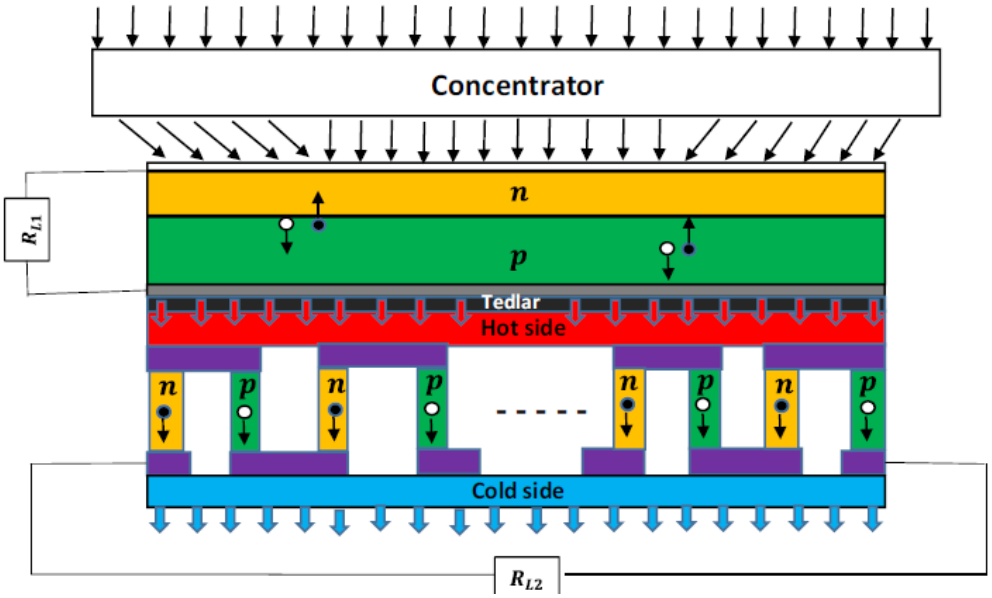

Figure 2-18: the schematic of the PV-TED system (Lamba and Kaushik, 2016)

Beeri et al. (2015) investigated the performance of the concentrated PV-TED system theoretically and experimentally with different concentration ratios of up to 300X. A multi-junction PV cell was used with the TED based on Bi2Te3. The commercial software COMSOL was used to execute the theoretical analyses. The results indicate that the efficiency of the PV-TED system reached 32% at the optimal concentration of 200X. In this case, the TED contributed 40% of the electrical output.

Kossyvakis et al. (2016) analysed the performance of the PV-TED experimentally. They investigated the performance of two types of PV cells – polysilicon cells and dye-sensitised cells – with two different thermoelement lengths based on Bi2Te3. The electrical output of this system was measured separately for the PV cells and the TED under different temperatures ranging from 25 °C to 85 °C. The theoretical results show that the operation efficiency of the polysilicon cell decreased by 24% from 15.2% to 12.4% when the temperature

increased from 25 °C to 85 °C. Its efficiency decreased experimentally by 53.94% at 86 °C, reaching 7%.

Ju et al. (2012) numerically modelled the concentrated PV-TED system by splitting the sunlight according to the wavelength, as depicted in Figure 2-19. This research used the GaAs PV cell type and $CoSb_3$ TED type with a concentration ratio of the solar sun of up to 800. The results show that the PV-TED electrical output is higher than the output of the PV cell alone, and the contribution of the TED output reached approximately 10%. In addition, the cooling system for the TED and PV had a significant impact on the electrical output of this concentrated PV-TED system.

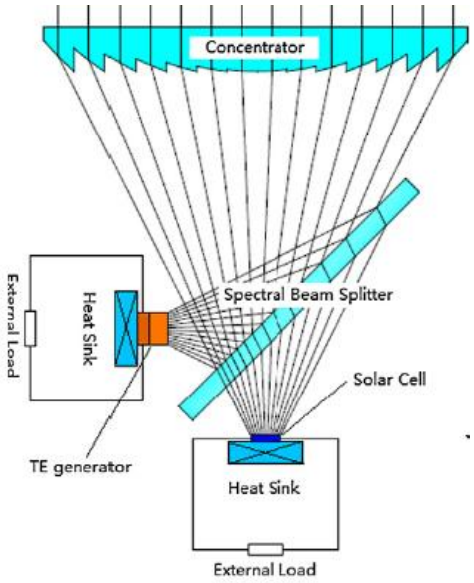

Figure 2-19: Concentrated PV-TED system with light filter (Ju et al., 2012).

Li et al. (2014) designed a new system to harvest a higher percentage of sunlight, as depicted in Figure 2-20, where the concentrator was used with a splitter to focus the sunbeam in two different areas. The first area was the PV cell, and the second area was the storage system. The theoretical results illustrate that the output power could be increased by 30% by adding the storage system. In addition, the efficiency of this system increased when the hot-side temperature of the TED increased.

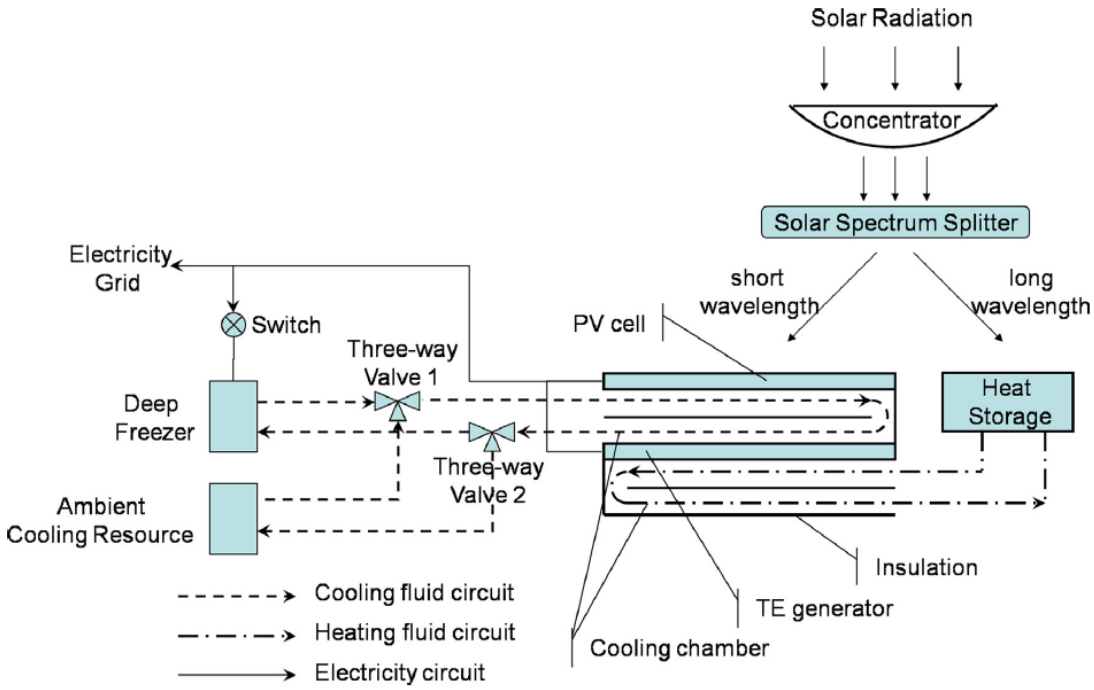

Figure 2-20: the combined PV-TED system (Li et al., 2014)

(Bjørk and Nielsen, 2015) investigated the performance of four types of PV cells accompanied by the Bi2Te3 TE module. The power outputs of the three types of PV-TED systems (c-Si-TE, CIGS-Te, and CdTe-TE) were lower than the power output of the PV cell alone. However, the power output of the a-Si-TED system was greater than the electrical output of the PV cell alone.

2.4 PV-PCM

In order to reduce the PV cell temperature, using a PCM that is incorporated into the back surface of a PV cell is one of the most promising techniques. The most important feature of the PCM is that it can absorb a large amount of heat when solid phase change to a liquid phase at a constant temperature. This feature can be used to manage PV cells at uniform and desired temperatures without having to consume extra power to circulate coolants. In the beginning, a PCM absorbs heat energy sensibly until reaching the melting temperature (Browne et al., 2015); then, it starts melting, and the temperature remains constant within the melting boundary. This melting boundary moves in the opposite direction of the PV cell. This movement is a function of the thermophysical properties of the PCM, the heat of fusion, the space between the melting boundary and the PV panel, the

solar radiation intensity, and the boundary conditions. Finally, the stored heat inside the PCM is released into the atmosphere during the night. These processes lead to a decreased PV cell temperature and, in turn, an increased efficiency.

In order to predict the temperature alongside the depth of the PCM, the moving melting boundary is a function of time and space, which causes what is called Stefan problems. Therefore, a transient model should be used instead of an analytical model (Hu and Argyropoulos, 1996). The three main methods used to simulate the heat transfer for the PCM are the apparent heat capacity method, the latent heat method, and the enthalpy method. The apparent heat capacity method assumes that the melting process occurs within a range of temperatures, and the specific heat capacity of the PCM during the melting process is equal to the sum of the specific heat for solid and the latent heat divided by the melting temperature range (Poirier and Salcudean, 1988). While the latent heat method assumes the melting process happens at a constant temperature and that the melting process is described by the melting percentage (Poirier and Salcudean, 1988). The enthalpy method uses the enthalpy change along with temperature change and this method assumed the melting process happens at a range of temperatures (Poirier and Salcudean, 1988).

The research that studied the impact of the PCM on the PV panel can be organised into two parts. First is the research that used numerical software packages, such as ANSYS Fluent and COMSOL Multiphysics, which use the latent heat method (Manual, 2001) and the enthalpy method (Fayaz et al., 2019), respectively. Second is the research that generated or used a one-dimensional PV-PCM model.

2.4.1 The research that used software packages

A noteworthy study on PV-PCM was carried out by Hung et al. (2000 cited in (Browne et al., 2015). This study has been reported as the first numerical research that achieved agreement with experimental results. Several cases were investigated, such as incorporated PV with an aluminium container for a PCM both with and without fins. The experimental results show a good agreement with the theoretical results (Browne et al., 2015). Many subsequent studies have used

these packages to investigate different parameters of the PV-PCM system such as:

2.4.1.1 The impact of different kinds of PCM on PV panel output

Different PCMs have different thermophysical properties, leading to different cooling effects on PV cell output. In order to explain these impacts, different types of PCMs combined with monocrystalline PV cells were studied by Hasan et al. (2010). They used five PCMs: paraffin wax (RT20), capric–lauric acid (C–L), capric–palmitic acid (C–P), pure salt hydrate ($CaCl_2 6H_2O$), and commercial blend (SP22). Each PCM was encapsulated in four different containers: two aluminium (with two different widths: system A [5 mm] and system C [3 mm]) and two perspex (with two widths: system B [5 mm] and system D [3 mm]). This experimental study used three different solar intensities: 500, 750, and 1000 W/m^2. The results indicate that the maximum decrease in PV cell temperature was caused by the salt hydrate in the 5-mm-thick aluminium container. This result can be attributed to the high thermal conductivity of $CaCl_2$. Figure 2-21 illustrates how long the PV cell temperature remained below 10°C compared to that of the reference PV cell. The y-axis represents this duration. The impacts of different types of the PCM and different containers with solar radiation 1000 W/m^2 are also illustrated. It can be seen that the salt hydrate within the aluminium container was able to remain a PV cell temperature lower than 10°C than the reference PV cell temperature for the longest period of time. Here, the aluminium container worked as a fin and had a high impact on the cooling of the PV cell. However, in this study, the surrounding air temperature was fixed at 20 °C, which means the surroundings significantly affected the results.

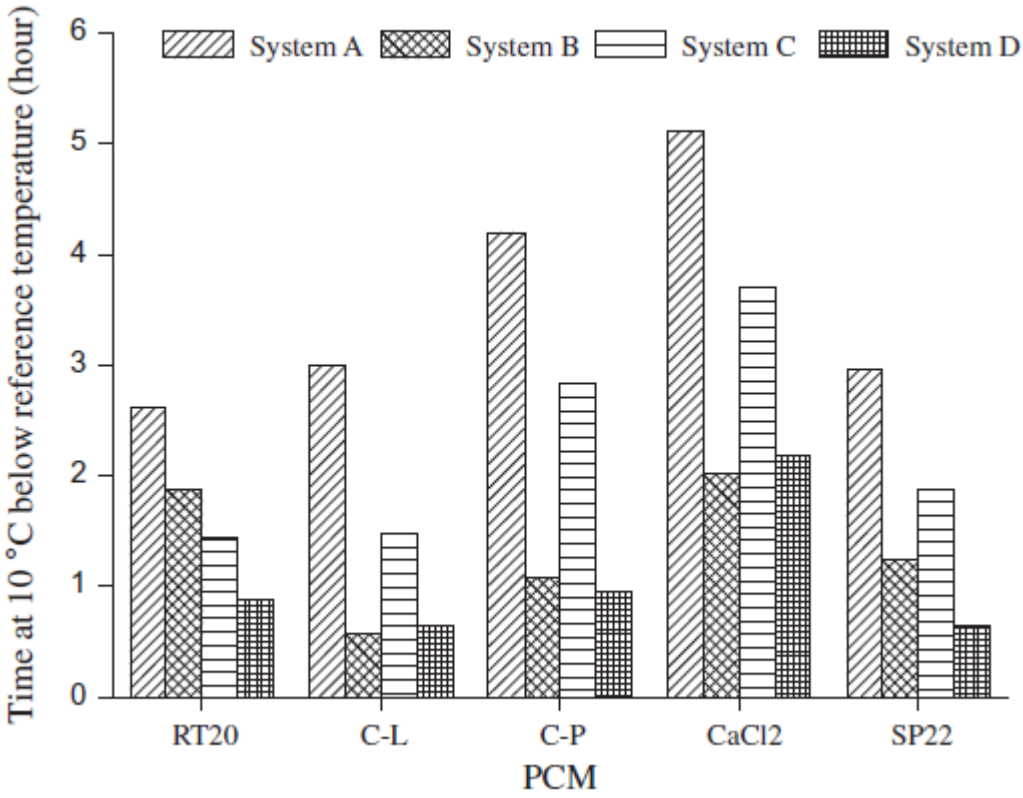

Figure 2-21: The y-axis represents how much longer the PV cells could be kept below 10 °C than the reference PV cell; the x-axis represents different PCMs and different containers (Hasan et al., 2010).

Also, Cellura et al. (2008) studied the effect of several PCM melting temperatures on the performance of PV cells. Three paraffin varieties were used with different melting temperature ranges (PCM1: 26–28 °C, PCM2: 31 °C, and PCM3: 28–32 °C). The theoretical result using COMSOL software indicates that the PCM3 with a melting range of 28–32 °C significantly reduced PV cell temperature. The difference between the PV cell and the PV-PCM is illustrated in Figure 2-22. This result was achieved on a typical summer day in Palermo, Italy. However, the thickness of the PCM is not mentioned.

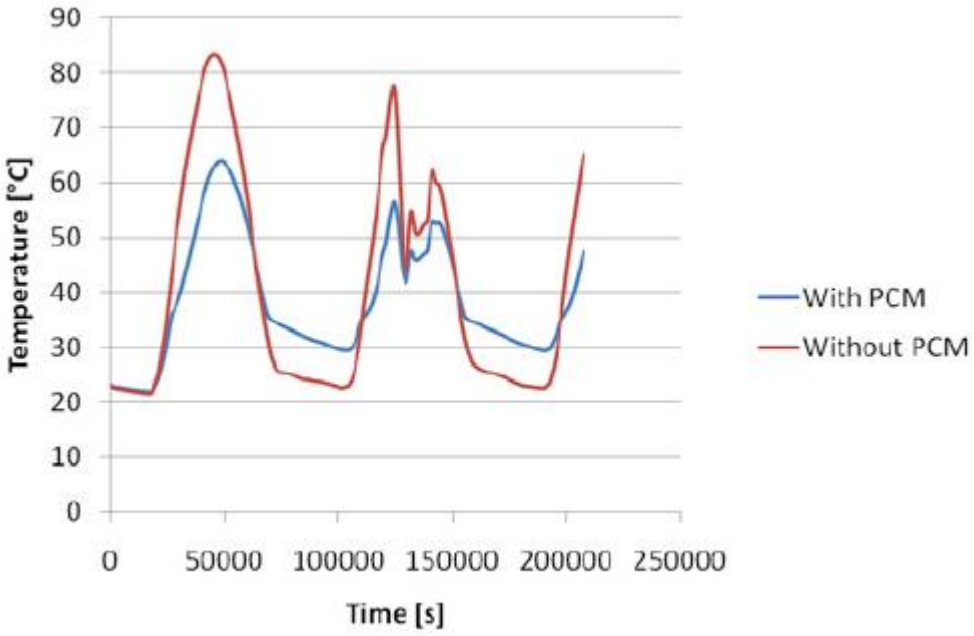

Figure 2-22: Different theoretical temperatures for the PV cell alone and PV-PCM on a summer day in Palermo, Italy (Cellura et al., 2008).

However, some studies in the literature have indicated that using different types of PCMs has the same impact on the output of PV cells. Tanuwijava et al. (2013) examined the impact of two PCMs with different melting temperatures (26 °C and 34 °C) on the performance of PV cells. They studied the two PCMs using microencapsulation. The results show no noticeable difference between using the two PCMs.

In contrast, the impact of two PCMs on the temperature of PV cells was explored experimentally (Hasan et al., 2014). The melting temperatures of the two PCMs studied were 22.5 °C and 29.8 °C for capric-palmitic acid (PCM1) and calcium chloride hexahydrate (PCM2), respectively. These systems were tested in Dublin, Ireland and Vehari, Pakistan. Figure 2-23 explains the impact of PCMs with different melting temperatures on the cooling of PV cells. It can be seen from Figure 2-23 that PCM1 reduced the temperature of the PV cells in Dublin and Vehari by 7 °C and 17 °C, respectively, compared to PCM2, which reduced the temperature by 10 °C and 21 °C, respectively. This means there was an approximate 3.5 °C reduction in temperature using PCM2 in both cities, while PCM2 has a higher melting temperature than PCM1 by 7.3 °C. It seems the high

thermal conductivity of PCM2 (0.56 W $m^{-1}°C^{-1}$ for liquid) compared to that of PCM1 (0.14 W m^{-1} $°C^{-1}$ for liquid) led to the different cooling rates for the PV cells.

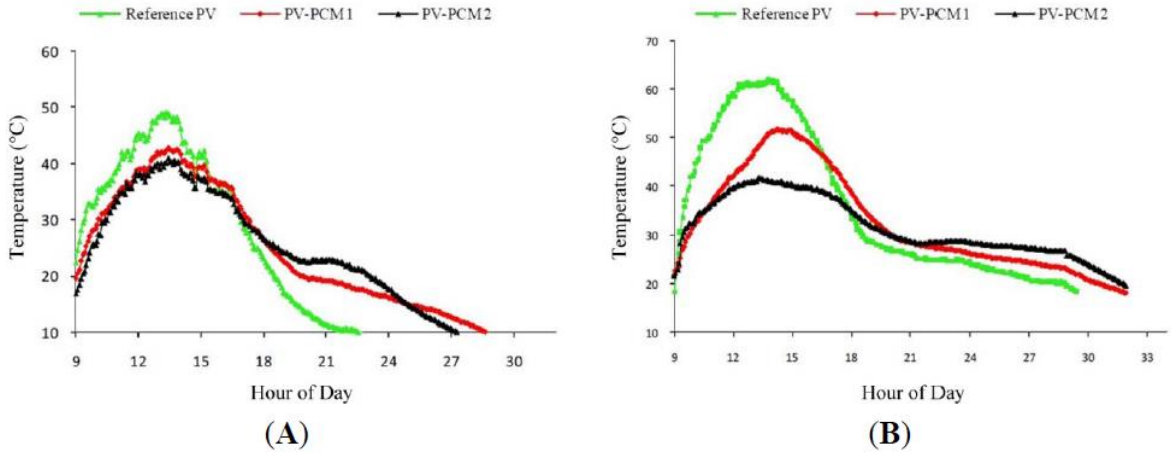

Figure 2-23: PV cell temperatures using two PCMs in (A) Dublin (12 September 2009) and (B) Vehari (30 October 2009) (Hasan et al., 2014).

Another development study was carried out by Huang (2011b) where two shapes of containers, i.e. triangular and semi-circular, were used with PCMs with various melting temperatures (RT21, RT27, RT31, and RT60). The results indicate that the triangular cell shape with RT27 had the highest performance, followed by RT21.

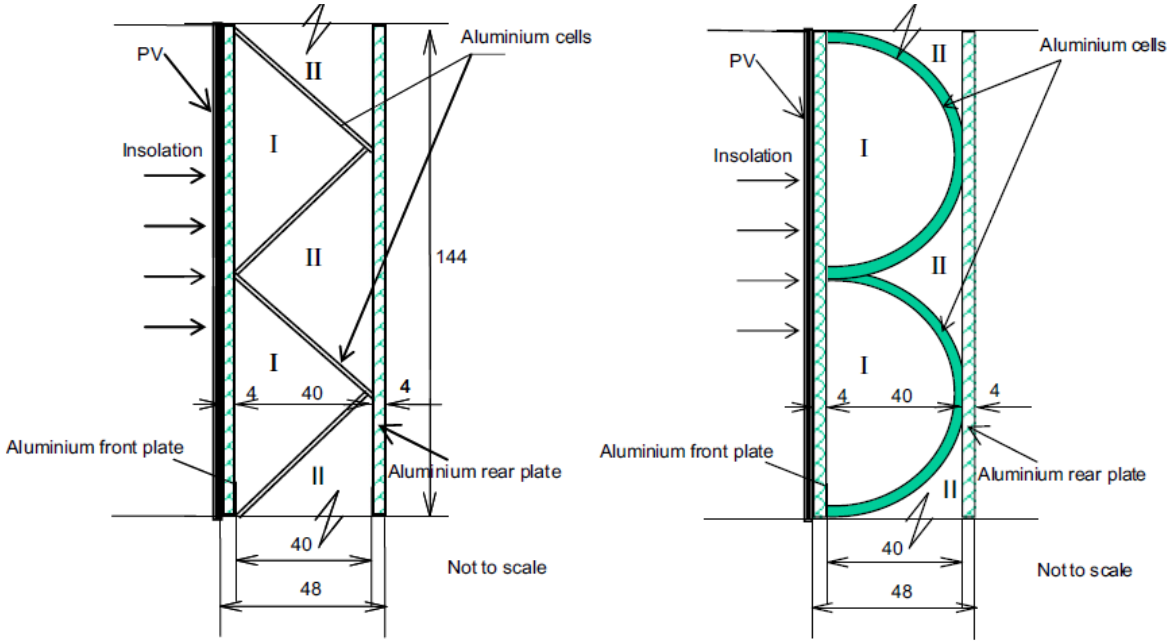

Figure 2-24: Using two PCMs inside one system (Huang, 2011b).

In summary, the effect of the different types of PCMs on the output of PV cells depends on several factors:

- Melting temperature of the PCM
- Thermal conductivity of the PCM
- Heat of fusion of the PCM
- Specific heat capacity of the PCM
- Ambient temperature
- Solar radiation
- Thickness of the PCM
- Fins inside the PCM

2.4.1.2 The impact of different thicknesses of PCM on the PV output

The thickness of the PCM plays a key role in controlling the temperature of PV cells. The heat generated inside the PV cell should be absorbed by the PCM. In other words, the total heat energy generated during one day minus the loss of energy to the ambience should be equal the heat of fusion subtracted from the total PCM mass incorporated within the PV cell. The quantity of this mass depends on the density, thickness, and the unit area. The unit area is the same for the PV cell and the PCM. Therefore, the total heat of fusion depends on the thickness of the PCM. As a result, the cooling period depends on the PCM's thickness. The impact of this thickness on PV cells has been widely studied.

The effect of paraffin wax PCMs with three different thicknesses (20 mm, 30 mm, and 50 mm) on PV cell temperature was examined numerically by (Huang et al., 2004). These different designs were based on the ambient and solar radiation conditions in southeast England on 21 June using PCMs without fins. The results indicate that the PV cell temperature (represented by an aluminium plate) reached 55 °C, while the 30-mm-thick PCM controlled the PV cell temperature to below 35 °C during a three-day simulation, as shown in Figure 2-25. In contrast, using the PCM with a 20 mm thickness was inadequate, and all the mass melted

before the end of the day. This caused the temperature to increase to 45 °C. However, the results indicate that the PCM with a 50 mm thickness did not melt completely.

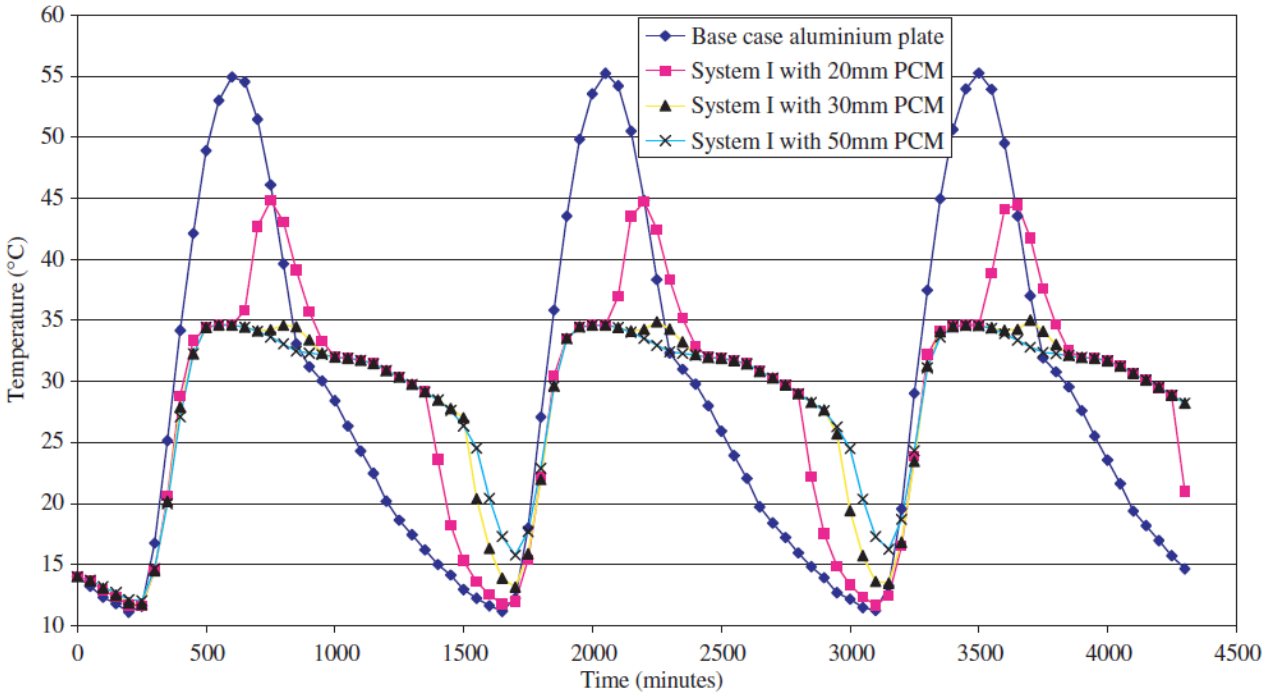

Figure 2-25: The temperature of the PV cell with PCMs of three different thicknesses (Huang et al., 2004).

2.4.1.3 The impact of different tilt angles on PV-PCM temperature distribution

The impact of different tilt angles on the temperature distribution of the PV-PCM system was discussed by Kant et al. (2016). The results indicate that when the tilt angle increased the velocity of the melted PCM decreased. Therefore, the temperature of the PV cell increased, as depicted in Figure 2-26. These tilt angles are from the vertical line. Another study was developed by Nehari et al. (2016b) to investigate the impact of the different tilt angles of a PV-PCM system with fins on PV cell temperature. The results indicate that the zero inclination of the PV-PCM system achieved a lower PV cell temperature, as shown in Figure 2-27. However, no study has discussed the impact of PV-PCM systems with fins with different fixed angles on the temperature distribution of the PV cell. This study

would be worthwhile in order to optimise the fin angle inside the PV-PCM system, which has fixed angle.

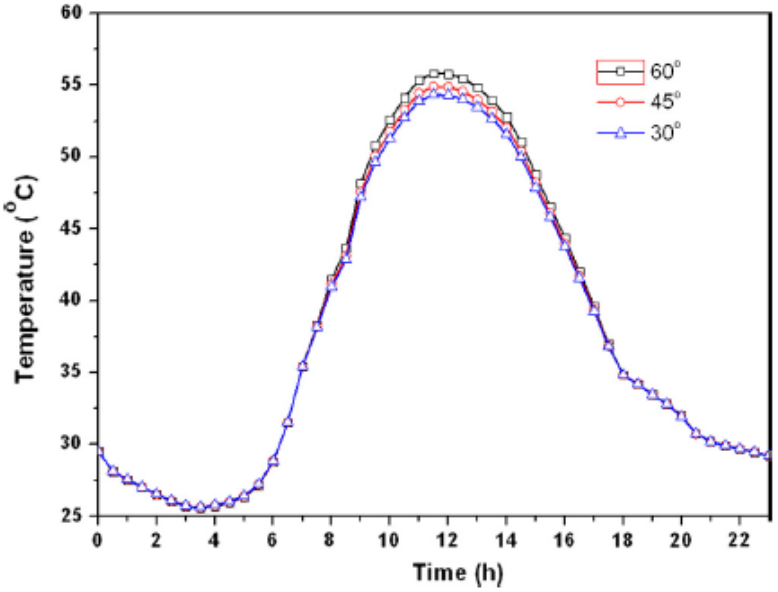

Figure 2-26: The effect of different PV-PCM tilt angles on PV cell temperature (Kant et al., 2016).

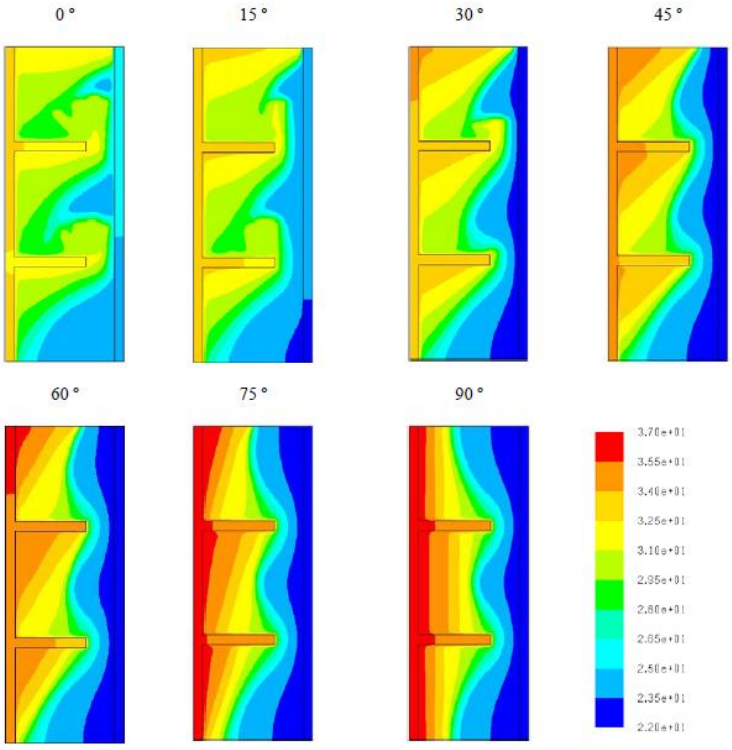

Figure 2-27: The impact of different tilt angles on the temperature of the PV-PCM system with fins (Nehari et al., 2016b).

2.4.1.4 PV-PCM fins

In 2004, (Huang et al., 2004) studied the temperature distribution of a PV-PCM that incorporated fins. The aim of this paper was to develop a simulation model and compare the results of this model to experimental results. The numerical simulation suggested that the heat transfer coefficients for the front of the PV and the back of the PCM are dependent on time. This study used the transient model. Also, the Boussinesq approximation was used to simulate free convection and diffusion in the molten phase. The experimental work used paraffin wax as the PCM and aluminium fins, as depicted in **Figure 2-28**. The results show good agreement between the numerical model and experimental results. In addition, the results indicate that the temperature of the PV alone reached up to 64 °C, while it could be as low as 44 °C when the PV is incorporated with the PCM. Moreover, the fins enhanced the heat transfer and reduced the average temperature of the PV. However, the result show that the large number of fins could reduce the convection heat transfer inside the PCM. This study paved the way for investigations on temperature distribution of PV-PCM-integrated building. However, this study did not mention the type of mesh that was used.

In 2006, Huang et al. attempted to solve the 3D problem instead of focusing on 2D alone. The aim of this research was to develop a numerical model to study the impact of the pin fins on the temperature distribution of the PV. There is a good agreement when comparing this 3D model to the 2D model. Also, the numerical results show that the five-pin fins enhanced the temperature homogeneity. In 2007, Huang et al. experimentally validated the 3D model with pin fins.

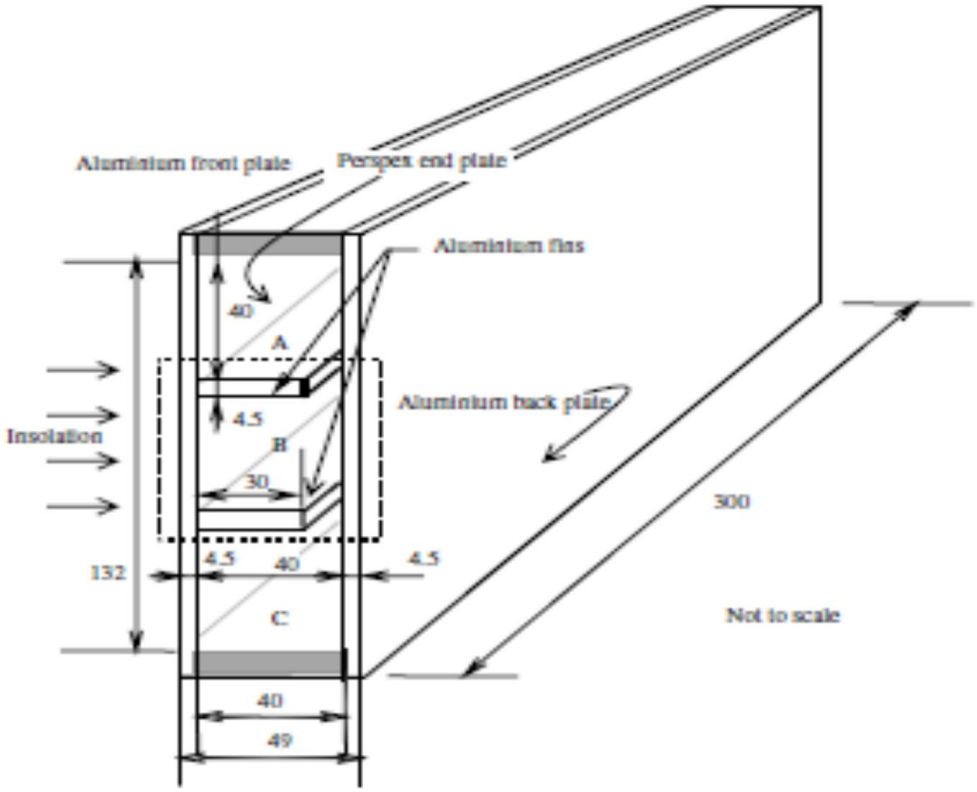

Figure 2-28: A PV-PCM-integrated building (Huang et al., 2004).

The effect of the different sizes of spaces between fins inside the PCM has been discussed in some papers. Huang et al. (2011) experimentally studied six different spaces (4 mm, 8 mm, 12 mm, 24 mm, 33 mm, and 42 mm) between fins and their impact on the temperature of PV cells. Huang et al. (2011) studied natural convection related to the spaces between the fins as well as fin lengths. The results indicate that adding fins inside the PCM led to a reduction in top cavity formation and greater temperature stability for the PV cell. In addition, the increased number of fins leads to decrease the thermal stratification and reduced the PV cell temperature. The relationship between the temperature and the spacing between two fins is illustrated in

Figure 2-29. It can be seen in

Figure 2-29 that the maximum temperature reduction occurred at a minimum spacing of 8 mm. However, the Rayleigh reduced as the spacing decreased. **Figure 2-30** illustrates the relationship between fin spacing and the Rayleigh number, which represents the buoyancy forces that cause the natural convection. An important drawback was mentioned in this research, i.e. increasing the number of fins leads to an increase in the metal mass. However, it seems natural

convection could be improved by using different fin angles. In addition, using different hollow shapes inside the fins could also increase natural convection and reduce the fin mass.

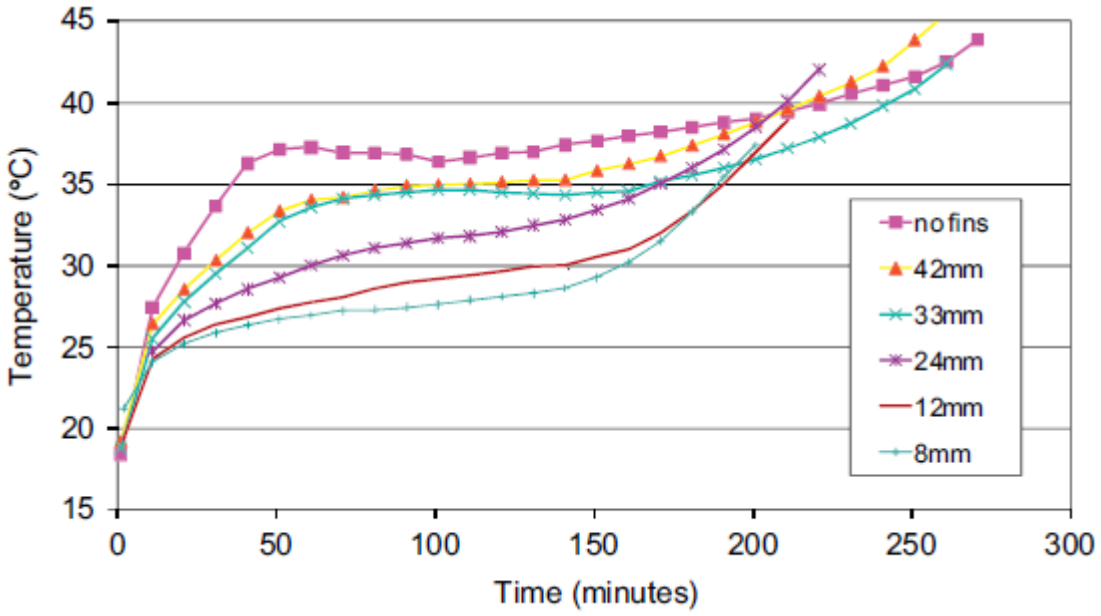

Figure 2-29: PV cell temperature with different spacings (Huang et al., 2011).

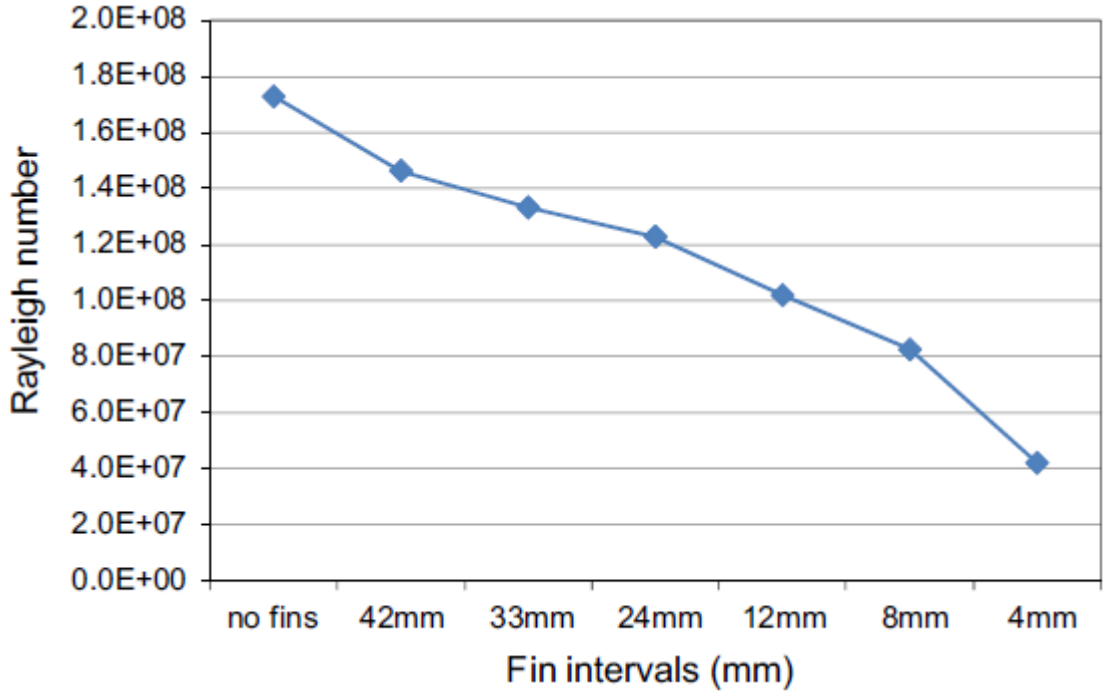

Figure 2-30: The relationship between fin spacing and the Rayleigh number inside the PCM (Huang et al., 2011).

Some studies discussed the relationships between the depth of the fin, the spacing between fins, the stable temperature for the PV cell, and the period of temperature stability, as depicted in **Figure 2-31**. The x-axis refers to the ratio of fin spacing–depth, the left y-axis refers to the PV temperature, and right y-axis refers to the period during which PV cell temperature remained unchanged. When the ratio of fin spacing-depth increased, the temperature of the PV increased, and the period also increased because in this case, when the fins were extruded, the heat transfer increased and the temperature of the PV cells decreased.

Nehari et al. (2016a) studied the impact of fin length on the melting process and the temperature distribution within the PV-PCM system. This system consisted of PV cells and aluminium fins of several different lengths (0, 5, 10, 15, 20, 25, 30, 35, and 40 mm) attached to the back of the PV cells, with the RT25 PCM inside the aluminium container. Fluent 6.3 was used to solve the heat and momentum equations. The results show that the 25-, 30-, and 35-mm fins had a greater effect on reducing the PV panel temperature than the fins of other lengths.

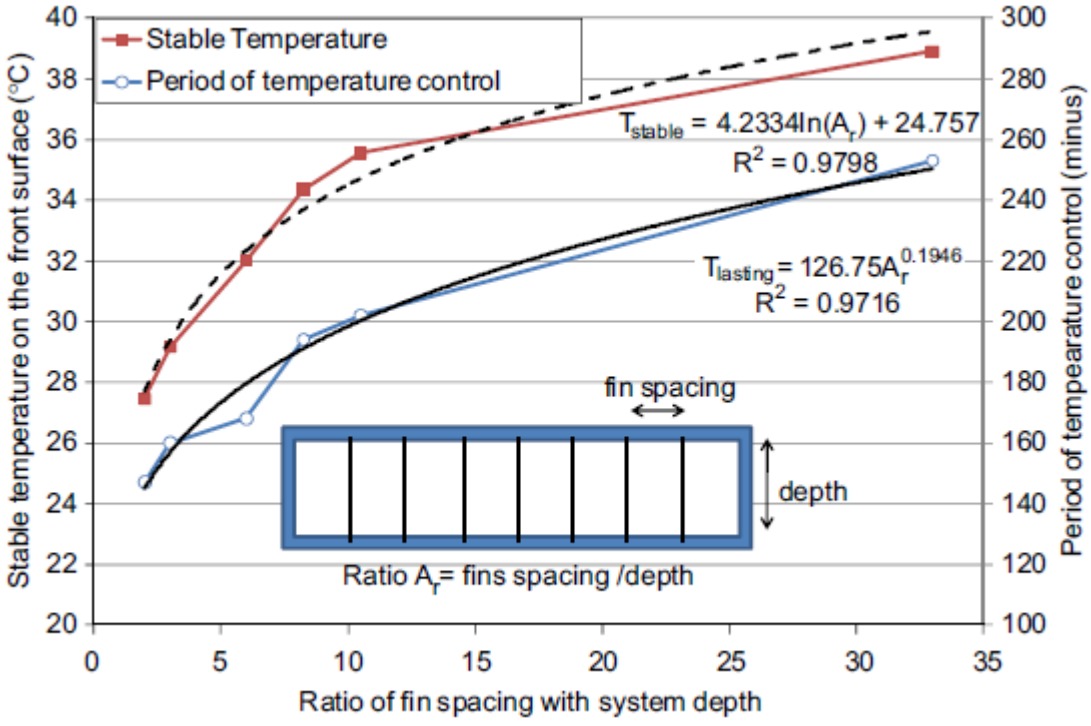

Figure 2-31: The temperature stability with the ratio of fin interval–depth (Huang et al., 2011).

Shukla et al. (2017) reviewed different methods of cooling PV cells. They mentioned that increasing the fins inside the PCM achieves a uniform temperature distribution. In contrast, this increased number of fins reduces the movements of the molten PCM. In addition, there is no paper that presents a solution for this problem.

Khanna et al. (2018) used ANSYS Fluent to study the optimal thickness of the PCM, the best aluminium fins inside the PCM, and the best space between the fins. This optimisation depended on studying the maximum electrical output of the PV- RT 25 PCM by simulating the PV-PCM with a 1 kwm^{-2} solar radiation intensity for two cases: 3.5 hours and 6 hours. The results indicate that the most suitable depth of the PCM for the first case is 2.8 cm, the most suitable fin thickness is 2 mm, and the best space between each two fins is 25 cm. This paper concludes that thicker fins or less space between the fins would not have a significant effect on the electrical output. Khanna et al. (2019) used the same methodology; they studied the impact of different wind speeds on the optimal thickness of the PCM. Lu et al. (2018) used a CFD package to study the impact of vertical and horizontal fins on the PV-PCM system with experimental lab work. The simulation and the experimental lab work only lasted 500 minutes, and they found that vertical fins are better than horizontal fins, while Benlekkam et al. (2018) used ANSYS Fluent to study different fin configurations, as shown in

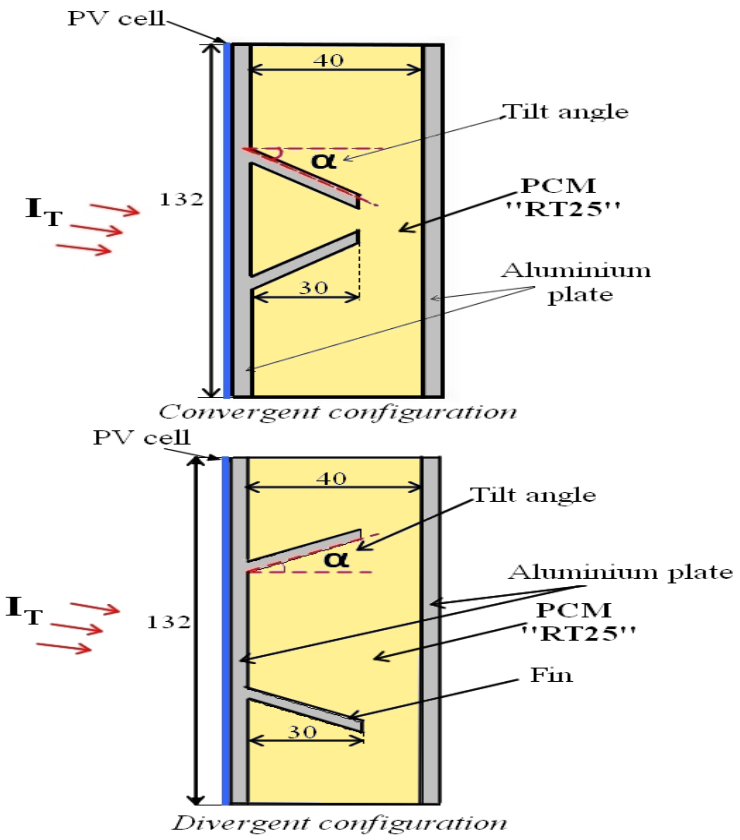

Figure 2-32, for only 200 minutes. The results indicate that the diverged configuration is better that the converged configuration.

Figure 2-32: Different fin configurations in the PV-PCM system (Benlekkam et al., 2018).

2.4.1.5 The impact of encapsulated PCM on PV panel output

Nouira and Sammouda (2018) studied the impact of aluminium-encapsulated PCM on PV panel electrical output for two days in July in Sousse, Tunisia using COMSOL. In addition, they studied the impact of wind direction and different dust deposits on the PV-PCM system. They mentioned that when the dust intensities are 3 gm^{-2} and 9 gm^{-2}, the absorbed solar radiation decreased by 72 and 227, and the efficiencies were 13.1% and 13.5%, respectively. The results of this paper are not logical.

2.4.2 The one-dimensional PV-PCM simulation

The solid/liquid moving boundary during the melting and solidification processes was first reported by Lame and Clapeyron in 1831 and first identified as a problem by Stefan in 1889 (Zalba et al., 2003). This problem is related to the thermal analysis where the movement of this boundary depends on the speed of the absorbed or lost latent heat, while this speed depends on the unknown position of this boundary, which makes the thermal analysis problem more complicated, and thus it is referred to as the Stefan problem (Zalba et al., 2003). Therefore, since 1889, several methods have been adopted to investigate thermal behaviour during the melting and solidification processes.

Zalba et al. (2003) conducted a review of heat storage; they focused on three parts: heat transfer, materials, and appliances. They discussed the literature on the thermal analysis of PCMs and the developments up to 2003. This study showed that there are two kinds of numerical solutions for the thermal analysis of PCM; the first kind only considers heat conduction, while the second kind considers both conduction and convection to model the heat transfer equations.

Malvi et al. (2011) implemented thermal analysis for the PV-PCM combined with water cooling. In order to estimate the performance of this system, one-dimensional modelling was described and used with a time step of one second. This model depended on the finite difference and energy balance equation. The results indicate that the output of the PV-PCM-solar thermal system increased by

9% compared to PV alone. Smith et al. (2014) used the same modelling procedure to predict the annual PV-PCM energy output with a one-hour time step. However, neither of these studies mention anything about the convergence of the model used. In addition, these studies have not validated this model.

Ciulla et al. (2012) studied the finite difference solution for the PV-PCM, and they created a one-dimensional model. The results show this model was valid for investigating the performance of the PV-PCM system. This study used the finite difference method to analyse the PV-PCM system. It was suggested that the PCM is isothermal, and the system is divided into four layers: glass (3.2 mm), silicon cells, interface region, and the PCM layer. This research presents two groups of equations for the PCM; the first group describes the energy balance for the external nodes, while the second group describes the energy balance for the eternal nodes. However, this model is not valid for predicting thermal behaviour during the night (Ciulla et al., 2012).

Hendricks and Sark (2013) used the one-dimensional model to predict the impact of the PCM on the PV performance integrated with buildings in Utrecht, the Netherlands and Malaga, Spain. The results indicate that the PV output could be increased by 3% using the PCM. This study used a heat absorbance factor instead of using any type of heat of fusion model. This heat absorbance is a function of absorbing heat based on the results of previous numerical studies.

In contrast to Ciulla et al. (2012) and Malvi et al. (2011), Brano et al. (2014) used the explicit finite deference scheme and enthalpy balance method to simulate the one-dimensional modelling of the PV-PCM system. This study assumed that the liquid phase has high viscosity in order to neglect the natural convection inside the PCM. The numerical and experimental results have good agreement with a margin of error of less than 7%, as shown in Figure 2-33, where the x-axis represents the time per hour for three days, the left y-axis represents the temperature (°C), and the right y-axis represents the power output (W). These experimental and numerical data were observed in Palermo between 30 June and 2 July. Notably, almost similar figures and results have been published by the same authors in another journal (Lo Brano et al., 2013).

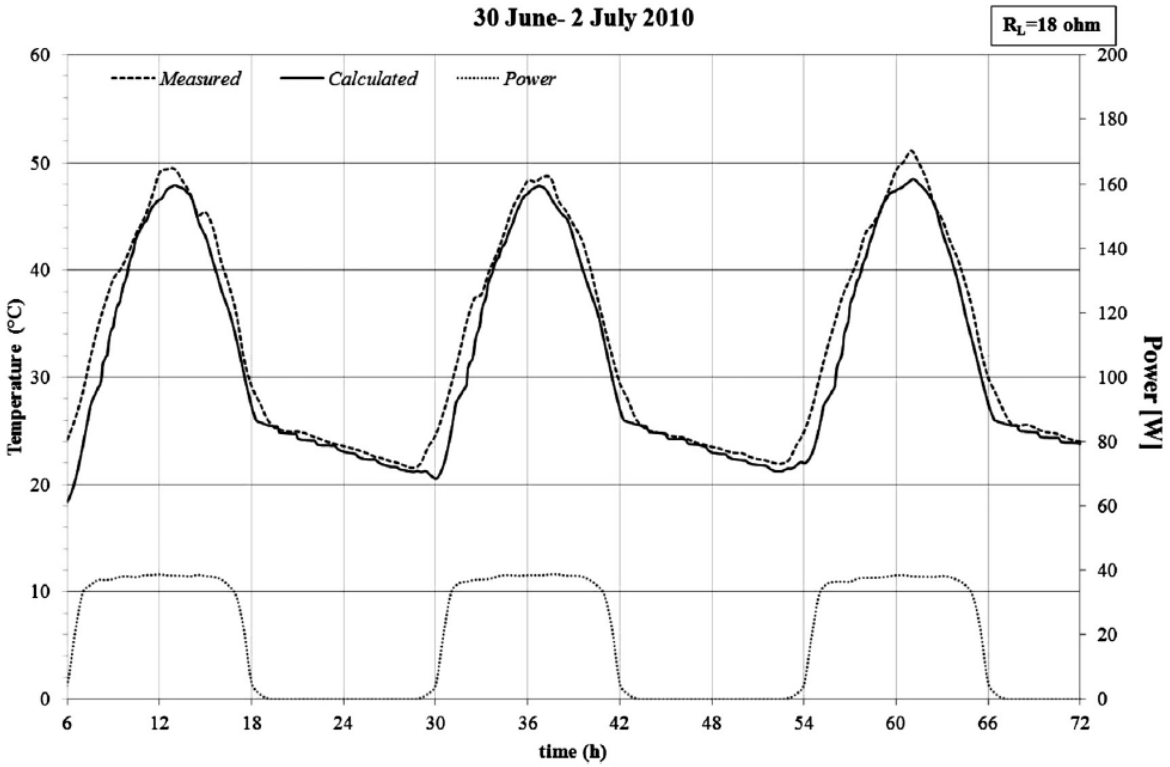

Figure 2-33: The numerical and experimental results for the PV-PCM, 30 June to 2 July in Palermo, Italy (Brano et al., 2014).

On the other hand, Kladisios and Stegou-Sagia (2015) introduced a new one-dimensional model to study the impact of the PCM on the PV output. This one-dimensional model depends on the effective heat capacity method. In addition, this paper used the implicit expression. However, this paper had not validated this model. In addition, the convergence, stability, and the compatibility were not mentioned.

Mahamudul et al. (2016) studied the impact of using a PCM to reduce PV cell temperature in Malaysia using the Matlab software. This study used heat balance for the PV cell without mentioning any equations for heat transfer inside the PCM. This paper also carried out experimental work and the results indicated that the temperature of the PV-PCM reduced by 10°C as compared with the PV cell alone. However, this paper described strange and unacceptable method to validate the numerical model. This method compared the result with other papers regardless of the different weather conditions and different PCMs.

Kibria et al. (2016) further developed the one-dimensional model, where full implicit schemes and energy balance equations were used. This paper used the total enthalpy method to solve the PCM problem. The results showed good agreement with a literature experimental result. In addition the results indicated that increasing the space division leads to better agreement with the experimental results. However, this paper mentioned that increasing the space division lead to an expensive computational solution.

Aly et al. (2017) developed a solar radiation model which connects with a two-dimensional transient PV-PCM model. In their study, the energy balance method for each spatial node and the fully implicit time scheme have been used. The results indicated that the heat transfer from the PV panel sides did not have a noticeable impact. Same fully implicit method for one dimensional method has been used by Waqas and Ji (2017) to study the impact of the shutters on the PV-PCM performance. In contrast, Hasan et al. (2017) have investigated the impact of the PCM on the PV panel output experimentally and numerically in the United Arab Emirates, using the Crank–Nicholson time-discretization method. The results indicated that when PCM passive cooling is used, the annual energy production of the PV panel increased by 5.9%. However, these papers have not iterated the process to find the correct temperature for the convection and radiation model, which means it has not tested convergence. In addition, compatibility with different time and space discretisation has not been tested, nor the mathematical equations described correctly.

Hachem et al. (2017) studied the effects of using two PCMs on the electrical output of the PV panel experimentally. The results illustrated that PV panel efficiency increased by 3% if one PCM was used compared to 5.8% if a combination of PCMs was used. This paper claimed that a thermal PV-PCM model was used. However, the time-discretization method has not been mentioned.

Arıcı et al. (2018) developed a one dimensional PV-PCM model to predict the PV panel temperature, the power output increment and the economic assessment. The aims of this paper were to make optimization for PV-PCM system and to investigate the economic value of using the PCM on two Turkish cities: Ankara and Mersin. This paper has neglected the two EVA layers and assumed the there

is no temperature difference in silicon layer. This paper has used the explicit finite difference method with latent heat method for the PCM. Only one organic PCM was used in this paper with no change for the thermophysical properties with different phases (liquid and solid). This paper studied the performance of PV power output for two days 21st of May and 21st of December, the results seem for day time without night time. Then for these two days, the authors used different melting temperature started from 1 ^{0}C to 50 ^{0}C with 1 ^{0}C interval. In addition, the authors used three different latent heat 180, 200 and 250 kJ kg^{-1}. Then, this paper found the optimal thickness of the PCM and optimal melting temperature for each month for the two cities. Nižetić et al. (2018) have used the same numerical method with experimental work for three days in Split in Croatia. However, these papers have not mentioned the time step and the node number that used. In addition, these papers have not investigated the time independent and increment size independent. In these papers, it is not mentioned how the model predicted the power output for each month, however a typical day seems be used for each month. This, paper has not mentioned anything about the PCM solidification simulation during the night.

Zhao et al. (2019) have studied the impact of the PCM on the PV panel electric output for a whole year for Shanghai. They used the apparent heat capacity method to simulate the melting and solidification process. They used time step as 0.1 second. They used the explicit time discretization has been used. This paper used only one node from the PV panel without mentioned any more details. The results indicated the maximum power improvement was 2.46% yearly.

Gaur et al. (2017) developed a mathematical model for a PV thermal system with and without PCM. This paper neglected the heat capacitance of the glass. In addition, it considered that the temperature of the PCM was constant during the solidification and melting processes, and so the equations have been solved analytically. The results of this model have not been validated with experimental work or in the literature. In addition, there is no justification for considering the temperature of the whole PCM during the solidification and melting processes. Furthermore, the mathematical equations have not been described correctly, and the boundary conditions for the equations have not been mentioned.

On the other hand, Yuan et al. (2018) has studied the impact of the PCM and water cooling on the performance of the PV thermal system experimentally and numerically. While, Al-Waeli et al. (2019) have added the nano particle to the water to study the impact of the PCM and nanofluid on the performance of the PV thermal system. These studies has not described each layer of the PV panel and the time discretization has not been mentioned. Table 1 summaries the literature reviewed in this paper.

Using the PCMs to control the PV cells temperature has been reviewed by Ma et al. (2015) in term of materials, numerical methods, heat transfer improvements and simulation. They highlighted that the numerical methods which used to solve the transient heat transfer problem can be improved by using new numerical methods. They mentioned that these new methods should be compared with experimental results to validate it. In addition, Islam et al. (2016) also, reviewed the PV-PCM system and they conclude that the numerical model for the PV-PCM systems should be developed to simulate the these systems precisely.

2.5 Conclusions

The aim of this chapter is to present an overview of the fundamentals of PV cells and describe the problems and the promising solutions in order to encourage the development of techniques to overcome these problems. The first problem is that non-useful energy from solar radiation leads to increased PV cell temperatures. Consequently, the efficiency of the PV cell decreases by approximately 0.45%/k. Second, the non-uniform temperature of PV cells leads to different voltage outputs, which leads to electrical losses when PV cells connect in parallel. In addition, this non-uniform temperature results in to hot spots, which increase the likelihood that the PV cell will be damaged.

In order to overcome the first two problems, passive air cooling, floating cooling, incorporating the PCM, and TED with PV panels have been reviewed and discussed. First, passive air cooling with an open duct beneath the PV panel could achieve a 1.1 m/s^{-1} air speed inside the duct. However, the wind speed could reach more than twice this air speed. This means the wind could cool the PV panel more effectively than the open air duct beneath the PV panel. In

addition, this cooling method can achieve uniform cooling for the PV panel. Second, the floating cooling method should place the PV panel in contact with water, which means the PV panel is either installed horizontally or at a tilted angel. If the PV panel is installed horizontally, which is not the optimal angle, the solar radiation that strikes the PV panel is less than the solar radiation that strikes the PV panel with an optimal tilted angle and results in less electrical power output, while if the floating PV panel is tilted, it needs electrical power to circulate the water and requires maintenance. Third, using the TED could achieve uniform cooling, but it consumes a significant amount of electrical power. Finally, using the PCM as a coolant could be one of the most promising methods to control the temperature of the PV panel.

Numerical software, such as ANSYS Fluent and COMSOL Multiphysics, have been used to investigate the impact of different parameters, such as the type of PCM, thickness, and weather conditions, on PV-PCM performance over different periods of time. In 2000, Hung et al. (Browne et al., 2015) reported agreement with experimental results using ANSYS Fluent. Consequently, several studies have used ANSYS Fluent software, such as (Huang et al., 2004), (Nehari et al., 2016a), (Emam et al., 2017), (Luo et al., 2017), and (Qureshi et al., 2018), while others (Cellura et al., 2008) have used COMSOL Multiphysics. (Shukla et al., 2017) carried out a review of different methods of cooling PV cells using numerical software, which have also been used to design the PV-PCM system. However, they have only been used to simulate one or two days of results because to simulate an entire year would be time consuming and complicated.

In order to simulate an entire year of data, a more practical approach would be to build a one-dimensional model using MATLAB software. Based on the literature review, several techniques have been developed. These include one-dimensional models to investigate the impact of the PCM on the performance of PV panels. These studies have used either implicit or explicit methods, which consume computing time. Therefore, the first contribution of this study, a novel one-dimensional model for the PV-PCM, will be introduced and implemented based on a combined lumped-numerical model to reduce computing time consumption. Compared to those of the literature, the main advantage of this model is that the time step can be increased compared to an explicit model with

a stable solution; if it is compared to the implicit model, it will not need to iterate for each time step. This means the time required for the numerical solution can be reduced. In addition, the computing time for the three models (implicit, explicit and lumped-numerical) will be calculated and compared.

The models in the literature did not consider thermal contact conductance between the PV panel and the container of the PCM. Therefore, the second contribution of this study is to develop these three models – implicit, explicit and lumped-numerical – of the PV-PCM module to include thermal contact conductance. Then, the impact of different levels of thermal contact conductance on the performance of the PV-PCM system will be investigated.

According to the literature, the one-dimensional numerical models for the PV-PCM did not consider the volume change for the PCM during the phase change. Thus, the third contribution of this PhD study is to consider the volume change and study the impact of the volume change on the temperature and the efficiency of the PV panel.

The three primary methods used to simulate the heat transfer for the PCM are the apparent heat capacity method, the latent heat method, and enthalpy method. Within the literature, when these methods were used with implicit discretisation, the researchers calculated the apparent specific heat according to the temperature of the previous time step. However, mathematically, the apparent specific heat should be calculated according to the temperature of the current time step, which could significantly impact the results of the temperature. This problem could occur with the PCM and with these two methods only as a result of significant change in the apparent specific heat when the temperature increases from below melting temperature to the melting temperature. Therefore, the fourth contribution is to introduce a loop inside the numerical model to calculate the apparent specific heat according to the current time step. Then, the results will be compared by calculating the apparent specific heat according to the previous time step.

In addition, there is no study that investigates the impact of using the PCM on the annual electrical output of PV panels in Baghdad or Milan. Therefore, the fifth contribution of this study is to investigate the impact of a composite paraffin PCM

on the annual electrical output of PV panels in Baghdad and Milan. In Baghdad, observed data for solar radiation will be used. To complement this research, the impact of different PCMs with different thicknesses on PV panel electrical output will be investigated in Baghdad and Milan. This investigation will lead to the identification of the best PCM with optimal thickness.

Finally, according to the literature review, increasing the number of fins inside the PCM in the PV-PCM system leads to a reduction in the temperature of the PV panel (these studies only last for several days). However, there is no study that investigates the impact of using metal foam with different PCMs on the yearly electrical output of the PV panel. Thus, the final contribution of this study is to investigate the impact of using different aluminium foam percentages with different PCMs and different thicknesses on the yearly electrical output of PV panels in Baghdad and Milan.

Chapter 3 Mathematical Models

3.1 Outline

This chapter presents the development of three mathematical models. Firstly, a transient lumped model for the temperature of the stand-alone PV panel. Secondly, a novel lumped-distributed parameter model for the lumped temperatures of the PV panel and the aluminium walls of the container, and the temperature distribution within the PCM for the combined PV-PCM system. Finally, a 1D distributed parameter model of the temperature distributions throughout the entire PV-PCM system. In the first model, perfect contact exists between all the layers comprising the PV panel, and a thermal contact resistance exists between the PV panel and the PCM container, with volume change occurs during the solid/liquid phase change.

3.2 The PV panel stand-alone model

In order to predict the performance of the PV panel, the thermal analysis for the PV panel requires acceptable assumptions. Figure 3-1 and Figure 3-2 depict the heat transfer schematic diagrams for the PV panel, which are the foundations for the one-dimensional models. The assumptions are:

1. According to the dimensions of PV panel from the figure 1, the areas of x-y and y-z << the areas of x-z. Therefore, the heat losses from these sides are very low and neglected. This assumption has been considered by several researchers to simplify the modelling of a combined PV-PCM system for example Brano et al. (2014) and Smith et al. (2014)
2. The heat transfer is only by conduction inside the PV panel.
3. One-dimensional heat transfer. The problem of PCM can be considered one-dimensional as a result of:
    - The heat transfer from the sides is neglected
    - The heat transfer occurs by conduction only, and
    - The symmetry of the PV panel.

Therefore, heat transfer occurs in the orthogonal direction to the PV panel surface only (x-direction) (Brano et al., 2014, Mahamudul et al., 2016, Kibria et al., 2016), as illustrated in Figure 3-1 and Figure 3-2.

4. Heat generation occurs inside the PV cell.
5. In order to linearize the problem, the contributions from the free convection and radiation heat transfer are non-linear and so free convection and radiation heat transfer coefficients are used to keep the overall set of equations linear (Sakin et al., 2009).

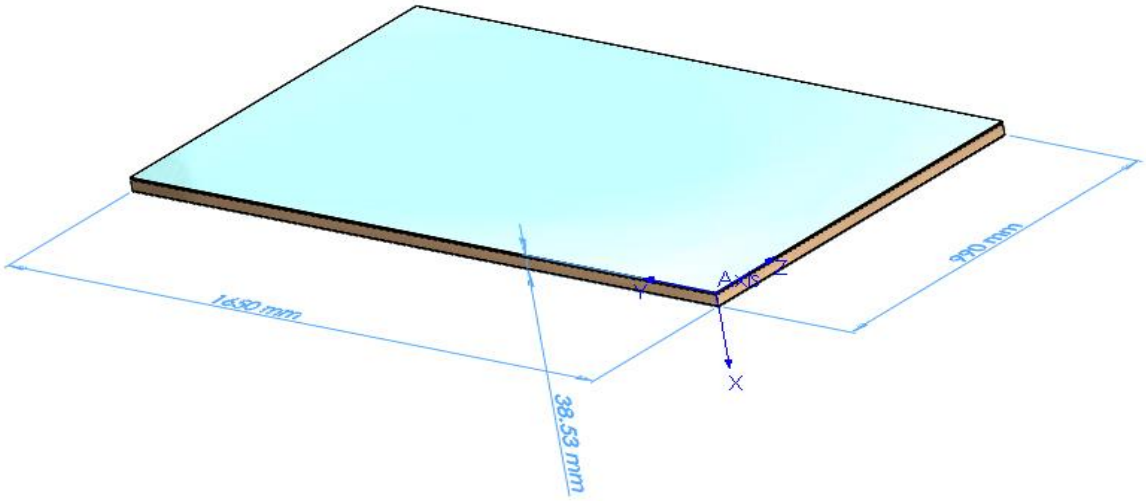

Figure 3-1: The PV panel with the dimensions are in mm.

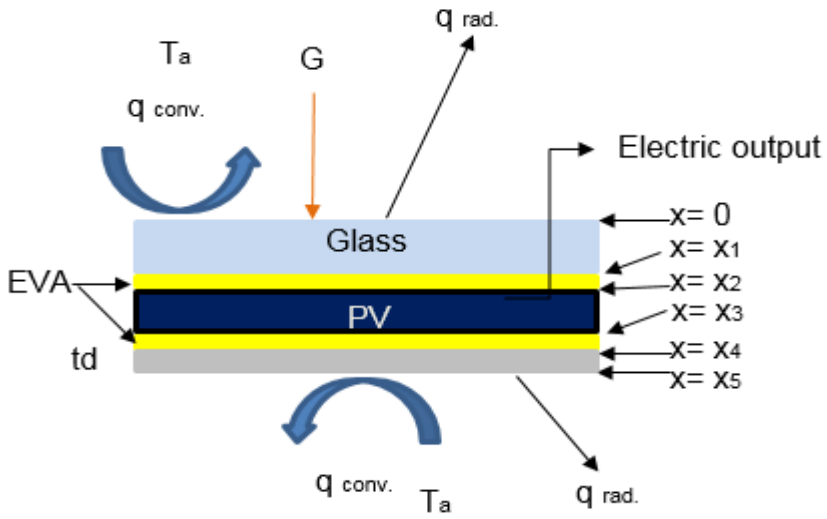

Figure 3-2: The schematic diagram of the PV panel.

Figure 3-2 is a schematic diagram of the PV panel and consists of five layers. The first layer is glass with a thickness of 0.0032 m (x_1). The second and fourth layers are ethylene vinyl acetate [EVA] each of thickness 0.0005 m and represented by (x_2-x_1) and (x_4-x_3), respectively. The third layer is the PV cell with a thickness of 0.00025 m (x_4-x_3). The fifth layer is the Tedlar and is 0.0001 m thick (x_5-x_4). *T* represents the temperature and the subscript *a* represents the ambient. *G* denotes the solar radiation flux received by the PV panel; q_{conv} denotes the convection heat transfer and q_{rad} represents the radiation to the sky.

For a one-dimensional representation of conductive heat flow in the x direction within the PV panel for the glass, EVA and Tedlar layers, the Fourier equation applies:-

$$\rho_k \, C_k \frac{\partial T_k}{\partial t} = \lambda_k \frac{\partial^2 T_k}{\partial x^2} \qquad \textbf{3-1}$$

for $t > 0, 0 \leq x \leq x_2$, $x_3 \leq x \leq x_5$ and $k = 1,2,3\,4$, and where, T is the temperature (^0C), ρ is the density ($kg\ m^{-3}$), C is the specific heat capacity ($J\ kg^{-1}\ K^{-1}$) and λ is the thermal conductivity ($W\ m^{-1}\ K^{-1}$).

While, for the PV cell layer, the Poisson equation applies due to the heat generation term:

$$\rho_3 \, C_3 \frac{\partial T_3}{\partial t} = \lambda_3 \frac{\partial^2 T_3}{\partial x^2} + \beta_{PV} G(1 - \eta_{PV})/(x_3 - x_2) \qquad \textbf{3-2}$$

for $t > 0$ and $x_2 \leq x \leq x_3$, and where, β_{PV} is the absorptivity of the PV panel for the solar radiation and η_{PV} is the efficiency of the PV cell. The η_{PV} is described in Equ. 2-3.

The initial condition for the PV panel is:

At $t < 0$, $0 \leq x \leq x_5$ and $k = 1\ to\ 5$:

$$T_k = T_{in} = T_a \qquad \textbf{3-3}$$

The boundary conditions for Equs. 3-1 and 3-2 are as follows:

At $t > 0$ & at $x = 0$:

$$\lambda_g \left.\frac{\partial T_1}{\partial x}\right|_{x=0} = h_{a1}\,(T_a - T_1|_{x=0}) + h_{r2}(T_{sky} - T_1|_{x=x0}) \qquad \textbf{3-4}$$

At $t > 0$ & at $x = x_k$ and k = 1, 2, 3 and 4:

$$-\lambda_k \left.\frac{\partial T_k}{\partial x}\right|_{x_k} = -\lambda_{k+1} \left.\frac{\partial T_{k+1}}{\partial x}\right|_{x_{k+1}} \qquad \textbf{3-5}$$

and

$$T_k = T_{k+1} \qquad \textbf{3-6}$$

At $t > 0$ & at $x = x_5$:

$$\lambda_{td} \left.\frac{\partial T_5}{\partial x}\right|_{x_5} = h_{a2}\,(T_a - T_5|_{x_5}) + h_{r2}(T_{ground} - T_5|_{x5}) \qquad \textbf{3-7}$$

The substitution of the definition of the average temperature, Equ. 3-8 into the distributed parameter Equs. 3-1 and 3-2 provides lumped (average or mean) temperature values over the thickness of each layer.

$$\bar{T}_k^{(t)} = \frac{1}{(x_k - x_{k-1})} \int_{x_{k-1}}^{x_k} T_j\,(x,t)dx \qquad \textbf{3-8}$$

For example, the following procedure is for Equ. 3-2 and the PV cell: (and the same procedure applies for Equ. 3-1 and the other 4 layers):

$$\rho_3\, C_3 \int_{x_2}^{x_3} \frac{\partial T_k}{\partial t}\,\mathrm{d}x = \lambda_3 \int_{x_2}^{x_3} \frac{\partial^2 T_3}{\partial x^2}\,\mathrm{d}x + \int_{x_2}^{x_3} \beta_{PV} G(1-\eta_{PV})/(x_3 - x_2)\mathrm{d}x \qquad \textbf{3-9}$$

Rearrangement of the first two terms in Equ. 3-9 gives the following expression:

$$\rho_3\, C_3 \frac{\partial}{\partial t} \int_{x_2}^{x_3} T_3\,\mathrm{d}x = \lambda_3 \int_{x_2}^{x_3} \frac{\partial}{\partial x}\left(\frac{\partial T_3}{\partial x}\right)\mathrm{d}x + \int_{x_2}^{x_3} \beta_{PV} G(1-\eta_{PV})/(x_3 - x_2)\mathrm{d}x \qquad \textbf{3-10}$$

Completion of the integrands and substituting Equ. 3-8 into the first term provides the next equation:

$$\rho_3\, C_3(x_3 - x_2)\frac{d\bar{T}_3}{dt} = \lambda_3 \left|\frac{\partial T_3}{\partial x}\right|_{x_2}^{x_3} + \beta_{PV} G(1-\eta_{PV})]_{x_3 - x_2} \quad \textbf{3-11}$$

The use of the boundary condition Equ. 3-5 in Equ. 3-11 provides the following expression for the PV cell:

$$\rho_3\, C_3(x_3 - x_2)\frac{d\bar{T}_3}{dt} = \left(\lambda_4 \frac{\partial T_4}{\partial x}\right]_{x_3} - \lambda_2 \frac{\partial T_2}{\partial x}\right]_{x_2}\Bigg) + \beta_{PV} G(1-\eta_{PV}) \quad \textbf{3-12}$$

Application of this procedure to the other layers of the PV panel provides the following expressions:

For the glass layer:

$$\rho_1\, C_1\, x_1 \frac{d\bar{T}_1}{dt} = h_{a1}\,(T_a - \bar{T}_1) + h_{r2}\big(T_{sky} - \bar{T}_1\big) + \lambda_2 \frac{\partial T_2}{\partial x}\right]_{x_2} \quad \textbf{3-13}$$

For the first EVA layer:

$$\rho_2\, C_2(x_2 - x_1)\frac{d\bar{T}_2}{dt} = \left(\lambda_3 \frac{\partial T_3}{\partial x}\right]_{x_2} - \lambda_1 \frac{\partial T_1}{\partial x}\right]_{x_1}\Bigg) \quad \textbf{3-14}$$

For the second EVA layer:

$$\rho_4\, C_4(x_4 - x_3)\frac{d\bar{T}_4}{dt} = \left(\lambda_5 \frac{\partial T_5}{\partial x}\right]_{x_4} - \lambda_3 \frac{\partial T_3}{\partial x}\right]_{x_3}\Bigg) \quad \textbf{3-15}$$

For the final Tedlar layer:

$$\rho_5\, C_5(x_5 - x_4)\frac{d\bar{T}_5}{dt} = h_{a2}\,(T_a - \bar{T}_5) + h_{r2}\big(T_{ground} - \bar{T}_5\big) - \lambda_4 \frac{\partial T_4}{\partial x}\right]_{x_4} \quad \textbf{3-16}$$

The assumption of intimate contact between the layers, Equ. 3.6, means that a single lumped temperature, $\bar{T}_{PVL}$, represents the PV panel. The summation of the Equs. 3-12 to 3-16 and the use of Equs. 3-5 and 3-4 provides an expression for the response of this lumped temperature of the PV panel as follows:

$$\sum_{j=1}^{j=5} \rho_k\, C_k(x_k - x_{k-1})\frac{d\,\bar{T}_{PVL}}{dt} \quad \textbf{3-17}$$
$$= -[h_{a1} + h_{a2} + h_{r1} + h_{r1}]\bar{T}_{PVL} + h_{a1}T_a + h_{a2}T_a$$
$$+ h_{r1}T_{sky} + h_{r2}T_{ground} + \beta_{PV}\, G[1-\eta_{PV}]$$

3.3 The combined lumped - distributed parameter model of a combined PV-PCM system

Figure 3.3 is a schematic in the x-direction through a PV panel attached to an aluminium container filled with a PCM material. The dimensions and layers of the PV panel are identical to those detailed in Section 3.2. There are three additional layers in the combined system. The sixth and eighth layers are the aluminium container walls each with a thickness of 0.002 m and, correspondingly (x_6-x_5) and (x_8-x_7).The seventh layer is the PCM of thickness 0.03 m (x_7-x_6). This PVM in this layer will change phase depending upon the day or night operation of the combined system. A contact resistance exists between the Tedlar layer and the upper aluminium wall of the container. All the interfaces within the aluminium container are in intimate contact.

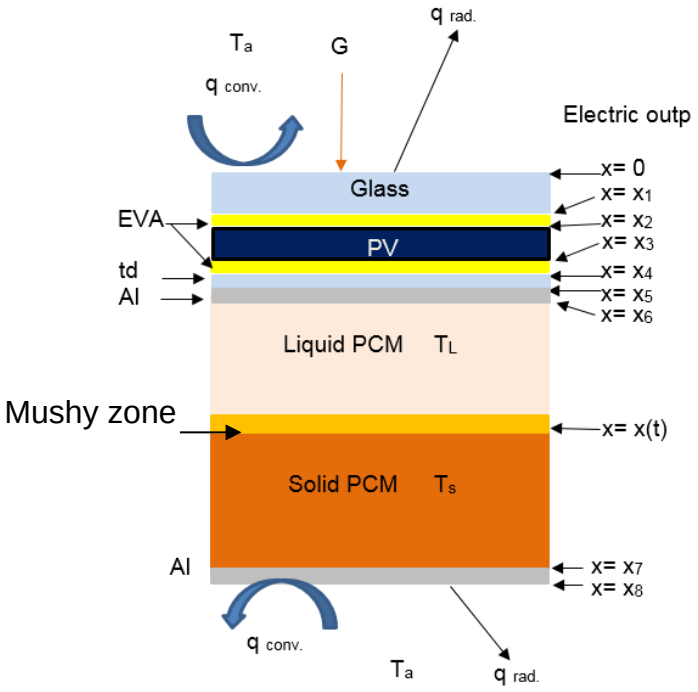

Figure 3-3: The schematic diagram of the combined PV-PCM system

The development of this model assumes a combination of lumped temperature relationships for all the layers except the PCM layer, which is a distributed parameter representation. This development is to reduce the computer time for

the assessment for a whole year simulation. The main assumptions for this model include the assumptions in section 3.2 and the following for the PCM:

1- The PCM is homogeneous (Brano et al., 2014, Kibria et al., 2016).

2- The specific thermo-physical properties of the molten and solid phases are independent of temperature (constant). This approximation is not far from reality, because the temperatures will not change greatly in each phase. The solid phase has different thermo-physical properties than the liquid phase. This hypothesis has been implemented by Smith and Forester (Smith et al., 2014) and (Brano et al., 2014). However, several papers (e.g. Kibria et al. (2016)) have considered also that the thermo-physical properties are constant for both phases.

3- The heat transfer is only by conduction inside the PCM. This hypothesis is a result of low natural convection within the molten PCM compared with heat transfer by conduction. This hypothesis can be assessed by the Peclet number Incropera and De Witt (2005), which represents the ratio of heat transfer by convection over the heat transfer by conduction (Holman, 2002). Several papers have neglected the effect of the natural convection inside the PCM to simplify the modelling (Malvi et al., 2011); (Brano et al., 2014); (Mahamudul et al., 2016); (Kibria et al., 2016).

4- The heat capacity method represents the latent heat effect caused by the phase change within the PCM (Poirier and Salcudean, 1988). This method assumes that during the phase change, the specific heat capacity equals the summation of the latent heat divided by the melting temperature range and specific heat capacity of the PCM. The melting occurs over a temperature range, called the mushy zone as illustrated in figure 2, which in this study is 2 ^{0}C.

A contact resistance exists between the PV panel and the top surface of the aluminium container – layers 5 and 6 and the following boundary condition applies:

$$\text{At } x = 5, \quad -\lambda_5 \left.\frac{\partial T_5}{\partial x}\right|_{x=5} = \frac{(T_5 - T_6)}{\mathrm{R}_{5\to6}} = -\lambda_6 \left.\frac{\partial T_6}{\partial x}\right|_{x=6} \text{ and } T_5 \neq T_6 \qquad \textbf{3-18}$$

where $\mathrm{R}_{5\to6} = \left(\Delta x_{gap}\right)/\lambda_{gap}$ is the reciprocal of the conductive heat transfer coefficient h_{cond} between the two layers. The lumped expression for the Tedlar layer Equ. 3.16 now becomes:

$$\rho_5\, C_5(x_5 - x_4)\frac{d\bar{T}_5}{dt} = h_{cond5\to6}\,(\bar{T}_5 - \bar{T}_6) - \lambda_4 \frac{\partial T_4}{\partial x}\Big]_{x_4} \qquad \textbf{3-19}$$

The response of the lumped temperature of the PV panel is now

$$\sum_{j=1}^{j=5} \rho_k\, C_k(x_k - x_{k-1})\frac{d\,\bar{T}_{PVL}}{dt} \qquad \textbf{3-20}$$
$$= -[h_{a1} + h_{a2} + h_{cond5\to6}]\bar{T}_{PVL} + h_{a1} + h_{r1}T_{sky}$$
$$+ h_{cond5\to6}\bar{T}_6 + \beta_{PV}\, G[1 - \eta_{PV}]$$

The response of the lumped temperatures of the walls of the aluminium container are as follows: for the upper wall:

$$\rho_6\, C_6(x_7 - x_6)\frac{d\bar{T}_6}{dt} = h_{cond5\to6}\,(\bar{T}_5 - \bar{T}_6) - \lambda_7 \frac{\partial T_7}{\partial x}\Big]_{x=6} \qquad \textbf{3-21}$$

and for the lower surface:

$$\rho_8\, C_8(x_8 - x_7)\frac{d\bar{T}_8}{dt} = -\lambda_7 \frac{\partial T_7}{\partial x}\Big]_{x=7} + h_{a2}(T_a - \bar{T}_8) + h_{r2}\left(T_{ground} - \bar{T}_8\right) \qquad \textbf{3-22}$$

The Fourier equation represents the temperature distribution within the PCM (layer 7 in figure 3.3) for $t > 0, x_6 \le x \le x_7$

$$\rho_7\, C_7 \frac{\partial T_7}{\partial t} = \lambda_7 \frac{\partial^2 T_7}{\partial x^2} \qquad \textbf{3-23}$$

The boundary values for Equ. 3-23 with intimate contact between the interfaces between the aluminium walls and the PCM are as follows:

At $x = x_6$

$$h_{cond5\to6}\,(\bar{T}_5 - \bar{T}_6) - \rho_6\, C_6(x_7 - x_6)\frac{d\bar{T}_6}{dt} = -\lambda_7 \frac{\partial T_7}{\partial x}\Big]_{x=6} \text{ and } \bar{T}_6 = T_7 \qquad \textbf{3-24}$$

and at $x = x_7$

$$-\lambda_7 \frac{\partial T_7}{\partial x}\Big]_{x=7} = \rho_8 C_8 (x_8 - x_7) \frac{d\bar{T}_8}{dt} + h_{a2} (T_a - \bar{T}_8) + h_{r2}\left(T_{ground} - \bar{T}_8\right) \text{ and } T_7 = \bar{T}_8 \quad \textbf{3-25}$$

The thermo-physical properties of the PCM depend on the temperature of the PCM at positions within the layer and whether the phase is a solid a liquid or the phase change is taking place as:

For solid phase:

If $T_{7,x} < T_{melting}$ **3-26**

$C_7 = C_{PCM-solid}$, $\rho_7 = \rho_{PCM-solid}$, $\lambda_7 = \lambda_{PCM-solid}$

For the liquid phase:

If $T_{7,x} > T_{liquid}$ **3-27**

$C_7 = C_{PCM-liquid}$, $\rho_7 = \rho_{PCM-liquid}$, $\lambda_7 = \lambda_{PCM-liquid}$

For the transient between solid and liquid:

If $T_{melting} \leq T_{7,x} \leq T_{liquid}$ **3-28**

$$C_7 = \frac{(T_{liquid} - T_{melting}) C_{PCM-solid} + Latent\ heat}{(T_{liquid} - T_{melting})}$$

$\rho_7 = \rho_{PCM-solid}$, $\lambda_7 = \lambda_{PCM-solid}$

The initial condition for the PV-PCM model is:

$$\text{At } t < 0 \quad \text{and} \quad \text{for} \quad 0 \leq k \leq 8, \; T_{x=1\ to\ 8} = T_a \quad \textbf{3-29}$$

3.3 A one dimensional distributed parameter model a PV-PCM

The final mathematical model of a PV-PCM is a one dimensional distributed parameter representation. The equations in the previous two sections provide the description as follows:

The Fourier Equ. 3.1 represents the temperature distribution in all the layers in Figure 3.3 except for the PV layer, where the Poisson Equ. 3.2 applies.

The Equ. 3.4 applies at the top surface of the PV.

Intimate contact occurs between all interface within the system and equs 3.5 and 3.6 apply.

However, Equ. 3.18 represents the contact resistance between the base of the PV and the aluminium container.

Equs. 3.27, 3.28 and 3.29 represent the PCM.

The complete mathematical representation requires the boundary condition on the base of the aluminium container and this is:

$$\lambda_8 \frac{\partial T_8}{\partial x}\Big]_{x_8} = h_{a2}\left(T_a - T_8|_{x_8}\right) + h_{r2}\left(T_{ground} - T_8|_{x8}\right) \quad \textbf{3-30}$$

The initial condition for this model is Equ. 3.30.

3.4 Summary

This chapter introduces three mathematical models: firstly, a model to predict the transient average lumped temperature of the PV panel stand alone, secondly, a lumped-distributed parameter representation of the PV-PCM system and finally, a complete distributed parameter model for the PV-PCM module. The second and third models have a thermal contact resistance between the PV panel and the container housing the PCM, otherwise all interfaces are in intimate contact.

Chapter Four Discretization and Stability Analysis

4.1 Introduction

This chapter introduces the space and the time discretization for the three mathematical models. These models are the PV stand alone, the lumped-distributed model and the distributed model. Then, investigations have implemented for the stability of these three models.

4.2 The discretization

The finite difference method can be used to make the space discretization by using central node:

$$\left.\frac{\partial T}{\partial x}\right|_{i+1/2} \approx \frac{T_{i+1} - T_i}{\Delta x} \quad \textbf{4-1}$$

$$\left.\frac{\partial T}{\partial x}\right|_{i-1/2} \approx \frac{T_i - T_{i-1}}{\Delta x} \quad \textbf{4-2}$$

$$\left.\frac{\partial^2 T}{\partial x^2}\right|_i \approx \frac{\left.\frac{\partial T}{\partial x}\right|_{i+\frac{1}{2}} - \left.\frac{\partial T}{\partial x}\right|_{i-\frac{1}{2}}}{\Delta x} \approx \frac{T_{i+1} + T_{i-1} - 2T_i}{(\Delta x)^2} \quad \textbf{4-3}$$

where, *i* refer to the space node, the derivative is represented by the average approximately. Similarly, by using the time discretisation depending on the explicit and implicit methods:-

$$\left.\frac{\partial T}{\partial t}\right|_i = \frac{T_{i,j+1} - T_{i,j}}{\Delta t} \quad \textbf{4-4}$$

For the explicit method Equ. 3-1 will be:

$\theta = 0$

$$\rho C \left.\frac{\partial T}{\partial t}\right|_{i,j} = \lambda \left.\frac{\partial^2 T}{\partial x^2}\right|_{i,j} \quad \textbf{4-5}$$

For the implicit method Equ. 3-1 will be:

$\theta = 1$

$$\rho C \left.\frac{\partial T}{\partial t}\right|_{i+1,j} = \lambda \left.\frac{\partial^2 T}{\partial x^2}\right|_{i+1,j} \quad \textbf{4-6}$$

Consequently, these Equs. 4-5 and 4-6 will be:

$$\frac{T_{i,j+1} - T_{i,j}}{\Delta t} = \frac{1}{\rho C}\frac{\lambda}{(\Delta x)^2}\Big[\theta\big[T_{(i-1,\ j+1)} - 2T_{(i,\ j+1)} + T_{(i+1,\ j+1)}\big] + (1-\theta)\big[T_{(i-1,\ j)} - 2T_{(i,\ j)} + T_{(i+1,\ j)}\big]\Big] \quad \textbf{4-7}$$

Where, j represents the instance time step, θ is different for each time discretization scheme and it equals to 0 and 1 for explicit and implicit method respectively as illustrated in Figure 4-1.

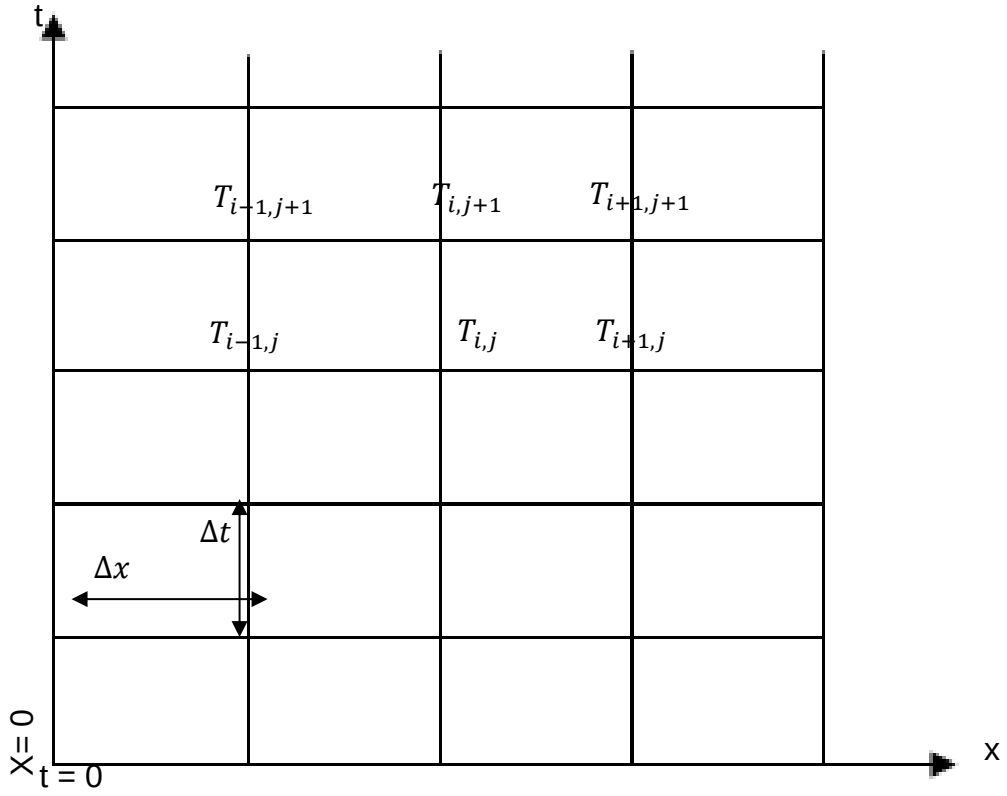

Figure 4-1: the time and space discretization

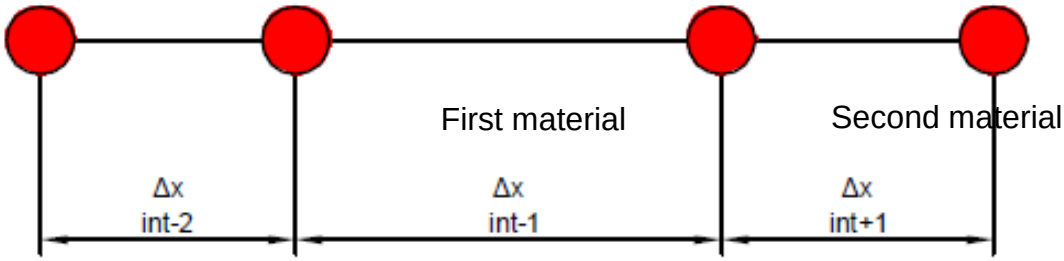

Figure 4-2: The one dimensional interface between two materials with different mesh size.

While, Figure 4-2 is the schematic of the one dimensional interface point between two different materials with non-uniform mesh distance. The subscribe int represents the interface point between two materials such as the glass and the EVA, the subscribe $int-1$ represents the first solid material like the glass and the subscribe $int+1$ represents the second solid material like the EVA. Equs. 4-5 and 4-6 will be:

$$\rho_{int}\, C_{int} \int_{\Delta x_{int}-1}^{\Delta x_{int}+1} \frac{\partial T_{int}}{\partial t}\, dx \;=\; \lambda_{int} \int_{\Delta x_{int}-1}^{\Delta x_{int}+1} \frac{\partial}{\partial x}\left(\frac{\partial T_{int}}{\partial x}\right) dx \qquad \textbf{4-8}$$

where:

$$\rho_{int} = (\Delta x_{int-1} * \rho_{int} - 1 \; + \Delta x_{int+1} * \rho_{int} + 1)/(\Delta x_{int-1} + \Delta x_{int+1}) \qquad \textbf{4-9}$$

$$Cp_{int} = \quad (Cp_{int-1} * \Delta x_{int-1} * \rho_{int} - 1 \; + Cp_{int+1} * \Delta x_{int+1} * \rho_{int} + 1)/\rho_{int} * (\Delta x_{int-1} + \Delta x_{int+1}) \qquad \textbf{4-10}$$

$$\lambda_{int} = \; (Cp_{int-1} * \Delta x_{int-1} * \rho_{int} * \lambda_{int-1} \; + Cp_{int+1} * \Delta x_{int+1} * \rho_{int} * \lambda_{int+1})/ \; \rho_{int} * (\Delta x_{int-1} + \Delta x_{int+1}) \qquad \textbf{4-11}$$

Then, Equ. 4-8 will be:

$$\rho_{int}\, C_{int}\, \frac{\partial}{\partial t} \int_{\Delta x_{int}-1}^{\Delta x_{int}+1} T_{int}\, dx = \lambda \left.\frac{\partial T_{int}}{\partial x}\right|_{x=\Delta x_{int}-1}^{x=\Delta x_{int}+1} \qquad \textbf{4-12}$$

$$= \lambda_{int+1} \left.\frac{\partial T_{int}}{\partial x}\right|_{x=(\Delta x_{int+1})} - \lambda_{int-1} \left.\frac{\partial T_{int}}{\partial x}\right|_{x=(\Delta x_{int-1})}$$

Then, this equation will be:

$$(\Delta x_{int-1} + \Delta x_{int+1})\rho_{int}\, C_{int}\, \frac{\partial T_{int}}{\partial t} = \quad \textbf{4-13}$$

$$= \lambda_{int+1}\, \frac{\partial T_{int}}{\partial x}\bigg|_{x=\Delta x_{int+1}} - \lambda_{int-1} \frac{\partial T_{int}}{\partial x}\bigg|_{x=\Delta x_{int-1}}$$

The time discretization depending on the explicit and implicit methods can be written as:

$$(\Delta x_{int-1} + \Delta x_{int+1})\rho_{int}\, C_{int}\, \frac{T_{(int,\ j+1)} - T_{(int,\ j)}}{\Delta t} \quad \textbf{4-14}$$

$$= 2(1 - \theta)\left[\frac{\lambda_{int+1}}{\Delta x_{int+1}}\left(T_{(int+1,\ j)} - T_{(int,\ j)}\right) + \frac{\lambda_{int-1}}{\Delta x_{int-1}}\left(T_{(int-1,\ j)} - T_{(int,\ j)}\right)\right] + 2\theta\left[\frac{\lambda_{int+1}}{\Delta x_{int+1}}\left(T_{(int+1,\ j+1)} - T_{(int,\ j+1)}\right) + \frac{\lambda_{int-1}}{\Delta x_{int-1}}\left(T_{(int-1,\ j+1)} - T_{(int,\ j+1)}\right)\right]$$

Then, it will be:

$$T_{(int,\ j+1)} = T_{(int,\ j)} \quad \textbf{4-15}$$

$$+ \frac{2\Delta t}{(\Delta x_{int-1} + \Delta x_{int+1})\rho_{int}\, C_{int}}\left\{\theta\left[\frac{\lambda_{int+1}}{\Delta x_{int+1}}\left(T_{(int+1,\ j+1)} - T_{(int,\ j+1)}\right) + \frac{\lambda_{int-1}}{\Delta x_{int-1}}\left(T_{(int-1,\ j+1)} - T_{(int,\ j+1)}\right)\right] + (1-\theta)\left[\frac{\lambda_{int+1}}{\Delta x_{int+1}}\left(T_{(int+1,\ j)} - T_{(int,\ j)}\right) + \frac{\lambda_{int-1}}{\Delta x_{int-1}}\left(T_{(int-1,\ j)} - T_{(int,\ j)}\right)\right]\right\}$$

Kladisios and Steggou-Sagia (2015) has used almost same Equ. 4-15 when $\theta = 1$. However, He has not used the λ_{int} correctly, where, he used only λ_{int} without separation for each location: before and after the interface. The discretization will be applied for the three mathematical models in chapter three:

4.2.1 The discretization for the PV panel stand-alone lumped model

For the PV panel stand-alone lumped model Equ. 3-17 with explicit time discretization will be:

$$\bar{T}_{PV2} = \bar{T}_{PV1} + \frac{\Delta t}{\rho_{PV}\, C_{PV}\, x_5} * [-[h_{a1} + h_{a2} + h_{r1} + h_{r1}]\bar{T}_{PV1} + h_{a1}T_a + h_{a2}T_a + h_{r1}T_{sky} + h_{r2}T_{ground} + \beta_{PV}\, G[1-\eta_{PV}]] \quad \textbf{4-16}$$

4.2.2 The discretization for the combined lumped-numerical model of the PV-PCM module

By applying Equ. 3-18 in Equ. 3-20 with time discretization, Equ. 3-20 will be:

$$T_{PVL(j+1)} = T_{PVL(j)} + \frac{\Delta t}{\rho_{PVL}\, C_{PVL} \Delta x_{PVL}} [h_a\,(T_a - T_{PVL}|_{x=0}) + h_{r-PVL}\big(T_{sky} - T_{PVL}|_{x=0}\big) + \beta_{PV} G(1-\eta_{PV}) - (\frac{T_{PVL}|_{x_5} - T_{AL}|_{x_5}}{\mathrm{R}_{5\to 6}})] \quad \textbf{4-17}$$

According to the heat capacity method for phase change situations, the specific heat capacity of the PCM during melting temperature range will equal to summation of the latent heat divided by the melting temperature range, then this value will be added to specific heat capacity of the PCM. Equ. 3-23 will be solved numerically by the finite difference relationship as:

$$T_{PCM(i,j+1)} - T_{PCM(i,j)} = \frac{\Delta t}{\rho C}\frac{\lambda}{(\Delta x)^2}\Big[\theta\big[T_{PCM(i-1,j+1)} - 2T_{(i,j+1)} + T_{(i+1,j+1)}\big] + (1-\theta)\big[T_{(i-1,j)} - 2T_{(i,j)} + T_{(i+1,j)}\big]\Big] \quad \textbf{4-18}$$

where the subscripts j and i represent a grid point in time and space, Δt and Δx are time and length steps respectively and θ = 0 results in an explicit technique. Implicit techniques are obtained if the θ = 1 which is the fully implicit backward difference (FIB) scheme. The FIB scheme is used in this solution.

Equ. 4-18 will be used and the thermos-physical properties can be described depending on the temperature of the PCM as:

For solid phase:

If $T_{(i,\ j+\theta)} < T_{melting}$ **4-19**

$C_{PCM} = C_{PCM-solid}$, $\rho_{PCM} = \rho_{PCM-solid}$, $\lambda_{PCM} = \lambda_{PCM-solid}$

For the liquid phase:

If $T_{(i,\ j+\theta)} > T_{soldification}$ **4-20**

$C_{PCM} = C_{PCM-liquid}$, $\rho_{PCM} = \rho_{PCM-liquid}$, $\lambda_{PCM} = \lambda_{PCM-liquid}$

For the transient between solid and liquid:

If $T_{melting} \leq T_{(i,\ j+\theta)} \leq T_{soldification}$ **4-21**

$$C_{PCM} = \frac{(T_{soldification} - T_{melting})C_{PCM-solid} + Latent\ heat}{(T_{soldification} - T_{melting})}$$

$\rho_{PCM} = \rho_{PCM-solid}$, $\lambda_{PCM} = \lambda_{PCM-solid}$

This solution will consider that the aluminium container is flexible and the width of the PCM is variable depending on the different densities of the solid and liquid phases of the PCM. Firstly, when the PCM is solid the density is ρ_s and the PCM increments width is assumed Δx_{PCM-S}. Secondly, according to the mass balance, the width of the liquid PCM increments will be calculated as flow:-

$$\rho_L * \Delta x_{PCM-L} * area = \rho_S * \Delta x_{PCM-S} * area \quad \textbf{4-22}$$

Therefore:

$$\Delta x_{PCM-L} = \rho_S * \Delta x_{PCM-S}/\rho_L \quad \textbf{4-23}$$

However, for the first node of the PCM, a fictitious temperature will be appeared which is $T_{PCM(-1,\ m+1)}$. To eliminate this fictitious temperature, the boundary condition from the Equs. 3-18 and 3-19 with Equ. 3-21 will be applied in Equ. 4-18, the result will be:

$$T_{PCM(0,\ m+1)} = T_{PCM(0,m)} + \frac{\Delta t}{\rho_{PCM}\ C_{PCM}} \frac{\lambda_{PCM}}{(\Delta x)^2} \left[\left[- \frac{2\Delta x_{PCM} \rho_{AL}\ C_{AL}\ (x_6 - x_5)}{\lambda_{PCM}} \frac{(T_{PCM(0,j+1)} - T_{PCM(0,j)})}{\Delta t} + \frac{2\Delta x_{PCM} h_{cond5\to6} \left(\bar{T}_{PVL(j+1)} - T_{PCM(0,j+1)} \right)}{\lambda_{PCM}} - 2T_{PCM(0,j+1)} + 2T_{PCM(1,j+1)} \right] \right] \quad \textbf{4-24}$$

Also, the last node of the PCM has a fictitious temperature will be appeared which is $T_{PCM(\ 7+1,\ \ j+1)}$. To eliminate this fictitious temperature, the boundary condition from the Equ. 3-24 with Equ. 3-25 will be applied in Equ.4-18, the result will be:

$$T_{PCM(i,\ m+1)} = T_{PCM(i,m)} + \frac{\Delta t}{\rho_{PCM}\ C_{PCM}} \frac{\lambda_{PCM}}{(\Delta x)^2} \left[\left[\frac{2\Delta x_{PCM} \rho_{AL}\ C_{AL}\ (x_6 - x_5)}{\lambda_{PCM}} \frac{(T_{PCM(i,j+1)} - T_{PCM(i,j)})}{\Delta t} - \frac{2\Delta x_{PCM} h_a \left(T_a - T_{PCM(i,j+1)} \right)}{\lambda_{PCM}} - \frac{2\Delta x_{PCM} h_{r-AL} \left(T_{ground} - T_{PCM(i,j+1)} \right)}{\lambda_{PCM}} - 2T_{PCM(i,j+1)} + 2T_{PCM(i-1,j+1)} \right] \right] \quad \textbf{4-25}$$

4.2.3 The discretization for the distributed model for the PV-PCM module

By using the space and time discretisation depending on the explicit and implicit methods Equs. 3-1 and 3-2will be:

$$\rho_k\ C_k \frac{[T_{k(i,\ j+1)} - T_{g(i,\ j)}]}{\Delta t} = \frac{\lambda_k}{(\Delta x)^2} \Big[\theta \left[T_{k(i-1,\ j+1)} - 2T_{k(i,\ j+1)} + T_{k(i+1,\ j+1)} \right] + (1-\theta) \left[T_{k(i-1,\ j)} - 2T_{g(i,\ j)} + T_{k(i+1,\ j)} \right] \Big] + \beta_{PV} G (1 - \eta_{PV}) \Big]_{for x_3 - x_2\ only} \quad \textbf{4-26}$$

Where k is for the layers 1, 2, 3, 4, 5 and 7. Equ. 4-26 will applied for the internal nodes for these layers.

For x=0, which means i=0 (the first node), Equ. 4-26 will be:

$$\rho_g \, C_g \frac{[T_{g(0,\ j+1)} - T_{g(0,\ j)}]}{\Delta t} \qquad \textbf{4-27}$$

$$= \frac{\lambda_g}{(\Delta x)^2}\Big[\, \theta\big[T_{g(-1,\ j+1)} - 2T_{g(i,\ j+1)} + T_{g(i+1,\ j+1)}\big] + (1-\theta)\big[T_{g(-1,\ j)} - 2T_{g(i,\ j)} + T_{g(i+1,\ j)}\big]\Big]$$

Equ. 4-27 has a fictitious temperature ($T_{g(-1,\ j)}$). In order to eliminate this fictitious temperature, the boundary condition from Equ. 3-4 will be used after time discretization. The boundary condition will be:

At $t > 0$ & $x = 0$:

$$-\lambda_g \frac{[T_{g(1,\ j+\theta)} - T_{g(-1,\ j+\theta)}]}{2\Delta x} = h_a \left[T_{a(0,\ j+\theta)} - T_{g(0,\ j+\theta)}\right] + h_{r1}\left(T_{sky} - T_g\big|_{x=0}\right) \qquad \textbf{4-28}$$

Then, this equation will be :-

$$T_{g(-1,\ j+\theta)} = \frac{2\Delta x h_a}{\lambda_g}\left[T_{a(0,\ j+\theta)} - T_{g(0,\ j+\theta)}\right] + T_{g(1,\ j+\theta)} + \frac{2\Delta x\, h_{r1}}{\lambda_g}\left(T_{sky} - T_g\big|_{x=0}\right) \qquad \textbf{4-29}$$

In order to eliminate the fictitious temperature ($T_{g(-1,\ j)}$), the Equ. 4-29 will be inserted in Equ. 4-27:

$$\rho_g\, C_g \frac{[T_{g(0,\ j+1)} - T_{g(0,\ j)}]}{\Delta t} \qquad \textbf{4-30}$$

$$= \theta \frac{\lambda_g}{(\Delta x)^2}\left[\frac{2\Delta x h_a}{\lambda_g}\left[T_{a(0,\ j+1)} - T_{g(0,\ j+1)}\right]\right.$$

$$+ \frac{2\Delta x\, h_{r1}}{\lambda_g}\left(T_{sky} - T_g\big|_{x=0}\right) + T_{g(1,\ j+1)} - 2T_{g(0,\ j+1)}$$

$$\left. + T_{g(1,\ j+1)}\right] + (1$$

$$- \theta) \frac{\lambda_g}{(\Delta x)^2}\left[\frac{2\Delta x h_a}{\lambda_g}\left[T_{a(0,\ j)} - T_{g(0,\ j)}\right]\right.$$

$$\left. + \frac{2\Delta x\, h_{r1}}{\lambda_g}\left(T_{sky} - T_g\big|_{x=0}\right) + T_{g(1,\ j)} - 2T_{g(0,\ j)} + T_{g(1,\ j)}\right]$$

Then, this equation will be:-

$$T_{g(0,\ j+1)} = T_{g(0,\ j)} + \theta \frac{\Delta t}{\rho_g\, C_g} \frac{\lambda_g}{(\Delta x)^2}\left[\frac{2\Delta x h_a}{\lambda_g}\left[T_{a(0,\ j+1)} - T_{g(0,\ j+1)}\right] + \right. \qquad \textbf{4-31}$$

$$\left. \frac{2\Delta x\, h_{r1}}{\lambda_g}\left(T_{sky} - T_g\big|_{x=0}\right) + T_{g(1,\ j+1)} - 2T_{g(0,\ j+1)} + T_{g(1,\ j+1)}\right] + (1 -$$

$$\theta) \frac{\Delta t}{\rho_g\, C_g} \frac{\lambda_g}{(\Delta x)^2}\left[\frac{2\Delta x h_a}{\lambda_g}\left[T_{a(0,\ j)} - T_{g(0,\ j)}\right] + \frac{2\Delta x\, h_{r1}}{\lambda_g}\left(T_{sky} - T_g\big|_{x=0}\right) + T_{g(1,\ j)} - \right.$$

$$\left. 2T_{g(0,\ j)} + T_{g(1,\ j)}\right]$$

At $t > 0$ & $x = 1, 2, 3\ and\ 4$, for the intimate contact Equ. 4-15 will be used.

At $t > 0$ & $x = 5$, by applying of Equ. 3-21 with boundary conditions of Equs. 3-6 and 3-18 with lumped expression from Equ. 3-8 for the aluminium in Equ. 4-26, the equation for the last node of the tedler will be:

$$T_{td(i,\ j+1)} = T_{td(i,\ j)} \qquad \textbf{4-32}$$

$$+ \frac{\Delta t}{\rho_{td}\, C_{td}} \frac{\lambda_{td}}{(\Delta x)^2}\left[\theta\left[T_{td(i-1,\ j+1)} - T_{td(i,\ j+1)}\right]\right.$$

$$\left. + (1-\theta)\left[T_{td(i-1,\ j)} - T_{td(i,\ j)}\right]\right] + \theta \frac{T_{PCM(0,\ j+1)} - T_{td(i,\ j+1)}}{\rho_{td}\, C_{td} \Delta x R_{td-Al}}$$

$$+ (1-\theta) \frac{T_{PCM(0,\ j+1)} - T_{td(i,\ j+1)}}{\rho_{td}\, C_{td} \Delta x R_{td-Al}}$$

The temperature of the aluminium layer is same as the temperature of the first node of the PCM and the boundary condition is:

$$\rho_{AL}\, C_{AL}\, (x_6 - x_5)\frac{T_{PCM(0,j+1)} - T_{PCM(0,j)}}{\Delta t} = \frac{\left(T_{te(n5,j+\theta)} - T_{PCM(0,j+\theta)}\right)}{R_{te-AL}} + \lambda_{PCM}\frac{\left(T_{PCM(1,j+\theta)} - T_{PCM(-1,j+\theta)}\right)}{2\Delta x_{PCM}} \quad \textbf{4-33}$$

For the first node of the PCM, a fictitious temperature will be appeared which is $T_{PCM(-1,\ m+1)}$. To eliminate this fictitious temperature, the boundary condition from the Equs. 3-6 and 3-18 with Equs 3-8 and 3-21 will be applied in Equ. 4-18, the result will be:

$$T_{PCM(0,\ j+1)} = T_{PCM(0,j)} + \frac{\Delta t}{\rho_{PCM}\, C_{PCM}}\frac{\lambda_{PCM}}{(\Delta x)^2}\left[\left[-\frac{2\Delta x_{PCM}\rho_{AL}\, C_{AL}\, (x_6 - x_5)}{\lambda_{PCM}}\frac{(T_{PCM(0,j+1)} - T_{PCM(0,j)})}{\Delta t} + \frac{2\Delta x_{PCM}\left(T_{te(n5,j+1)} - T_{PCM(0,j+1)}\right)}{\lambda_{PCM}R_{td-AL}} - 2T_{PCM(0,\ j+1)} + 2T_{PCM(1,\ j+1)}\right]\right] \quad \textbf{4-34}$$

Equ. 4-34 is for implicit, while for the explicit it will be:

$$T_{PCM(0,\ j+1)} = T_{PCM(0,j)} + \frac{\Delta t}{\rho_{PCM}\, C_{PCM}}\frac{\lambda_{PCM}}{(\Delta x)^2}\left[\left[\frac{2\Delta x_{PCM}\left(T_{te(n5,j)} - T_{PCM(0,j)}\right)}{\lambda_{PCM}R_{td-AL}} - 2T_{PCM(0,\ j)} + 2T_{PCM(1,\ j)}\right]\right] / \left(1 + 2 * \frac{\rho_{AL}\, C_{AL}\, (x_6 - x_5)}{\rho_{PCM}\, C_{PCM}\Delta x_{PCM}}\right) \quad \textbf{4-35}$$

For $x = x_7$, for the interface between the PCM and aluminium, if Equ. 4-18 be used, a fictitious temperature ($T_{PCM(+1,j+1)}$) will be appeared. In order to eliminate this fictitious temperature, Equs. 3-6, 3-8, and 3-25 will be used to be:

$$\rho_{AL}\, C_{AL}\,(x_8 - x_7)\frac{T_{PCM(n,j+1)} - T_{PCM(n,j)}}{\Delta t} = h_a\left(T_a - T_{PCMn,j+1}\right) + h_{rad}\left(T_{ground} - T_{PCMn,j+1}\right) + \lambda_{PCM}\frac{\left(T_{PCM(n+1,j+1)} - T_{PCM(n-1,j+1)}\right)}{2\Delta x_{PCM}} \quad \textbf{4-36}$$

By substituting Equ.4-36 in Equ. 4-18, the fictitious temperature will be eliminated.

$$T_{PCM(n,\ j+1)} = T_{PCM(n,j)} + \frac{\Delta t}{\rho_{PCM}\, C_{PCM}}\frac{\lambda_{PCM}}{(\Delta x)^2}\left[\left[\frac{2\Delta x_{PCM}\rho_{AL}\, C_{AL}\,(x_6 - x_5)}{\lambda_{PCM}}\frac{(T_{PCM(n,j+1)} - T_{PCM(n,j)})}{\Delta t} - \frac{2\Delta x_{PCM}h_a\left(T_a - T_{PCMn,j+1}\right)}{\lambda_{PCM}} - \frac{2\Delta x_{PCM}\epsilon_g\,\sigma h_{rad}\left(T_{ground} - T_{PCMn,j+1}\right)}{\lambda_{PCM}} - 2T_{PCM(n,\ j+1)} + 2T_{PCM(n-1,\ j+1)}\right]\right] \quad \textbf{4-37}$$

Equ. 4-37 is for implicit, while for the explicit it will be:

$$T_{PCM(n,\ j+1)} = T_{PCM(n,j)} + \frac{\Delta t}{\rho_{PCM}\, C_{PCM}}\frac{\lambda_{PCM}}{(\Delta x)^2}\left[\left[-\frac{2\Delta x_{PCM}h_a\left(T_a - T_{PCMn,j}\right)}{\lambda_{PCM}} - \frac{2\Delta x_{PCM}\epsilon_g\,\sigma h_{rad}\left(T_{ground} - T_{PCMn,j}\right)}{\lambda_{PCM}} - 2T_{PCM(n,\ j)} + 2T_{PCM(n-1,\ j)}\right]\right]/\left(1 + 2 * \frac{\rho_{AL}\, C_{AL}\,(x_8 - x_7)}{\rho_{PCM}\, C_{PCM}\Delta x_{PCM}}\right) \quad \textbf{4-38}$$

4.3 Data and correlations required for use in the model

The ambient temperature (T_a) is a function of the time, while, T_{sky} is a function of T_a and it can be calculated by the flowing equation:

$$T_{sky} = 0.0552\, T_a^{1.5} \quad \textbf{4-39}$$

$$h_r = \left(T_g{}^2 + T_{sky}{}^2\right) * (T_g + T_{sky}) \quad \textbf{4-40}$$

In addition, the h_a is a function of the T_a, and it can be calculated depending on the free and forced convection as flow:

$$h_a = [h_{free}{}^3 + h_{force}{}^3]^{1/3} \quad \textbf{4-41}$$

where, the free convection for the horizontal plate (the top is the hot side) can be modelled as (Incropera and De Witt, 2005):

$$h_{free} = 0.54 \frac{\lambda}{L} Ra_L^{1/4} \qquad for \quad 10^4 \le Ra_L \le 10^7 \quad \textbf{4-42}$$

$$h_{free} = 0.15 \frac{\lambda}{L} Ra_L^{1/3} \qquad for \quad 10^7 \le Ra_L \le 10^{11} \quad \textbf{4-43}$$

$$Ra_L = \frac{g\beta(T_{PVL} - T_a)L^3}{\nu\alpha} \quad \textbf{4-44}$$

$$L = 4\frac{A}{P} \quad \textbf{4-45}$$

where, Ra is the Rayleigh number, λ is the thermal conductivity ($Wm^{-1}K^{-1}$) of the air, β denotes the volumetric expansion coefficient (1/T(K)) of the air, ν is the kinetic viscosity and α is the thermal diffusivity for the air. All these air properties are calculated at the film temperature which is:

$$T_{film} = \frac{1}{2}(T_{PVL} + T_a) \quad \textbf{4-46}$$

On the other hand, if the hot surface is the lowest, the free convection for the horizontal plate will be:

$$h_{free} = 0.27 \frac{\lambda}{L} Ra_L^{1/4} \qquad for \quad 10^5 \le Ra_L \le 10^{10} \quad \textbf{4-47}$$

The forced convection for the laminar and isothermal flow depends on the wind speed (u_∞), and it can be accounted by the flowing equations:

$$h_{force} = 0.664 \frac{\lambda}{L} Re_L^{1/2} Pr^{1/3} \quad for \quad Pr \geq 0.6 \& Re \leq 5 * 10^5 \qquad \textbf{4-48}$$

where, Re and Pr numbers can be calculated by:

$$Re = \frac{u_\infty L}{\nu} \qquad \textbf{4-49}$$

$$Pr = \frac{\nu}{\alpha} \qquad \textbf{4-50}$$

4.4 Stability analysis of numerical solutions

Stability means that the numerical solution approaches the exact solution (Incropera and De Witt, 2005). According to the time and space discretization for the Equ. 4-7 and after rearrange it, it will be:

$$T_{i,j+1} = T_{i,j} + \frac{\Delta t}{\rho C} \frac{\lambda}{(\Delta x)^2} \Big[\theta \big[T_{(i-1,\ j+1)} - 2T_{(i,\ j+1)} + T_{(i+1,\ j+1)} \big] + (1-\theta) \big[T_{(i-1,\ j)} - 2T_{(i,\ j)} + T_{(i+1,\ j)} \big] \Big] \qquad \textbf{4-51}$$

where, θ is different for each numerical methods and it equals to 0 and 1 for the explicit and implicit respectively. This Equ. 4-51 represents the heat transfer through the wall and the stability of the solution for this equation can be assessed by using Von Neumann's method (Smith, 1985), where, this method is mathematically rigours (Tanimoto, 2014).

In order to apply Von Neumann's method, each $T_{(i,\ j)}$ will be represented by:

$$T_{pv(i,\ j)} = e^{I\beta i \Delta x} e^{\alpha j \Delta t} = e^{I\beta i \Delta x} \xi^j \qquad \textbf{4-52}$$

where, I represents the imaginary value which equals to $\sqrt[2]{-1}$, $\beta = n\pi$. In order to achieve the stability of the solution, one condition should be achieved which is $|\xi| \leq 1$.

4.4.1 The stability analysis of the Implicit by Von Neumann's method

After inserting Equ. 4-52 in Equ. 4-51 and θ =1 for the implicit method, it will be:

$$e^{I\beta i\Delta x}\xi^{j+1} = e^{I\beta i\Delta x}\xi^{j} + \frac{\Delta t}{\rho_{PV}\, C_{PV}}\frac{\lambda_{PV}}{(\Delta x)^2}\left[e^{I\beta i(\Delta x-1)}\xi^{j+1} - 2e^{I\beta i\Delta x}\xi^{j+1} + e^{I\beta i(\Delta x+1)}\xi^{j+1}\right] \quad \textbf{4-53}$$

By dividing Equ. 4-53 by $e^{I\beta i\Delta x}\xi^{j}$, it will be:

Mathematically, $cos\beta i = e^{-I\beta i} + e^{I\beta i}$, therefore , this equation will be:

$$\xi = 1 + \frac{\Delta t}{\rho_{PV}\, C_{PV}}\frac{\lambda_{PV}}{(\Delta x)^2}\xi\left[e^{-I\beta i} - 2 + e^{I\beta i}\right] \quad \textbf{4-54}$$

$$\xi = 1 + \frac{\Delta t}{\rho_{PV}\, C_{PV}}\frac{\lambda_{PV}}{(\Delta x)^2}\xi[2cos\beta i - 2] \quad \textbf{4-55}$$

Mathematically, $\sin^2\beta i = {}^1/_2 - {}^1/_2\cos 2\beta i$, therefore, this equation will be:

$$\xi = 1 - 4\frac{\Delta t}{\rho_{PV}\, C_{PV}}\frac{\lambda_{PV}}{(\Delta x)^2}\xi\left[\sin^2{}^{\beta i}/_2\right] \quad \textbf{4-56}$$

It will be :

$$\xi = \frac{1}{1 + 4\frac{\Delta t}{\rho_{PV}\, C_{PV}}\frac{\lambda_{PV}}{(\Delta x)^2}\left[\sin^2{}^{\beta i}/_2\right]} \quad \textbf{4-57}$$

For stability, $|\xi| \leq 1$, which is so for any positive value of $\frac{\Delta t}{\rho_{PV}\, C_{PV}}\frac{\lambda_{PV}}{(\Delta x)^2}$. Therefore, the implicit numerical solution is stable for any time step interval.

4.4.2 The stability analysis of the explicit solution by Von Neumann's method

After insert Equ.4-52 in Equ. 4-51 and θ =0 for the explicit method, the equation will be:

$$e^{I\beta i\Delta x}\xi^{j+1} = e^{I\beta i\Delta x}\xi^{j} + \frac{\Delta t}{\rho_{PV}\, C_{PV}}\frac{\lambda_{PV}}{(\Delta x)^2}\left[e^{I\beta i(\Delta x-1)}\xi^{j} - 2e^{I\beta i\Delta x}\xi^{j} + e^{I\beta i(\Delta x+1)}\xi^{j}\right] \quad \textbf{4-58}$$

Divide Equ. 4-58 by $e^{I\beta i\Delta x}\xi^{j}$, it will be:

$$\xi = 1 + \frac{\Delta t}{\rho_{PV}\, C_{PV}}\frac{\lambda_{PV}}{(\Delta x)^2}\left[e^{-I\beta i} - 2 + e^{I\beta i}\right] \quad \textbf{4-59}$$

Mathematically, $2\,cos\beta i = e^{-I\beta i} + e^{I\beta i}$, therefore , this equation will be:

$$\xi = 1 + \frac{\Delta t}{\rho_{PV}\, C_{PV}}\frac{\lambda_{PV}}{(\Delta x)^2}[2cos\beta i - 2] \quad \textbf{4-60}$$

Equ. 4-60 will be:

$$\xi = 1 - 2\frac{\Delta t}{\rho_{PV}\, C_{PV}}\frac{\lambda_{PV}}{(\Delta x)^2}[1 - cos\beta i] \quad \textbf{4-61}$$

The worst case when $\beta i = \pi$, then the equation will be:

$$\xi = 1 - 4\frac{\Delta t}{\rho_{PV}\, C_{PV}}\frac{\lambda_{PV}}{(\Delta x)^2} \quad \textbf{4-62}$$

Therefore, the stability condition is to achieve$|\xi| \leq 1$,

$$\frac{\Delta t}{\rho_{PV}\, C_{PV}}\frac{\lambda_{PV}}{(\Delta x)^2} \leq \frac{1}{2} \quad \textbf{4-63}$$

Conclusion: the above condition should be achieved to get stable result for the explicit numerical solution. Hence this condition agreed with (Smith, 1985).

4.5 The stability analysis of the combined lumped-numerical model of the PV-PCM system

The stability of the solution for the Equ. 4-17 can be assessed by using Von Neumann's method (Smith, 1985), where, this method is mathematically rigours (Tanimoto, 2014).

In order to apply Von Neumann's method, each $T_{PV(i,\ j)}$ represent will represented by:

$$T_{(i,\ j)} = e^{I\beta i\Delta x} e^{\alpha j\Delta t} = e^{I\beta i\Delta x}\xi^{j} \qquad \textbf{4-64}$$

here, I represents the imaginary value which equals to $\sqrt[2]{-1}$, $\beta = n\pi$. In order to achieve the stability of the solution, one condition should be achieved which is $|\xi| \leq 1$.

The stability checking procedure for the Equ. 4-17.

$$\rho_{PVL}\ C_{\mathrm{PVL}}\,(x_{\mathrm{PVL}})\frac{e^{I\beta i\Delta x}\xi^{j+1} - e^{I\beta i\Delta x}\xi^{j}}{\Delta t} = \qquad \textbf{4-65}$$

$$= h_a\left(e^{I\beta i\Delta x-1}\xi^{j} - e^{I\beta i\Delta x}\xi^{j}\right) + h_{rad}\left(e^{I\beta i\Delta x-1}\xi^{j} - e^{I\beta i\Delta x}\xi^{j}\right)$$

$$-\frac{\left(e^{I\beta i\Delta x}\xi^{j} - e^{I\beta i\Delta x+1}\xi^{j}\right)}{R_{\mathrm{PVL}-AL}} + \beta_{PV}\ G(1-\eta_{PV})$$

By dividing Equ. 4-65 by $e^{I\beta i\Delta x}\xi^{j}$

$$\rho_{PVL}\ C_{\mathrm{PVL}}\,(x_{\mathrm{PVL}})\frac{\xi-1}{\Delta t} = \qquad \textbf{4-66}$$

$$= h_a\left(e^{-I\beta i\Delta x} - 1\right) + \epsilon_g\,\sigma h_{rad}\left(e^{-I\beta i\Delta x} - 1\right) - \frac{\left(1-e^{I\beta i\Delta x}\right)}{R_{\mathrm{PVL}-AL}}$$

$$+ \beta_{PV}\ G(1-\eta_{PV})/\ e^{I\beta i\Delta x}\xi^{j}$$

The stability checking procedure for the Equ. 4-24, will be:

$$e^{I\beta i\Delta x}\xi^{j+1} = e^{I\beta i\Delta x}\xi^{j} + \frac{\Delta t}{\rho_{PCM}\, C_{PCM}}\frac{\lambda_{PCM}}{(\Delta x)^2}\left[\left[-\frac{2\Delta x_{PCM}\rho_{AL}\, C_{AL}\,(x_6 - x_5)}{\lambda_{PCM}}\frac{(e^{I\beta i\Delta x}\xi^{j+1} - e^{I\beta i\Delta x}\xi^{j})}{\Delta t} + \frac{2\Delta x_{PCM}\left(e^{I\beta i\Delta x-1}\xi^{j+1} - e^{I\beta i\Delta x}\xi^{j+1}\right)}{\lambda_{PCM}R_{td-AL}} - 2e^{I\beta i\Delta x}\xi^{j+1} + 2e^{I\beta i\Delta x+1}\xi^{j+1}\right]\right] \quad \textbf{4-67}$$

Divide Equ. 4-67 by $e^{I\beta i\Delta x}\xi^{j}$, it will be:

$$e^{I\beta i\Delta x}\xi^{j}\left(\rho_{PVL}\, C_{\mathrm{PVL}}\,(x_{\mathrm{PVL}})\frac{\xi - 1}{\Delta t} - h_a\left(e^{-I\beta i} - 1\right) - \epsilon_g\,\sigma h_{rad}\left(e^{-I\beta i} - 1\right) + \frac{\left(1 - e^{I\beta i}\right)}{R_{\mathrm{PVL}-AL}}\right) = \beta_{PV}\, G(1 - \eta_{PV}) \quad \textbf{4-68}$$

By taking Ln for both sided of Equ. 4-68, it will be:

$$\xi = 1 + \frac{\Delta t}{\rho_{PCM}\, C_{PCM}}\frac{\lambda_{PCM}}{(\Delta x)^2}\left[\left[-\frac{2\Delta x_{PCM}\rho_{AL}\, C_{AL}\,(x_6 - x_5)}{\lambda_{PCM}}\frac{(\xi - 1)}{\Delta t} + \frac{2\Delta x_{PCM}\left(e^{-I\beta i\Delta}\xi - \xi\right)}{\lambda_{PCM}R_{td-AL}} - 2\xi + 2\xi e^{I\beta i}\right]\right] \quad \textbf{4-69}$$

Then Equ. 4-69 will be:

$$\xi = 1 + \frac{2}{\rho_{PCM}\, C_{PCM}}\frac{\Delta x_{PCM}\rho_{AL}\, C_{AL}\,(x_6 - x_5)}{\Delta x_{PCM}} + \xi\frac{\Delta t}{\rho_{PCM}\, C_{PCM}}\frac{\lambda_{PCM}}{(\Delta x)^2}\left[\left[-\frac{2\Delta x_{PCM}\rho_{AL}\, C_{AL}\,(x_6 - x_5)}{\lambda_{PCM}\Delta t} + \frac{2\Delta x_{PCM}\left(e^{-I\beta i\Delta} - 1\right)}{\lambda_{PCM}R_{td-AL}} - 2 + 2e^{I\beta i}\right]\right] \quad \textbf{4-70}$$

Then Equ. 4-70 will be:

$$\xi\left[1-\frac{\Delta t}{\rho_{PCM}\,C_{PCM}}\frac{\lambda_{PCM}}{(\Delta x)^2}\left[\left[-\frac{2\Delta x_{PCM}\rho_{AL}\,C_{AL}\,(x_6-x_5)}{\lambda_{PCM}\Delta t}\right.\right.\right.$$

$$\left.\left.\left.+\frac{2\Delta x_{PCM}\left(e^{-I\beta i\Delta}-1\right)}{\lambda_{PCM}R_{td-AL}}-2+2e^{I\beta i}\right]\right]\right] \qquad \textbf{4-71}$$

$$=1+\frac{2}{\rho_{PCM}\,C_{PCM}}\frac{\Delta x_{PCM}\rho_{AL}\,C_{AL}\,(x_6-x_5)}{\Delta x_{PCM}}$$

Then Equ. 4-71 will be:

$$\xi=1+\frac{2}{\rho_{PCM}\,C_{PCM}}\frac{\Delta x_{PCM}\rho_{AL}\,C_{AL}\,(x_6-x_5)}{\Delta x_{PCM}} \qquad \textbf{4-72}$$

$$/\left[1\right.$$

$$-\frac{\Delta t}{\rho_{PCM}\,C_{PCM}}\frac{\lambda_{PCM}}{(\Delta x)^2}\left[\left[-\frac{2\Delta x_{PCM}\rho_{AL}\,C_{AL}\,(x_6-x_5)}{\lambda_{PCM}\Delta t}\right.\right.$$

$$\left.\left.+\frac{2\Delta x_{PCM}\left(e^{-I\beta i\Delta}-1\right)}{\lambda_{PCM}R_{td-AL}}-2+2e^{I\beta i}\right]\right]$$

Then Equ. 4-72 will be:

$$\xi=1+\frac{2}{\rho_{PCM}\,C_{PCM}}\frac{\Delta x_{PCM}\rho_{AL}\,C_{AL}\,(x_6-x_5)}{\Delta x_{PCM}} \qquad \textbf{4-73}$$

$$/\left[1\right.$$

$$-\frac{\Delta t}{\rho_{PCM}\,C_{PCM}}\frac{\lambda_{PCM}}{(\Delta x)^2}\left[\left[-\frac{2\Delta x_{PCM}\rho_{AL}\,C_{AL}\,(x_6-x_5)}{\lambda_{PCM}\Delta t}\right.\right.$$

$$\left.\left.+\frac{2\Delta x_{PCM}\left(e^{-I\beta i\Delta}-1\right)}{\lambda_{PCM}R_{td-AL}}-2+2e^{I\beta i}\right]\right]$$

Where:

$$e^{\pm i\beta} = \cos\beta \pm i\sin\beta \qquad \textbf{4-74}$$

By subtitling Equ. 4-74 in Equ. 4-73, Equ. 4-73 will be:

$$\xi = 1 + \frac{2}{\rho_{PCM}\, C_{PCM}} \frac{\rho_{AL}\, C_{AL}\,(x_6 - x_5)}{\Delta x_{PCM}} \qquad \textbf{4-75}$$
$$/\left[1 - \frac{\Delta t}{\rho_{PCM}\, C_{PCM}} \frac{\lambda_{PCM}}{(\Delta x)^2}\left[\left[-\frac{2\Delta x_{PCM}\rho_{AL}\, C_{AL}\,(x_6 - x_5)}{\lambda_{PCM}\Delta t} + \frac{2\Delta x_{PCM}(\,cosI\beta - isinI\beta - 1)}{\lambda_{PCM} R_{td-AL}} - 2 + 2(cosI\beta + isinI\beta)\right]\right]\right]$$

By applying $\beta = 0$, Equ. 4-75 will be:

$$\xi = \left[1 + \frac{2}{\rho_{PCM}\, C_{PCM}} \frac{\rho_{AL}\, C_{AL}\,(x_6 - x_5)}{\Delta x_{PCM}}\right] \qquad \textbf{4-76}$$
$$/\left[1 - \frac{\Delta t}{\rho_{PCM}\, C_{PCM}} \frac{\lambda_{PCM}}{(\Delta x)^2}\left[\left[-\frac{2\Delta x_{PCM}\rho_{AL}\, C_{AL}\,(x_6 - x_5)}{\lambda_{PCM}\Delta t} - \frac{4\Delta x_{PCM}}{\lambda_{PCM} R_{td-AL}} - 4\right]\right]\right]$$

The stability condition that should be achieved is $|\xi| \leq 1$. Therefore, absolute results of the right side of Equ. 4-76 should be less than 1.

Chapter Five Mathematical Models Results

5.1 Introduction

This chapter presents the results of the mathematical models, including the validation work for the implicit and explicit solution methods for the distributed parameter model and implicit solution for the lumped- distributed parameter model for the PV-PCM module and for the stand-alone PV panel. In addition, the impact of different thermal contact conductance will be investigated. Moreover, the impact of the volume change during the phase change will be studied. Finally, a comparison of the time consumption of the explicit and implicit methods of the PV-PCM module will be illustrated.

5.2 The validation work for the implicit numerical method for the PV-PCM module

In order to validate the results of the implicit numerical method for the PV-PCM systems, MATLAB algorithms have been built to implement the solutions of the heat transfer equations which have been described in the chapter 4.

5.2.1 The inputs

The thermos-physical properties of the PCM and each layer of the PV panel from the table 3 and table 4 respectively have been introduced to the program. In addition the solar radiation intensity, the wind speed and the ambient temperature data have been imported to the program. Moreover, the dimensions of the PV panel, the thickness of each PV panel layer have been given. Furthermore, the whole time that need to analysis the PV-PCM system, the time step and the number of the nodes in PCM layer should be given.

5.2.2 The calculation procedure

The calculation procedure has been illustrated in the Figure 5-2. Once the input data is imported, the time step loop will start, then T_{glass} will equal the temperature of the first point of the glass for the previous time step. The standard

temperatures $Tstd_{(i)}$ for the each node of the PCM will equal their temperatures from the previous time step. After that, H loop will start. In H loop, the radiation heat transfer coefficient and convection heat transfer coefficient will be calculated according to the Equs. 4-40 and 4-41 respectively. These calculations depend on the Tglass. The apparent heat capacity of the each PCM nodes be calculated from the Equs 3-26, 3-27 and 3-28 depending on the $Tstd_{(i)}$.

After that, according to the FIB method, the coefficients of the temperatures at the present time step will be calculated for each node according to the Equs. 4-15, 4-26, 4-31, 4-33, 4-35 and 4-38. For each time step, these equations will be arranged as:

$$A\,T_{(i-1,\ j+1)} + B\,T_{(i,\ j+1)} + C\,T_{(i+1,\ j+1)} = D \qquad \textbf{5-1}$$

Where, these coefficients A, B, C and D change for each node. Therefore they will be arranged in matrices as :

$$\begin{matrix} i \\ i+1 \\ \\ n \end{matrix}\begin{bmatrix} B_i & C_i & & \\ A_{i+1} & B_{i+1} & C_{i+1} & \\ & & & \\ & & A_n & B_n \end{bmatrix}\begin{bmatrix} T_{(i,\ j+1)} \\ T_{(i+1,\ j+1)} \\ \\ T_{(n,\ j+1)} \end{bmatrix} = \begin{bmatrix} D_1 \\ D_2 \\ \\ D_n \end{bmatrix}$$

Figure 5-1 : the matrices of the temperature coefficients

Once arranged this matrix, it will be solved to find the temperature for each internal node at the present time step. Then the K loop will start. After that, for each node of the PCM, the temperature of the current time step will be compared with the standard temperature for each node. This comparison of each temperature of node will produce one of five cases. Firstly, the standard temperature is less than the melting temperature and the temperature of the current time step is more than or equal the melting temperature. Secondly, the standard temperature is more than the liquid temperature and the current time step temperature is less than the liquid temperature. For these two cases, the C_{PCM} will be recalculated depending on the Equ 3-28 and the temperature coefficients will be recalculated. Thirdly, the standard temperature is more than or equal the melting temperature and the temperature of the current time step is

less than the melting temperature. For this case, the C_{PCM} will be recalculated depending on the Equ and 3-26 the temperature coefficients will be recalculated. Fourthly, the standard temperature is less than or equal to the liquid temperature and the current time step temperature is more than the liquid temperature. For this case, the C_{PCM} will be recalculated depending on the Equ 3-27 and the temperature coefficients will be recalculated. Finally, if these four cases have not been achieved by any PCM node, no change will be applied for the C_{PCM} for this node.

After calculating the new C_{PCM} and temperature coefficient for each node, the temperatures of the current time step will be saved as standard temperatures. Then, new temperatures for the current time step will calculated for each PCM nodes, depending on the these new C_{PCM} values and temperature coefficients for each node. Then, the temperature of the current time step will be compared with the standard temperature for each node. If the differences of these comparisons for any node is more than the accepted error, the K loop will be repeated. However, if the differences of these comparisons for all node are less than the accepted error or loop iteration finished, the K loop is finished. The loop iteration has been taken as 50 and the accepted error as 10^{-6}.

Then, the T_{glass} will be compared with temperature of the first node of the glass for the current time step. If the difference of this comparison is more than the accepted error, T_{glass} will be updated to be equal to the temperature of the current time step and the H loop will be repeated. However, if the difference is less than the accepted error or loop iteration finished, the software will move to the next time step. The loop iteration has been taken as 100 and the accepted error as 10^{-6} as described in the Figure 5-2.

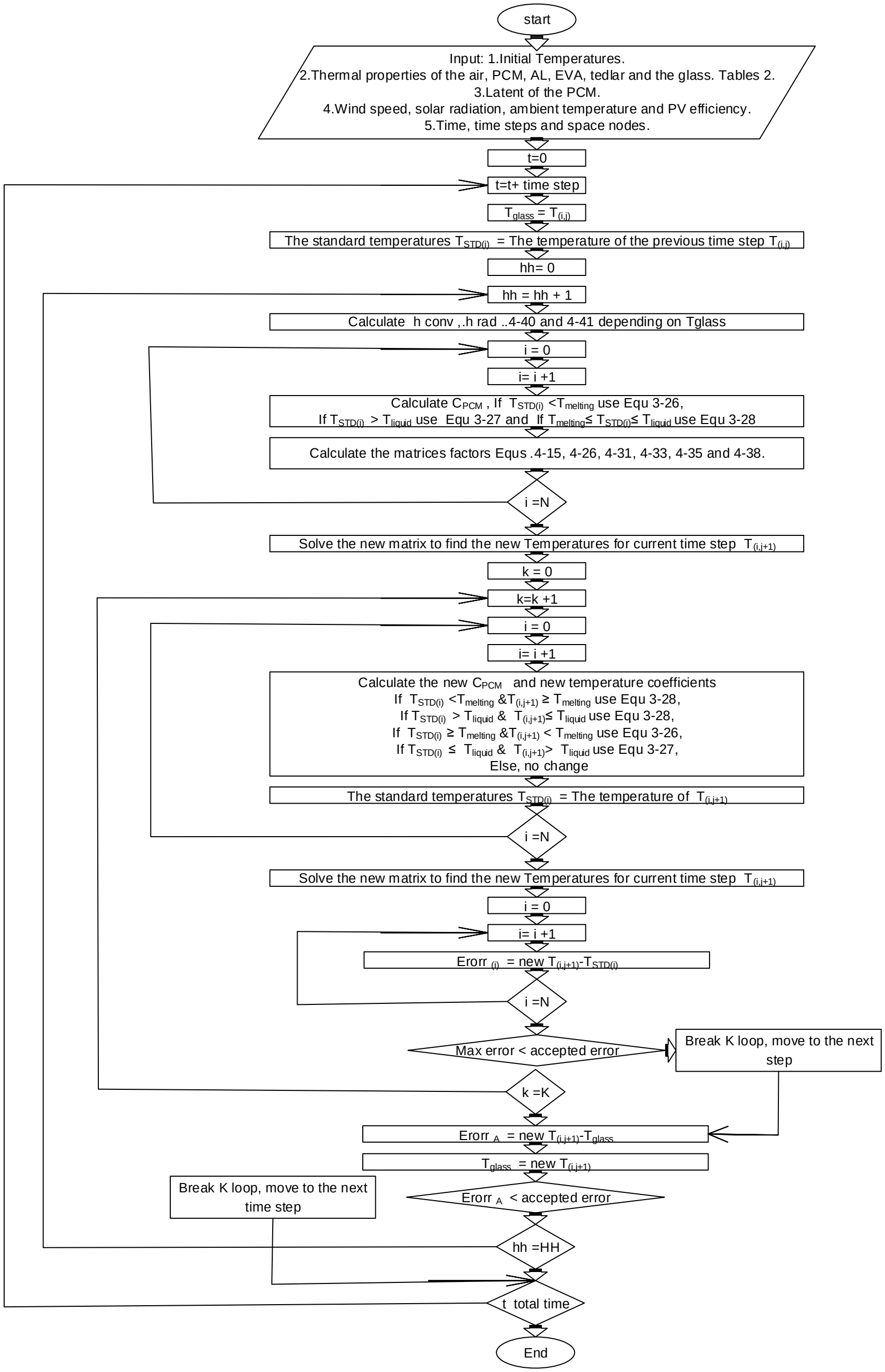

Figure 5-2: The flow chart of the MATLAB code of the using implicit method.

5.2.3 The results of the validation work

In order to validate the results of PV-PCM models, the results have been compared with the experimental work of Hasan et al. (2010), and also, the numerical results of Kibria et al. (2016). Table 3 and Table 4 show the thermos-physical properties of the each layer of the PV panel, also, the thermosphysical properties of each layer of the PV panel and also the properties of the PCM RT20 which are same as that used in Kibria et al. (2016). While, the Initial temperature inputted as 296K and the thickness is 3 cm.

Figure 5-3 illustrate the temperatures trends of the present simulated model and the experimental temperature of the PV-PCM system, it also illustrates the temperature differences between these two temperatures. From the Figure 5-3, the results illustrate the maximum temperature difference between the current simulated PV-PCM system, and the experimental results of Hasan et al. (2010) for the PV panel temperature is, 2.7104 K at time 9819 seconds.

Table 3: The thermos-physical properties for the RT20 (Kibria et al., 2016) .

PCM	Melting temperature ^0C	Latent heat J kg^{-1}	Thermal conductivity kg m s^{-3} K^{-1}	Specific Heat J kg^{-1} K^{-1}	Density kg m^{-3}
RT 20	21.23	140,300	0.2	2400	770

Table 4: The thicknesses and the thermos-physical properties of the silicon PV panel layers (Kibria et al., 2016).

PV layers	Density kg/m^3	Specific heat J kg^{-1} K^{-1}	Thickness m	Thermal conductivity kg m s^{-3} K^{-1}	Thermal diffusivity m^2 s^{-1}
Glass	3000	500	0.005	1.8	0.12×10^{-5}
EVA	960	2090	0.0005	0.35	8.01×10^{-8}
Silicon cells	2330	677	0.000225	148	9.38×10^{-5}
Tedler	1200	1250	0.0001	0.2	1.33×10^{-7}
AL	2700	900	0.002	237	9.75×10^{-5}

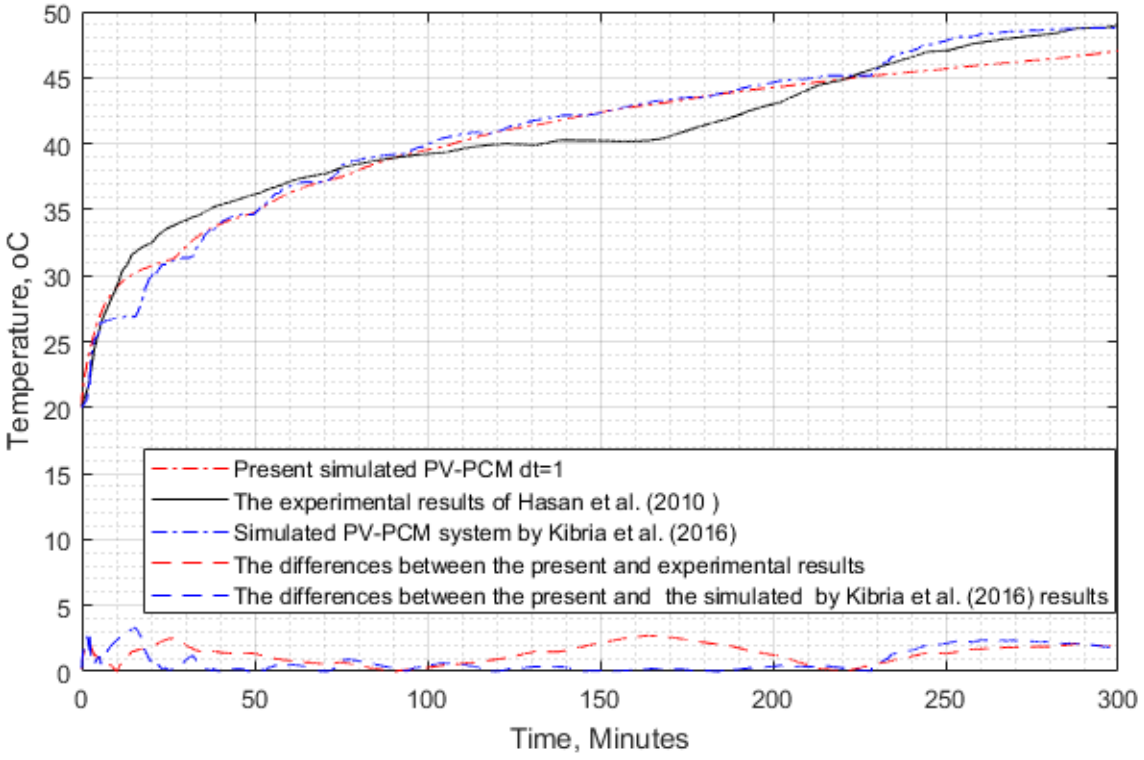

Figure 5-3: The temperatures trend of the PV cell of simulated PV-PCM system dt=1 s, the experimental results of Hasan et al. (2010) and simulated PV-PCM system by Kibria et al. (2016).

5.3 The results of the explicit numerical method for the PV-PCM module

The matlab algorithm has been built using the explicit discretizing, as illustrated in Figure 5-4. The inputs are same as in the section 5.4.15.2.1. The results show when the time step is equal to or more than 0.00001 s, the solution is diverted and the temperature values go to infinity as illustrated in Figure 5-5. The X axis in Figure 5-5 represents the time steps where each time step is 0.00001 s, while the Y axis represents the temperature. This is result of the thin layer of the silicon and the stability conditions for the explicit discretization. Therefore, the time step should be less than 0.00001 s.

Figure 5-6 illustrates the results of the PV silicon temperature with time step which is 0.000001 s. In this figure the whole simulated time is 1 s. However, the time consumed by the computer was 51,391.431 s. The specifications of the computer are: processor Intel (Cellura et al.) xeon (Cellura et al.) CPU E3-1240, 3.5GHz and the installed memory is 32 GB. In conclusion, if this explicit model is used to simulate one whole year of the performance of the PV-PCM system, the time that needed by this computer will be 51,391.431 years.

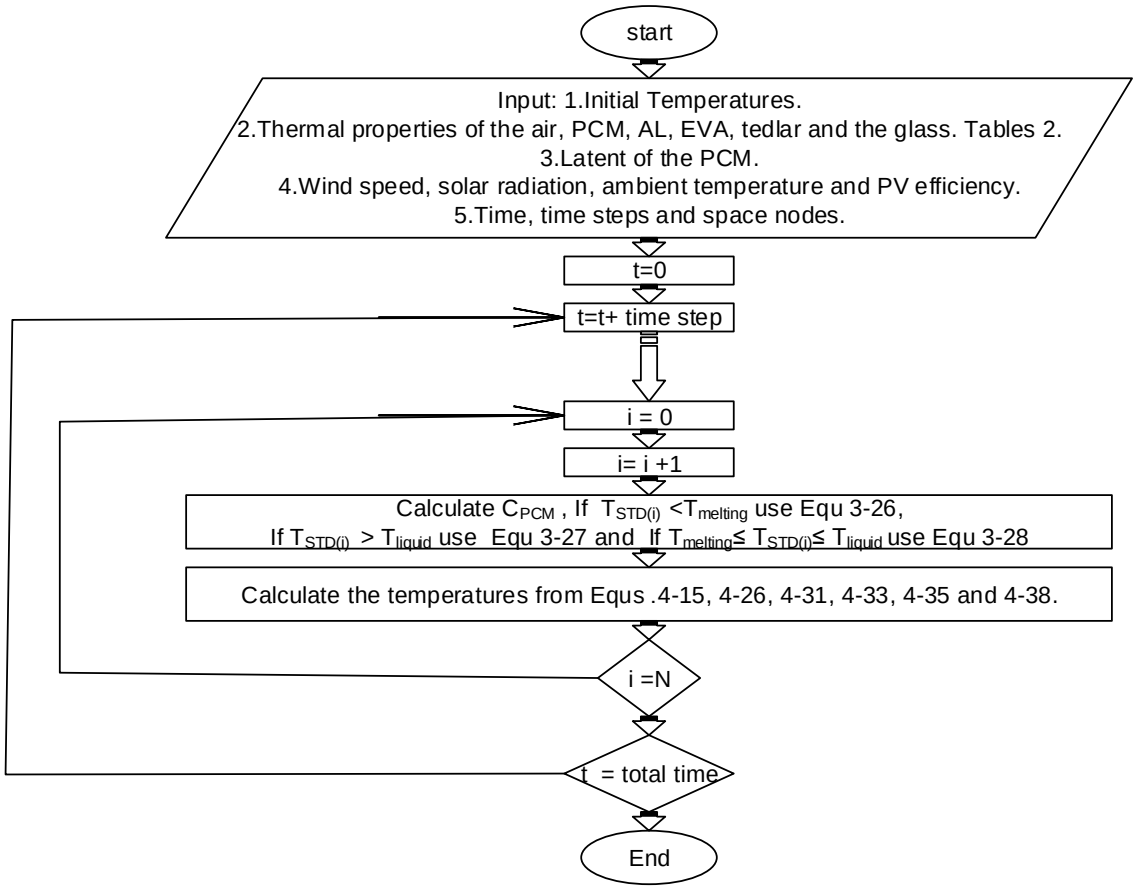

Figure 5-4: The flow chart of the MATLAB code of the using explicit numerical method.

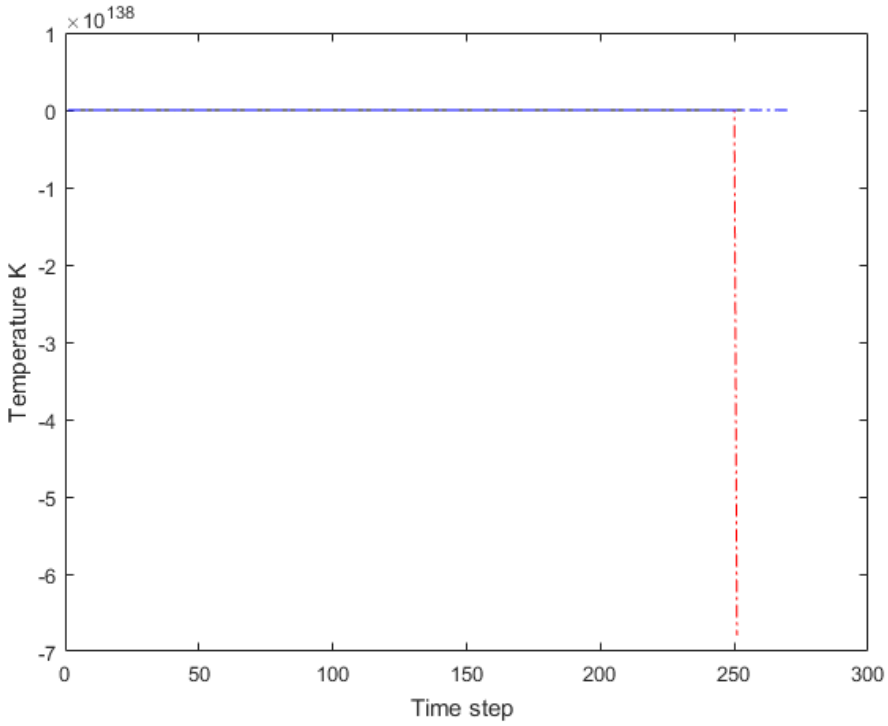

Figure 5-5: The result of explicit model with time step is 0.00001

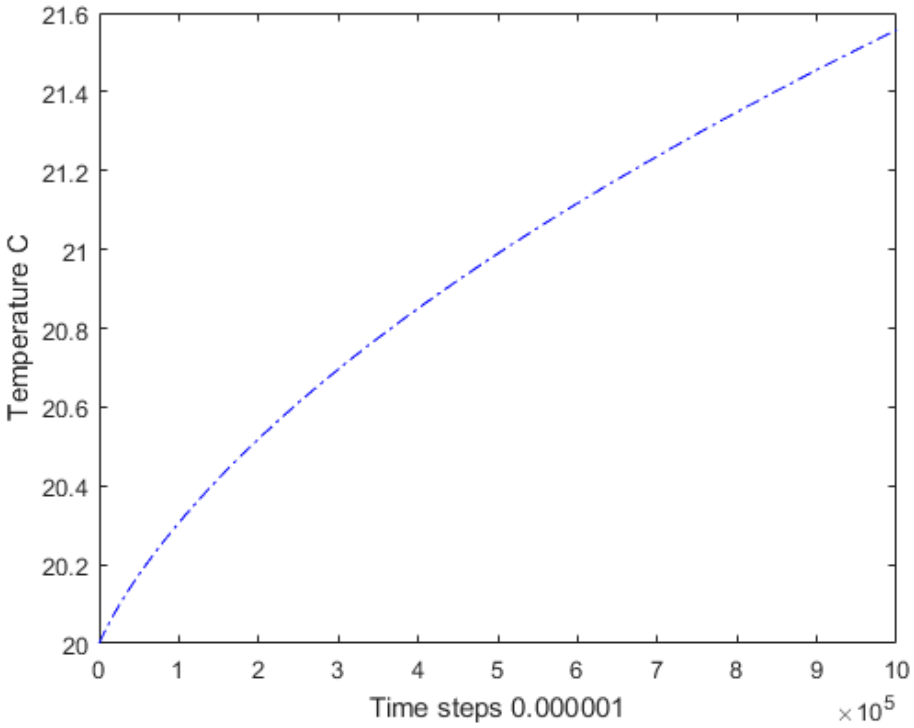

Figure 5-6: The result of explicit model with time step is 0.000001

5.4 The validation work for the lumped-numerical model for the PV-PCM module, the Cp depending on the previous time step.

5.4.1 The inputs

The thermophysical properties of the PCM and each layer of the PV panel from the Table 5 were input into the program. In addition, the solar radiation intensity, wind speed and the ambient temperature data were also input into the program from Luo et al. (2017). Moreover, the dimensions of the PV panel and the thickness of each PV panel layer have been given. Furthermore, the time duration, time step and the number of nodes in PCM layer were input.

Table 5: The thicknesses and the thermophysical properties of the silicon PV panel layers (Kibria et al., 2016).

PV layers	Density kg m^{-3}	Specific heat J kg^{-1} K^{-1}	Thickness m	Thermal conductivity kg m s^{-3} K^{-1}	Thermal resistance K m^2 W^{-1}
Glass	3000	500	0.0032	1.8	0.001778
EVA	960	2090	0.0005	0.35	0.001429
Silicon cells	2330	677	0.000225	148	1.52E-06
Tedler	1200	1250	0.0001	0.2	0.0005
AL	2700	900	0.002	237	8.44E-06
Composite PCM	600	1788	0.03	7.5	0.004

5.4.2 The calculation procedure

The radiation heat transfer coefficient and convection heat transfer coefficient were calculated according to the Equs. 4-40 and 4-41 respectively. These calculations depend on the temperature at the previous time step, according to the combined lumped-numerical method. The temperature of the PV panel was calculated from the Equ. 4-17 and the temperature coefficients from Equs. 4-18, 4-24 and 4-25.

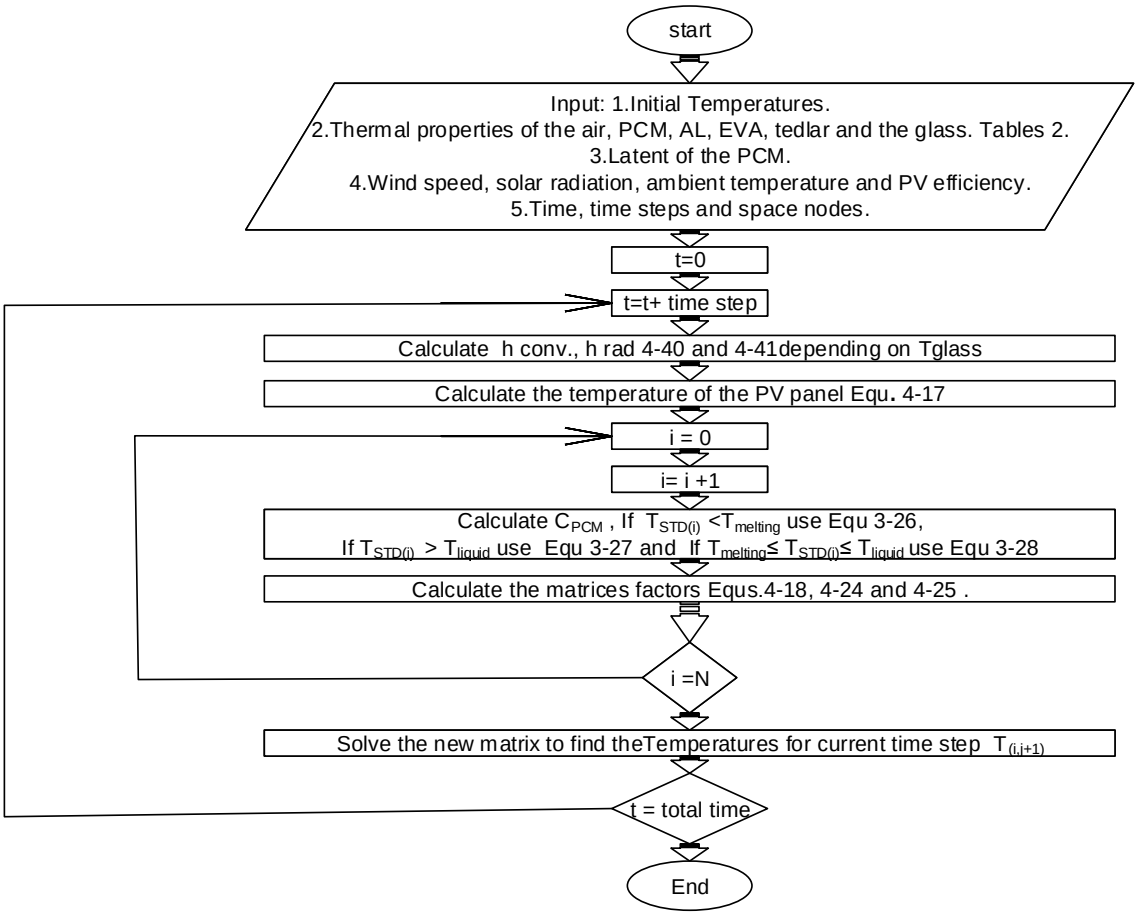

Figure 5-7: The flow chart of the MATLAB code of the using combined lumped-numerical method.

After that, according to the FIB method for the PCM nodes, the coefficients of the temperatures at the present time step were calculated for each node according to the Equs. 4-18, 4-24 and 4-25. For each time step these equations will be arranged as:-

$$A\,T_{(i-1,\ j+1)} + B\,T_{(i,\ j+1)} + C\,T_{(i+1,\ j+1)} = D$$

Where, these coefficients A, B, C and D change for each node. Therefore, they will be arranged in matrices as:

$$\begin{matrix} i \\ i+1 \\ \\ \\ n \end{matrix}\begin{bmatrix} B_i & C_i & & \\ A_{i+1} & B_{i+1} & C_{i+1} & \\ & & & \\ & & & A_nB_n \end{bmatrix}\begin{bmatrix} T_{(i,\ j+1)} \\ T_{(i+1,\ j+1)} \\ \\ T_{(n,\ j+1)} \end{bmatrix} = \begin{bmatrix} D_1 \\ D_2 \\ \\ D_n \end{bmatrix}$$

Figure 5-8 : The matrices of the temperature coefficients

Once arranged this matrix, the matrix is solved to find the temperature for each internal node at the present time step. After that, the calculation of the temperature is repeated for each time step, as described in Figure 5-7.

5.4.3 The results of the validation work

In order to validate the results of the Matlab program the results have been compared with the experimental work of Luo et al. (2017) in Figure 5-9. From Table 5, the thermophysical properties were used for each layer of the PV-PCM module and the latent heat of the PCM is 164,800 J kg^{-1} (Luo et al., 2017) and the initial temperature is 296K. The thermophysical properties for the PCM have been taken from Luo et al. (2017) , while the thermophysical properties for the PV panel layers have been taken from Kibria et al. (2016). The results of the three models: the explicit, implicit and combined lumped-numerical have been illustrated in the figures Figure 5-9 respectively.

Figure 5-9 illustrates the temperature trends of the present simulated model, and experimental temperature of the PV-PCM system, it also illustrates the temperature differences between them. From Figure 5-9, both the simulated and the experimental results have almost the same trend with some deviations. The maximum relative error is 9.82% for the results of this model at the time 10499 s. This error is due to a number of different factors. Firstly, they are as a result of the fluctuating solar radiation intensity owing to clouds. This led to inaccurate reading of the solar radiation intensity mentioned in Luo et al. (2017). Secondly, the initial temperature of the system has been assumed as 296K, while in reality it could be different. Thirdly, the wind speed has not been recorded, therefore it has been considered as 1 m s^{-1} same as the assumption of (Luo et al., 2017). This wind speed will affect the convective heat transfer and then will affect the PV panel temperature. Finally, there are some errors in the experimental test, which are 1% and 3% for the latent heat accuracy and thermal conductivity respectively for Luo et al. (2017). While, the maximum relative error between the numerical simulation results of Luo et al. (2017) with their experimental work was 14.49%.

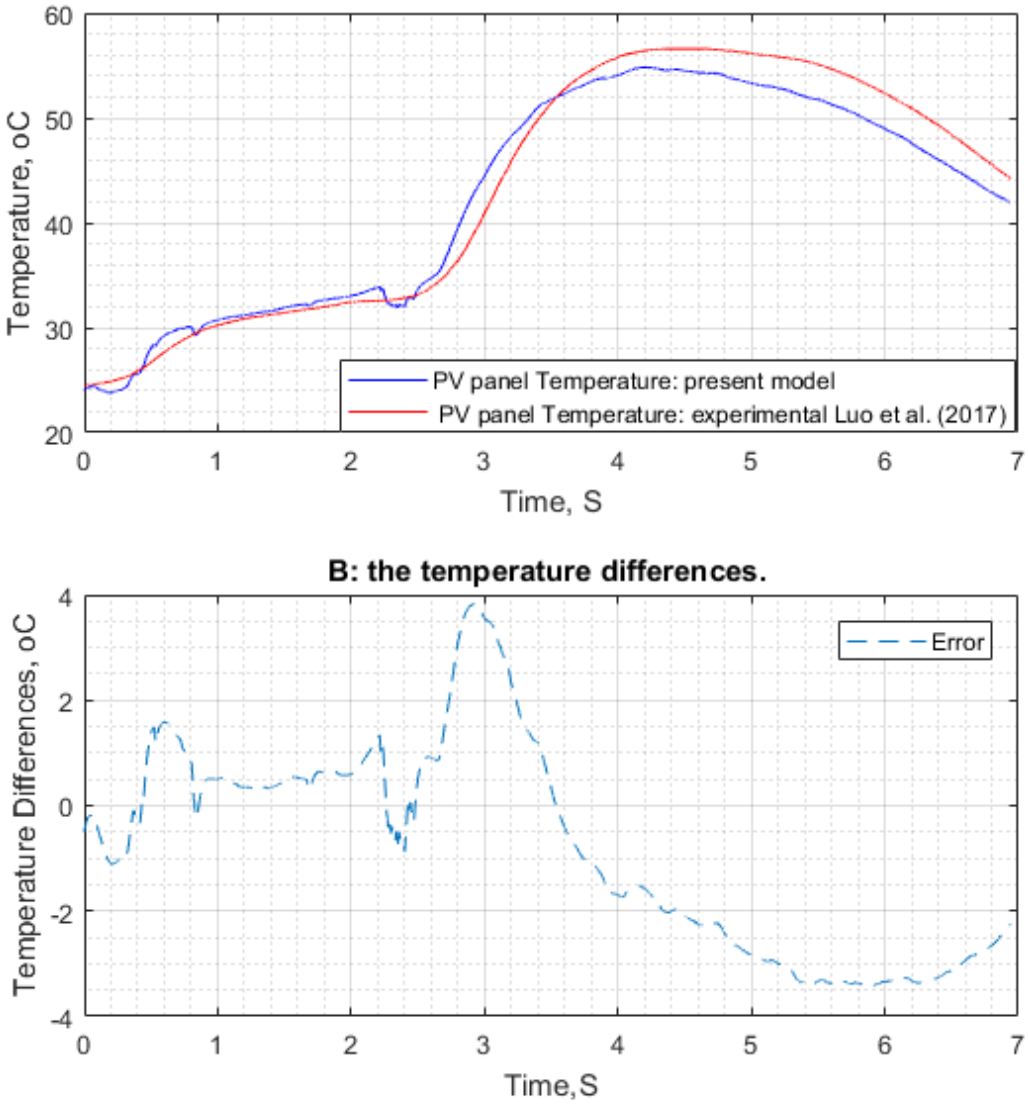

Figure 5-9: A: The temperatures trends of the present model and experimental of the PV-PCM system. B: The temperature differences between these models.

5.5 The validation work for the lumped-numerical model for the PV-PCM module, the C_{PCM} depending on the current time step.

This model has used same the inputs as in section 5.4.1, while the calculation procedures have been illustrated in Figure 5-10. The first loop starts for the time step, then the temperature of the PV panel calculated. After that, the temperature of the previous time step for each PCM node considered as a standard temperature. Then, the second loop starts for the each node of the PCM, where, the apparent heat capacity of the each PCM nodes has been calculated from the Equs 4-19, 4-20 and 4-21, depending on the temperature of the previous time step. Then, the temperature coefficient will be calculated and arranged in a matrix and the temperatures calculated for the current time step.

After that, the third and fourth loops will start where, for each node of the PCM, the temperature of the current time step will be compared with the standard temperature for each node. This comparison for temperatures of each node will produces five cases. Firstly, the standard temperature is less than the melting temperature, and the temperature of the current time step is more than or equal to the melting temperature. Secondly, the standard temperature is more than the liquid temperature and the current time step temperature is less than the liquid temperature. For these two cases, the C_{PCM} will be recalculated depending on the Equ 4-20 and the temperature coefficients will be recalculated. Thirdly, the standard temperature is more than or equal to the melting temperature and the temperature of the current time step is less than the melting temperature. For this case, Equ 4-19 and the temperature coefficients will be recalculated. Fourthly, the standard temperature is less than or equal to the liquid temperature and the current time step temperature is more than the liquid temperature. For this case, the C_{PCM} will be recalculated depending on the Equ 4-20 and the temperature coefficients will be recalculated. Finally, if these four cases have not been achieved by any PCM node, no change will be applied for the C_{PCM} for this node.

After calculating the new C_{PCM} and temperature coefficient for each node, the results of the temperatures of the current time step will be saved as a standard temperatures. Then, new temperatures for the current time step will calculated

for each PCM nodes, depending on the these new C_{PCM} and temperature coefficients for each node. Then, the temperature of the current time step will be compared with the standard temperature for each node. If the differences in these comparisons for any node is more than the accepted error, the fourth loop will repeated. However, if the differences of these comparisons for all nodes are less than the accepted error or loop iteration finished, the software will move to the next time step. The loop iteration has been taken as 100 and the accepted error as 10^{-6}.

The results have been illustrated in Figure 5-11. Compared to the experimental results of Luo et al. (2017), the maximum relative error is 6.47% of this model at the time 21161 s.

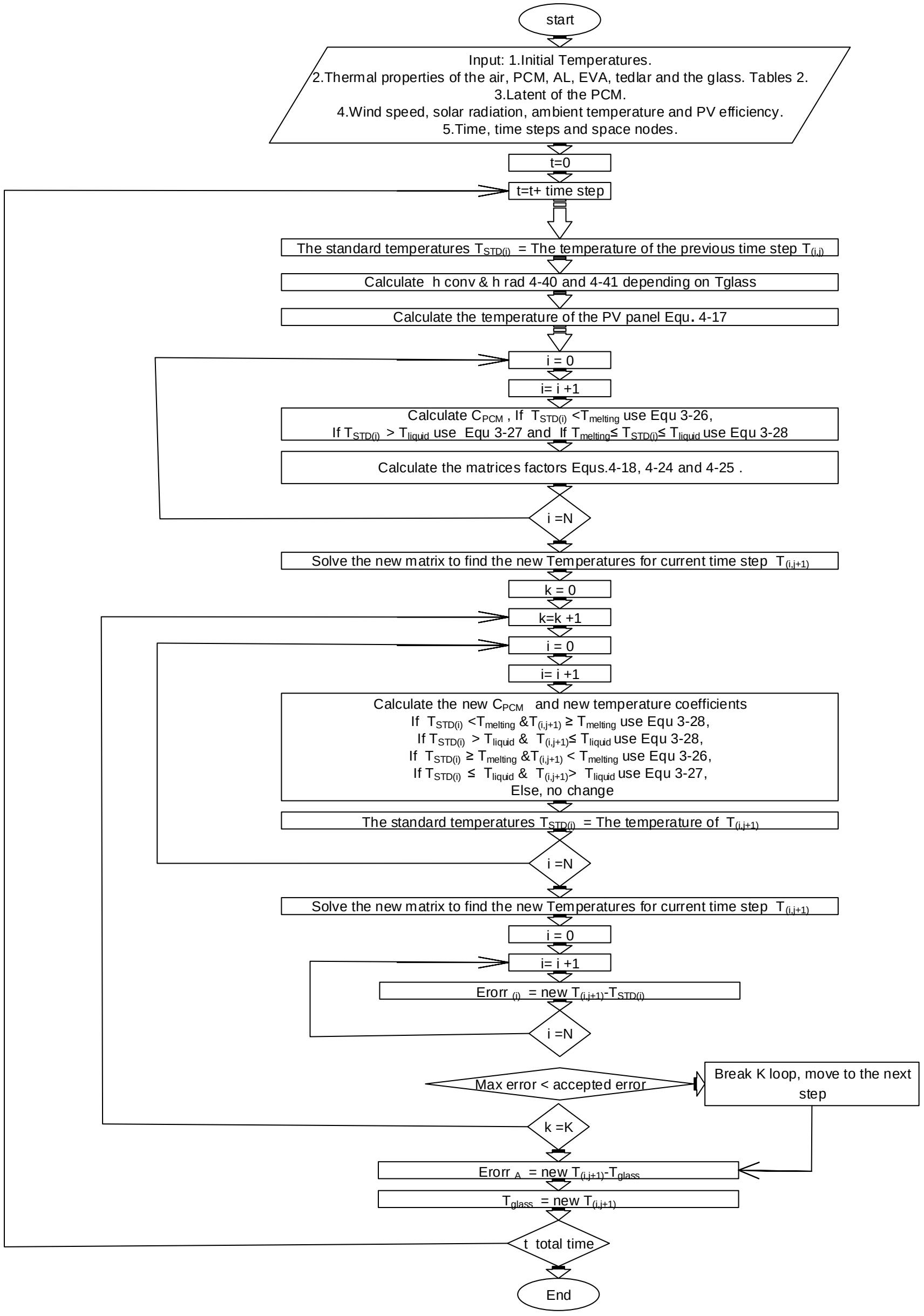

Figure 5-10: The flow chart of the MATLAB code of the using combined lumped-numerical method.

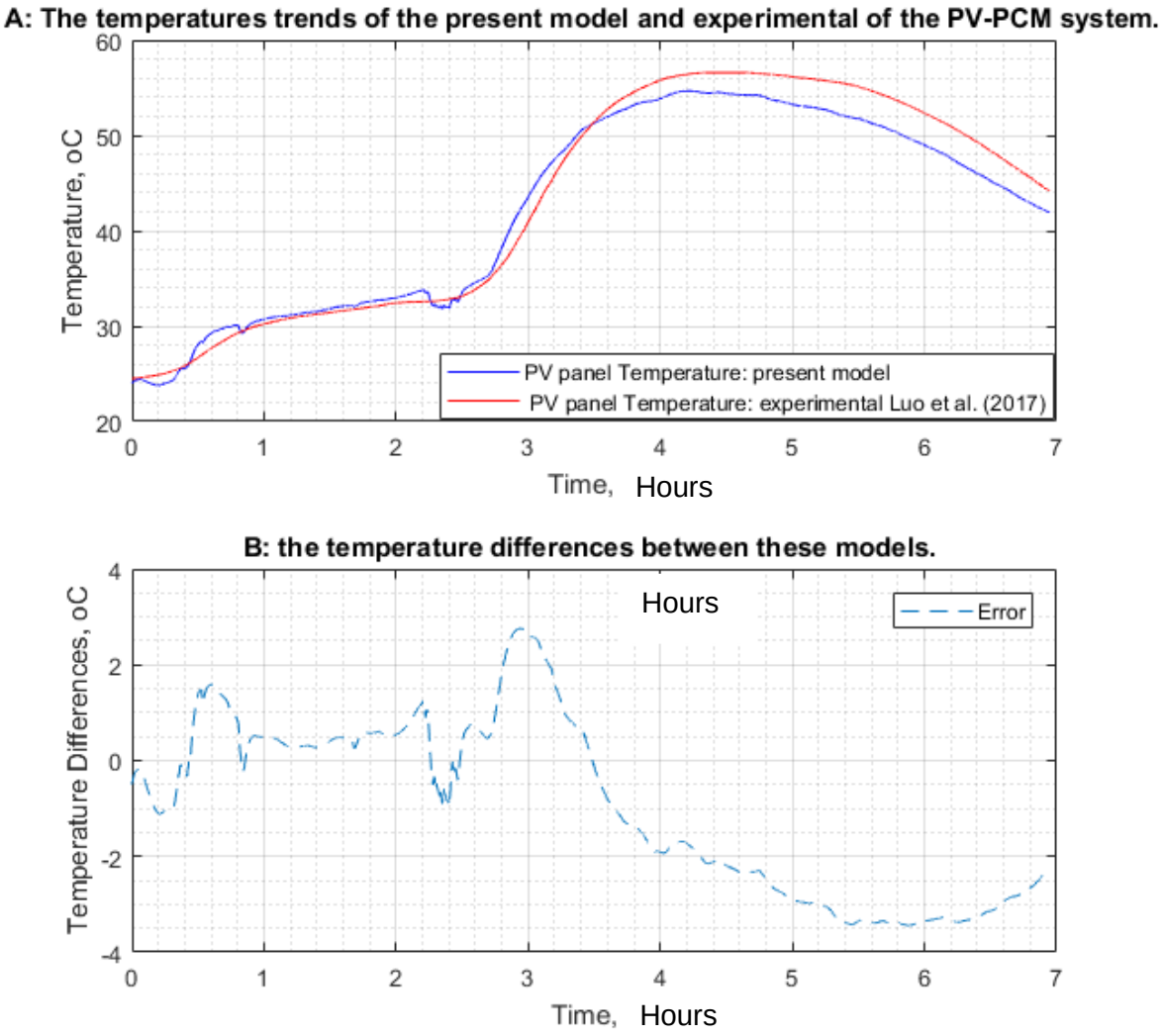

Figure 5-11: A: The temperatures trends of the present model and experimental of the PV-PCM system. B: The temperature differences between these models. For the current time step.

5.6 The impact of calculating the C_{PCM} based on the temperature of the previous and current time step.

Within literature, several papers calculate the apparent heat capacity depending on the previous time step for each node of the PCM when using FIB method. Hu and Argyropoulos (1996) said the apparent heat capacity can be calculated either depending on the previous time step or current time step temperature. However, mathematically, it should be calculated based on the current time step temperature. Therefore, the results for both cases from section 5.4 and 5.5 have been compared. This novel comparison has been illustrated in Figure 5-12 . T1 and T2 represent the PV panel temperatures when calculating the apparent heat capacity based on the temperature of the current and previous time step respectively. The maximum error is 1.3053 at time 9916 with relative error is 3.55%.

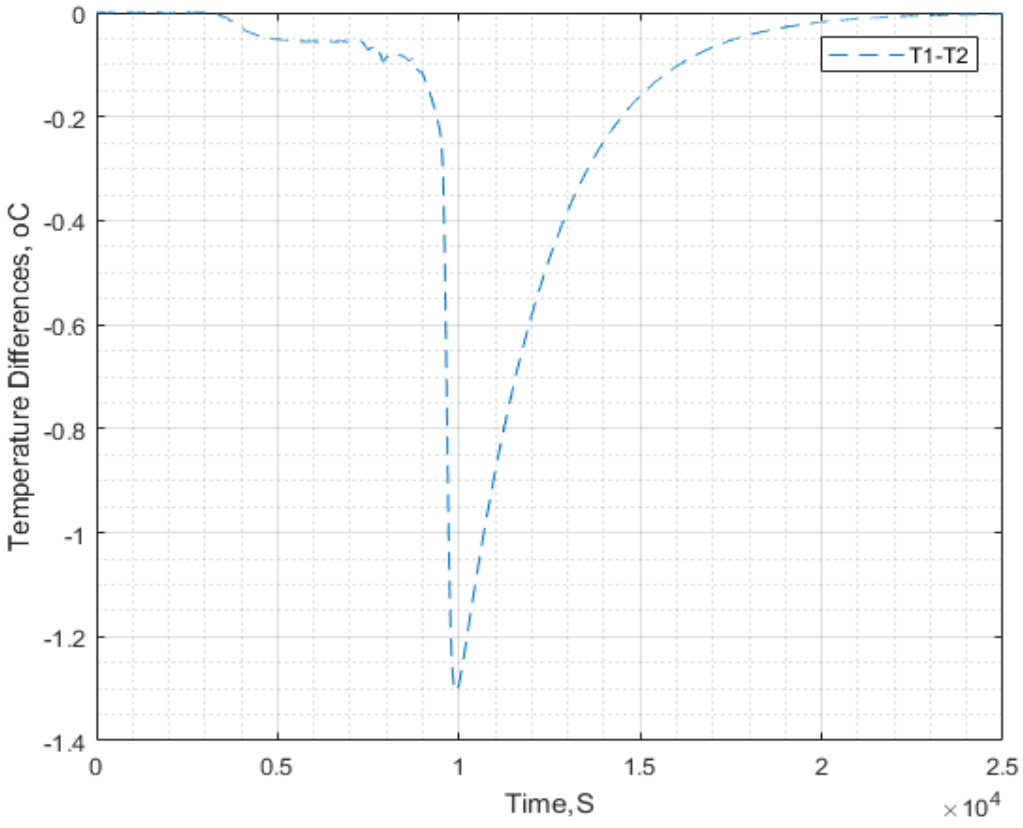

Figure 5-12: PV panel temperature difference for calculating the C_{PCM} based on the previous and current time step temperature.

5.7 Time independent studies for the lumped distributed parameter model:

In order to check the convergence and stability of the lumped distributed parameter model, different time steps are carried out. Three different numbers of time steps: 1, 2 and 4 have been carried out and results shown in Figure 5-13. The maximum difference in results between the 1 second time step and 2 second time step is 0.4941 ^{o}C at time 10017 second. While, the maximum results difference between the 1 second time step and 4 second time step is 0.7838 ^{o}C at time 9943 seconds.

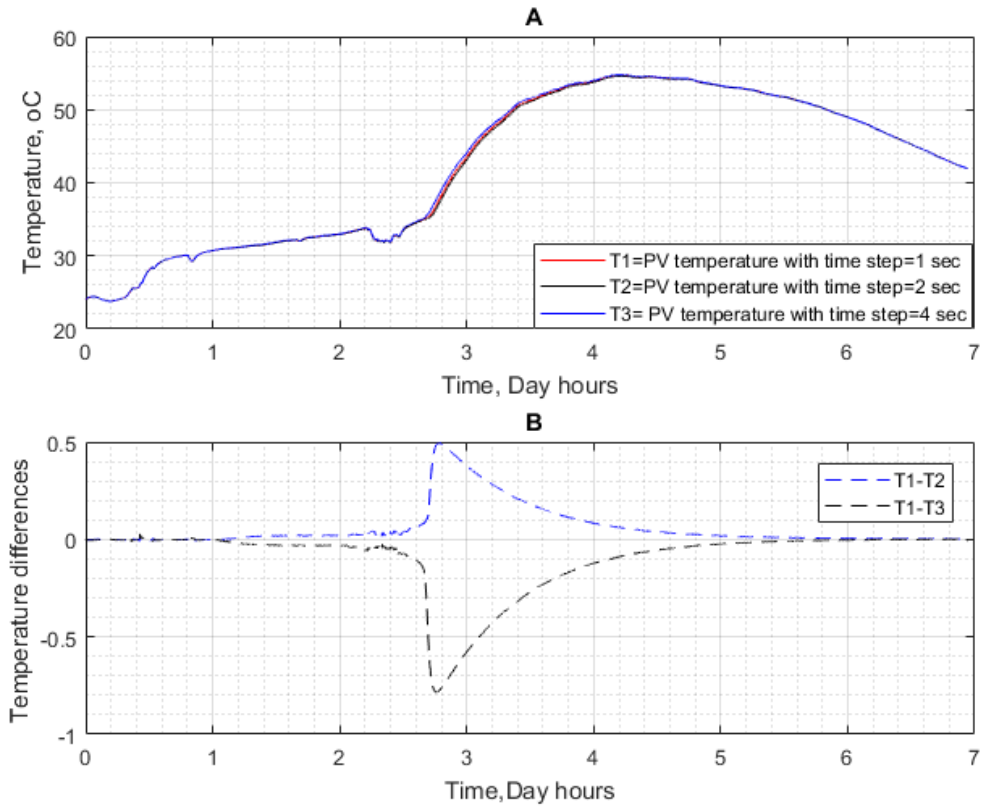

Figure 5-13: Time independent studies for the lumped distributed parameter model

The maximum temperature difference between the results of the 1 second time step and 10 second time step is 1.2189 at time 9923 second. While, the maximum temperature difference between the results of the 1 second time step and 100 second time step is 1.3988 at time 10000 second.

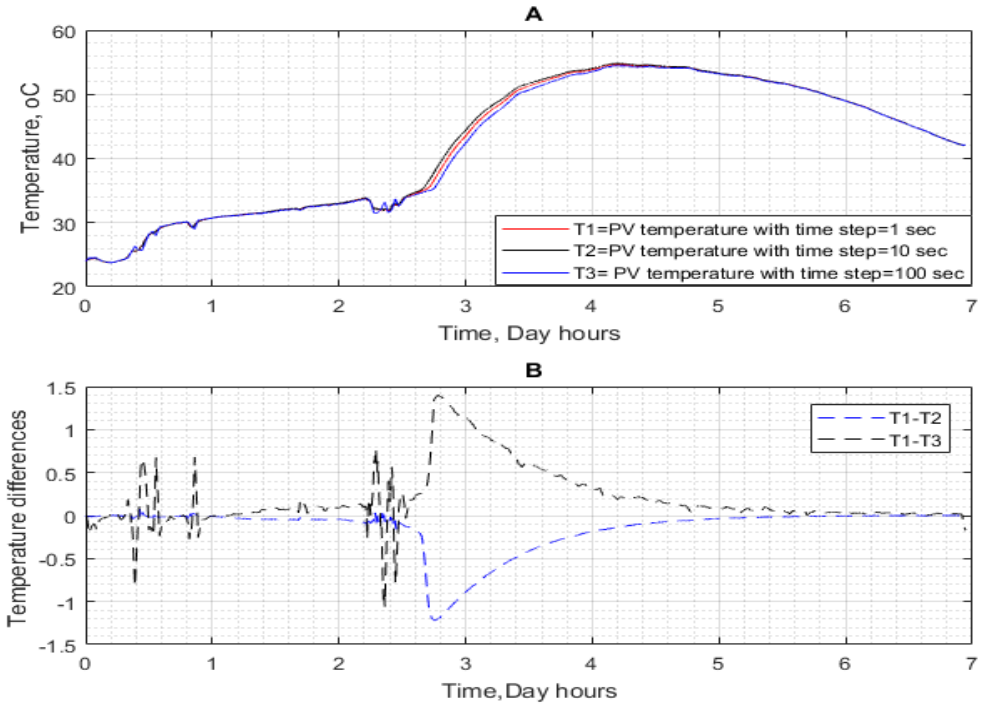

Figure 5-14: Time independent studies for the lumped distributed parameter model

5.8 The impact of different thermal contact conductance

In this section, the impacts of different heat transfer conductance coefficients have been studied. Thermal contact conductance depends on the technical contacting approaches between the PV panel and the PCM. Therefore, PV panel temperature for several scenarios have been investigated. These are firstly, the PCM is inside an aluminium box in contact with the PV panel and with thermal contact adherence. Secondly, this case is without thermal contact adherence. Thirdly, a 0.5mm air gap is assumed between the aluminium box and PV panel. The heat transfer coefficient for these cases will be 20,000 (Incropera and De Witt, 2005), 4,000 and 52.6 (Yovanovich et al., 1997)W m^{-2} k^{-1} respectively.

The simulated results of the PV panel temperature for these three cases, represented by T_1, T_2 and T_3 are shown in Figure 5-15 respectively. The left y-axis represents the temperature of the PV panel, the x-axis represent the times in second and the right y-axis represents the temperature differences between the first case and second case, and between the first case and third case.

The results have been illustrated in Figure 5-15. It can be seen that there is small impact for adding the thermal contact adherence, where the maximum PV panel temperature difference is 0.1069 ^{0}C compared to the second case without thermal contact adherence at 7765 second. While, the temperature difference between the first and third cases reached 8.5195 ^{0}C at time 7957 second. That means that any gap between the aluminium container and the PV panel could cause high impact on the PV panel temperature. Consequently, figure 8 depicts the impact of these temperature differences on the PV panel efficiency based on the reference efficiency which is usually measured at 25^{0}C according to the ASTM. This reference efficiency is considered 100% and any change in efficiency is compared with it. From Figure 5-15, the efficiency differences reach 3.493% between the first case and third case at time 7957 seconds.

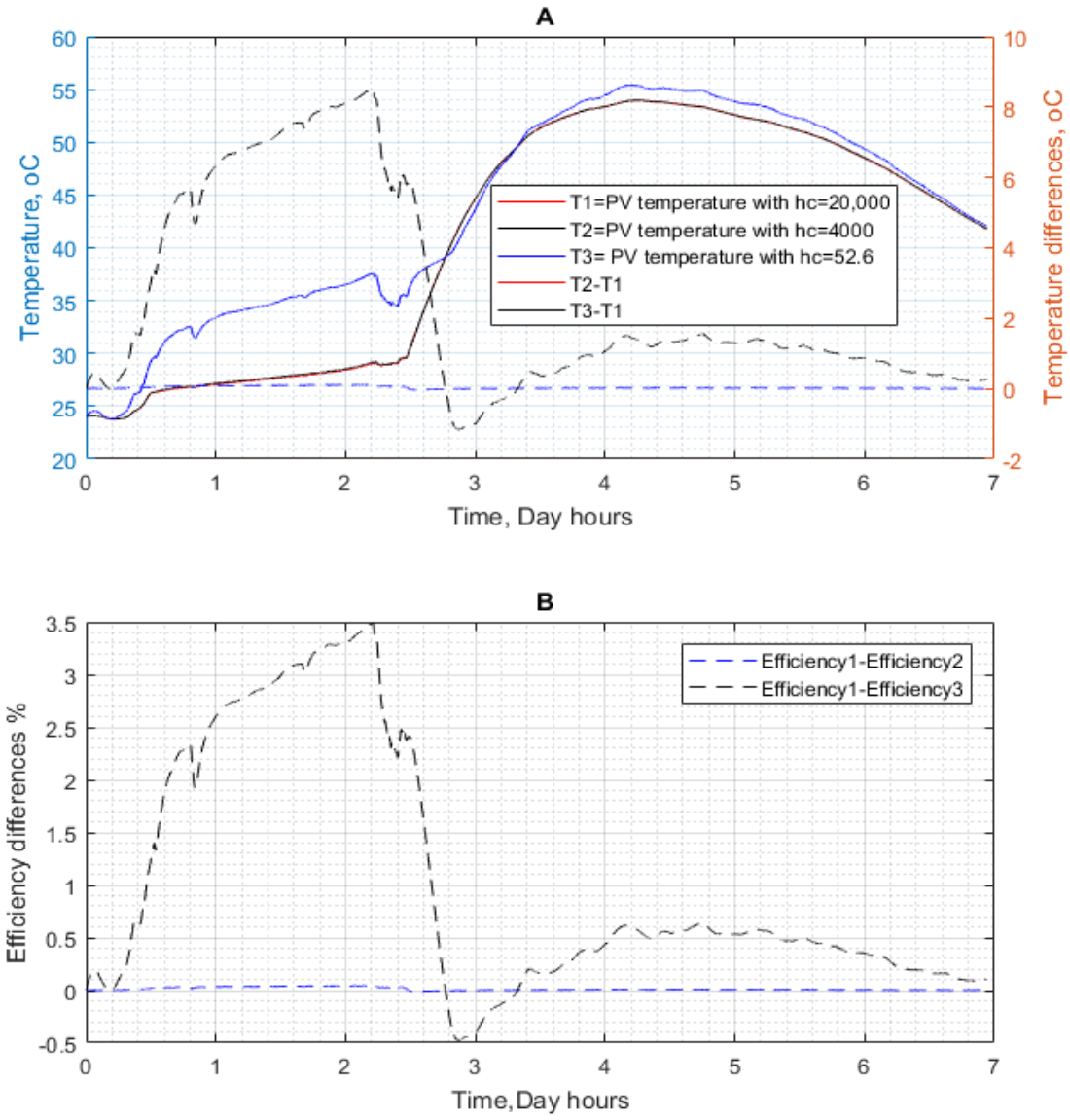

Figure 5-15: The impact of the temperature differences on the PV panel efficiency based on different heat transfer conductance.

5.9 The impact of the volume change during the phase change.

In order to investigate the impact of the volume changing between the solid and liquid phases, the lumped-numerical model for the PV-PCM module has been used. The inputs and the calculation procedure are the same as in the sections 5.4.1 and 5.4.2 respectively, except the PCM properties. The RT35HC PCM has been used and the RT35HC PCM thermophysical properties are

indicated in Table 6 (Nouira and Sammouda, 2018). The PCM thickness was input as 3 cm and the increments were 10, the time step is 1 s.

Table 6: The thermophysical properties of the RT35HC (Nouira and Sammouda, 2018).

PCM	Melting temperature ^0C	Latent heat J kg^{-1}	Thermal conductivity kg m s^{-3} K^{-1}	Specific Heat J kg^{-1} K^{-1}	Density solid kg m^{-3}	Density liquid kg m^{-3}
RT35HC	35	240	0.2	2000	880	770

Figure 5-16 illustrates the PV panel temperature results, and the differences between considering and not considering the volume changing during phase change in the PV-PCM model. The left y-axis represents the temperature of the PV panel, the x- axis represents the day time by hours. The blue dot line denotes the temperature of the PV panel with considering the volume changing during phase change. While, the black line denotes the temperature of the PV panel without considering the volume changing during phase change. The difference between these two cases has been illustrated by the red dot line and corresponds with right y-axis. The maximum temperature difference between these two models is 1.7954 ^oC at time 6965 seconds. This maximum difference happens after the PCM changed to the molten phase which means the thickness of the PCM has been increased. This leads to an increase of the thermal resistance to the back side of the PV-PCM module reducing the released heat. Therefore, when the volume change has been considered during the phase change, the PV panel temperature has been increased. In conclusion, this model for the PV-PCM system is closer to reality, and the volume change during the phase change should be considered.

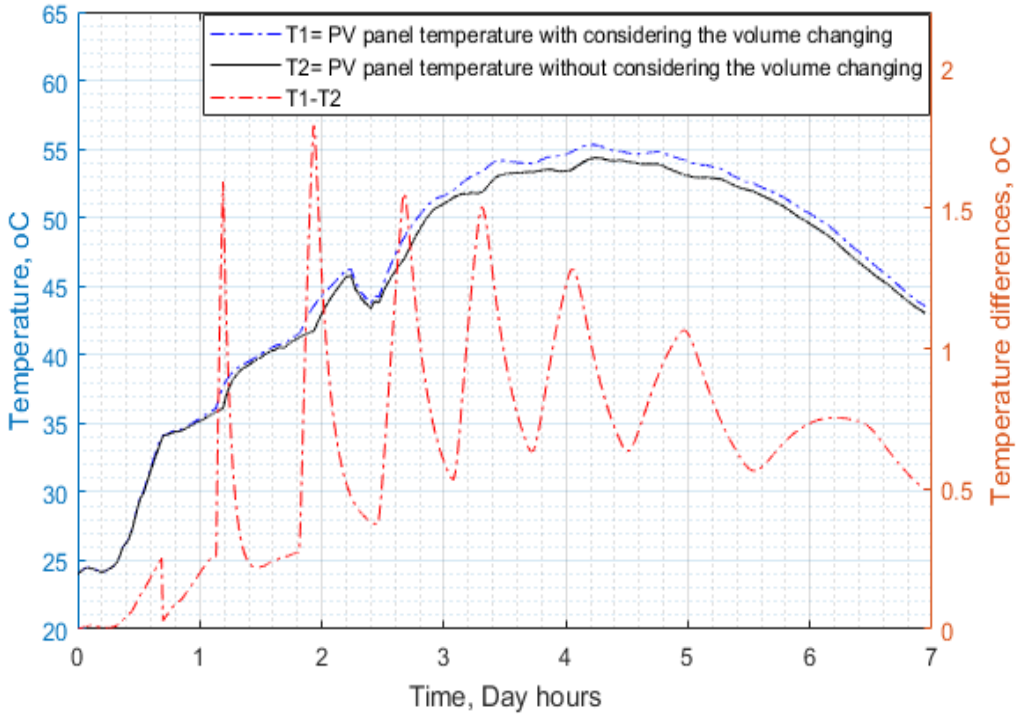

Figure 5-16: PV panel temperatures in the PV-PCM system with and without considering the volume changing during phase change.

Figure 5-17 illustrates the PV panel efficiency differences if the volume change during the phase change has been considered or not. In this case, this efficiency difference reached 0.7361 % based on the reference efficiency, which is usually measured at 25^0C according to the ASTM. This reference efficiency considered 100% and any change in efficiency compared with it. This efficiency difference has been calculated based on the temperature difference, where each PV panel temperature rise, the efficiency decreased by 0.41% based on the reference efficiency.

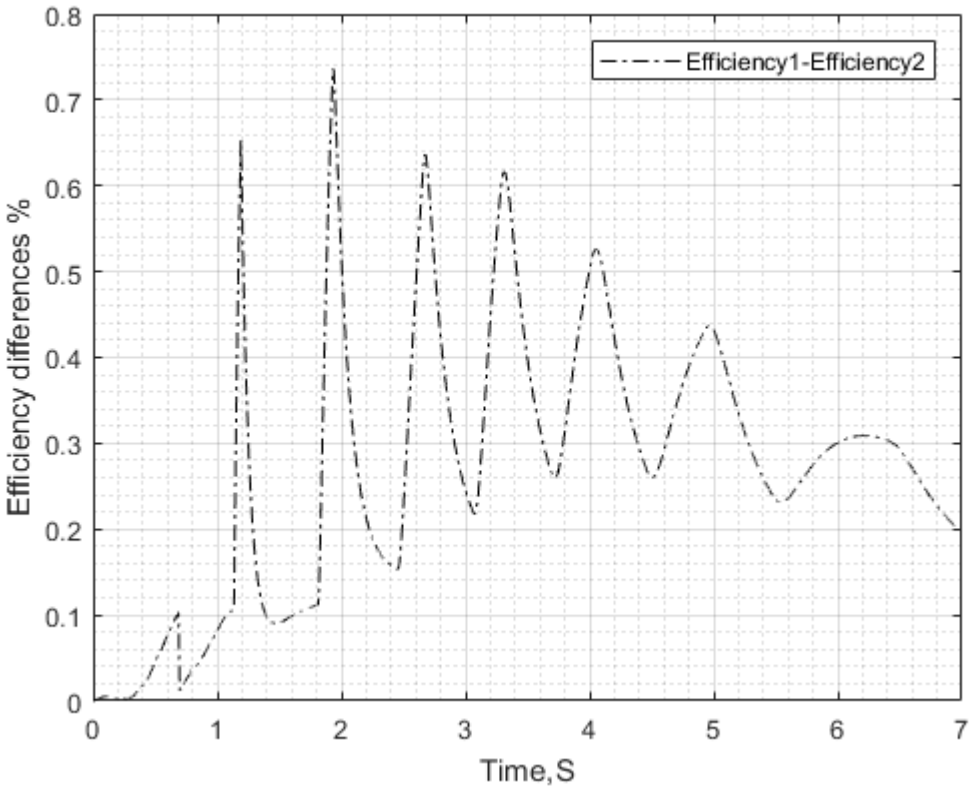

Figure 5-17: the effect of the considering the volume change during phase change on the PV panel efficiency result.

5.10 The comparison of the time consuming for the explicit, implicit and lumped-numerical models for the PV-PCM module.

In order to compare the time consumption for the implicit and lumped-numerical models for the PV-PCM module, the time step has been set at 1 s and the total time is 18000s. In addition, the number of the increments for the PCM was set as 10. Also, for each layer of the PV panel, the increments are 10 for implicit model. The specifications of the computer that was used are: processor Intel (R) xeon (R) CPU E3-1240, 3.5GHz and the installed memory is 32 GB. The results have indicated that the real time taken to solve the implicit model using this computer is 525.045 s with iteration accuracy is 10^{-6}. While the real time taken to solve the lumped distributed parameter model is 16.813 s with iteration accuracy is 10^{-6} using the apparent heat capacity for the current time step. If the apparent heat capacity is calculated depending on the previous time step temperature, the

computer real time taken is 3.934 second. In contrast, according to the section 5.3, the computer time that required to simulate 1 second of the PV-PCM system using the explicit method is 51,391.431 seconds. Moreover, the implicit method for the both distributed parameter model and lumped distributed parameter model can be run with time step 100 s.

5.11 The validation work for the PV panel stand-alone model

In order to validate the results for the PV panel stand-alone model, a matlab code has been written and the thermophysical properties for DAH PV panel and the nominal operating condition test (NOCT) have been input. The nominal operating condition test, is a measurement test for PV panel power and temperature under specific conditions. These conditions are 800 W m^{-1}, 1 m s^{-1} and 20 ^{o}C for the solar intensity, the wind speed and the wind temperature respectively. The results of nominal operating condition test for the DAH PV panel temperature is 45 ± 2 ^{o}C as mentioned in data sheet, while the temperature results of the this lumped PV panel stand-alone model have been illustrated in the Figure 5-18 based on the Equ. 4-16. It can be seen from the Figure 5-18 that the temperature of the PV panel agrees with the result of the NOCT.

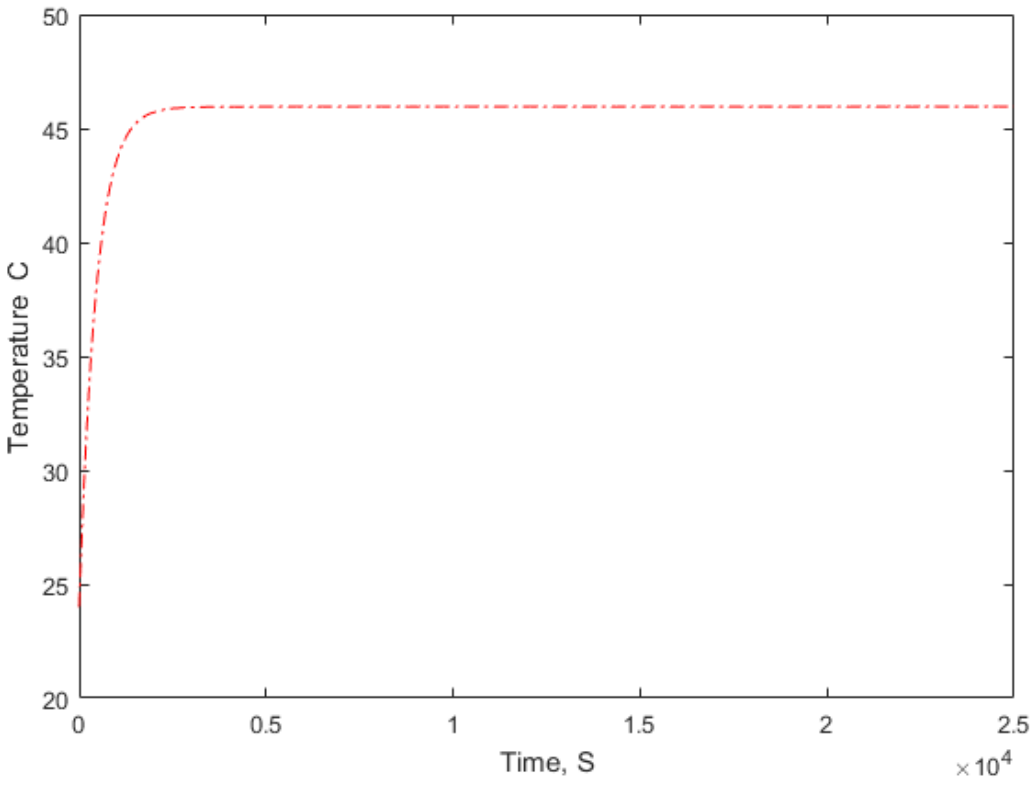

Figure 5-18: the temperature results of the lumped PV panel stand-alone model

5.12 Summary

This chapter has presented the results of the explicit, implicit methods for the distributed parameter model and the novel lumped- distributed parameter model for the PV-PCM module. Then, the required computer time to solve this method has been compared among these methods. The results of these models have shown close results values to the literature with little errors. These errors were owing to assumption of wind speed and other factors. In addition, the mesh independency has been investigated for the implicit method for the lumped-distributed parameter model. The results indicate that the maximum error that occurred between the 10 and 40 increment cases solutions of the PCM is 0.0158 ^{o}C. Furthermore, the impact of different contact conductance between the PV panel and the PCM has been implemented and investigated by this model.

To study the impact of thermal conductance between the PV panel and the aluminium container of the PCM, three cases have been investigated. These three cases have assumed: firstly, there is a contact adherence between the

aluminium container and the PV panel. Secondly, there is no contact adherence. Thirdly, there is 0.5 mm air gap. The results show the maximum electric PV-PCM efficiency difference reaches 3.8%, if comparing the first case with third case.

More development for this lumped distributed parameter model has implemented by considering the impact of the volume change of the PCM during the phase change from solid to liquid. The results indicate that the maximum temperature difference reach to 1.7954 ^{o}C between considering and non-considering the volume change.

A novel comparison between using the apparent heat capacity of the PCM depending on the temperature of the previous and current time step has implemented. The results show the temperature difference could reach 1.3053 ^{o}C with relative error is 3.55%.

Furthermore, three matlab algorithms have been built for the PV-PCM system by the MATLAB software using the implicit method for the lumped-distributed parameter model, the explicit and implicit methods for the distributed parameter model. The results indicate the time required for the implicit method for the distributed parameter, implicit method for the lumped-distributed parameter model with calculating the Cp based on temperature of current time step and implicit method for the lumped-distributed parameter model with calculating the Cp based on temperature of previous time step, to simulate transient 18000s for the PV-PCM system reach 525.045 seconds, 16.813 seconds and 3.934 seconds, if time step is 1 s, each layer of the PV-PCM system has been divided to 10 increments and the accuracy of the implicit model is 10-6. These models can be run with time step 100 s. While, the real time taken for the explicit model to simulate 1 second reaches to 51,391.431 seconds.

Chapter Six The impact of the PCM On The PV Panel

6.1 Outline

This chapter presents the sources of solar radiation, and how to calculate solar radiation on an inclined surface from measured solar radiation for a horizontal surface. Then, this solar radiation for a whole year will be used to study the impact of PCM on the electric energy and the temperature of the PV panel, for Baghdad and Milan.

6.2 Solar radiation

6.2.1 Introduction

The amount of solar energy that reaches the earth is approximately 885 million terawatt hours annually, and there are several methods to assess the amount of solar radiation for each square meter of earth (InternationalEnergyAgency, 2011). One of the most promising methods is by measuring the solar radiation that reaches a horizontal plane in a specific location. Then, depending on both this measured solar radiation and the sun's path in the sky, solar radiation can be calculated for any inclined surface. Therefore, this section will describe both the source of the measured solar radiation and the procedure of calculating solar radiation on an inclined surface.

6.2.2 Solar radiation dataset resources

Direct normal irradiation (DNI) also represented by (G_b) and diffuse horizontal irradiation (Bahaidarah et al.) which represented also by (G_d) are the main components of Global Horizontal Irradiation (GHI), which are available in different forms (Bahaidarah et al., 2016). Usually, a pyranometer is used to record these direct and diffuse radiations for a horizontal plane in geostationary plants. These geostationary plants are located worldwide and have different pixel accuracies

(Duffie and Beckman, 2013b). While satellite-based records depend on solar radiation measured by satellites and the transmittance of the atmosphere. These records have been used with several algorithm models to reproduce solar radiation data with more pixel accuracy. These solar radiation data are available at different intervals of time: each minute, hourly, average daily and average monthly (Sengupta et al., 2017). These solar radiation data are available from several resources, such as the National Solar Radiation Database (NSRDB), the Surface Radiation Budget (SRB) dataset from NASA, the DLR-ISIS model, HelioClim-1, HelioClim-3, Solar Energy Mining (SOLEMI), MACC-RAD services, Solargis, the NOAA Global Surface Insolation Project and the EnMetSol model.

In 1977, France launched the first geostationary satellite to record data for the Meteosat project service. Since then, the European Space Agency has been involved in this project (European-Space-Agency, 11 2017). The Meteosat project uses 12 channels, and data have been recorded every 15 minutes since 2004. Based on the Meteosat project, Heliosat-2, HelioClim-1 and HelioClim-3 solar radiation data have been generated (Marchand et al., 2018). The comparison of global solar radiation from HelioClim-3 version 5 to ground measurements in Morocco has indicated the error between 0% to –4% (Marchand et al., 2018).

For this study, the global horizontal irradiation, ambient temperature and wind speed in Baghdad have been collected from the Ministry of Agriculture's. GHI can be used to calculate the solar irradiation striking an inclined surface. Then, global normal irradiation from HelioClim-3 will be validated against the geostationary plants in Iraq. Next, the solar radiation for the inclined surface from HelioClim-3 will be used for Milan.

6.2.3 Solar irradiation model for an inclined surface

GHI represents the total amount of solar radiation that strikes a horizontal surface per square meter. However, the PV panel could be installed at an inclined angle, therefore, the total amount of solar radiation that strikes an inclined PV panel surface should be calculated. Calculation of the solar radiation for inclined surface depends on DNI and DHI, which are functions of solar radiation on a horizontal

surface; solar time; location; plane angles; the sun's path in the sky and the transmittance of the atmosphere.

6.2.3.1 Solar time

Solar time can be defined as the time depending on the sun's position and the meridian related to the observer's location. Solar time can be calculated from the local time with two corrections. The first correction is the time difference between the longitude of the observer and the longitude of the stander of the local time based. Each degree of longitude is equal to four minutes. The second correction is based on the day of the year. Solar time can be calculated from the flowing equations (Duffie and Beckman, 2013b):

$$\text{Solar time } (t_s) = \text{Standard local time} + 4(\mathrm{L}_{st} - \mathrm{L}_{loc}) + E \qquad \textbf{6-1}$$

where, L_{st} represents the longitude on which the local time is based. L_{loc} is the longitude of the observer. E is the function of time which can be calculated from this equation:

$$\mathrm{E} = 3.82(0.000075 + 0.001868\cos B - 0.032077\sin B - 0.014615\cos 2B - 0.04089\sin 2B) \qquad \textbf{6-2}$$

$$\mathrm{B} = 360° \frac{(n-1)}{365} \qquad \textbf{6-3}$$

where, n represents the day of the year ['1' corresponds to 1 January].

Solar time can be converted to the hour angle [ω] representing the degree of the sun moving across the sky.

$$\omega = (t_s - 12) * 15 \qquad \textbf{6-4}$$

6.2.3.2 Solar angles

The angles of the PV panel surface (the plane) are illustrated in Figure 6-1 . β represents the tilted angle of a PV panel with a horizontal surface. Z_S is the surface azimuth angle, which is between the normal on the PV panel surface and the North direction. Z represents the solar azimuth angle, which is between the South direction and the sun. θ is the angle of the incidence, meaning the angle between the sun's beam radiation and the normal to the surface. Φ is the zenith angle, which is between the sun line and the vertical. In addition, the other important angle is the declination angle (δ), which represents the tilt angle of the rotational axis of the Earth tangent to the Earth's orbit around the sun. The declination angle ranges between 23.45° to –23.45° (org, 2018). The declination angle can be calculated from this equation:

$$\delta = \left(\frac{180}{\pi}\right)(0.006918 - 0.399912\cos B + 0.070257\sin B - 0.006758\cos 2B + 0.000907\sin 2B - 0.002697\cos 3B + 0.00148\sin 3B) \quad \textbf{6-5}$$

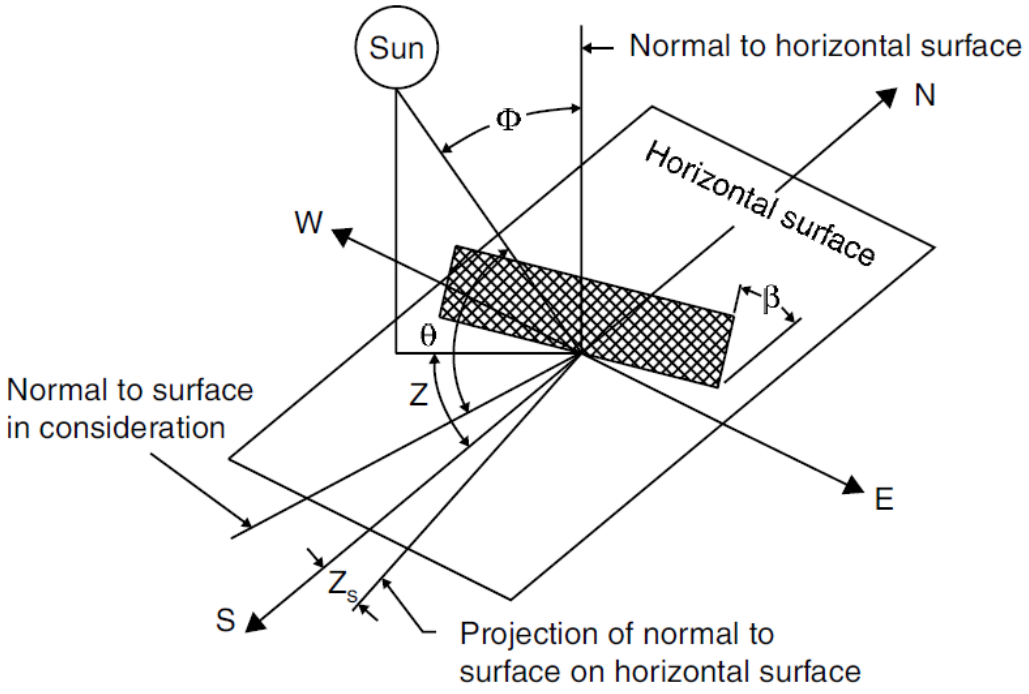

Figure 6-1: The angles of an inclined surface with the sun (Kalogirou, 2013).

For a PV surface with any orientation, the angle of incidence can be calculated using the following equation:

$$\cos\theta = \sin\emptyset \sin\delta \cos\beta - \cos\emptyset \sin\delta \sin\beta \cos Z_s + \cos\emptyset \cos\delta \cos\beta \cos\omega + \sin\emptyset \cos\delta \sin\beta \cos\omega \cos Z_s + \cos\delta \sin\beta \sin\omega \sin Z_s \quad \textbf{6-6}$$

Where, $\emptyset$ is the latitude ranging from zero to 90 in the northern hemisphere.

The zenith angle can be calculated from this equation:

$$\cos\Phi = \cos\emptyset \cos\delta \cos\omega + \sin\emptyset \sin\delta \quad \textbf{6-7}$$

6.2.3.3 Direct and diffuse solar radiation on a horizontal surface

The measured solar radiation on horizontal plane (G) can be divided into beam (G_b) and diffuse (G_d) solar radiation depending on the hourly clearance index K_t by:

$$\frac{\mathrm{G}_d}{G} = \begin{cases} 1 - 0.09K_t & for\ K_t \le 0.22 \\ 0.9511 - 0.1604K_t + 4.388{K_t}^2 & for\ 0.22 < K_t \le 0.8 \\ 0.165 & for\ K_t > 0.8 \end{cases} \quad \textbf{6-8}$$

$$K_t = \frac{G}{G_o} \quad \textbf{6-9}$$

where, G_o is the solar radiation in the horizontal plan in extra-terrestrial, which can be calculated using the following equation (Sukhatme and Sukhatme, 1996):

$$G_o = \frac{12 * \Delta t}{3.14} * 1367 \left(1 + 0.033 \cos\frac{366n}{365}\right) \left[\cos\emptyset \cos\delta \left(\sin\omega_2 - \sin\omega_1\right) + \frac{\pi(\omega_2 - \omega_1)}{180} \sin\emptyset \sin\delta\right] \quad \textbf{6-10}$$

Where, Δt the time interval (S). ω_1 and ω_2 are the beginning and ending solar time for the time interval, respectively.

6.2.3.4 Direct and diffuse solar radiation on an inclined surface

In order to predict the amount of solar radiation that strikes an inclined PV panel, the direct beam, diffuse radiation and ground-reflected solar radiation should be calculated.

$$G_t = G_{Bt} + G_{Dt} + G_{Gt} \quad \textbf{6-11}$$

where, G_{Bt}, G_{Dt} and G_{Gt} are the direct beam, diffuse radiation and ground-reflected solar radiation on a tilted PV panel (W m^{-2}), respectively. G_{Bt} can be calculated using the following equation (Duffie and Beckman, 2013b):

$$G_{Bt} = DNI * Rb \quad \textbf{6-12}$$

where, Rb stands for the ratio of beam radiation on the tilted surface to beam radiation on the horizontal surface, and it can be calculated using this equation (Duffie and Beckman, 2013b):

$$Rb = \frac{\cos\theta}{\cos\Phi} \quad \textbf{6-13}$$

G_{Dt} includes isotropic diffuse radiation from the sky and horizontal diffuse radiation. G_Dt be calculated using this equation:

$$G_{Dt} = G_D \left[(1 - Ai)\left(\frac{1+\cos\beta}{2}\right)\left(1 + \mathcal{F}\left(\sin^3\frac{\beta}{2}\right)\right) + Ai * Rb\right] \quad \textbf{6-14}$$

Where, Ai represents the transmittance of the atmosphere for direct solar radiation which can be calculated from:

$$Ai = \frac{G_b}{G_o} \quad \textbf{6-15}$$

$$\mathcal{F} = \sqrt{\frac{G_b}{G}} \quad \textbf{6-16}$$

The ground-reflected solar radiation can be calculated using the following equation (Kalogirou, 2013):

$$G_{Gt} = GHI * \rho_g \left(\frac{1-\cos\beta}{2}\right) \quad \textbf{6-17}$$

where, ρ_g is the reflectance of the ground.

According to the equations **6-12**, **6-14** and **6-17**, the total solar radiation on the tilted surface will be:

$$G_t = (DNI + Ai * DHI)Rb + DHI(1-Ai)\left(\frac{1+\cos\beta}{2}\right)\left(1+\mathcal{F}\,(\sin\frac{\beta}{2})^3\right) + GHI * \rho_g \left(\frac{1-\cos\beta}{2}\right) \quad \textbf{6-18}$$

6.2.4 Comparison of the solar radiation data for the inclined surface

The data for global horizontal solar radiation have been collected from Abu Graib, Baghdad, Iraq. In order to calculate the total solar radiation on an inclined surface, the mathematical model in section 6.2.3 was used, and a MATLAB code has implemented for this model. The flow chart of this mathematical model has been illustrated in **Figure 6-2**. First, the collected data for global horizontal solar radiation was uploaded for a point in Baghdad, Iraq (44.23° longitude, 33.32° latitude). Then, the loop of the time intervals was initiated. Inside the loop, the solar time was calculated using equations **6-1**, **6-2**, **6-3** and **6-4**. Subsequently, the solar angles were identified according to the equations **6-5**, **6-6** and **6-7**. Finally, the total solar radiation on an inclined surface will be calculated from equation **6-18**.

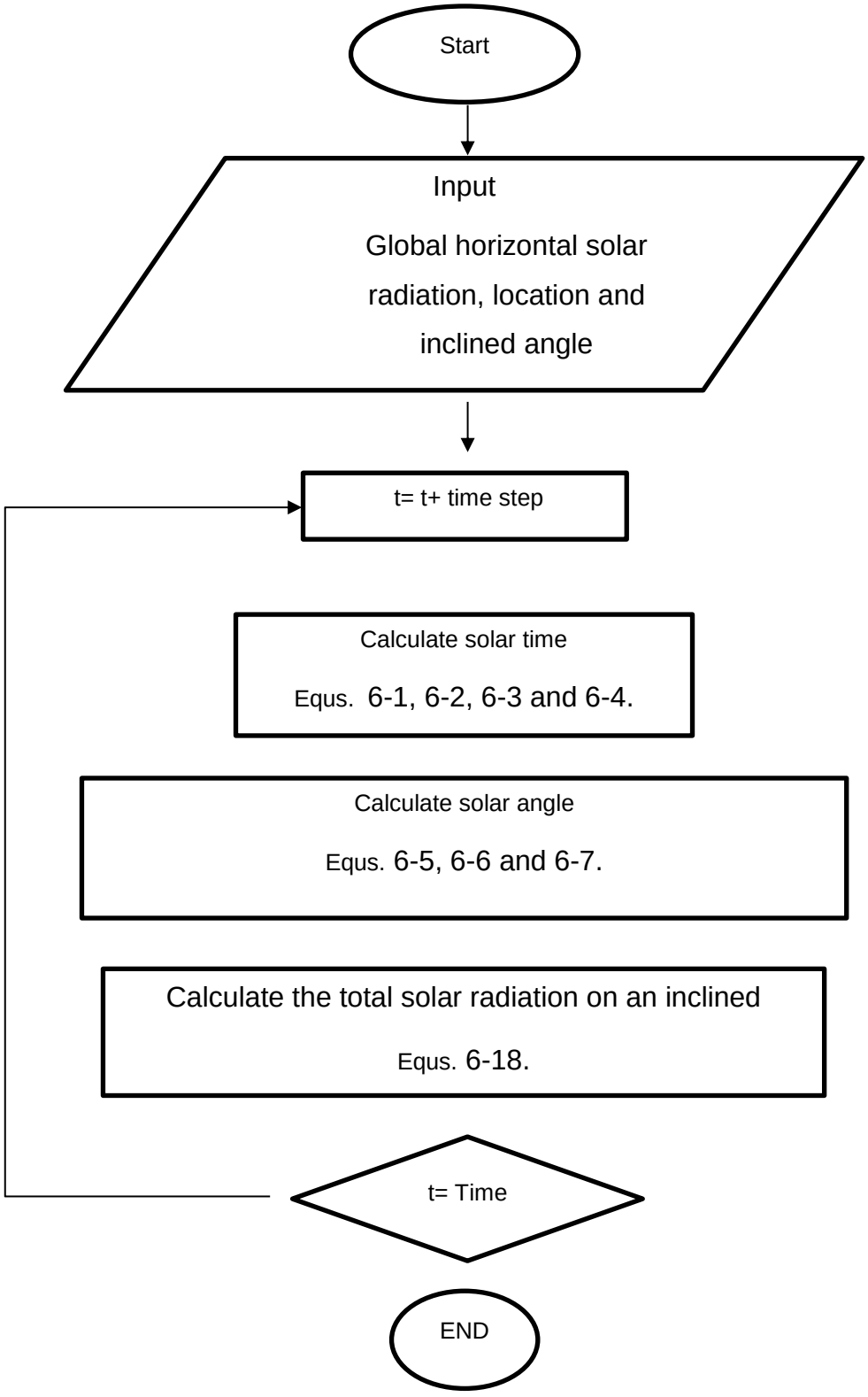

Figure 6-2: The flow chart of the mathematical model to calculate the total solar radiation on an inclined surface.

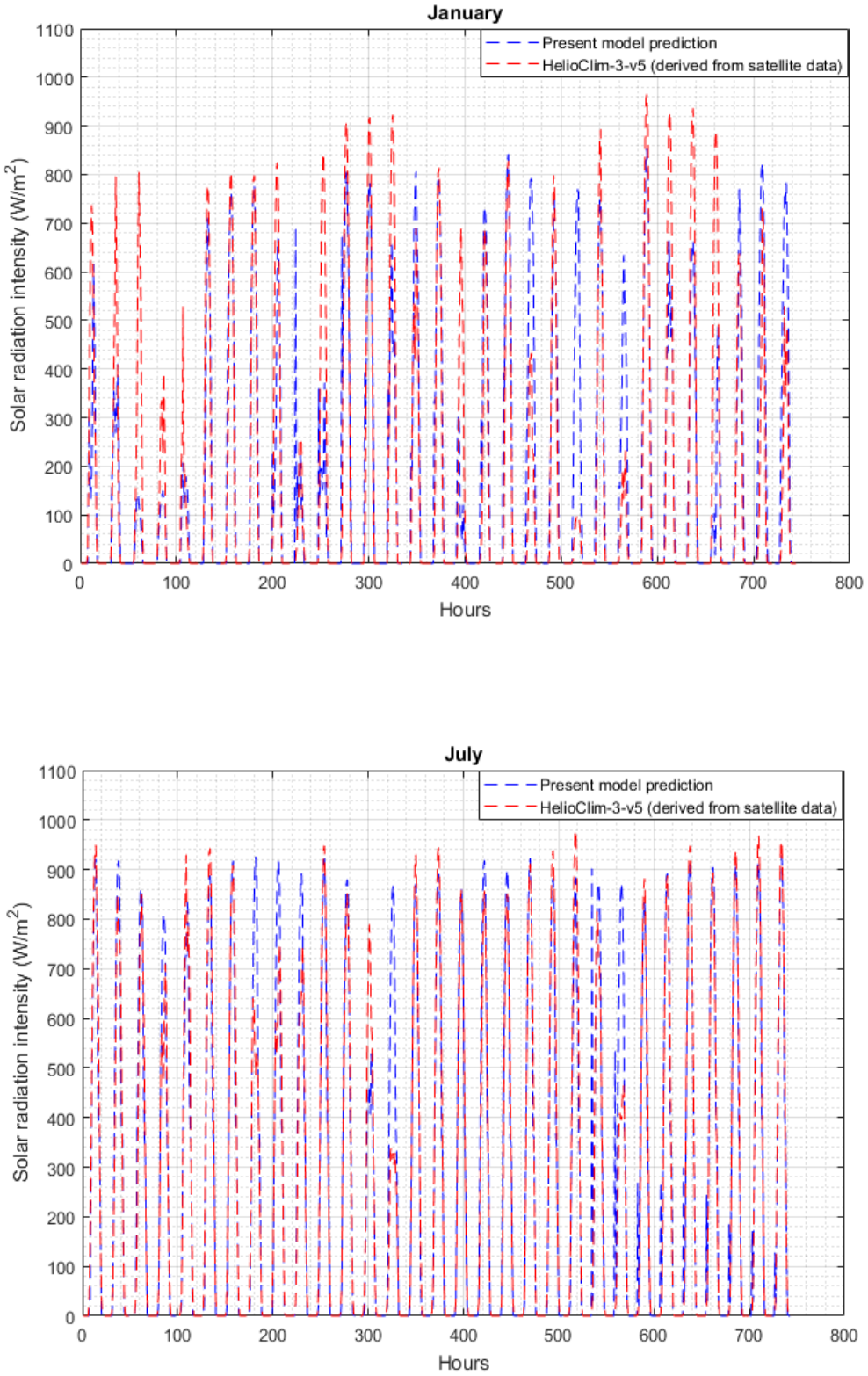

Figure 6-3: The current and HelioClim-3 v5 hourly results of solar radiation intensity (with time on a 29˚-inclined surface for January and July – Baghdad, Iraq.

The results of the total solar radiation from the present model for the 29˚-inclined surface have been compared to data from the HelioClim-3 v5 for the same location. The results of this comparison have been illustrated in Figure 6-3 for each hour of solar radiation intensity in January and July. The blue line represents the results of the current model based on the real collected data for 2014 from the Ministry of Agriculture's geostationary plant, while the red line represents the results of HelioClim-3 v5 for 2005, which are derived from satellite data. Therefore, it can be seen from Figure 6-3 that the hourly solar radiation intensities are not the same for both results. These differences could be the result of sky clearance and different years of recording. These differences in the solar radiation resources lead to different amounts of accumulated solar radiation for each month, which reached 12.49% in June, as shown in Figure 6-4. Therefore, the results of the current model will be used in this study.

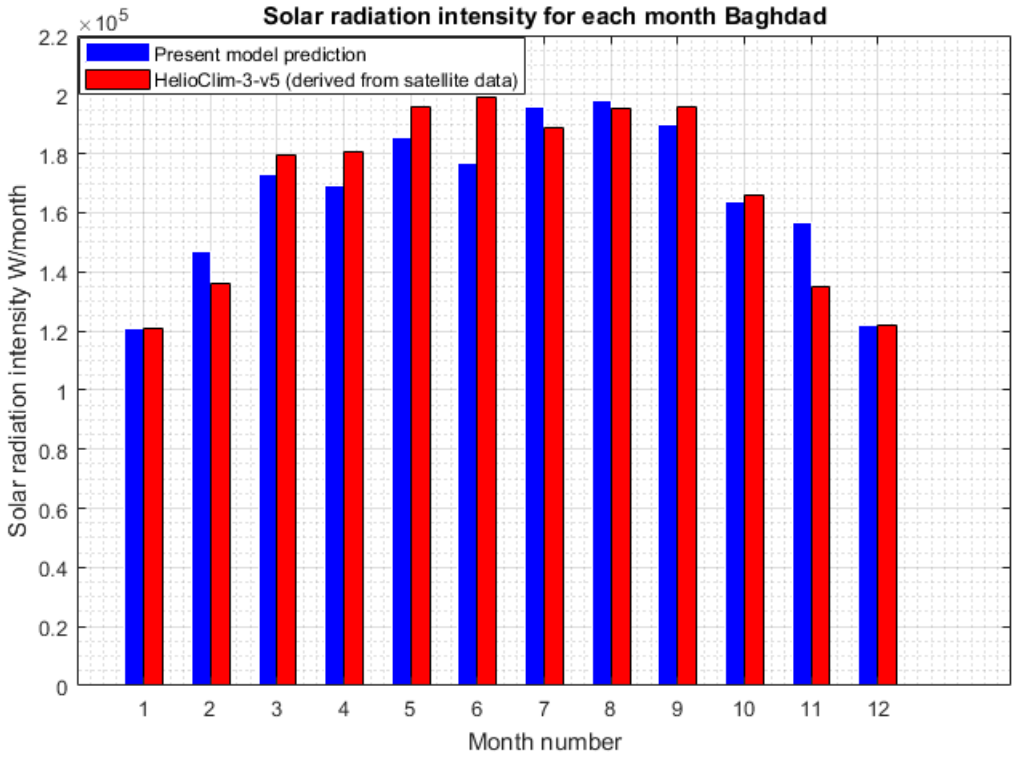

Figure 6-4: The current and HelioClim-3 v5 monthly results of solar radiation intensity for 2014 and 2005, respectively, on a 29°-inclined surface for January and July – Baghdad, Iraq.

6.2.5 The impact of PCM on the electrical energy and the temperature of a PV panel: case studies in Baghdad and Milan Baghdad

The impact of a PCM on the electrical energy of the PV panel for one year in Baghdad has been investigated. First, the thermophysical properties (Table 5) for the PCM and PV panel layers have been imported to the MATLAB algorithm. Second, the collected horizontal solar radiation intensity, the ambient temperature and the wind speed data for each hour of 2014 have also been imported. This horizontal solar radiation intensity data has been used to calculate the inclined solar radiation intensity for a surface tilted at 30° using the algorithm that was described in section 6.2.4. Finally, the MATLAB algorithms from sections 5.5 and 5.11 have been used to predict the energy output and the temperature trends for the PV-PCM module and the stand-alone PV panel, respectively. The thickness of the PCM is considered 0.05 m.

The results of the simulated impact of PCM on the PV panel's electrical output in Baghdad, for 2014 have been illustrated in Figure 6-5. The x-axis in Figure 6-5 represents the month, while the y-axis represents the accumulated electrical energy production (WH) per month from a 1 kW PV panel. The blue bars represent the electrical energy production of the PV-PCM system, while the red bars represent the electrical energy production of the stand-alone PV panel. From Figure 6-5, it can be seen that the electrical energy production of the PV-PCM system from January through November are more than that of the stand-alone PV panel. However, in July and August, the electrical energy production from the stand-alone PV panel is close to the electrical energy production of the PV-PCM system. This is owing to the impact of the PCM cooling, as illustrated in the next paragraph. In 2014 in Baghdad, the estimated impact of the PCM on the electrical energy production of PV panels is increasing by 1.96%. The electrical energy production from the PV-PCM system and the stand-alone PV panel for 1 kW PV panels are 1,849.8 kWh and 1,814.2 kWh, respectively.

The temperature trends of the PV panel that attached with PCM, PV panel stand alone and ambient, for the first ten days of January, April, July and October have been illustrated in Figure 6-6, Figure 6-7, Figure 6-8 and Figure 6-9, respectively.

In these figures, the y-axis represent the temperature in degrees kelvin, and the x-axis represent the time in seconds to the energy of 10^5. In this study, the simulation started at zero from the first midnight of each month. In each figure, the blue dashed line, the red dashed line, the green dashed line, the blue dotted line and the black dotted line represent the temperatures of the PV panel in the PV-PCM system, the stand-alone PV panel, the mid-PCM node, the solidification of the PCM and the ambient temperature, respectively.

From Figure 6-6, it can be seen that the temperature of the midpoint of the PCM has never been above the solidification temperature line. This means part of the PCM did not melt during those ten days. This non-melted part worked as a thermal barrier that prevented heat releasing from the rear side by convection to the ambient air. In contrast, the PCM slightly cools the PV panel as a result of the sensible amount of heat stored by the PCM. As a result of this, during the day, the temperature of the PV panel of the PV-PCM system has been less than that of the stand-alone PV panel, as shown by the dashed blue and red lines. However, at night, the temperature of the PV panel that attached with PCM is higher than the temperature of the stand-alone PV panel. Therefore, the efficiency increased, and in January the electrical energy of the PV-PCM system is more than the electrical energy of the stand-alone PV panel.

Figure 6-7 illustrates the results of the temperature trends in April. The temperatures of the PV panel attached to PCM and the stand-alone PV panel exceed the solidification temperature of the PCM during the day, then at night they decrease to the melting temperature of the PCM. Therefore, for most days in April, the PCM solidified at night and then became molten during the day. This melting process during the day absorbs the heat from the PV panel and keeps the temperature of the PV panel attached to PCM lower than the temperature of the stand-alone PV panel. This cooling of the PV panel that attached with PCM leads to an increase in the efficiency of the PV panel by 0.41 for each 1 K decrease. Therefore, in April, the electrical energy production of the PV panel attached to PCM is higher than that of the stand-alone PV panel, as illustrated in Figure 6-5. In October, the situation is almost the same as in April, as shown in Figure 6-9.

In July, the midpoint of the PCM has never been below the dotted black solidification temperature line, as shown in Figure 6-8. Also, in this situation, the PCM has cooled the PV panel to a sensible level of heat, and the PCM has made a thermal barrier. Therefore, the temperature of the PV panel in PV-PCM is lower than the temperature of the stand-alone PV panel for the first hours of the day. Later, the temperature increases. As a result of this, in July, the energy production of the PV-PCM is slightly more than the energy production of the stand-alone PV panel.

The PV panel temperature trend and the electrical energy production with and without PCM for each 100 seconds of the entire year is illustrated by 24 figures in Appendix A.

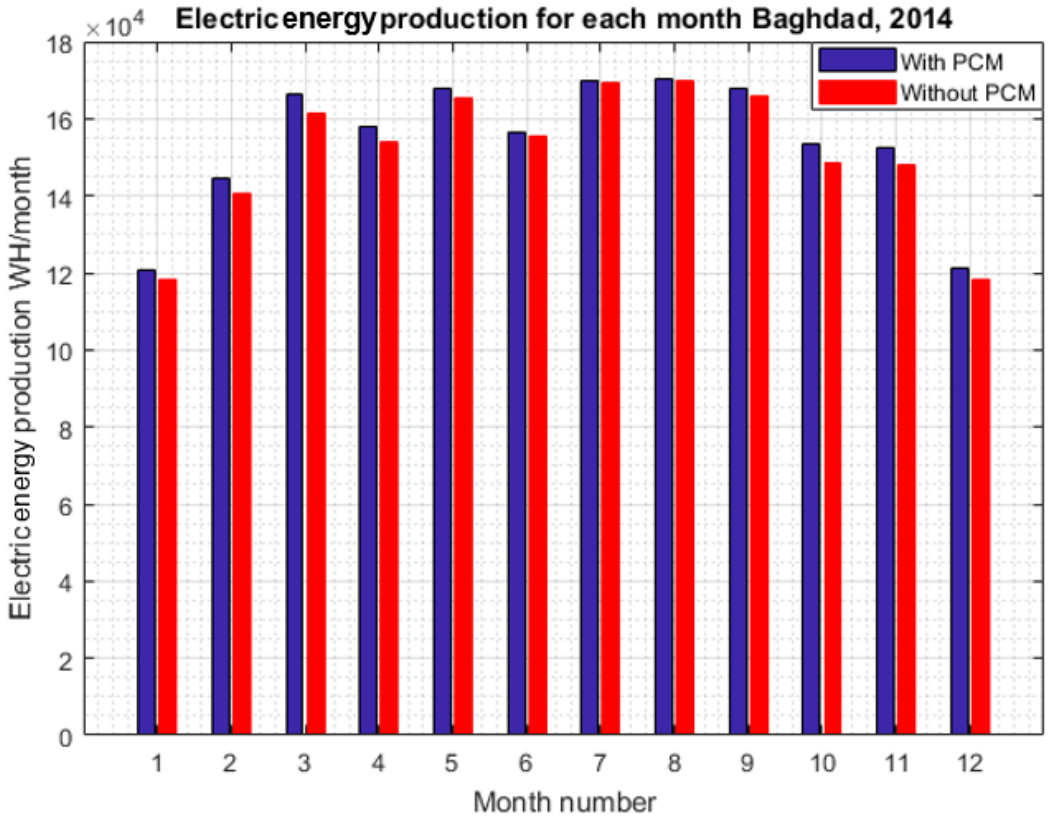

Figure 6-5: The estimated electrical energy output for the PV-PCM and stand-alone PV panel – Baghdad, 2014.

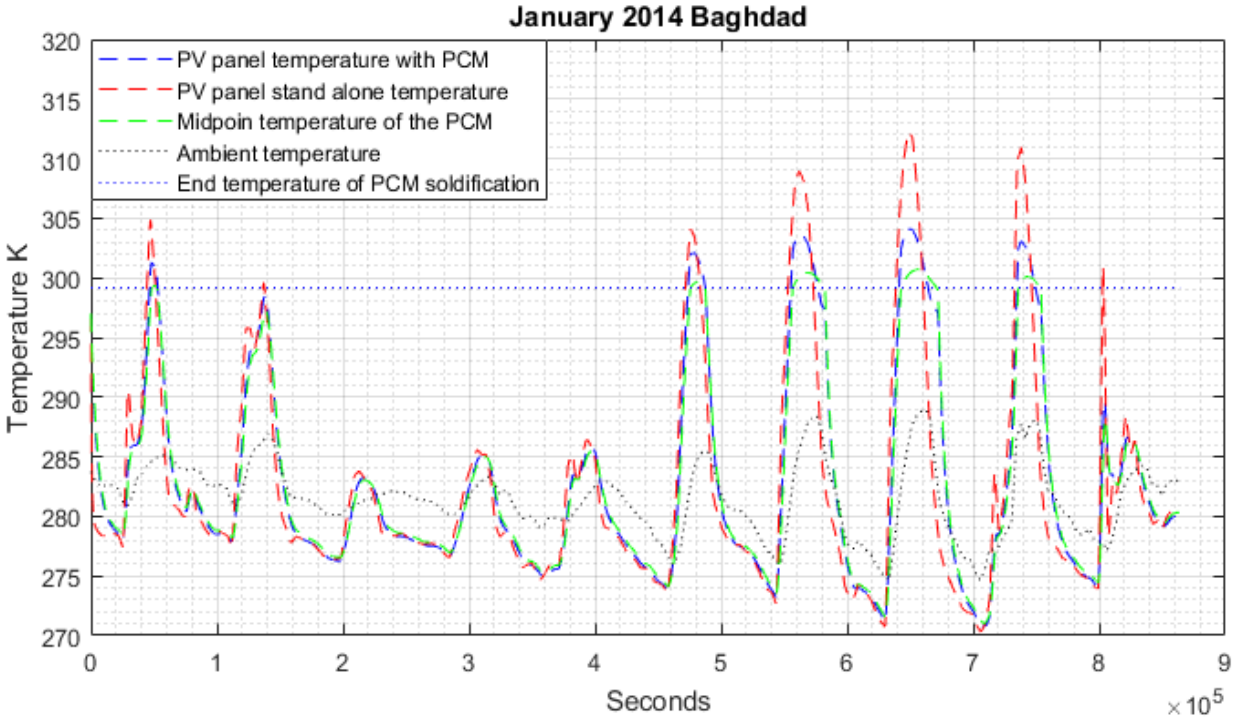

Figure 6-6: Temperature trends for the PV-PCM, stand-alone PV panel and ambient for the first ten days of January – Baghdad, 2014.

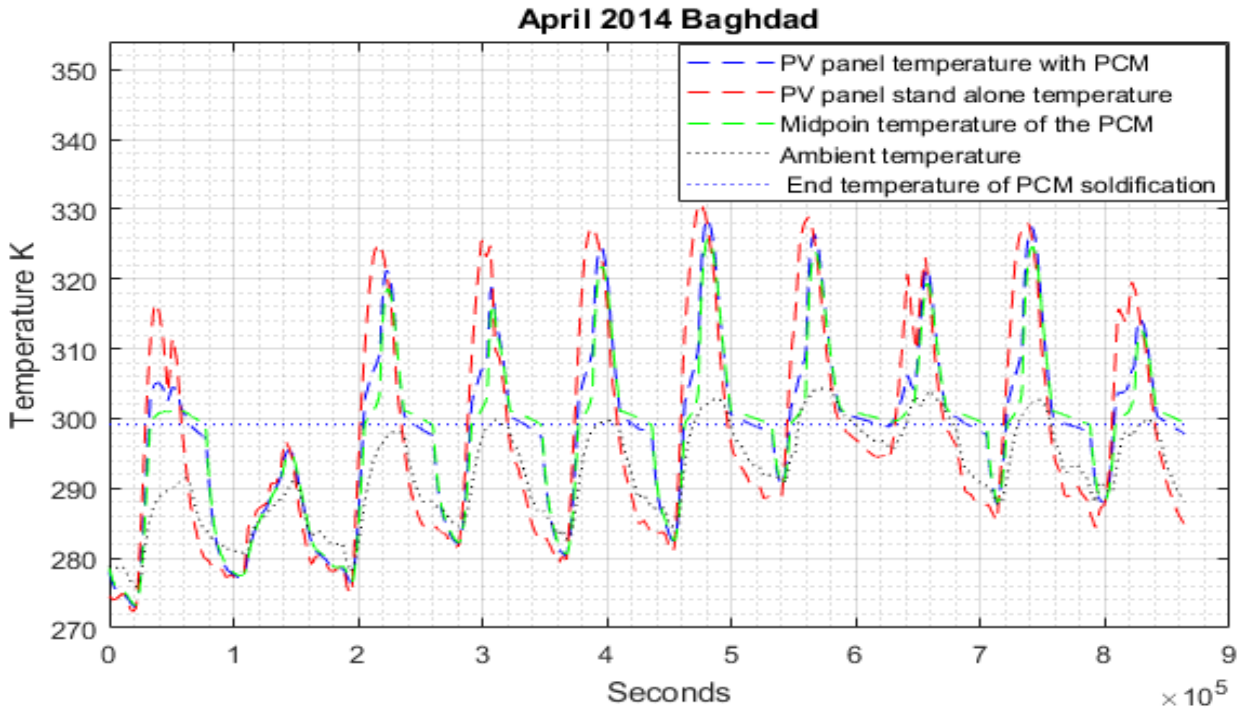

Figure 6-7: Temperature trends for the PV-PCM, stand-alone PV panel and ambient for the first ten days of April – Baghdad, 2014.

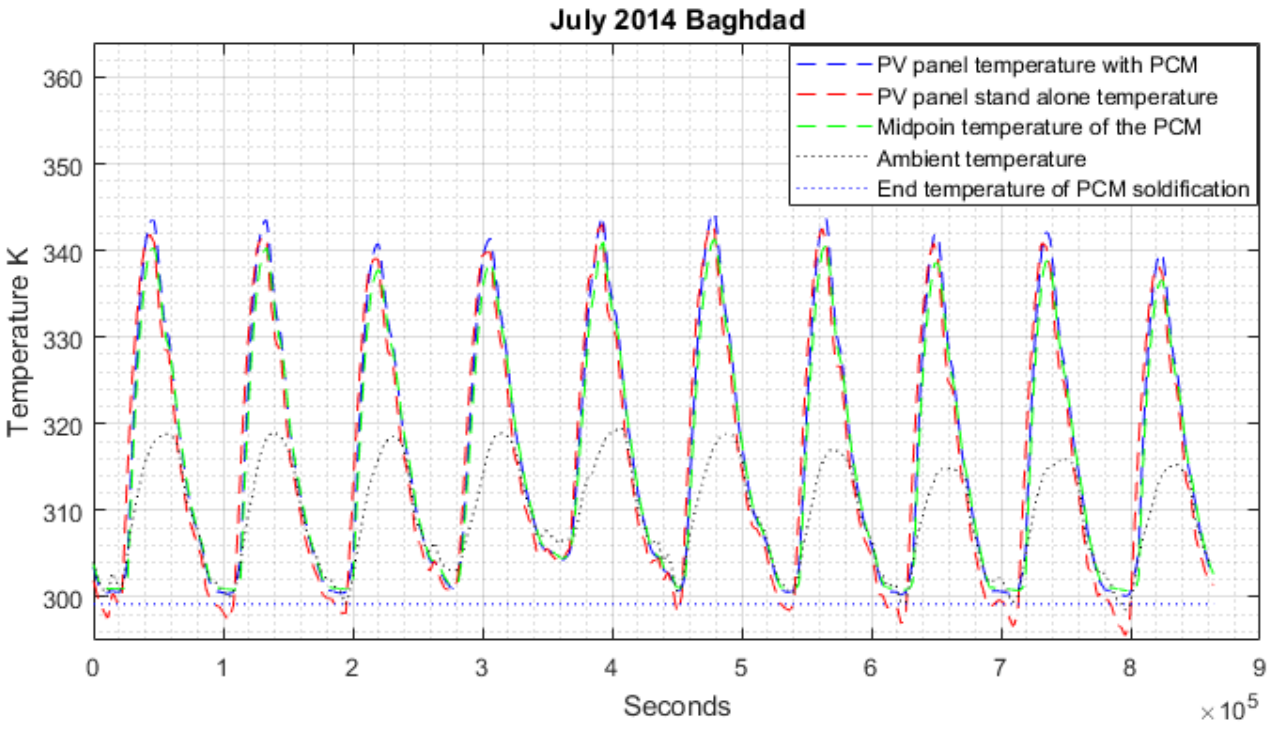

Figure 6-8: Temperature trends for the PV-PCM, stand-alone PV panel and ambient for the first ten days of July – Baghdad, 2014.

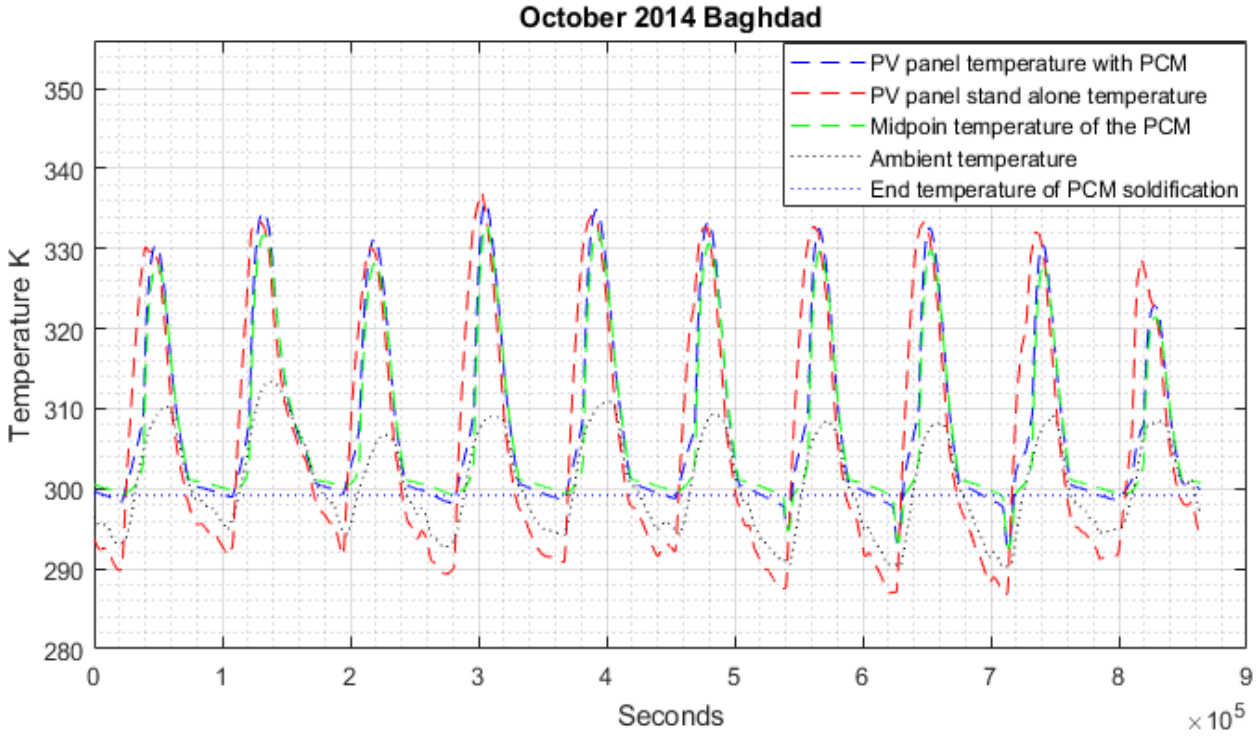

Figure 6-9: Temperature trends for the PV-PCM, stand-alone PV panel and ambient for the first ten days of October – Baghdad, 2014.

6.2.6 Milan

This section studies the impact of the composite paraffin-PCM on the electrical energy output of the PV panel in Milan. In this section the same procedures detailed in section 6.2.5 have been used. The ambient temperature, wind speed and solar radiation from the SoDa HelioClim-3 v5 (SoDA, 2019) for Milan have been downloaded and used. The results are presented in Figure 6-10. The electrical energy output for the 1 kW PV panels attached to PCM and for the stand-alone PV panel are 1648 kWh and 1609.4 kWh per year, respectively, with an enhancement rate of 2.39%, while using the PCM with a PV panel in Baghdad has increased the energy by 1.96%.

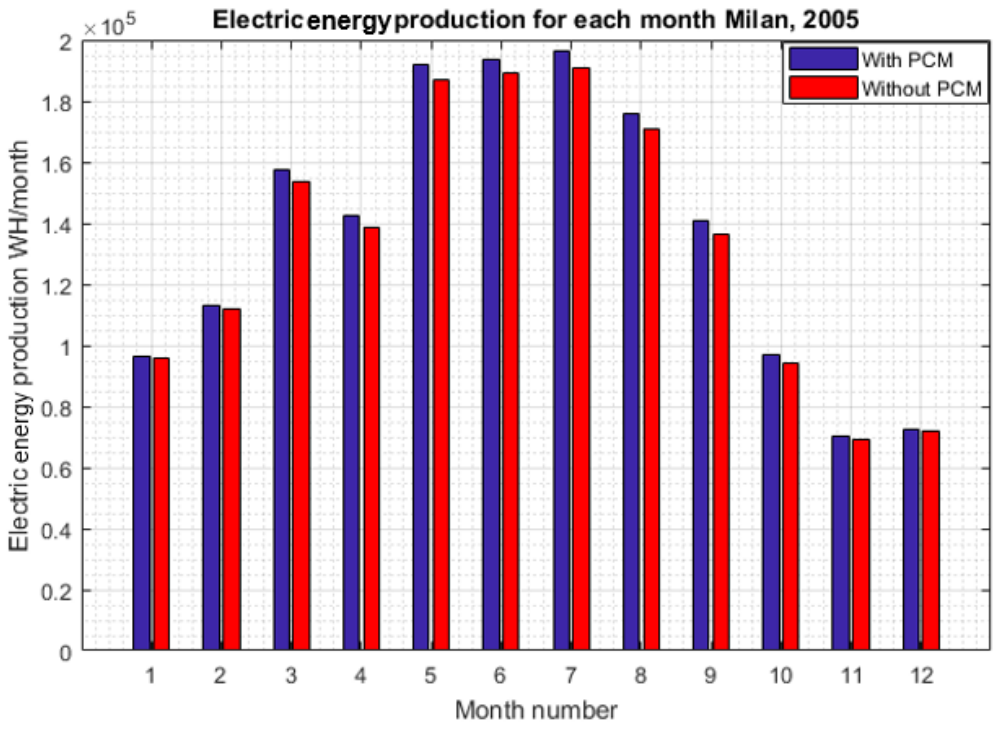

Figure 6-10: The estimated electrical energy output for the PV-PCM and stand-alone PV panel – Milan 2005.

The impact of the composite paraffin-PCM on the temperature of the PV panel for the first ten days of January, April, July and October are presented in Figure 6-11, Figure 6-12, Figure 6-13 and Figure 6-14, respectively. The y-axis represent the temperature in degrees kelvin, and the x-axis represent the time in seconds to the energy of 10^5. In each figure, the blue dashed line, the red dashed line, the green dashed line, the blue dotted line and the black dotted line represent the temperatures of the PV panel in the PV-PCM system, the stand-alone PV panel, the mid-PCM node, the solidification of the PCM and the ambient temperature, respectively.

In January, the temperature of the PV panel attached to PCM sometimes exceeds the melting temperature of the PCM for short time, as shown in Figure 6-11. Therefore, the PCM does not melt completely, and there is no significant temperature difference between the PV panel attached to PCM and the stand-alone PV panel. As a result of this, the electrical energy production from the PV panel attached to PCM is slightly more than the electrical energy produced from the stand-alone PV panel, as illustrated in Figure 6-10. While in April and October, the temperatures of the PV panel attached to PCM sometimes exceed the PCM melting temperature by about 20 K as shown in Figure 6-12 and Figure 6-14, respectively. Therefore, during these two months, the electrical energy of the PV panel attached to PCM is more than that of the stand-alone PV panel, as shown in Figure 6-10. In Milan, the most significant impact of this composite paraffin-PCM on the PV panel output was in July, as shown in Figure 6-10. This is a result of melting all the PCM during the day, and at night the PCM solidified completely, as shown in Figure 6-13. This is illustrated by the temperature of the midpoint of the PCM, which is represented by the green dashed line, which exceeds the melting temperature during the day and then at night decreases below the PCM melting temperature.

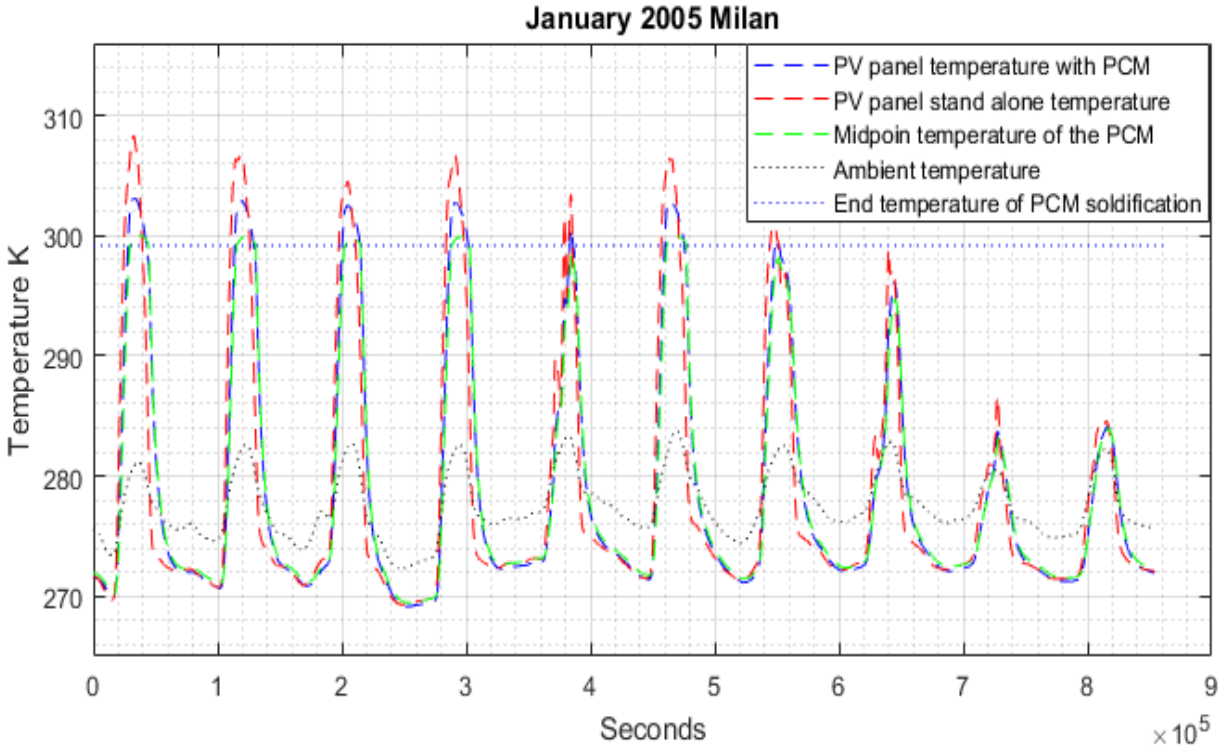

Figure 6-11: Temperature trends for the PV-PCM, stand-alone PV panel and ambient for the first ten days of October – January, 2005.

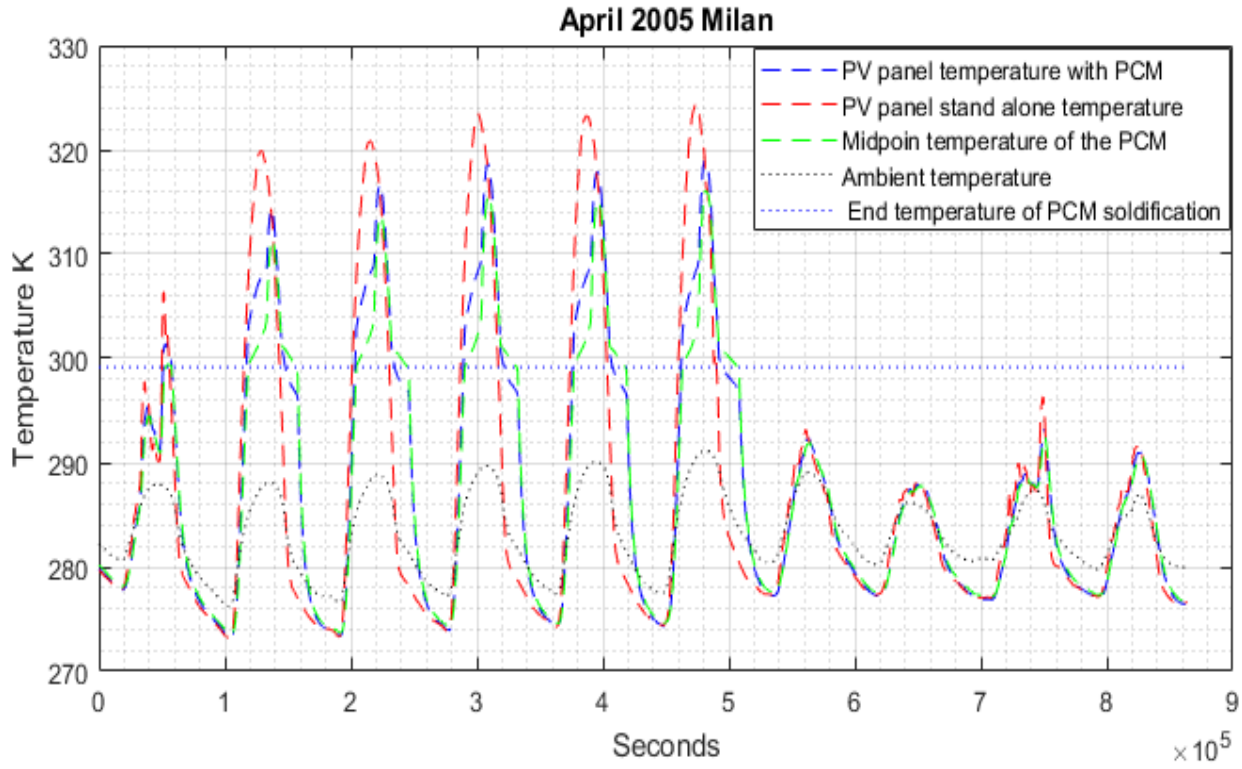

Figure 6-12: Temperature trends for the PV-PCM, stand-alone PV panel and ambient for the first ten days of April – Milan, 2005.

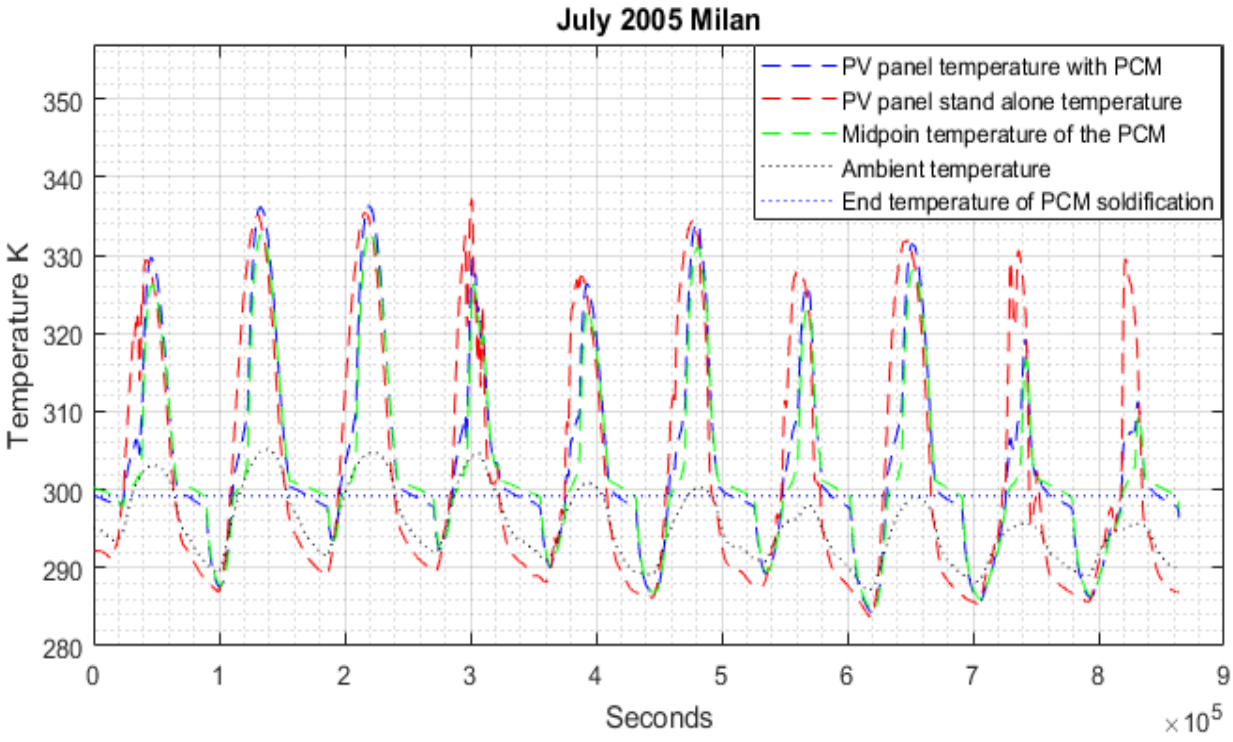

Figure 6-13: Temperature trends for the PV-PCM, stand-alone PV panel and ambient for the first ten days of July – Milan, 2005.

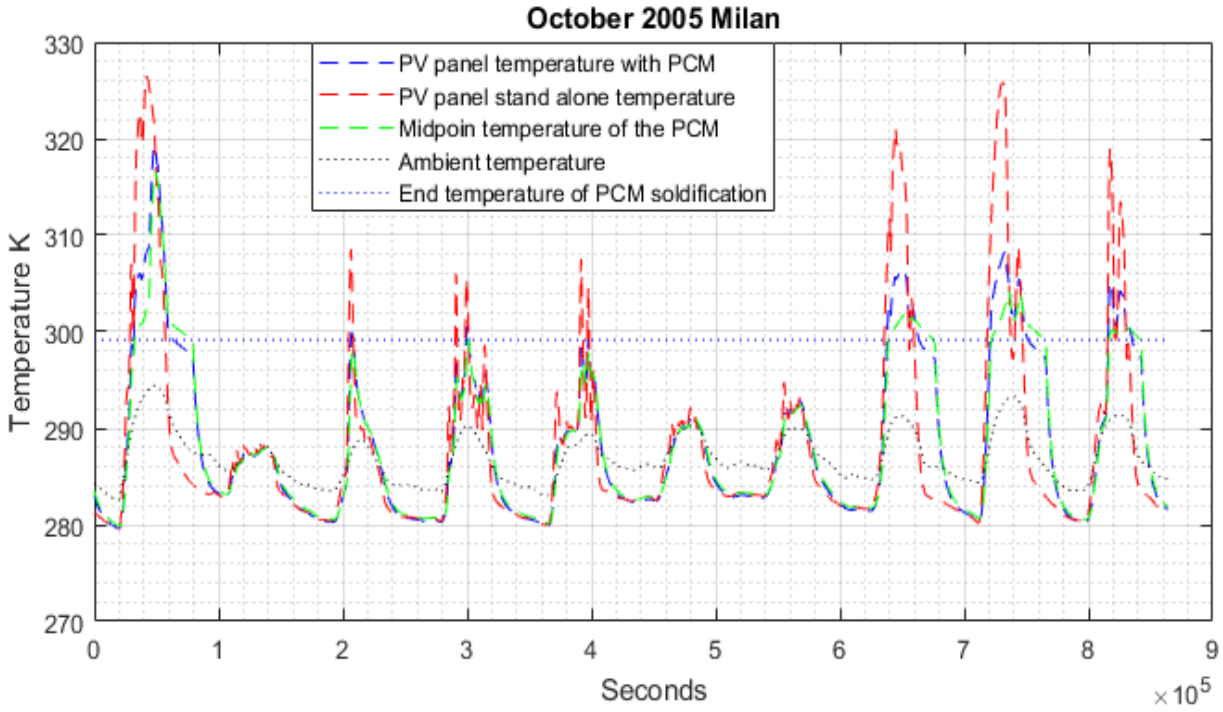

Figure 6-14: Temperature trends for the PV-PCM, stand-alone PV panel and ambient for the first ten days of October – Milan, 2005.

6.3 Conclusion

This chapter has presented the main sources of solar radiation. Two resources have been chosen in this study. The first used the SoDa for the Milan case study; the second resource is the observed data measured for horizontal surfaces in the Baghdad case study. Next, a mathematical model was presented to calculate solar radiation for an inclined surface based on the observed solar radiation for a horizontal surface. Then, the MATLAB algorithms for the mathematical models: the stand-alone PV panel and the lumped-distributor model for the PV-PCM system from Chapter 5 were used. These models have been used to investigate the impact of using 5 cm of the composite paraffin-PCM on the temperature and the electrical output of the PV panel in Baghdad and Milan for one year with time intervals of 100 seconds. The results have indicated that using composite paraffin-PCM could increase the year-round electrical energy output by 1.96% and 2.39% in Baghdad and Milan, respectively. In addition, the results have shown that the melting temperature of the PCM is very important. The composite paraffin-PCM could have a significant impact on the electrical output of the PV panel. If the PV panel temperature exceeds the melting temperature during the day and the PCM melts completely, then at night it decreases below the melting temperature and solidifies completely, such as in July in Milan.

Chapter Seven The impact of the Foam-PCM On The PV Panel

7.1 Outline

This chapter presents the procedures and results of the two main contributions in this PhD study. Firstly, in order to find the best PCM type with the optimal thickness to produce the maximum electrical energy from the PV panel, a range of the PCMs with thermophysical properties was collected. Then the impact of each PCM (with varying thicknesses) on the annual electrical output of the PV panel was investigated. Secondly, a model to predict the thermophysical properties of PCMs with metal foams was implemented. This chapter will then go on to present the impact of the different PCMs, with different Al foam percentages and different thicknesses, on the annual performance of PV panels in Baghdad and Milan.

7.2 PCM types

The most useful PCMs for cooling PV panels should have a suitable melting temperature, which could range from 10 ^{0}C to 60 ^{0}C. According to the literature, there are a few PCMs that can be used to cool down the PV panels. However, important information about these PCMs is not discussed, such as the maximum operating temperature, density and thermal conductivity for both solids and liquids. Therefore, this section presents data about the PCMs which have melting temperatures between 10 ^{0}C to 60 ^{0}C. This information has been from literature papers that discuss PV-PCM modules, PCM-thermal building management, PCM-cooling electronic devices and company data-sheets. This information is tabulated in **Table 7** and was the key data used to build the PV-PCM model.

These PCMs can be classified based on material into: organic, inorganic and eutectic (Shah, 2018), as illustrated in Figure 7-1. The organic PCMs can be further classified into fatty-acids and paraffin. The main advantages of the organic PCMs are that they are stable, available in a wide melting-temperature range and have high latent heat. However, organic PCMs do have low thermal conductivity (Jaguemont et al., 2017). The inorganic PCMs can be divided into hydrated salt, molten salt and others. These PCMs have a higher thermal conductivity and a

lower cost when compared with organic PCMs. However, inorganic PCMs are corrosive and not stable.

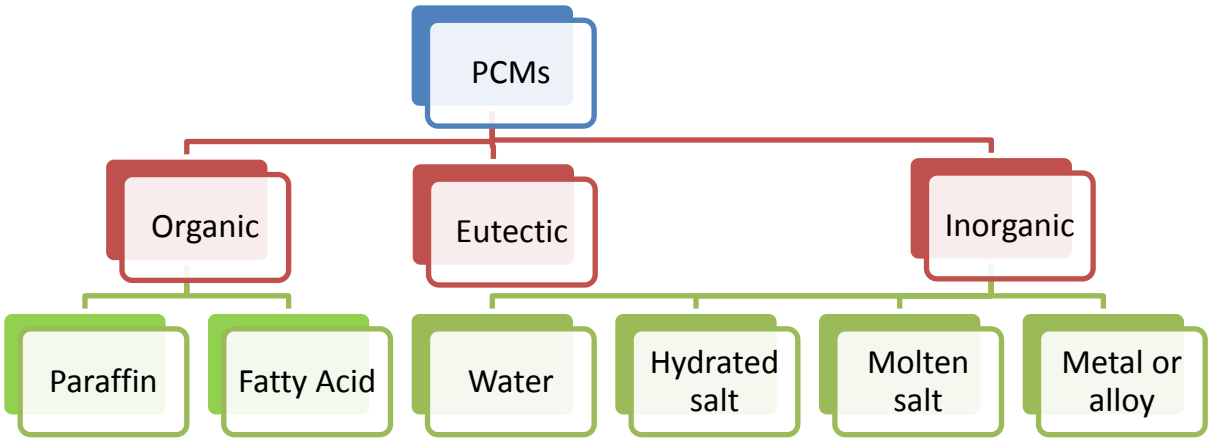

Figure 7-1: PCMs categories

Table 7 shows the information about the some PCMs. This information includes the PCM type, the melting temperature, the latent heat capacity, the flash point temperature, the maximum operating temperature, the density, the heat capacity and the thermal conductivity. However, it can be seen from **Table 7**, there are some data missing for some products. Thus, if the some properties mentioned to the either solid or liquid phase, they will be considered for the both phases.

Table 7: The thermosphysical properties of PCMs.

NO.	PCM	Type	Melting temperature ^{0}C	Flash point temperature 0C	Maximum Operating Temperature 0C	Latent heat capacity kJ kg-1	Density kg m^{-3}		Specific heat kJ kg^{-1}K^{-1}		Thermal Conductivity W m^{-1}K^{-1}	
							solid	liquid	solid	liquid	solid	liquid
1	n-Hexadecane (Koschenz and Lehmann, 2004)	Paraffin (CH3–(CH2)14–CH3)	18			236	780		1.650	2.100	0.17	
2	RT25 (Weinläder et al., 2005)	Paraffin	25			147	804	763	2.9	2.1	0.19	0.17
3	n-octadecane (Kuznik et al., 2011)	Paraffin (CH3–(CH2)16–CH3)	27			243.5	870	750 (Cui et al., 2017)	1.934	2.196	0.358	0.148
4	A32 (Products, 2013)	organic	32		300	130	845		2.20		0.21	
5	Paraffin RT44HC (Mazraeh et al., 2018)	Paraffin	41–45			255	780	760	2.0	2.0	0.2	0.2
6	OM32 (Pluss, 2018)	organic	33	160	120	187	926	870	3.2	2.81	0.219	0.145
7	OM35 (Pluss, 2018)	organic	35	200	120	202	969	870	2.57	2.78	0.20	0.16
8	A36 (Products, 2013)	organic	36		300	217	790		2.37		0.104	
9	OM37 (Pluss, 2018)	organic	37	200	120	231	973	860	2.55	2.63	0.16	0.13
10	A40 (Products, 2013)	organic	40		300	230	810		2.43		0.18	
11	A43 (Products, 2013)	organic	43		300	165	780		2.37		0.18	
12	A44 (Products, 2013)	organic	44		300	242	805		2.15		0.18	
13	OM42 (Pluss, 2018)	organic	44	200	120	221	903	863	2.71	2.78	0.19	0.1
14	A48 (Products, 2013)	organic	48		300	234	810		2.85		0.18	
15	OM46 (Pluss, 2018)	organic	48	200	120	196	917	880	2.5	2.7	0.20	0.10
16	A50 (Products, 2013)	organic	50		300	218	810		2.15		0.18	
17	OM48 (Pluss, 2018)	organic	51	200	120	172	960	875	2.02	2.35	0.20	0.10
18	OM50 (Pluss, 2018)	organic	51	200	120	223	961	859	3.33	2.78	0.21	0.14
19	OM55 (Pluss, 2018)	organic	55	200	120	208	935	841	2.68	2.76	0.16	0.1
20	A55 (Products, 2013)	organic	55		300	135	905		2.22		0.22	
21	S27 (Weinläder et al., 2005)	Hydrate salt (CaCl2.6H2O)	27			190	1700	1530	1.50	2.22	0.79	0.48
22	L30 (Weinläder et al., 2005)	Hydrate salt (LiNO3.3H2O)	30			270	1556	1400	1.23	1.79	1.02	0.56
23	S44 (Products, 2013)	Hydrate salt	44		120	100	1584		1.61		0.43	
24	S50 (Products, 2013)	Hydrate salt	50		120	100	1601		1.59		0.430	
25	C58 (climsel, 2018)	Hydrate salt	55			260	1400				0.57	0.47
26	S58 (Products, 2013)	Hydrate salt	58		120	145	1505		2.55		0.69	
27	Acetic Acid (Mukherjee, 2018)	eutectic mixtures	17			192	1214	1378	1.33	2.04	0.26	0.19
28	Lauric acid (Mukherjee, 2018)	eutectic mixtures	44			212	1007	1144	2.02	2.15	0.22	0.15
29	FS30 (Khanna et al., 2018, Pluss, 2018)	eutectic mixtures	31	200	120	172	1058	960	2.46	2.77	0.34	0.496

7.3 Optimum design for PV-PCM system

This section will investigate how to find the best PCM for each city. The procedures used in the investigation are illustrated in Figure 7-2 and a MATLAB code was built to implement these procedures. The main data required was imported to MATLAB. The first loop (H loop) was started, which included all the PCM types from Figure 7-2. The first PCM was chosen and the thermophysical properties imported. If some of the properties of a PCM were only mentioned for the solid or liquid phase, it was considered for both. The second loop (A loop) was then started, which represented different PCM thicknesses. For each PCM thickness, the annual electrical production was calculated and compared with the maximum energy production. If the current energy production was more than the recorded maximum energy, the current energy production was saved as the maximum energy and the PCM type, with PCM thickness, was recorded. Then, the PCM thickness was increased until the end of A loop was reached. After that, the type of PCM changed until the end of the H loop. This investigation was executed for both Baghdad and Milan.

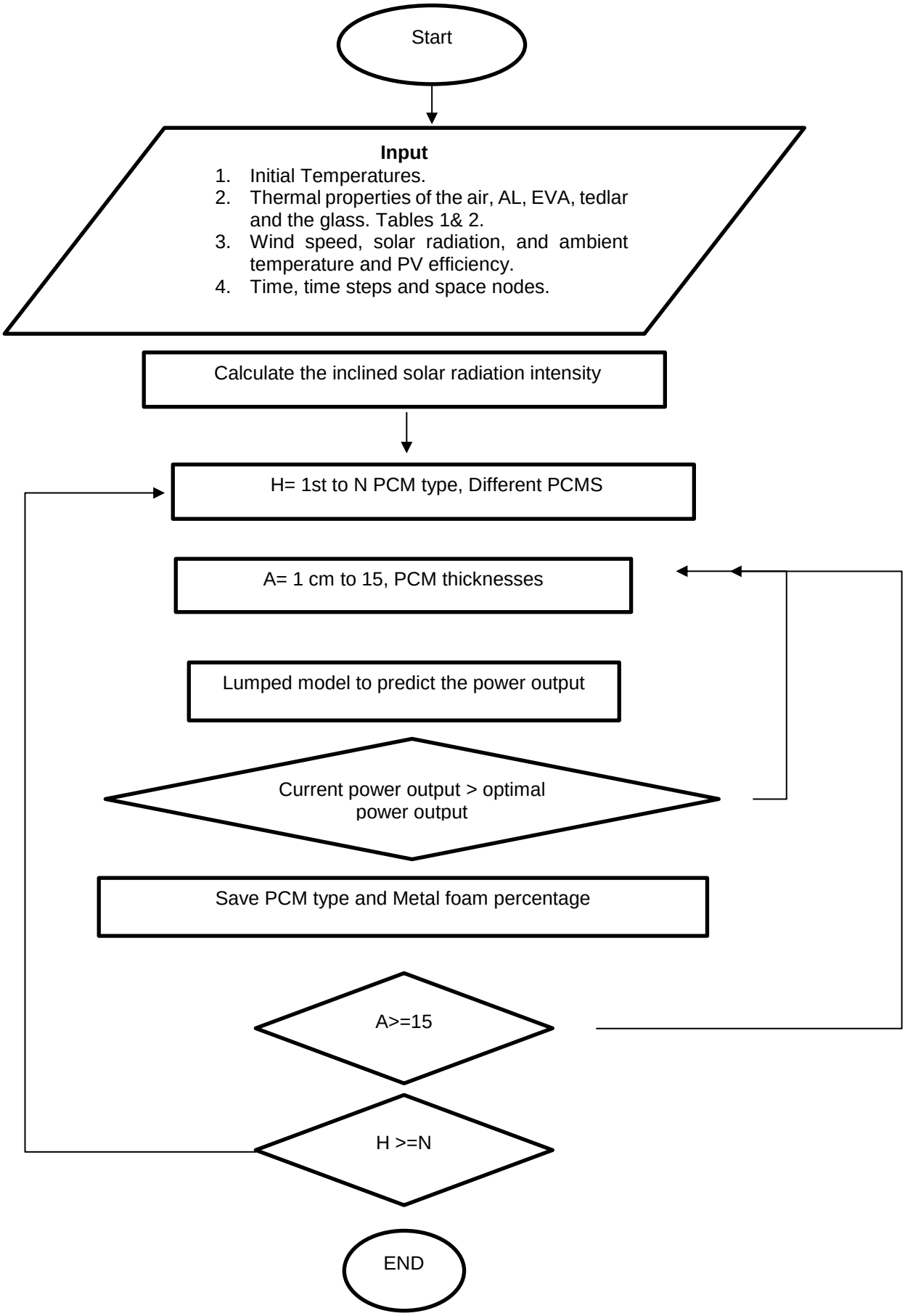

Figure 7-2: The procedure to find the best PCM for each city.

7.3.1 Baghdad

The results of the optimisation for Baghdad are illustrated in **Figure 7-3**, where the x-axis represents the number of the PCM according to **Table 7**, and the y-axis represents the ratio of the electrical energy produced from the PV panel attached to the PCM, divided by the electrical energy produced from the PV panel when stand-alone. Each line with different colours represents a specific thickness, starting from 1 cm up to 15 cm. In addition, the results for each thickness and each PCM are listed in **Table 8**.

It can be seen from **Figure 7-3** and **Table 8** that the maximum ratio is 1.003 for PCM number 29 with 2 cm thickness, which means that the maximum enhancement is 0.3%. The main features for this PCM are that its thermal conductivity is high and the melting temperature is 31^{o}C. It can also be seen that the PCM number 22 has a positive impact for first two thicknesses only, but it is lower than the impact of the PCM number 29. The rest of the PCMs have a negative impact due to low thermal conductivity. This as a result of the thermal resistance generated by adding a PCM.

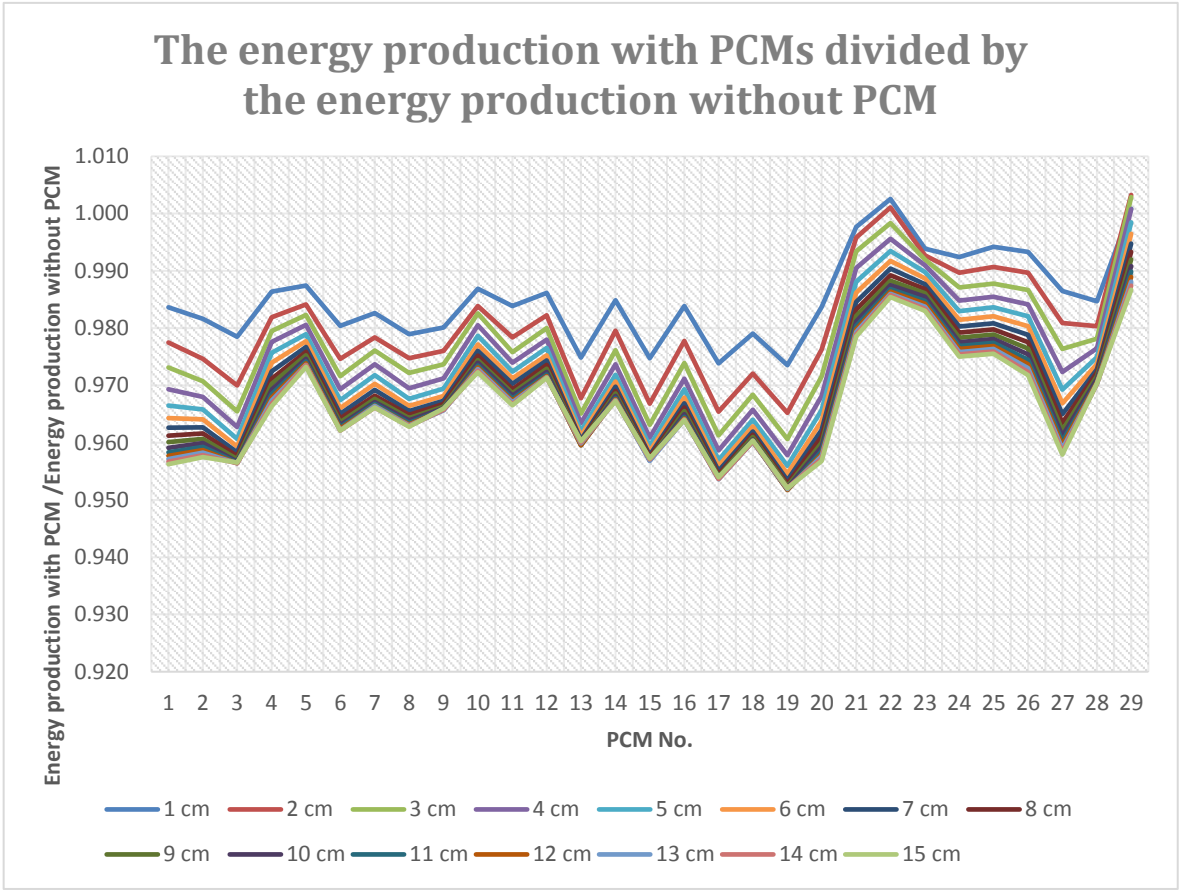

Figure 7-3: The annual impact of the different PCMs with different thicknesses on the electrical energy output of the PV panel, Baghdad.

Table 8 : The ratio of electrical energy output for whole year with PCM / Electrical energy output for whole year without PCM Baghdad.

PCM No.	PCM thicknesses														
	1 cm	2 cm	3 cm	4 cm	5 cm	6 cm	7 cm	8 cm	9 cm	10 cm	11 cm	12 cm	13 cm	14 cm	15 cm
	Electric energy output with PCM / Electric energy output without PCM Baghdad, for whole year														
1	0.984	0.977	0.973	0.969	0.966	0.964	0.963	0.961	0.960	0.959	0.958	0.958	0.957	0.957	0.956
2	0.982	0.975	0.971	0.968	0.966	0.964	0.963	0.962	0.961	0.960	0.959	0.959	0.958	0.958	0.957
3	0.979	0.970	0.965	0.963	0.961	0.959	0.958	0.958	0.957	0.957	0.957	0.956	0.956	0.956	0.957
4	0.986	0.982	0.980	0.978	0.976	0.974	0.972	0.971	0.970	0.969	0.968	0.968	0.967	0.967	0.966
5	0.987	0.984	0.982	0.981	0.979	0.978	0.977	0.976	0.975	0.975	0.974	0.974	0.974	0.973	0.973
6	0.980	0.975	0.972	0.969	0.967	0.966	0.965	0.964	0.964	0.963	0.963	0.962	0.962	0.962	0.962
7	0.983	0.978	0.976	0.974	0.972	0.970	0.969	0.968	0.968	0.967	0.967	0.966	0.966	0.966	0.966
8	0.979	0.975	0.972	0.969	0.968	0.966	0.966	0.965	0.964	0.964	0.963	0.963	0.963	0.963	0.963
9	0.980	0.976	0.974	0.971	0.969	0.968	0.967	0.967	0.966	0.966	0.966	0.966	0.966	0.966	0.966
10	0.987	0.984	0.983	0.981	0.979	0.977	0.976	0.975	0.974	0.974	0.973	0.973	0.973	0.973	0.972
11	0.984	0.978	0.976	0.974	0.972	0.971	0.970	0.969	0.969	0.968	0.968	0.967	0.967	0.967	0.967
12	0.986	0.982	0.980	0.978	0.977	0.975	0.974	0.974	0.973	0.972	0.972	0.972	0.971	0.971	0.971
13	0.975	0.968	0.965	0.963	0.962	0.961	0.960	0.960	0.960	0.960	0.960	0.960	0.960	0.960	0.960
14	0.985	0.980	0.976	0.974	0.972	0.971	0.970	0.969	0.969	0.968	0.968	0.968	0.967	0.967	0.967
15	0.975	0.967	0.963	0.961	0.959	0.958	0.958	0.957	0.957	0.957	0.957	0.957	0.957	0.957	0.957
16	0.984	0.978	0.974	0.971	0.969	0.968	0.967	0.966	0.965	0.965	0.965	0.964	0.964	0.964	0.964
17	0.974	0.965	0.961	0.959	0.957	0.956	0.955	0.954	0.954	0.954	0.954	0.954	0.954	0.954	0.954
18	0.979	0.972	0.968	0.966	0.964	0.963	0.962	0.961	0.961	0.961	0.960	0.960	0.960	0.960	0.960
19	0.974	0.965	0.961	0.958	0.956	0.955	0.953	0.953	0.952	0.952	0.952	0.952	0.952	0.952	0.952
20	0.984	0.976	0.972	0.968	0.966	0.964	0.962	0.961	0.960	0.959	0.959	0.958	0.958	0.957	0.957
21	0.998	0.996	0.993	0.991	0.988	0.986	0.985	0.983	0.982	0.981	0.980	0.980	0.979	0.979	0.979
22	1.003	1.001	0.998	0.996	0.993	0.992	0.990	0.989	0.988	0.988	0.987	0.986	0.986	0.986	0.985
23	0.994	0.993	0.992	0.991	0.990	0.989	0.988	0.987	0.986	0.985	0.985	0.984	0.984	0.983	0.983
24	0.992	0.990	0.987	0.985	0.983	0.981	0.980	0.979	0.978	0.978	0.977	0.976	0.976	0.975	0.975
25	0.994	0.991	0.988	0.985	0.984	0.982	0.981	0.980	0.979	0.978	0.977	0.977	0.976	0.976	0.976
26	0.993	0.990	0.987	0.984	0.982	0.980	0.979	0.978	0.976	0.975	0.974	0.974	0.973	0.972	0.972
27	0.986	0.981	0.976	0.972	0.969	0.967	0.965	0.963	0.962	0.961	0.960	0.960	0.959	0.958	0.958
28	0.985	0.980	0.978	0.976	0.975	0.974	0.973	0.972	0.972	0.971	0.971	0.970	0.970	0.970	0.970
29	1.001	1.003	1.003	1.001	0.998	0.996	0.995	0.993	0.992	0.991	0.990	0.989	0.988	0.987	0.987

7.3.2 Milan

The results of the annual impact of different PCMs with different thicknesses on the electrical energy output of the PV panel are revealed in

Figure 7-4 and Table 9. The result of the optimisation shows that the best PCM is number 22 (in Table 7) with a 3 cm thickness. The maximum annual enhancement is 0.5%. The main properties of the best PCM for Milan is a melting temperature of 30°C and with a high thermal conductivity when compared to the other PCMs in Table 7.

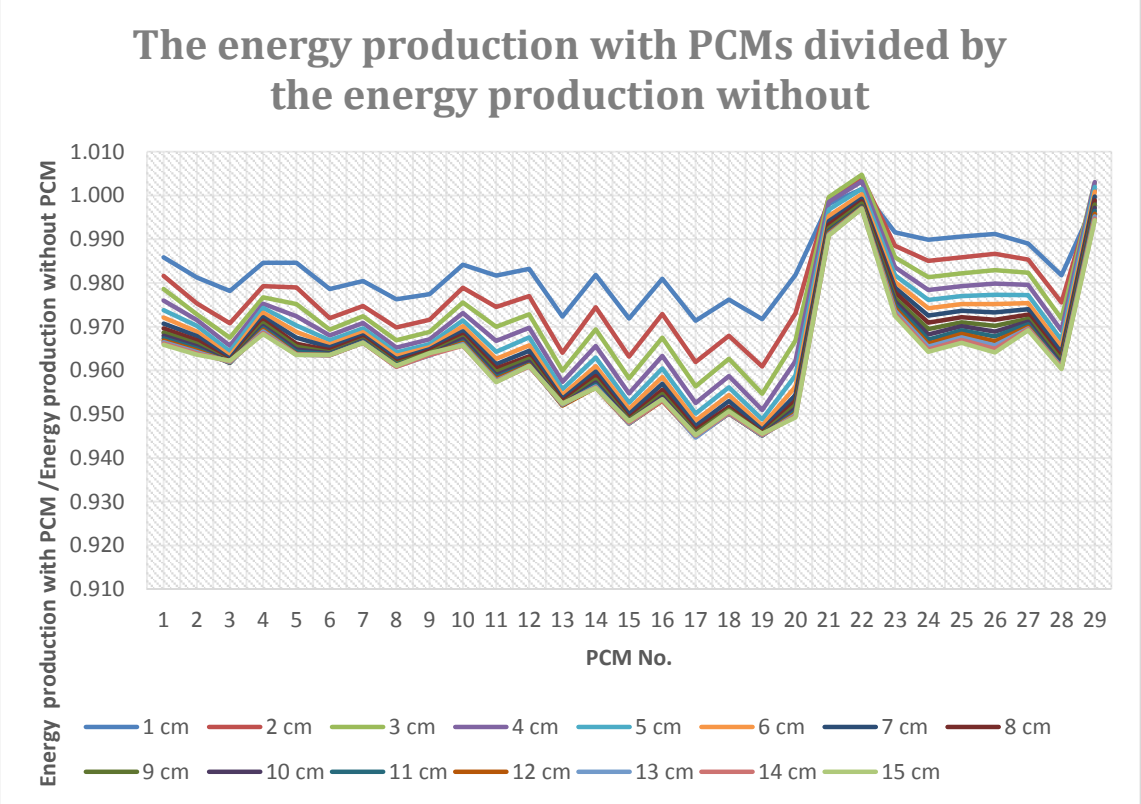

Figure 7-4: The annual impact of the different PCMs with different thicknesses on the electrical energy output of the PV panel, Milan.

Table 9: The ratio of electrical energy output for whole year with PCM / Electrical energy output for whole year without PCM Milan.

PCM No.	PCM thicknesses														
	1 cm	2 cm	3 cm	4 cm	5 cm	6 cm	7 cm	8 cm	9 cm	10 cm	11 cm	12 cm	13 cm	14 cm	15 cm
	Electric energy output with PCM / Electric energy output without PCM Baghdad, for whole year														
1	0.986	0.982	0.979	0.976	0.974	0.972	0.971	0.970	0.969	0.968	0.967	0.967	0.966	0.966	0.966
2	0.981	0.975	0.973	0.971	0.970	0.969	0.968	0.967	0.966	0.965	0.965	0.965	0.964	0.964	0.964
3	0.978	0.971	0.968	0.966	0.964	0.963	0.963	0.962	0.962	0.962	0.962	0.962	0.962	0.962	0.962
4	0.985	0.979	0.977	0.975	0.974	0.973	0.972	0.971	0.971	0.970	0.970	0.969	0.969	0.969	0.968
5	0.985	0.979	0.975	0.972	0.970	0.969	0.968	0.966	0.965	0.965	0.964	0.964	0.964	0.964	0.964
6	0.979	0.972	0.969	0.968	0.967	0.966	0.965	0.965	0.964	0.964	0.964	0.964	0.963	0.963	0.964
7	0.980	0.975	0.972	0.971	0.970	0.969	0.968	0.967	0.967	0.967	0.967	0.966	0.966	0.966	0.966
8	0.976	0.970	0.967	0.965	0.964	0.963	0.963	0.962	0.962	0.961	0.961	0.961	0.961	0.961	0.961
9	0.977	0.972	0.969	0.967	0.966	0.965	0.965	0.964	0.964	0.964	0.963	0.964	0.963	0.964	0.964
10	0.984	0.979	0.976	0.973	0.971	0.970	0.969	0.968	0.968	0.967	0.967	0.966	0.966	0.966	0.966
11	0.982	0.975	0.970	0.967	0.964	0.963	0.961	0.960	0.960	0.959	0.958	0.958	0.958	0.957	0.957
12	0.983	0.977	0.973	0.970	0.968	0.966	0.964	0.963	0.963	0.962	0.961	0.961	0.961	0.961	0.961
13	0.972	0.964	0.960	0.957	0.956	0.954	0.954	0.953	0.952	0.952	0.952	0.952	0.952	0.952	0.952
14	0.982	0.974	0.969	0.966	0.963	0.961	0.960	0.959	0.958	0.957	0.957	0.956	0.956	0.956	0.956
15	0.972	0.963	0.958	0.955	0.953	0.951	0.950	0.949	0.949	0.948	0.948	0.948	0.948	0.948	0.948
16	0.981	0.973	0.967	0.963	0.960	0.958	0.957	0.956	0.955	0.954	0.953	0.953	0.953	0.953	0.953
17	0.971	0.962	0.956	0.953	0.950	0.949	0.947	0.946	0.946	0.945	0.945	0.945	0.945	0.945	0.945
18	0.976	0.968	0.963	0.959	0.956	0.954	0.953	0.952	0.951	0.950	0.950	0.950	0.950	0.950	0.951
19	0.972	0.961	0.955	0.951	0.949	0.947	0.946	0.946	0.945	0.945	0.945	0.945	0.945	0.945	0.946
20	0.982	0.973	0.967	0.962	0.959	0.956	0.954	0.953	0.952	0.951	0.951	0.950	0.950	0.950	0.949
21	0.998	0.999	1.000	0.999	0.997	0.995	0.994	0.993	0.993	0.992	0.992	0.991	0.991	0.991	0.991
22	1.001	1.004	1.005	1.003	1.002	1.000	0.999	0.999	0.998	0.998	0.997	0.997	0.997	0.997	0.997
23	0.992	0.988	0.986	0.984	0.982	0.980	0.979	0.978	0.977	0.976	0.975	0.974	0.974	0.973	0.972
24	0.990	0.985	0.981	0.978	0.976	0.974	0.973	0.971	0.969	0.968	0.967	0.966	0.965	0.965	0.964
25	0.991	0.986	0.982	0.979	0.977	0.975	0.974	0.972	0.971	0.970	0.969	0.968	0.968	0.967	0.966
26	0.991	0.987	0.983	0.980	0.977	0.975	0.973	0.972	0.970	0.969	0.968	0.967	0.966	0.965	0.964
27	0.989	0.985	0.982	0.980	0.977	0.975	0.974	0.973	0.972	0.971	0.971	0.970	0.970	0.969	0.969
28	0.982	0.976	0.972	0.969	0.967	0.965	0.964	0.963	0.962	0.961	0.961	0.961	0.961	0.961	0.960
29	0.998	1.001	1.003	1.003	1.002	1.001	1.000	0.999	0.998	0.997	0.997	0.996	0.995	0.995	0.994

7.3.3 Results analysis

It can be seen from Figure 7-3 and

Figure **7-4** that the worst impact on the annual PV panel electrical energy output is caused by three PCMs, number 15, 17 and 19. From **Table 7**, it can be seen that using PCMs with a low thermal conductivity lead to an increase in the PCM's thermal resistance. This thermal resistance is explained in **Figure 7-5**. This high PCM thermal resistance will need a high-temperature difference between the PV panel and the melting region to transfer the same heat flow when compared to other PCMs. This will lead to the temperature of the PV panel being high, which causes a reduction in the PV panel efficiency. Therefore, to increase the thermal conductivity of the PCM, it would be better to investigate different PCMs with different metal foam percentages.

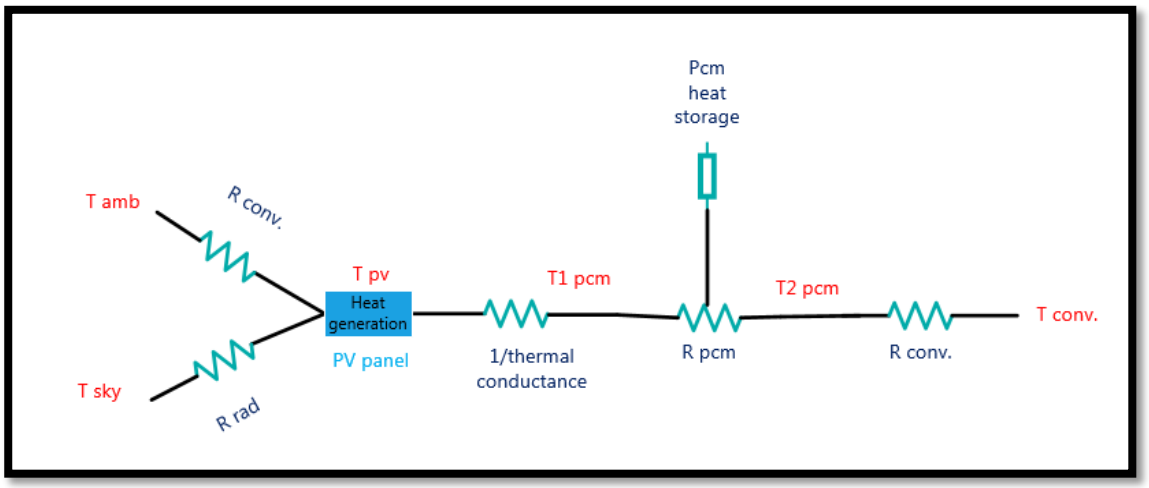

Figure 7-5: The thermal analysis of the PV-PCM system.

7.4 Optimum design for PV-PCM system-metal foam composite

In order to choose the best PCM type, one which has the optimal PCM thickness with the best ratio of AL foam, the impact of using a metal foam PCM composite on a PV panel's electrical output for a whole year has been investigated based on two cities: Baghdad and Milan. The PCM assumed will combined with metal foam when it melt. Firstly, the thermophysical properties and formula of the PCM metal foam have been presented and used based on the available literature.

Then different percentages of metal foam have been used. Secondly, the optimum design for PV-PCM metal foam has been investigated using the procedure in section 7.3 for each percentage of metal foam. Finally, the results are presented and discussed.

7.4.1 The thermophysical properties of the PCM-metal foam

It can be seen from **Table 7** that the maximum thermal conductivity for pure PCMs is 1.02 $W\ m^{-1}K^{-1}$, which is very low. Therefore, several sets of research in the literature have developed different techniques to increase the thermal conductivity of PCMs. These techniques depend on nanoparticles, fins, expanded graphite and metal foams (Qureshi et al., 2018). The metal foam techniques will be used in this study. Information about PCMs with metal foam enhancement techniques is collected in Table 10.

Table 10: The thermos-physical properties of composite PCM-Metal foam

PCM	Additive Type	Melting temperature ^0C	porosity ratio	Latent heat capacity kJ kg-1	Density kg m^{-3}		Specific heat kJ $kg^{-1}K^{-1}$		Thermal Conductivity W $m^{-1}K^{-1}$	
					solid	liquid	solid	liquid	solid	liquid
Paraffin (Xiao et al., 2013)	nickel foam	60–62	97.28 %	182.4	914	769	1.59	1.802	1.2	
Paraffin (Qureshi et al., 2018)	nickel foam		97%					1.16		
Paraffin (Wang et al., 2016)	copper foam	42.24	97.3%	170.4					3.11	
Paraffin (Xiao et al., 2013)	copper foam	60–62	96.83 %	182.4	914	769	1.617	1.617	4.8	
Paraffin (Xiao et al., 2014)	copper foam		96.95 %		)CH_3–$(CH_2)_{16}$–CH_3				5.04	
Paraffin (Xiao et al., 2014)	copper foam		92.31 %						11.33	
Paraffin (Xiao et al., 2014)	copper foam		88.89 %						16.01	
Sodium acetate trihydrate	copper foam	56.75	92.4%	271.09			1.54		6.8	.

It can be seen from Table 10 that not all the thermophysical properties of the PCM-foam composite are available. In addition, within the literature there are a lot of PCMs, as mentioned in **Table 7** that have not been investigated with regards to their thermophysical properties with metal foam. Therefore, a formula will be used to predict the thermophysical properties of the PCM-metal foam composite based on the PCMs in **Table 7**.

Bhattacharya et al. (2002) investigated the effective thermal conductivity of fibre metal foam with fluid, air and water experimentally. The metal foam used was Al, as shown in **Figure 7-6**. Bhattacharya et al. (2002) presented a formula to predict the effective thermal conductivity of the fluid-metal foam composite. This formula has been investigated by Xiao et al. (2013) experimentally. They used paraffin as

a PCM with a copper and nickel metal foam. Their results, of effective thermal conductivity, show an acceptable agreement with Bhattacharya et al. (2002) formula. This formula is:

$$\lambda_e = A(\varepsilon_b \lambda_{PCM} + (1-\varepsilon_b)\lambda_{Metal}) + \frac{1-A}{\frac{\varepsilon_b}{\lambda_{PCM}} + \frac{(1-\varepsilon_b)}{\lambda_{Metal}}} \quad \textbf{7-1}$$

where, λ_e is the effective thermal conductivity, A represents the percentage of the metal foam in parallel with heat flow, ε_b is the volume porosity percentage of the foam metal and λ_{PCM} and λ_{Metal} represent the thermal conductivity of the PCM and the metal, respectively. For the porosity range (90.5%–97.8%), A can be represented by 35% (Xiao et al., 2013).

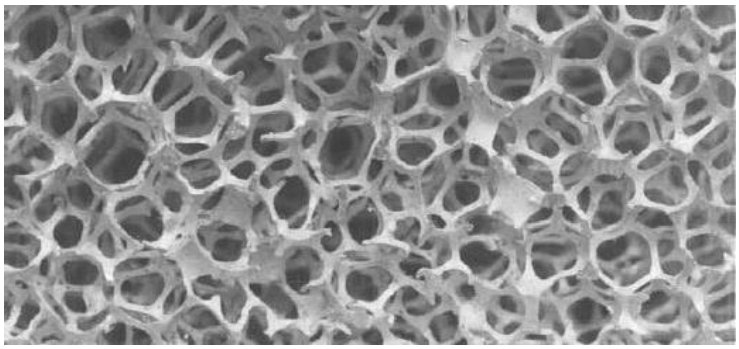

Figure 7-6: AL metal foam (Bhattacharya et al., 2002).

The density and the specific heat capacity of the PCM-metal foam composite can be calculated by the rule of mixture:

$$\rho_{comp} = \rho_{PCM} * \varepsilon_b + \rho_F * [1-\varepsilon_b] \quad \textbf{7-2}$$

$$C_{comp} = [\, C_{PCM} * \rho_{PCM} * \varepsilon_b + C_F * \rho_F * [1-\varepsilon_b] \,]/\rho_{comp} \quad \textbf{7-3}$$

where, ρ_{comp} is the density of the PCM-foam composite (kg m^{-3}), ρ_F is the density of the foam material (kg m^{-3}), C_{comp} is the specific heat capacity of the PCM-foam composite (J Kg^{-1} ^{0}C^{-1}) and C_F is the specific heat capacity of the foam (J Kg^{-1} ^{0}C^{-1}).

7.4.2 Results of optimum design for PV-PCM system-metal foam composite for Baghdad.

The impact of different Al foam percentages, with different PCMs and different thicknesses, on the annual electrical energy output of a PV panel have been investigated for Baghdad. The volume percentages of the Al foam are 3%, 4%, 5%, 6%, 7%, 8% and 9% and the results are revealed in Figure 7-7, Figure 7-8, Figure 7-9, Figure 7-10, Figure 7-11, Figure 7-12 and Figure 7-13 respectively. In these figures, the x-axis is the PCM number according to Table 7 and the y-axis is the energy ratio of electrical energy output for the PV panel attached to Al foam-PCM, divided by the electrical energy output for the PV panel when it is stand-alone. In these Figures, we present the results of different Al foam PCM thickness, from 1 cm to 15 cm. Each thickness is represented by a line. The results indicate that the best PCM is number 8, from Table 7, with 9% Al foam, a 15 cm thickness and with energy ratio of 1.0319. Based on this study, this means that the maximum annual electrical energy output enhancement for Baghdad is 3.19%. The main feature for this PCM is that the melting temperature is 36^{o}C.

However, it can be seen from Figure 7-7, Figure 7-8, Figure 7-9, Figure 7-10, Figure 7-11, Figure 7-12 and Figure 7-13 that when the thickness increased up to 7cm, the energy output ratio also increased significantly. While, when the Al foam PCM thickness increased from 7 cm to 15 cm, there is no considerable increase in the energy ratio. In addition, it can be seen from these figures that when the Al foam increased from 3 to 9 volume percentage, the energy ratio also increased, very slightly, by 0.21%, from 1.0297 to 1.0319 for the PCM number 8. In contrast, if Figure 7-3 is compared with Figure 7-7, it can be seen that the energy ratios for 15 cm of PCM number 8, both without Al foam and with 3% of Al foam, are 0.963 and 1.0297 respectively. This means that the energy ratio has increased by 6.61% by adding only 3% of Al foam.

From Figure 7-7, Figure 7-8, Figure 7-9, Figure 7-10, Figure 7-11, Figure 7-12 and Figure 7-13, it can be seen that the PCMs with melting temperatures near to 36^{o}C are better than the PCMs that have melting temperatures far from 36^{o}C. The melting temperatures for the PCMs number 1, 20, 25 and 26 are 18^{o}C, 55^{o}C, 55^{o}C and 58^{o}C respectively, and the energy ratios for these PCMs, are the lowest

among all of the 29 PCMs. The results take into account the ambient conditions, such as the wind speed, air temperature and the solar radiation intensity throughout a whole year. These conditions play a vital role in melting the PCM during the day or in solidifying it during the night, which impacts the cooling of the PV panel, which turns on PV panel electrical output.

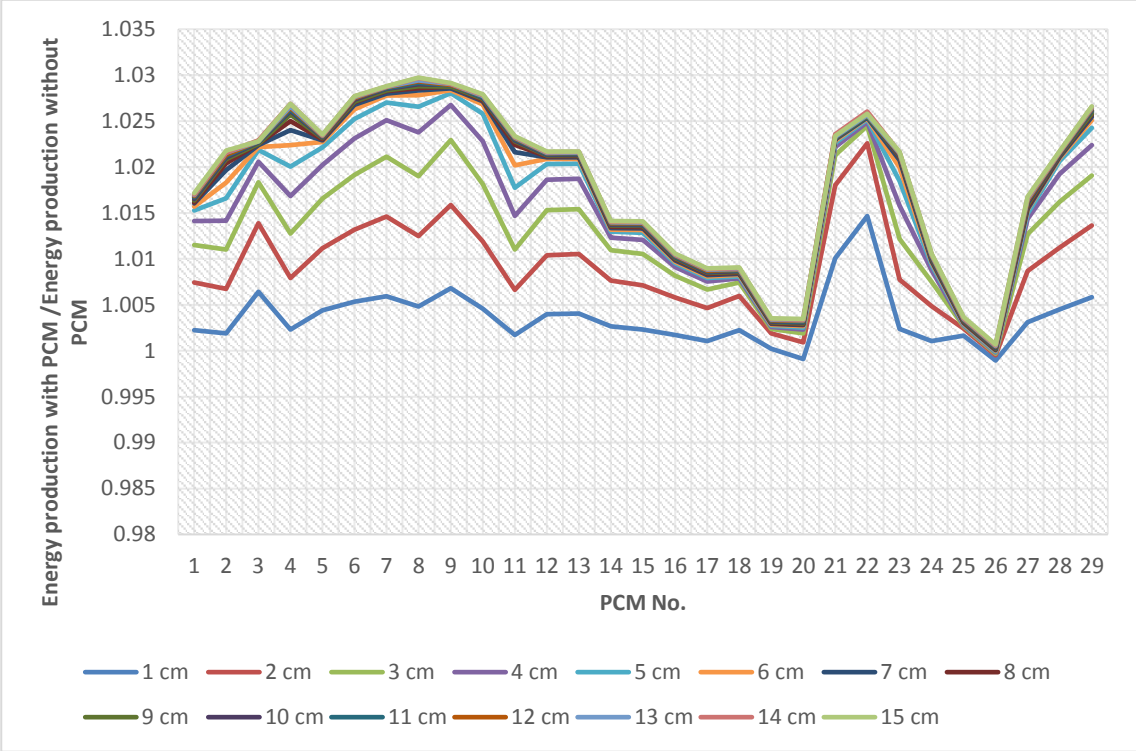

Figure 7-7 : The annual impact of the different PCMs with 3% Al foam for different thicknesses on the electric energy output of the PV panel, Baghdad.

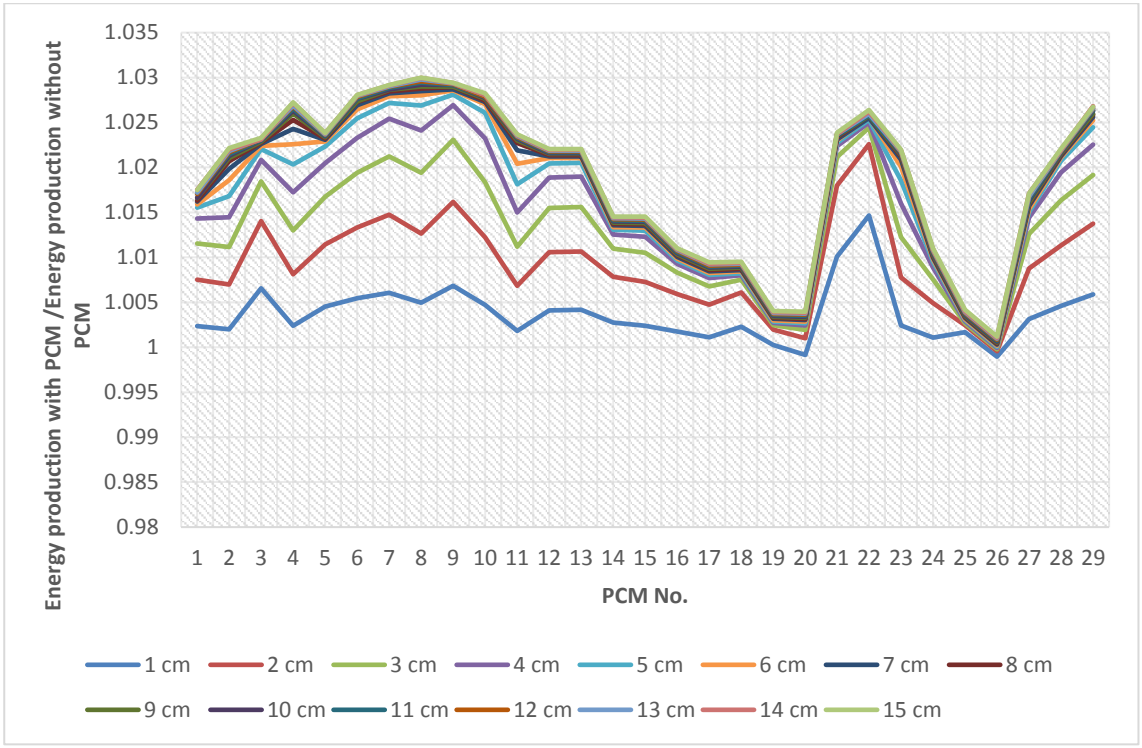

Figure 7-8 : The annual impact of the different PCMs with 4% Al foam for different thicknesses on the electric energy output of the PV panel, Baghdad.

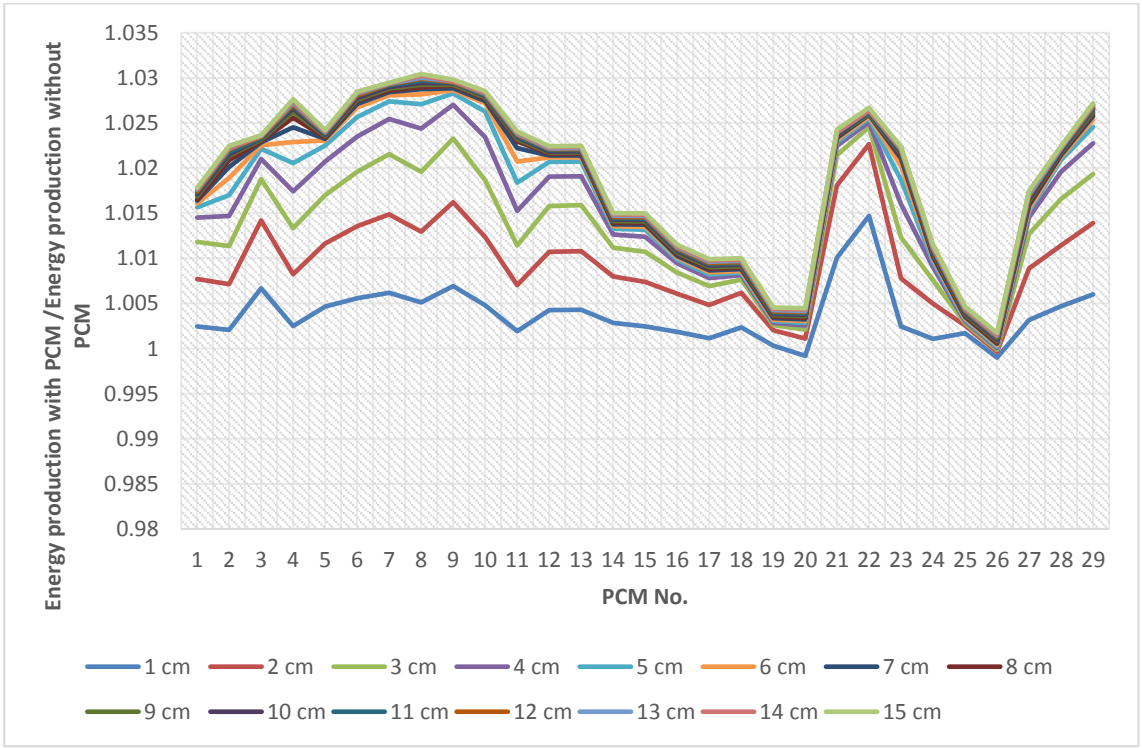

Figure 7-9 : The annual impact of the different PCMs with 5% Al foam for different thicknesses on the electric energy output of the PV panel, Baghdad.

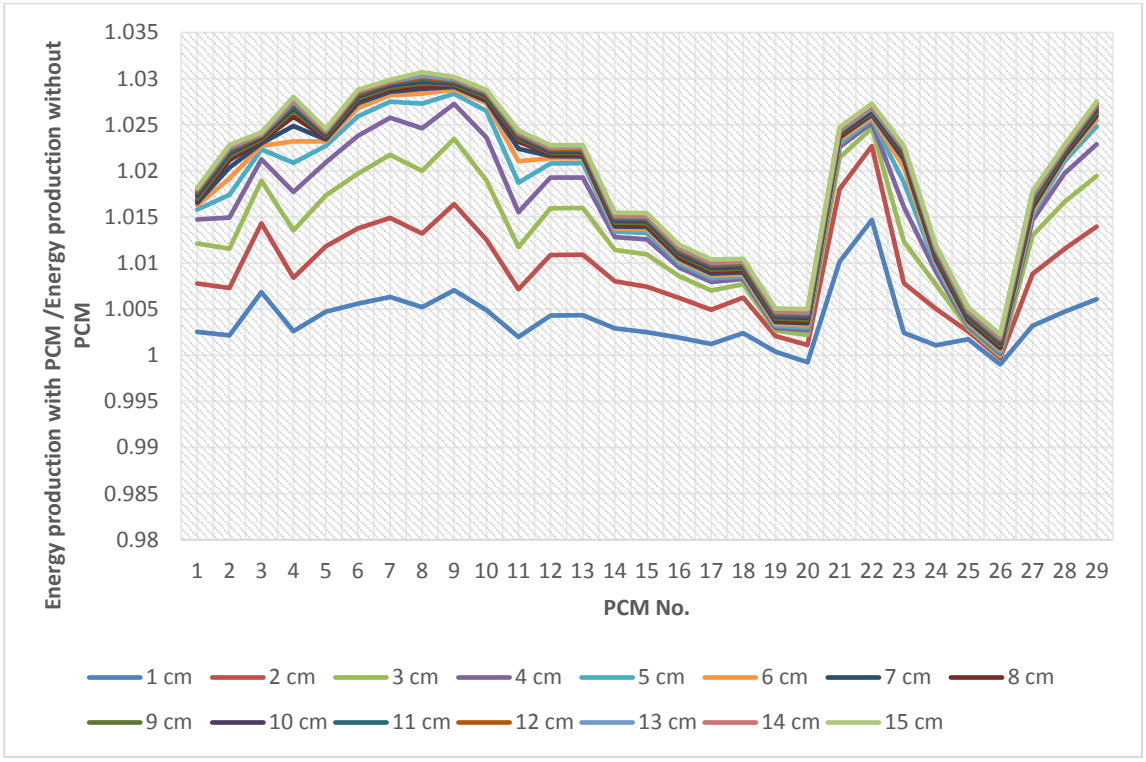

Figure 7-10 : The annual impact of the different PCMs with 6% Al foam for different thicknesses on the electric energy output of the PV panel, Baghdad.

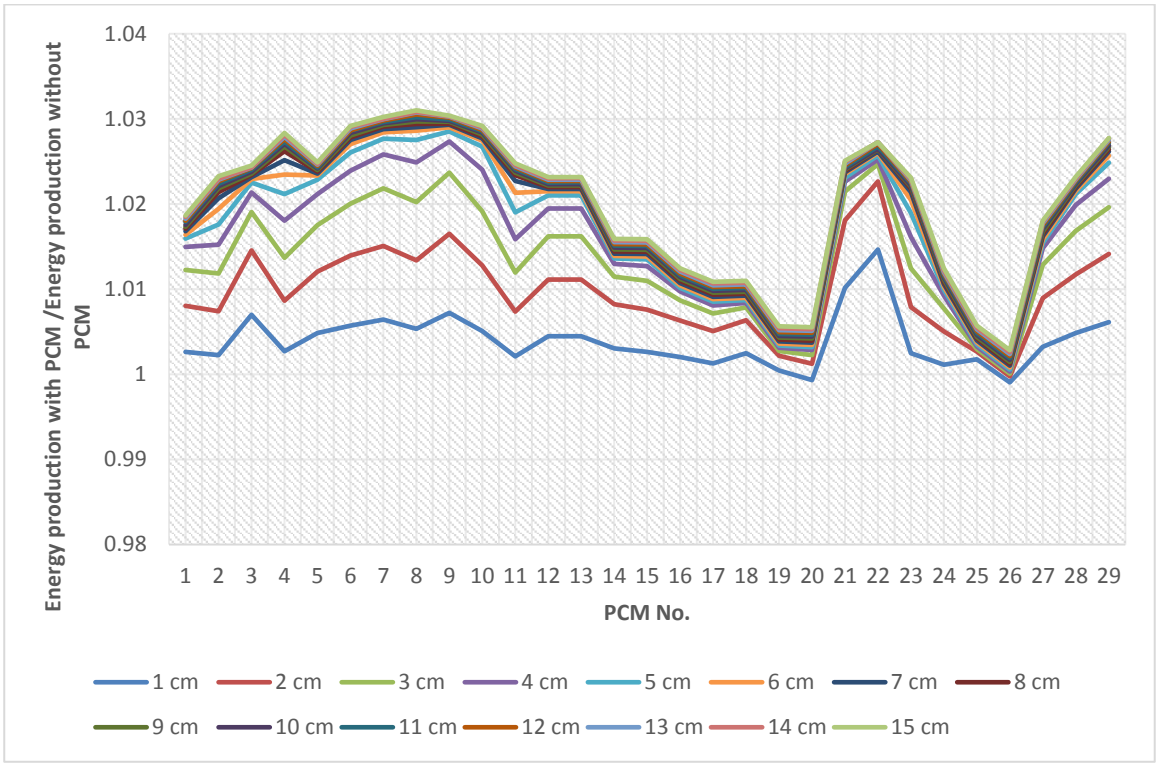

Figure 7-11 : The annual impact of the different PCMs with 7% Al foam for different thicknesses on the electric Energy output of the PV panel, Baghdad.

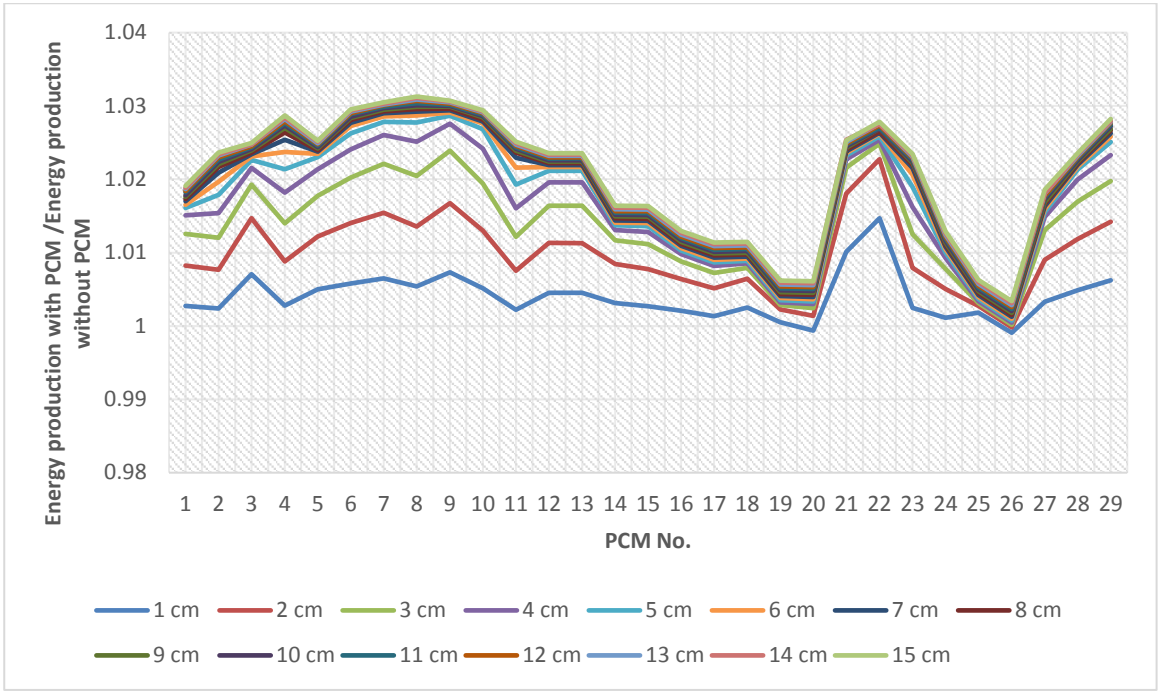

Figure 7-12 : The annual impact of the different PCMs with 8% Al foam for different thicknesses on the electric Energy output of the PV panel, Baghdad.

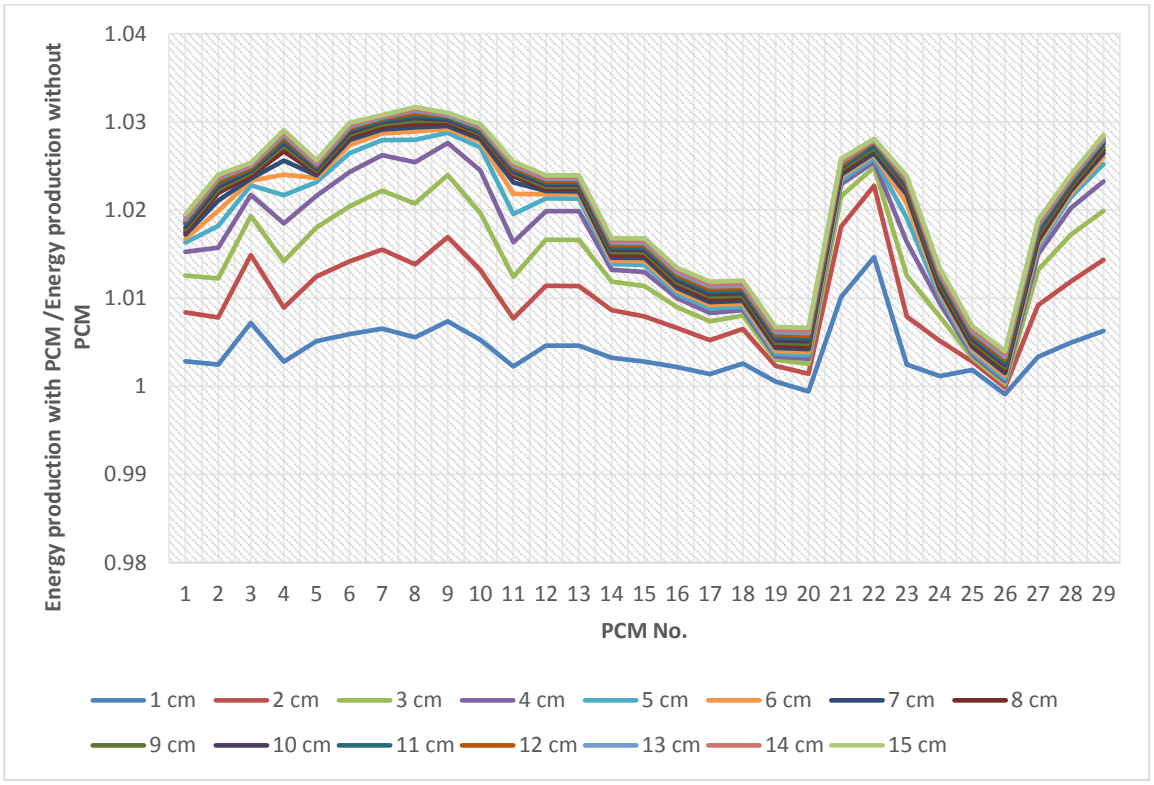

Figure 7-13 : The annual impact of the different PCMs with 9% Al foam for different thicknesses on the electric energy output of the PV panel, Baghdad.

7.4.3 The results of optimum design for PV-PCM system metal foam composite for Milan.

This section investigates the impact of using different PCMs with different Al foam percentages on the annual PV panel electrical energy output for Milan. The results for different Al foam percentages of 3%, 4%, 5%, 6%, 7%, 8% and 9% have been presented in Figure 7-14, Figure 7-15, Figure 7-16, Figure 7-17, Figure 7-18, Figure 7-19 and Figure 7-20 respectively. According to the results, PCM number 21 has the highest annual electrical output, with a 14 cm thickness and 9% Al foam percentage. The energy ratio for this optimal PCM is 1.04116. According to the results, the best three PCMs for Milan are number 3, 21 and 29, which have melting temperatures of 27^{o}C, 27^{o}C and 31^{o}C respectively. While, the worst PCMs are number 20 and 26, which have melting temperatures of 55^{o}C and 58^{o}C respectively. This means the best PCM melting temperature for Milan should be about 27^{o}C.

From Figure 7-14, Figure 7-15, Figure 7-16, Figure 7-17, Figure 7-18, Figure 7-19 and Figure 7-20, it can be seen that when the thickness of the PCM increased up to 7cm the energy ratio increased, but when the PCM thickness increased from 7 cm to 15 cm, there is no considerable increase in the energy ratio. In addition, for Figure 7-20 with 9% Al foam percentage when the thickness increased from 14 cm to 15 cm, the energy ratio decreased slightly.

According to the results, when the Al foam volme percentage increased from 3% to 9%, the energy ratio increased only slightly, as illustrated in Figure 7-21 by the blue line. In Figure 7-21, the x-axis represents the thickness of the PCM number 21 and the y-axis represents the division of two energy ratios. In this figure, the blue line represents the results of the energy ratio when using 9% Al foam [energy ratio 3], divided by the energy ratio when using 3% Al foam [energy ratio 2]. It can be seen from this blue line that there is no improvement when increasing the percentage of Al foam from 3% to 9%. The red line represents the results of the energy ratio when using 3% Al foam [energy ratio 2] divided by the energy ratio of using a PCM without Al foam [energy ratio 1]. The results indicate that the energy ratio has increased by 5.07% only when adding this 3% of Al foam for the 15 cm thickness PCM. Therefore, adding 3% of Al foam has a high impact in

increasing the annual electrical output of PV panels for a whole year in Milan. However, increasing this percentage to 9% does not have a considerable improvement for the annual electrical output of PV panels for a whole year in Milan.

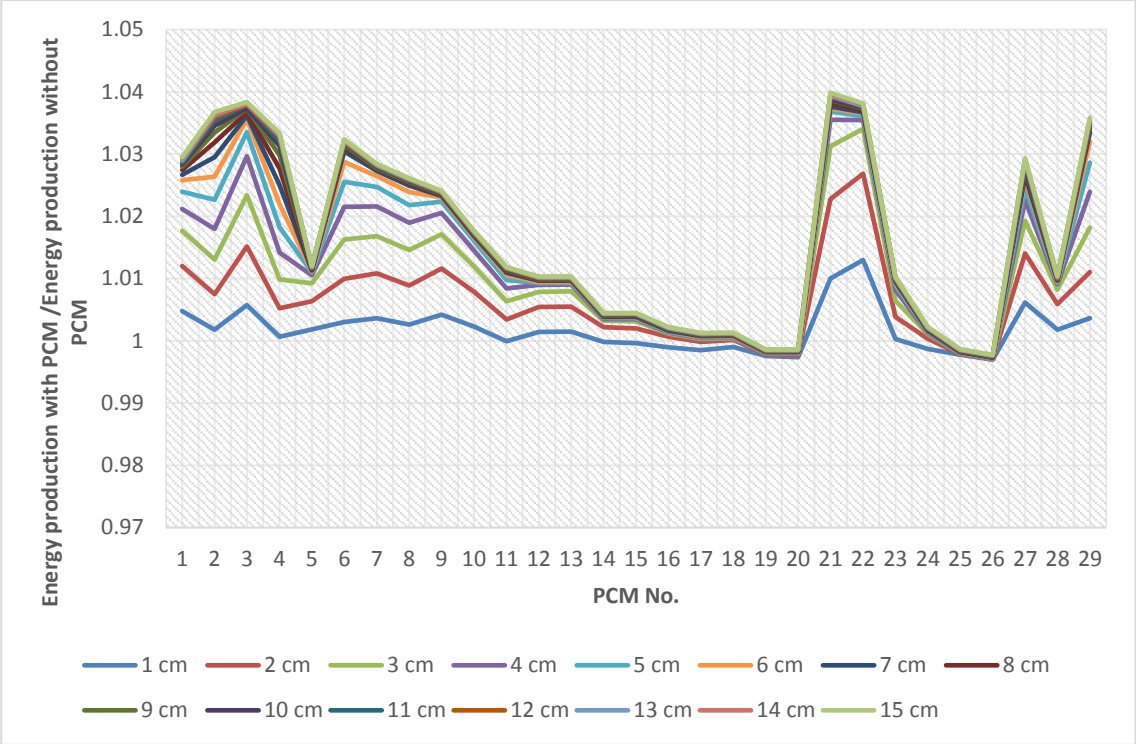

Figure 7-14 : The annual impact of the different PCMs with 3% Al foam for different thicknesses on the electric energy output of the PV panel, Milan.

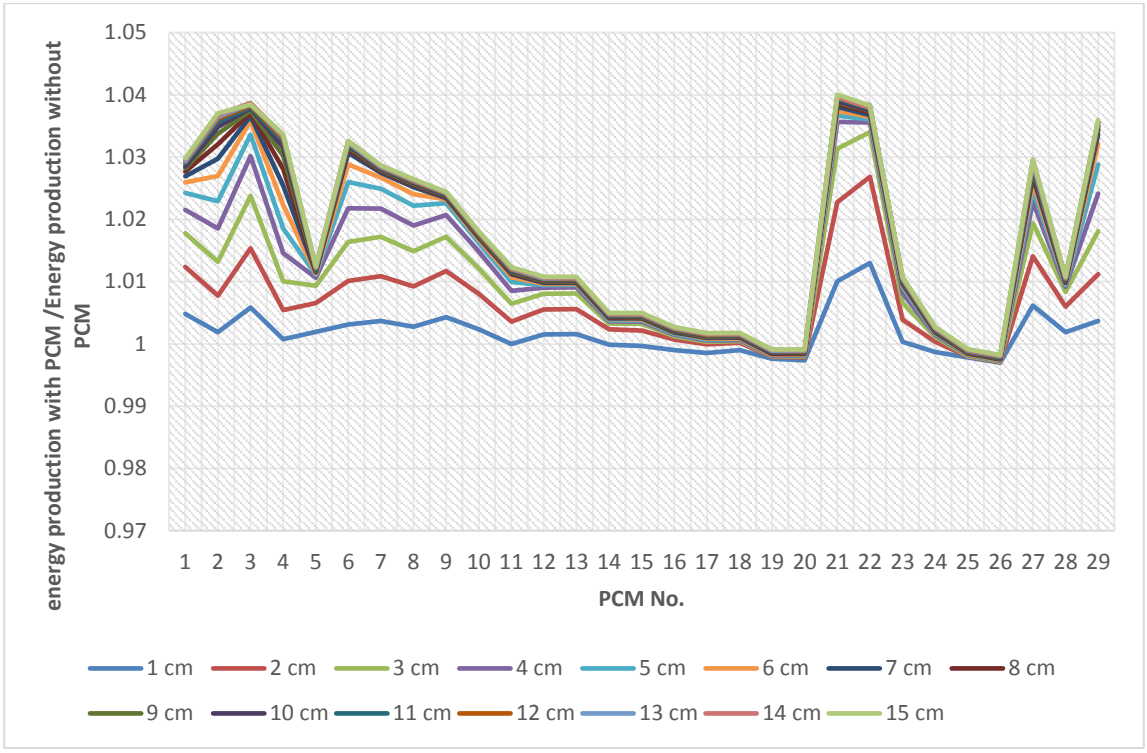

Figure 7-15 : The annual impact of the different PCMs with 4% Al foam for different thicknesses on the electric energy output of the PV panel, Milan.

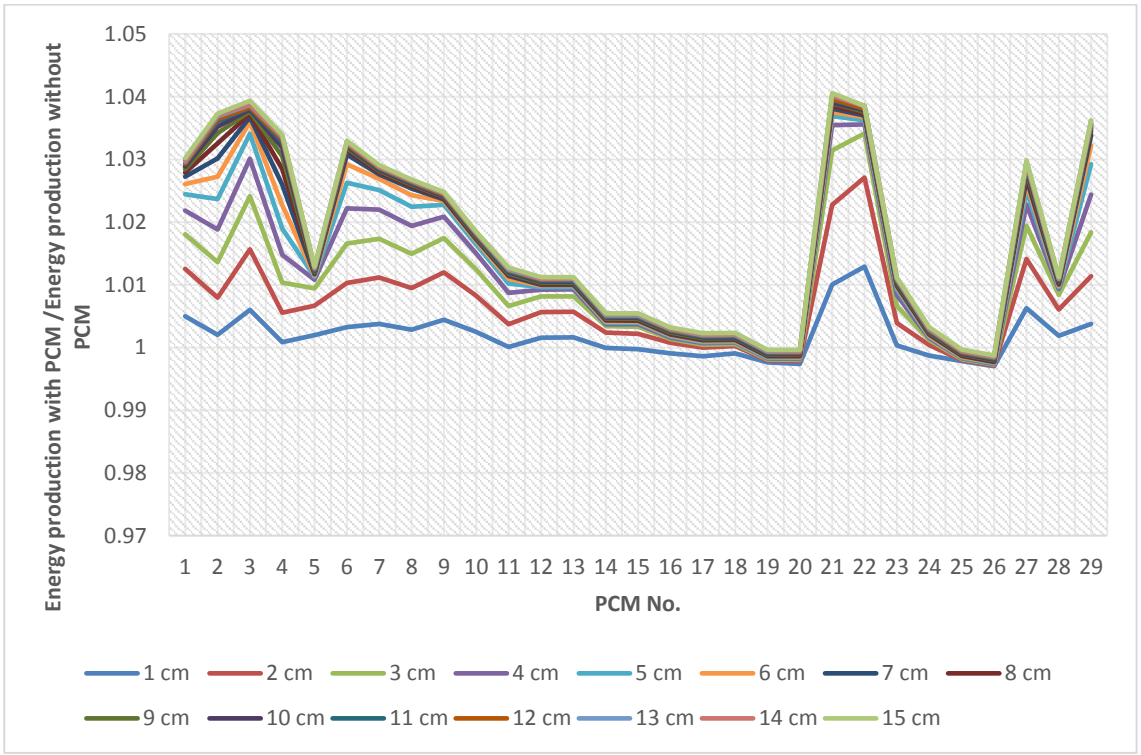

Figure 7-16 : The annual impact of the different PCMs with 5% Al foam for different thicknesses on the electric Energy output of the PV panel, Milan.

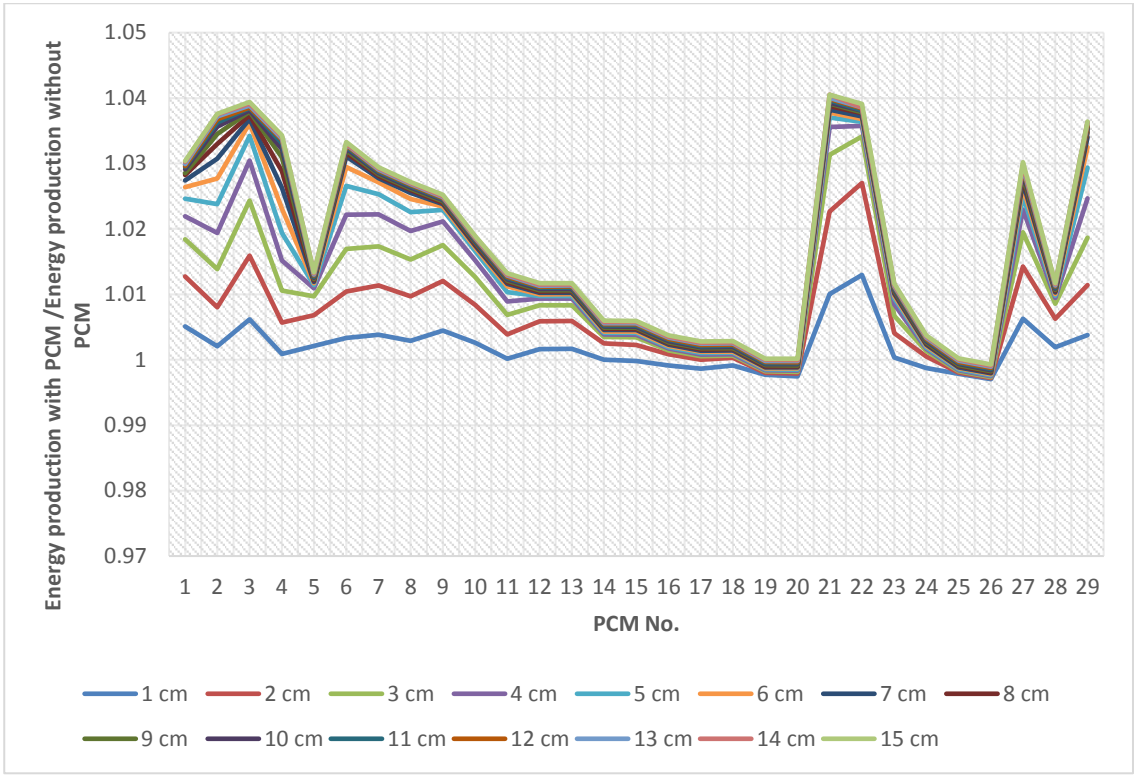

Figure 7-17 : The annual impact of the different PCMs with 6% Al foam for different thicknesses on the electric Energy output of the PV panel, Milan.

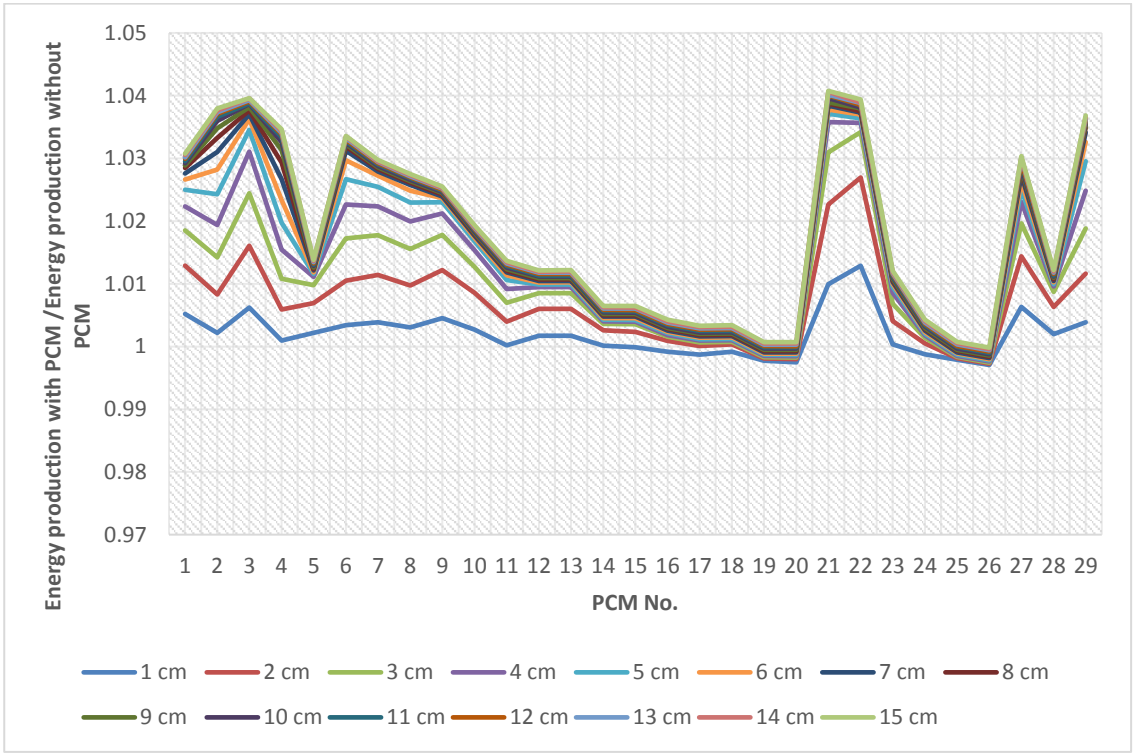

Figure 7-18: Annual impact of the different PCMs with 7% Al foam for different thicknesses on the electric energy output of the PV panel, Milan.

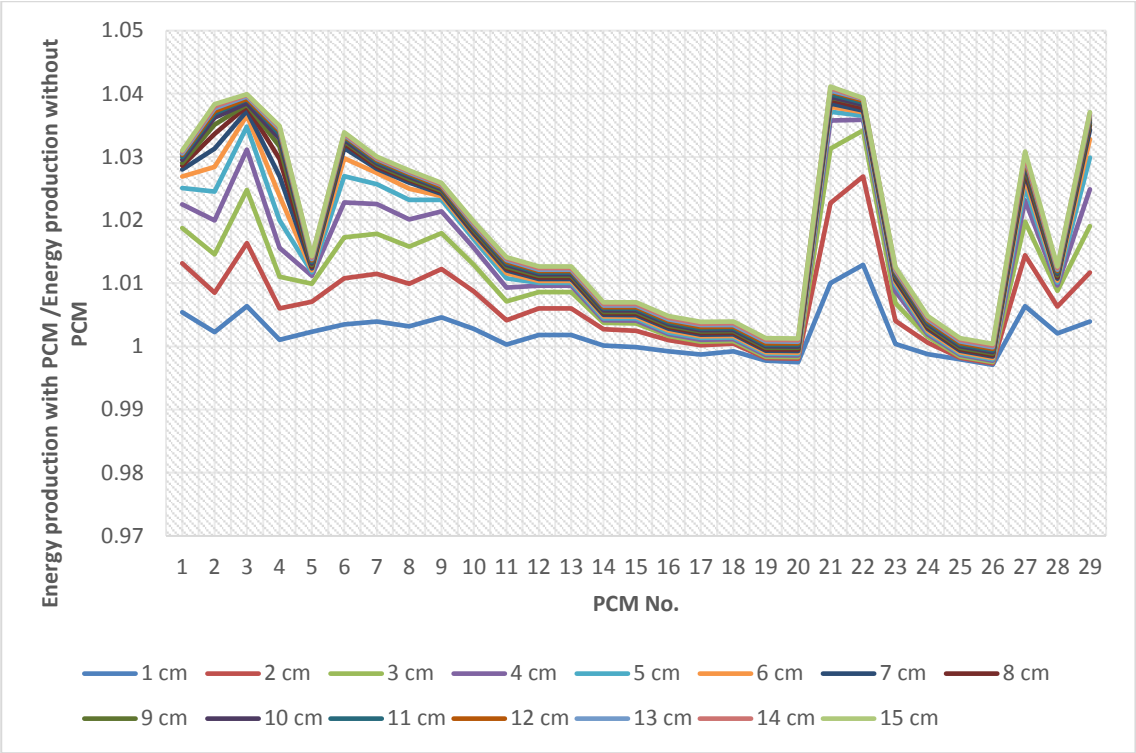

Figure 7-19: Annual impact of the different PCMs with 8% Al foam for different thicknesses on the electric energy output of the PV panel, Milan.

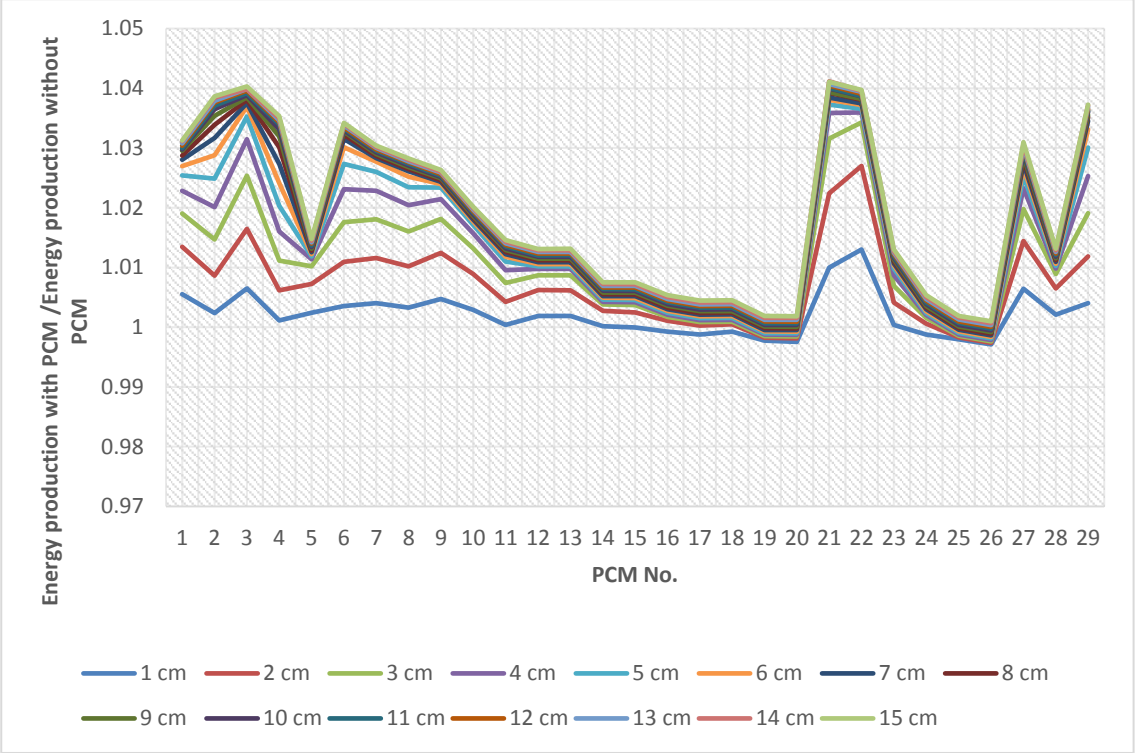

Figure 7-20 : The annual impact of the different PCMs with 9% Al foam for different thicknesses on the electric energy output of the PV panel, Milan.

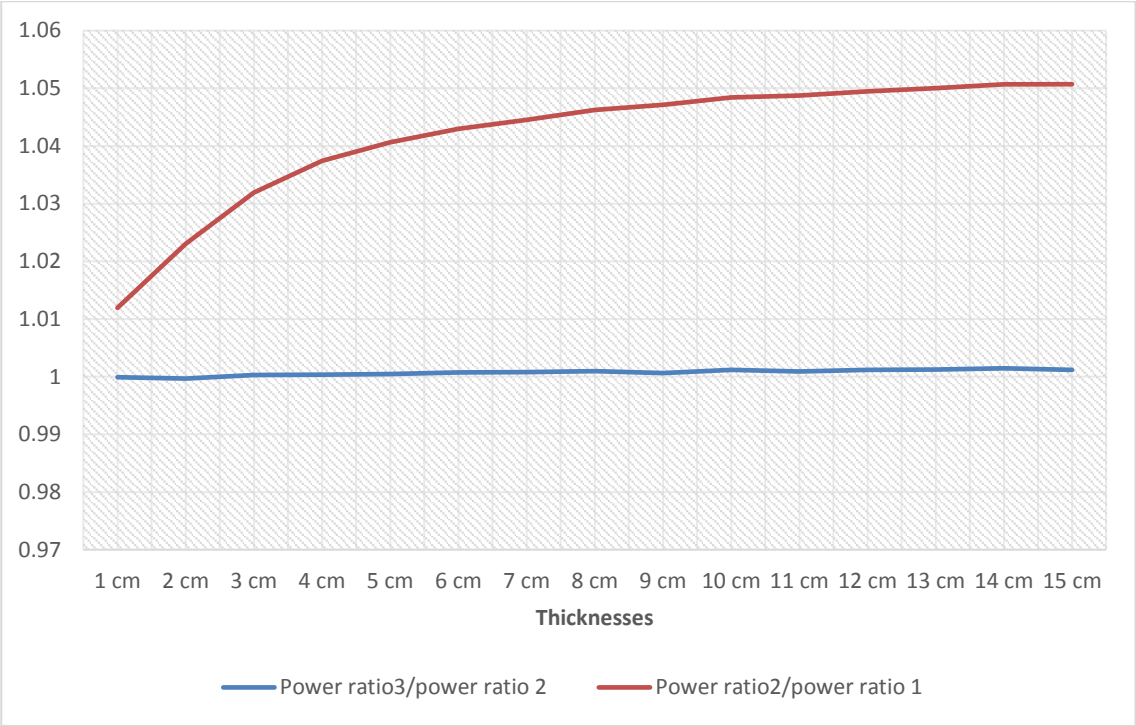

Figure 7-21: Energy ratios variations with different Al foam percentages.

7.5 Summary

This chapter presents the results of the best PCM and best thickness without and with Al foam to produce the maximum electrical energy from the PV panel for two cities: Baghdad and Milan. Firstly, the properties of 29 PCMs has been collected, then the impacts of these PCMs with different thicknesses have been investigated. The results indicate that the best PCM for Baghdad is FS30 from (Khanna et al., 2018, Pluss, 2018) with 2 cm thickness and annual electrical energy enhancement is 0.3%. While the best PCM for Milan is L30 from (Weinläder et al., 2005) with 3 cm thickness and the annual electrical energy enhancement is 0.5%. Secondly, the impacts of adding different Al foam percentages to the PCMs with different thicknesses have been studied. The maximum annual electrical energy of the PV panel have been enhanced by 3.19% and 4.11% for Baghdad and Milan respectively. These results are by using PCM number 8 and number 21 from Table 7 with 9% of Al foam and 15 cm and 14 cm thicknesses for Baghdad and Milan respectively.

Chapter Eight Conclusions And Future Works

8.1 Conclusions

One of the promising methods to cool down and increase the efficiency of photovoltaic panels is through inclusion a phase change material. The first novelty of this study is a new mathematical model, which is accurate, and very quick computationally for the assessment of the impact on the efficiency of a Photovoltaic (PV) panel by the attachment of a Phase Change Material onto the panel. The new model is fully developed for a typical sized rectangular PV-PCM assembly and the assumptions and their relevance are detailed. The Poisson equation for transient one-dimensional conductive heat flow applies solely for the PV layer and the heat generated is related to a portion of the solar heat flux striking the panel. The Fourier equation applies for the other layers above and below the PV of the assembly (glass, EVA, EVA and Tedlar) as well as the aluminium layers of the container for the PCM. These equations are reduced to an overall lumped equation by considering the average temperature within each layer and intimate thermal contact between layers. The Stefan problem for the phase change of the PCM is accommodated by the apparent heat capacity methodology. Transient heat transfer by both thermal radiation and convection to the surroundings occurs at the top and bottom faces of the overall assembly. A numerical solution of the coupled ordinary and partial differential equations representing the PV-PCM assembly is developed in MATLAB and a flow chart of the algorithm is displayed. Convergence of the numerical solution is demonstrated. The model is used to predict experimental data from the literature over a 7 hour period. The model base of the panel and the top aluminium surface of the PCM container predicts the trends of the experimental data very well and the maximum relative error in the temperature difference of the PV panel is 6.47%. The computer computational times taken for the implicit method for the both the lumped-distributed parameter model and fully distributed parameter model to study a transient 18,000 seconds for the PV-PVM system are 16.813 s and 525.045 s respectively with some conditions mentioned in results, while the explicit solution has consumed 51,392 seconds to study 1 second of the PV-PCM module.

The second novelty is to implement the thermal contact conductance. To study the impact of thermal conductance between the PV panel and the aluminium container of the PCM, three cases have been investigated. These three cases have differed in the following: In the first case, there is a contact adherence between the aluminium container and the PV panel. In the second, there is no contact adherence, and in the third case, there is 0.5 mm air gap. The results show the maximum electric PV-PCM efficiency difference reaches 3.8 percent, if comparing the first and third cases.

The third novelty is by more development for the mathematical models. This development has been implemented by considering the impact of the volume change of the PCM during phase change from solid to liquid. The results indicate that the maximum temperature difference was 1.7954^{o}C when considering the volume change as compared with when volume change was not considered.

A novel comparison between using the apparent heat capacity of the PCM depending on the temperature of the previous and current time step has been implemented. The results show the temperature difference could reach 1.3053^{o}C with a relative error of 3.55 percent.

The lumped-distributed parameter model for the PV-PCM system has been used to study the impacts of using 0.05 m of composite paraffin-PCM on the PV panels and studying the performance over a whole year in Baghdad and Milan. Observed data for the solar radiation of horizontal surfaces has been used for Bagdad. Then, a mathematical model has been used to calculate the solar radiation for the inclined surface. While in Milan, the solar radiation for inclined surface has been downloaded from the SoDA HelioClim-3 v5 (SoDA, 2019). The results indicated these changes have increased the year-round electrical energy output by 1.96 and 2.39 percent in Baghdad and Milan, respectively.

The impact of the different types of PCMs on the annual electrical output of PV panels depends on several factors such as the melting temperature, thermal conductivity, latent heat, specific heat capacity, and thickness of the PCM, as well as the ambient temperature, wind speed and the solar radiation intensity. Therefore, in order to find the best PCMs for Baghdad and Milan, thermophysical

properties of pure 29 PCMs have been collected. Fifteen thicknesses were studied, ranging from one to fifteen cms, of each PCM and the annual electrical output of the PV panel for Baghdad and Milan were investigated. The results show that the best PCM for Baghdad is FS30, (Khanna et al., 2018, Pluss, 2018) with two cm thickness and annual electrical energy enhancement of 0.3 percent. While the best PCM for Milan is L30, (Weinläder et al., 2005) with three cm thickness and annual electrical energy enhancement of 0.5 percent. These PCMs have low impacts on the annual electrical enhancements due to their low thermal conductivity.

In order to increase the thermal conductivity of the PCM, different Al foam percentages, which ranged from three to nine percent, have been theoretically combined with the pure 29 PCMs. The impacts of these different PCMs, with different Al foam percentages and different PCM thicknesses on the annual electrical PV output, were then investigated in both Baghdad and Milan. The maximum annual electrical energy of the PV panel have been enhanced by 3.19 and 4.11 percent for Baghdad and Milan respectively. These results were maintained by using the PCMs A36, (Products, 2013) and L30, (Weinläder et al., 2005) with nine percent of Al foam and 15 and 14 cm thicknesses for Baghdad and Milan respectively. In addition, the results indicate that the energy ratio has increased by 5.07 percent only when adding three percent of Al foam for the 15 cm thickness PCM. Therefore, adding three percent of Al foam has an impact on the annual electrical output of PV panels in Milan over a year. However, increasing this percentage to nine percent does not make a considerable improvement. Resulting in is 0.118 percent for the annual electrical output of PV panels in Milan over a year. Increasing the PCM thickness from five to fifteen cm has a little impact of 0.366 percent for the annual electrical output of PV panels in Milan over a whole year.

8.2 Future works

There is further research related to this PhD study which could be implemented:

8.2.1 First proposal

The impact of cooling the PV panel could increase the life span of the EVA layers inside the PV panel and turns on increasing the life span of the PV panel. Therefore, it would be worthy to investigate that.

8.2.2 Second proposal

The PCMs can be used to cool down the PV panel in solar street lights and increase the efficiency of the PV panel. Figure 8-1 illustrates the main components of the solar street light. In addition, the PCMs can be used to control the temperature of the lithium iron phosphate inside the solar street light during the day, especially in hot climates and increase the life span of the battery see It can be seen in Figure 8-2 that the lifecycle of the battery reduced from about 4,250 cycles to about 2,030 cycles when the run temperature of the battery changed from 25 to 55 °C. Moreover, the PCMs can be used to heat the battery inside the solar street light during the night in cold countries to increase the capacity of the battery see Figure 8-3.

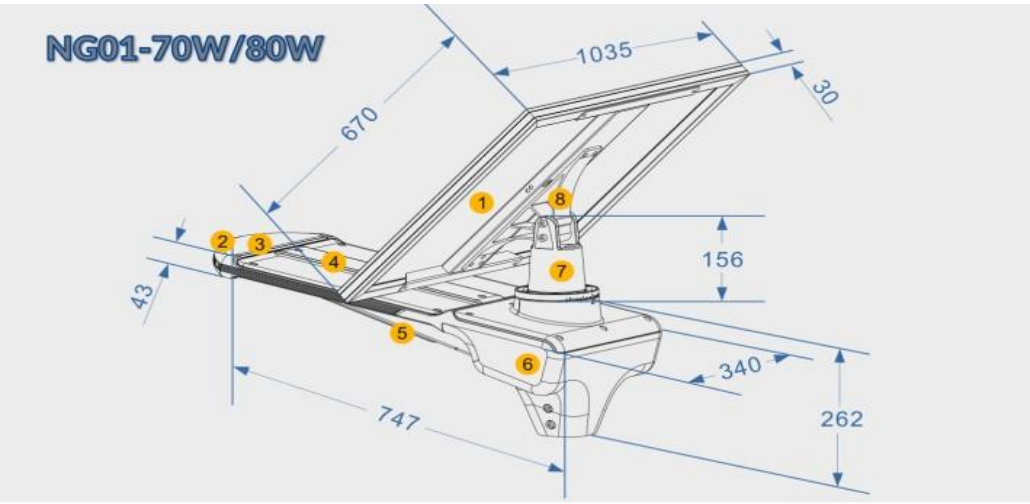

1.Solar panel 2.Pathway LED indicator 3.Microwave sensor 4.MPPT controller 5. LED source6. Lithium battery 7. Horizontal bracket 8. Vertical bracket

Figure 8-1: Solar street light (Bella, 2019).

Figure 8-2: The depth of discharge for the batter with number of cycles for different temperatures (Gloria, 2019).

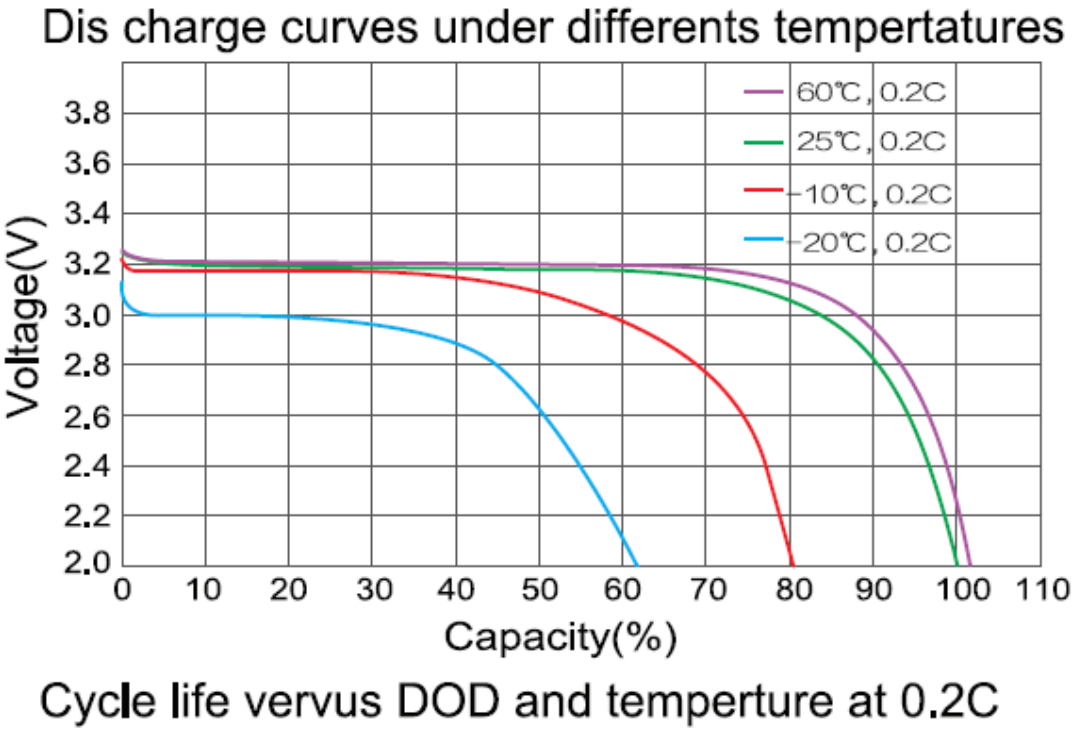

Cycle life vervus DOD and temperture at 0.2C

Figure 8-3: the capacity of the lithium iron phosphate battery with different temperatures (Gloria, 2019).

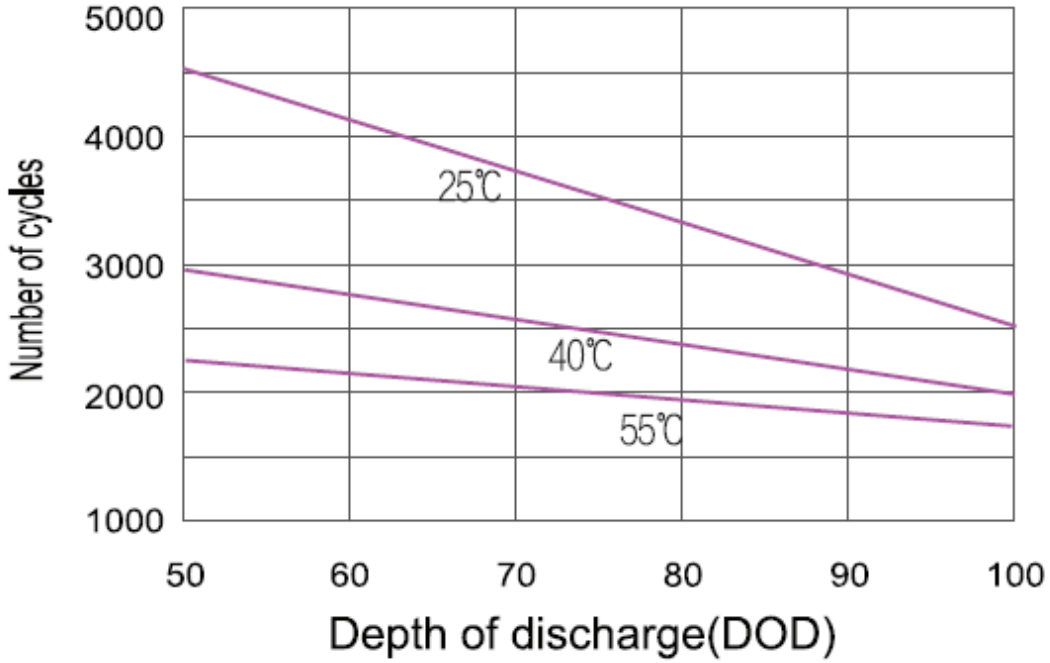

References

AL-WAELI, A. H., CHAICHAN, M. T., SOPIAN, K., KAZEM, H. A., MAHOOD, H. B. & KHADOM, A. A. 2019. Modeling and experimental validation of a PVT system using nanofluid coolant and nano-PCM. *Solar Energy,* 177**,** 178-191.

ALAMI, A. H. 2014. Effects of evaporative cooling on efficiency of photovoltaic modules. *Energy Conversion and Management,* 77**,** 668-679.

ALLAN, J. 2015. *The development and characterisation of enhanced hybrid solar photovoltaic thermal systems.* Brunel University London.

ALY, S. P., AHZI, S., BARTH, N. & FIGGIS, B. W. 2017. Two-dimensional finite difference-based model for coupled irradiation and heat transfer in photovoltaic modules. *Solar Energy Materials and Solar Cells*.

ARıCı, M., BILGIN, F., NIŽETIĆ, S. & PAPADOPOULOS, A. M. 2018. Phase change material based cooling of photovoltaic panel: A simplified numerical model for the optimization of the phase change material layer and general economic evaluation. *Journal of Cleaner Production,* 189**,** 738-745.

BAGHER, A. M., VAHID, M. M. A. & MOHSEN, M. 2015. Types of Solar Cells and Application. *American Journal of Optics and Photonics,* 3**,** 94-113.

BAHAIDARAH, H. M., BALOCH, A. A. & GANDHIDASAN, P. 2016. Uniform cooling of photovoltaic panels: A review. *Renewable and Sustainable Energy Reviews,* 57**,** 1520-1544.

BAHRAMI, A., MOHAMMADNEJAD, S. & SOLEIMANINEZHAD, S. 2013. Photovoltaic cells technology: principles and recent developments. *Optical and Quantum Electronics,* 45**,** 161-197.

BEERI, O., ROTEM, O., HAZAN, E., KATZ, E. A., BRAUN, A. & GELBSTEIN, Y. 2015. Hybrid photovoltaic-thermoelectric system for concentrated solar energy conversion: Experimental realization and modeling. *Journal of Applied Physics,* 118**,** 115104.

BELLA 2019.

BENLEKKAM, M. L., NEHARI, D. & MADANI, H. 2018. The thermal impact of the fin tilt angle and its orientation on performance of PV cell using PCM. *INTERNATIONAL JOURNAL OF HEAT AND TECHNOLOGY,* 36**,** 919-926.

BHATTACHARYA, A., CALMIDI, V. V. & MAHAJAN, R. L. 2002. Thermophysical properties of high porosity metal foams. *International Journal of Heat and Mass Transfer,* 45**,** 1017-1031.

BJØRK, R. & NIELSEN, K. K. 2015. The performance of a combined solar photovoltaic (PV) and thermoelectric generator (TEG) system. *Solar Energy,* 120**,** 187-194.

BRANO, V. L., CIULLA, G., PIACENTINO, A. & CARDONA, F. 2014. Finite difference thermal model of a latent heat storage system coupled with a photovoltaic device: Description and experimental validation. *Renewable Energy,* 68**,** 181-193.

BROWNE, M., NORTON, B. & MCCORMACK, S. 2015. Phase change materials for photovoltaic thermal management. *Renewable and Sustainable Energy Reviews,* 47**,** 762-782.

CELLURA, M., BRANO, V. L. & MARVUGLIA, A. 2008. 582. A Photovoltaic panel coupled with a phase changing material heat storage system in hot climates.

CHOI, Y.-K. 2014. A study on power generation analysis of floating PV system considering environmental Impact. *development,* 8.

CIULLA, G., BRANO, V. L., CELLURA, M., FRANZITTA, V. & MILONE, D. 2012. A finite difference model of a PV-PCM system. *Energy Procedia,* 30**,** 198-206.

CLIMSEL 2018. product specification sheet.

CONTI, J., HOLTBERG, P., DIEFENDERFER, J., LAROSE, A., TURNURE, J. T. & WESTFALL, L. 2016. International energy outlook 2016 with projections to 2040. USDOE Energy Information Administration (EIA), Washington, DC (United States ….

CUI, T., XUAN, Y. & LI, Q. 2016. Design of a novel concentrating photovoltaic–thermoelectric system incorporated with phase change materials. *Energy Conversion and Management,* 112**,** 49-60.

CUI, Y., XIE, J., LIU, J., WANG, J. & CHEN, S. 2017. A review on phase change material application in building. *Advances in Mechanical Engineering,* 9**,** 1687814017700828.

DUFFIE, J. A. & BECKMAN, W. A. 2013a. *Solar engineering of thermal processes*, Wiley New York.

DUFFIE, J. A. & BECKMAN, W. A. 2013b. *Solar engineering of thermal processes*, John Wiley & Sons.

EMAM, M., OOKAWARA, S. & AHMED, M. 2017. Performance study and analysis of an inclined concentrated photovoltaic-phase change material system. *Solar Energy,* 150**,** 229-245.

EUROPEAN-SPACE-AGENCY 11 2017. History of Europe in space

FAYAZ, H., RAHIM, N. A., HASANUZZAMAN, M., RIVAI, A. & NASRIN, R. 2019. Numerical and outdoor real time experimental investigation of performance of PCM based PVT system. *Solar Energy,* 179**,** 135-150.

FESHARAKI, V. J., DEHGHANI, M., FESHARAKI, J. J. & TAVASOLI, H. The effect of temperature on photovoltaic cell efficiency. Proceedings of the

1stInternational Conference on Emerging Trends in Energy Conservation–ETEC, Tehran, Iran, 2011. 20-21.
FU, Q. & TONG, N. A complex-method-based PSO algorithm for the maximum power point tracking in photovoltaic system. information technology and computer science (ITCS), 2010 second international conference on, 2010. IEEE, 134-137.
GAUR, A., MÉNÉZO, C. & GIROUX, S. 2017. Numerical studies on thermal and electrical performance of a fully wetted absorber PVT collector with PCM as a storage medium. *Renewable Energy,* 109**,** 168-187.
GLORIA. March 2019. Type to AL-ASADI, H.
GRAY, J. L. 2003. The physics of the solar cell. *Handbook of photovoltaic science and engineering,* 2**,** 82-128.
GREEN, M. A., EMERY, K., HISHIKAWA, Y., WARTA, W. & DUNLOP, E. D. 2015. Solar cell efficiency tables (Version 45). *Progress in photovoltaics: research and applications,* 23**,** 1-9.
HACHEM, F., ABDULHAY, B., RAMADAN, M., EL HAGE, H., EL RAB, M. G. & KHALED, M. 2017. Improving the performance of photovoltaic cells using pure and combined phase change materials–Experiments and transient energy balance. *Renewable Energy,* 107**,** 567-575.
HALLER, J., VOSWINCKEL, S. & WESSELAK, V. 2013. The effect of quantum efficiencies on the optimum orientation of photovoltaic modules–a comparison between crystalline and thin film modules. *Solar Energy,* 88**,** 97-103.
HASAN, A., MCCORMACK, S., HUANG, M. & NORTON, B. 2010. Evaluation of phase change materials for thermal regulation enhancement of building integrated photovoltaics. *Solar Energy,* 84**,** 1601-1612.
HASAN, A., MCCORMACK, S. J., HUANG, M. J. & NORTON, B. 2014. Energy and cost saving of a photovoltaic-phase change materials (PV-PCM) system through temperature regulation and performance enhancement of photovoltaics. *Energies,* 7**,** 1318-1331.
HASAN, A., SARWAR, J., ALNOMAN, H. & ABDELBAQI, S. 2017. Yearly energy performance of a photovoltaic-phase change material (PV-PCM) system in hot climate. *Solar Energy,* 146**,** 417-429.
HASHIM, H. 2015. *Full-spectrum solar energy harvesting using nanotechnology-enabled photovoltaic/thermoelectric hybrid system.* Cardiff University.
HENDRICKS, J. & SARK, W. 2013. Annual performance enhancement of building integrated photovoltaic modules by applying phase change materials. *Progress in Photovoltaics: Research and Applications,* 21**,** 620-630.
HERSCH, P. & ZWEIBEL, K. 1982. Basic photovoltaic principles and methods. Solar Energy Research Inst., Golden, CO (USA).
HO, C., CHOU, W.-L. & LAI, C.-M. 2015. Thermal and electrical performance of a water-surface floating PV integrated with a water-saturated MEPCM layer. *Energy Conversion and Management,* 89**,** 862-872.
HO, C., CHOU, W.-L. & LAI, C.-M. 2016. Thermal and electrical performances of a water-surface floating PV integrated with double water-saturated MEPCM layers. *Applied Thermal Engineering,* 94**,** 122-132.
HOLMAN, J. 2002. Heat transfer 9th Edition. *New York, Boston, McGraw-Hill, Inc*.

HU, H. & ARGYROPOULOS, S. A. 1996. Mathematical modelling of solidification and melting: a review. *Modelling and Simulation in Materials Science and Engineering,* 4**,** 371.

HUANG, M. Two phase change material with different closed shape fins in building integrated photovoltaic system temperature regulation. World Renewable Energy Congress-Sweden; 8-13 May; 2011; LinkÃ¶ ping; Sweden, 2011a. Linköping University Electronic Press, 2938-2945.

HUANG, M., EAMES, P. & NORTON, B. 2004. Thermal regulation of building-integrated photovoltaics using phase change materials. *International Journal of heat and mass transfer,* 47**,** 2715-2733.

HUANG, M., EAMES, P., NORTON, B. & HEWITT, N. 2011. Natural convection in an internally finned phase change material heat sink for the thermal management of photovoltaics. *Solar Energy Materials and Solar Cells,* 95**,** 1598-1603.

HUANG, M. J. 2011b. The effect of using two PCMs on the thermal regulation performance of BIPV systems. *Solar Energy Materials and Solar Cells,* 95**,** 957-963.

INCROPERA, F. P. & DE WITT, D. P. 2005. *Fundamentals of heat and mass transfer*.

INTERNATIONALENERGYAGENCY. 2011. *Solar Energy Perspective* [Online]. Available: https://www.iea.org/publications/freepublications/publication/solar_energy_perspectives2011.pdf [Accessed 11 1 2017.

ISLAM, M., PANDEY, A., HASANUZZAMAN, M. & RAHIM, N. 2016. Recent progresses and achievements in photovoltaic-phase change material technology: A review with special treatment on photovoltaic thermal-phase change material systems. *Energy Conversion and Management,* 126**,** 177-204.

JAGUEMONT, J., OMAR, N., VAN DEN BOSSCHE, P. & VAN MIERLO, J. 2017. Phase-change materials (PCM) for automotive applications: a review. *Applied Thermal Engineering*.

JU, X., WANG, Z., FLAMANT, G., LI, P. & ZHAO, W. 2012. Numerical analysis and optimization of a spectrum splitting concentration photovoltaic–thermoelectric hybrid system. *Solar Energy,* 86**,** 1941-1954.

KALOGIROU, S. A. 2009. *Solar Energy Engineering: Processes and Systems*, Academic Press.

KALOGIROU, S. A. 2013. *Solar energy engineering: processes and systems*, Academic Press.

KANT, K., SHUKLA, A., SHARMA, A. & BIWOLE, P. H. 2016. Heat transfer studies of photovoltaic panel coupled with phase change material. *Solar Energy,* 140**,** 151-161.

KHANNA, S., NEWAR, S., SHARMA, V., REDDY, K. & MALLICK, T. K. 2019. Optimization of fins fitted phase change material equipped solar photovoltaic under various working circumstances. *Energy conversion and management,* 180**,** 1185-1195.

KHANNA, S., REDDY, K. & MALLICK, T. K. 2018. Optimization of finned solar photovoltaic phase change material (finned pv pcm) system. *International Journal of Thermal Sciences,* 130**,** 313-322.

KIBRIA, M., SAIDUR, R., AL-SULAIMAN, F. & AZIZ, M. M. A. 2016. Development of a thermal model for a hybrid photovoltaic module and phase change materials storage integrated in buildings. *Solar Energy,* 124**,** 114-123.

KLADISIOS, P. & STEGGOU-SAGIA, A. 2015. Using phase change materials in photovoltaic systems for cell temperature reduction: A finite difference simulation method. *Journal of Thermal Engineering,* 2**,** 897-906.

KLADISIOS, P. & STEGOU-SAGIA, A. 2015. USING PHASE CHANGE MATERIALS IN PHOTOVOLTAIC SYSTEMS FOR CELL TEMPERATURE REDUCTION: A FINITE DIFFERENCE SIMULATION METHOD.

KOSCHENZ, M. & LEHMANN, B. 2004. Development of a thermally activated ceiling panel with PCM for application in lightweight and retrofitted buildings. *Energy and buildings,* 36**,** 567-578.

KOSSYVAKIS, D., VOUTSINAS, G. & HRISTOFOROU, E. 2016. Experimental analysis and performance evaluation of a tandem photovoltaic–thermoelectric hybrid system. *Energy Conversion and Management,* 117**,** 490-500.

KUZNIK, F., DAVID, D., JOHANNES, K. & ROUX, J.-J. 2011. A review on phase change materials integrated in building walls. *Renewable and Sustainable Energy Reviews,* 15**,** 379-391.

LAMBA, R. & KAUSHIK, S. 2016. Modeling and performance analysis of a concentrated photovoltaic–thermoelectric hybrid power generation system. *Energy Conversion and Management,* 115**,** 288-298.

LI, Y., WITHARANA, S., CAO, H., LASFARGUES, M., HUANG, Y. & DING, Y. 2014. Wide spectrum solar energy harvesting through an integrated photovoltaic and thermoelectric system. *Particuology,* 15**,** 39-44.

LO BRANO, V., CIULLA, G., PIACENTINO, A. & CARDONA, F. 2013. On the efficacy of PCM to shave peak temperature of crystalline photovoltaic panels: An FDM model and field validation. *Energies,* 6**,** 6188-6210.

LU, W., LIU, Z., FLOR, J.-F., WU, Y. & YANG, M. 2018. Investigation on designed fins-enhanced phase change materials system for thermal management of a novel building integrated concentrating PV. *Applied energy,* 225**,** 696-709.

LUO, Z., HUANG, Z., XIE, N., GAO, X., XU, T., FANG, Y. & ZHANG, Z. 2017. Numerical and experimental study on temperature control of solar panels with form-stable paraffin/expanded graphite composite PCM. *Energy Conversion and Management,* 149**,** 416-423.

MA, T., YANG, H., ZHANG, Y., LU, L. & WANG, X. 2015. Using phase change materials in photovoltaic systems for thermal regulation and electrical efficiency improvement: A review and outlook. *Renewable and Sustainable Energy Reviews,* 43**,** 1273-1284.

MAHAMUDUL, H., RAHMAN, M. M., METSELAAR, H. & MEKHILEF, S. 2016. Temperature Regulation of Photovoltaic Module Using Phase Change Material: A Numerical Analysis and Experimental Investigation.

MALVI, C., DIXON-HARDY, D. & CROOK, R. 2011. Energy balance model of combined photovoltaic solar-thermal system incorporating phase change material. *Solar Energy,* 85**,** 1440-1446.

MANUAL, F. 2001. Chapter 21: Modeling Solidification and Melting; ANSYS. *Inc.: Canonsburg, PA, USA*.

MARCHAND, M., GHENNIOUI, A., WEY, E. & WALD, L. 2018. Comparison of several satellite-derived databases of surface solar radiation against ground measurement in Morocco. *Advances in Science and Research,* 15**,** 21-29.

MARKVARTA, T. & CASTAÑERB, L. 2011. Principles of solar cell operation. *Practical Handbook of Photovoltaics: Fundamentals and Applications***,** 7.

MAZRAEH, A., BABAYAN, M., YARI, M., SEFIDAN, A. M. & SAHA, S. C. 2018. Theoretical study on the performance of a solar still system integrated with PCM-PV module for sustainable water and power generation. *Desalination,* 443**,** 184-197.

MITTELMAN, G., ALSHARE, A. & DAVIDSON, J. H. 2009. A model and heat transfer correlation for rooftop integrated photovoltaics with a passive air cooling channel. *Solar Energy,* 83**,** 1150-1160.

MUKHERJEE, D. 2018. A Review Study on the Thermo Physical Properties and Storage Applications of Phase Change Materials. *World Scientific News,* 98**,** 185-198.

NEHARI, T., BENLAKAM, M. & NEHARI, D. 2016a. Effect of the Fins Length for the Passive Cooling of the Photovoltaic Panels. *Periodica Polytechnica. Engineering. Mechanical Engineering,* 60**,** 89.

NEHARI, T., BENLEKKAM, M., NEHARI, D. & YOUCEFI, A. 2016b. The Effect of Inclination on the Passive cooling of the solar PV panel by using Phase change Material. *International Journal of Renewable Energy Research (IJRER),* 6**,** 132-139.

NERL. 2016. *Photovoltiac research* [Online]. Polycrystalline Thin-Film Materials and Devices R&D. Available: http://www.nrel.gov/pv/thinfilm.html [Accessed 11 9 2016].

NIŽETIĆ, S., ARıCı, M., BILGIN, F. & GRUBIŠIĆ-ČABO, F. 2018. Investigation of pork fat as potential novel phase change material for passive cooling applications in photovoltaics. *Journal of Cleaner Production,* 170**,** 1006-1016.

NOUIRA, M. & SAMMOUDA, H. 2018. Numerical study of an inclined photovoltaic system coupled with phase change material under various operating conditions. *Applied Thermal Engineering,* 141**,** 958-975.

ORG, P. E. 2018. *Declination Angle* [Online]. Available: https://www.pveducation.org/pvcdrom/properties-of-sunlight/declination-angle.

OSBORNE, M. 2018. Global solar market hit 98.9GW in 2017 - SolarPower Europe. PVTech.

PANDEY, A., TYAGI, V., JEYRAJ, A., SELVARAJ, L., RAHIM, N. & TYAGI, S. 2016. Recent advances in solar photovoltaic systems for emerging trends and advanced applications. *Renewable and Sustainable Energy Reviews,* 53**,** 859-884.

PERSPECTIVES, S. E. 2011. International Energy Agency (IEA).

PLUSS. 2018. *PCMs Product Range, properties* [Online]. Pluss. Available: http://www.pluss.co.in/product-range-PCM.php [Accessed 19/09 2018].

POIRIER, D. & SALCUDEAN, M. 1988. On numerical methods used in mathematical modeling of phase change in liquid metals. *Journal of heat transfer,* 110**,** 562-570.

PRODUCTS, P. 2013. PlusICE Phase Change Materials

PVEDUCATION.ORG. 2017. *Module Materials* [Online]. Available: http://www.pveducation.org/pvcdrom/modules/module-materials [Accessed 7 2 2017].
QURESHI, Z. A., ALI, H. M. & KHUSHNOOD, S. 2018. Recent advances on thermal conductivity enhancement of phase change materials for energy storage system: a review. *International Journal of Heat and Mass Transfer,* 127**,** 838-856.
RENOGY. 2016. *SOLAR MODULES* [Online]. Available: https://www.renogy.com/learn-solar-panels/ [Accessed 9 2016].
SAHU, A., YADAV, N. & SUDHAKAR, K. 2016. Floating photovoltaic power plant: A review. *Renewable and Sustainable Energy Reviews,* 66**,** 815-824.
SAKIN, M., KAYMAK-ERTEKIN, F. & ILICALI, C. 2009. Convection and radiation combined surface heat transfer coefficient in baking ovens. *Journal of food engineering,* 94**,** 344-349.
SANTBERGEN, R. & VAN ZOLINGEN, R. C. 2008. The absorption factor of crystalline silicon PV cells: a numerical and experimental study. *Solar energy materials and solar cells,* 92**,** 432-444.
SCHWINGSHACKL, C., PETITTA, M., WAGNER, J. E., BELLUARDO, G., MOSER, D., CASTELLI, M., ZEBISCH, M. & TETZLAFF, A. 2013. Wind effect on PV module temperature: Analysis of different techniques for an accurate estimation. *Energy Procedia,* 40**,** 77-86.
SENGUPTA, M., HABTE, A., GUEYMARD, C., WILBERT, S. & RENNE, D. 2017. Best practices handbook for the collection and use of solar resource data for solar energy applications. National Renewable Energy Lab.(NREL), Golden, CO (United States).
SHAH, K. W. 2018. A Review on Enhancement of Phase Change Materials-A Nanomaterials Perspective. *Energy and Buildings*.
SHUKLA, A., KANT, K., SHARMA, A. & BIWOLE, P. H. 2017. Cooling methodologies of photovoltaic module for enhancing electrical efficiency: A review. *Solar Energy Materials and Solar Cells,* 160**,** 275-286.
SINGH, P. & RAVINDRA, N. M. 2012. Temperature dependence of solar cell performance—an analysis. *Solar Energy Materials and Solar Cells,* 101**,** 36-45.
SMITH, C. J., FORSTER, P. M. & CROOK, R. 2014. Global analysis of photovoltaic energy output enhanced by phase change material cooling. *Applied Energy,* 126**,** 21-28.
SMITH, G. D. 1985. *Numerical solution of partial differential equations: finite difference methods*, Oxford university press.
SODA. 2019. *Solar Iradiation data* [Online]. Available: http://www.soda-pro.com/web-services/radiation/helioclim-3-archives-for-free 2019].
SUKHATME, K. & SUKHATME, S. P. 1996. *Solar energy: principles of thermal collection and storage*, Tata McGraw-Hill Education.
TANIMOTO, J. 2014. *Mathematical analysis of environmental system*, Springer.
TANUWIJAVA, A. O., HO, C. J., LAI, C.-M. & HUANG, C.-Y. 2013. Numerical investigation of the thermal management performance of MEPCM modules for PV applications. *Energies,* 6**,** 3922-3936.
TRAPANI, K. & MILLAR, D. L. 2014. The thin film flexible floating PV (T3F-PV) array: The concept and development of the prototype. *Renewable Energy,* 71**,** 43-50.

TRAPANI, K. & REDÓN SANTAFÉ, M. 2015. A review of floating photovoltaic installations: 2007–2013. *Progress in Photovoltaics: Research and Applications,* 23**,** 524-532.

TWAHA, S., ZHU, J., YAN, Y. & LI, B. 2016. A comprehensive review of thermoelectric technology: Materials, applications, modelling and performance improvement. *Renewable and Sustainable Energy Reviews,* 65**,** 698-726.

WANG, C., LIN, T., LI, N. & ZHENG, H. 2016. Heat transfer enhancement of phase change composite material: Copper foam/paraffin. *Renewable Energy,* 96**,** 960-965.

WAQAS, A. & JI, J. 2017. Thermal management of conventional PV panel using PCM with movable shutters–A numerical study. *Solar Energy,* 158**,** 797-807.

WEINLÄDER, H., BECK, A. & FRICKE, J. 2005. PCM-facade-panel for daylighting and room heating. *Solar Energy,* 78**,** 177-186.

XIAO, X., ZHANG, P. & LI, M. 2013. Preparation and thermal characterization of paraffin/metal foam composite phase change material. *Applied energy,* 112**,** 1357-1366.

XIAO, X., ZHANG, P. & LI, M. 2014. Effective thermal conductivity of open-cell metal foams impregnated with pure paraffin for latent heat storage. *International Journal of Thermal Sciences,* 81**,** 94-105.

YOVANOVICH, M., CULHAM, J. & TEERTSTRA, P. 1997. Calculating interface resistance. *Electronics Cooling,* 3**,** 24-29.

YUAN, W., JI, J., MODJINOU, M., ZHOU, F., LI, Z., SONG, Z., HUANG, S. & ZHAO, X. 2018. Numerical simulation and experimental validation of the solar photovoltaic/thermal system with phase change material. *Applied Energy,* 232**,** 715-727.

ZALBA, B., MARíN, J. M., CABEZA, L. F. & MEHLING, H. 2003. Review on thermal energy storage with phase change: materials, heat transfer analysis and applications. *Applied thermal engineering,* 23**,** 251-283.

ZHANG, Z., HE, Z., LIANG, C., LIND, A. H., DIYAF, A., PENG, Y. & WILSON, J. I. 2014. A preliminary development in hybrid a-silicon/polymer solar cells. *Renewable Energy,* 63**,** 145-152.

ZHAO, J., MA, T., LI, Z. & SONG, A. 2019. Year-round performance analysis of a photovoltaic panel coupled with phase change material. *Applied energy,* 245**,** 51-64.

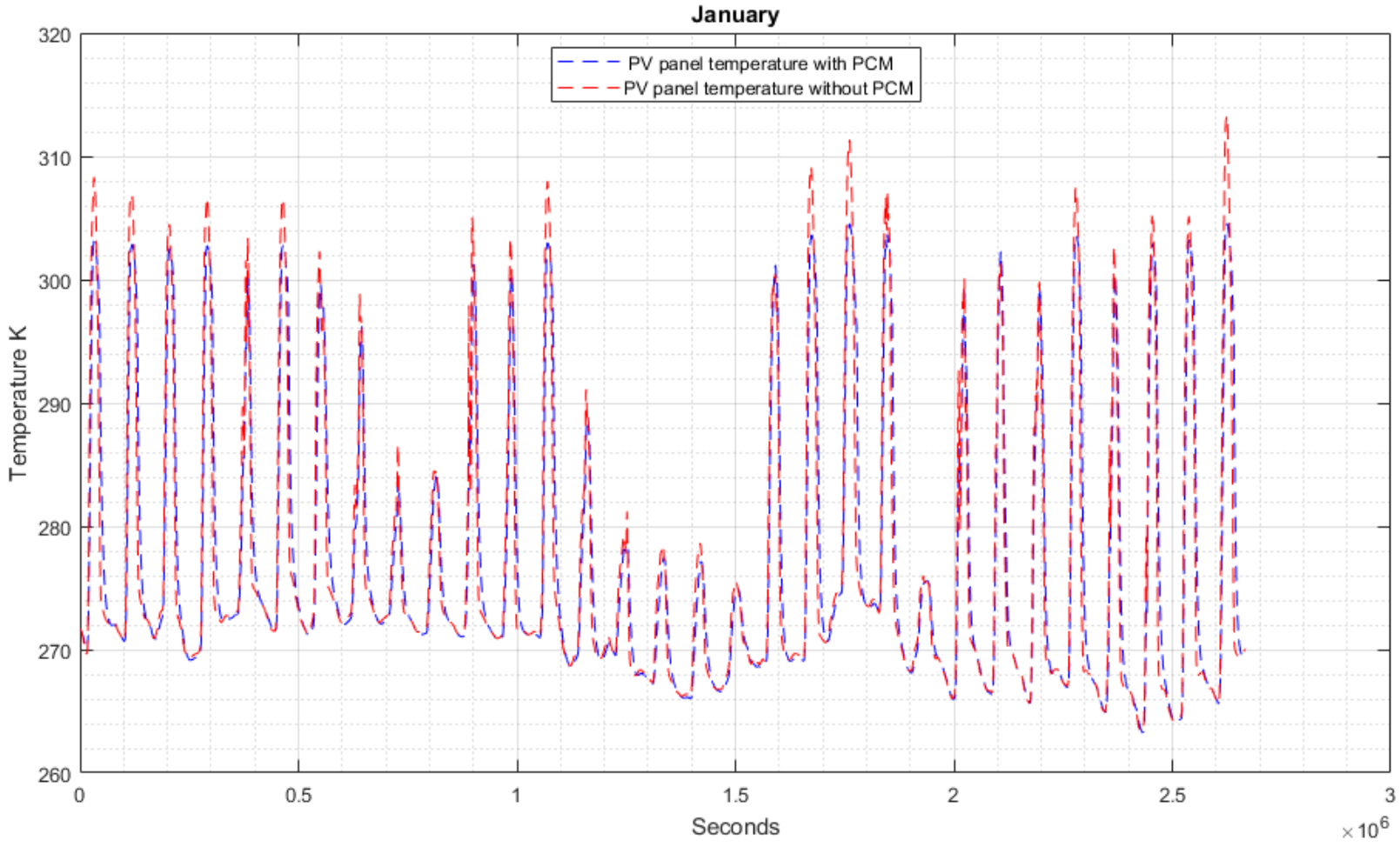

Appendix figure 1: Temperature trends for the PV-PCM & stand-alone PV panel Baghdad, January.

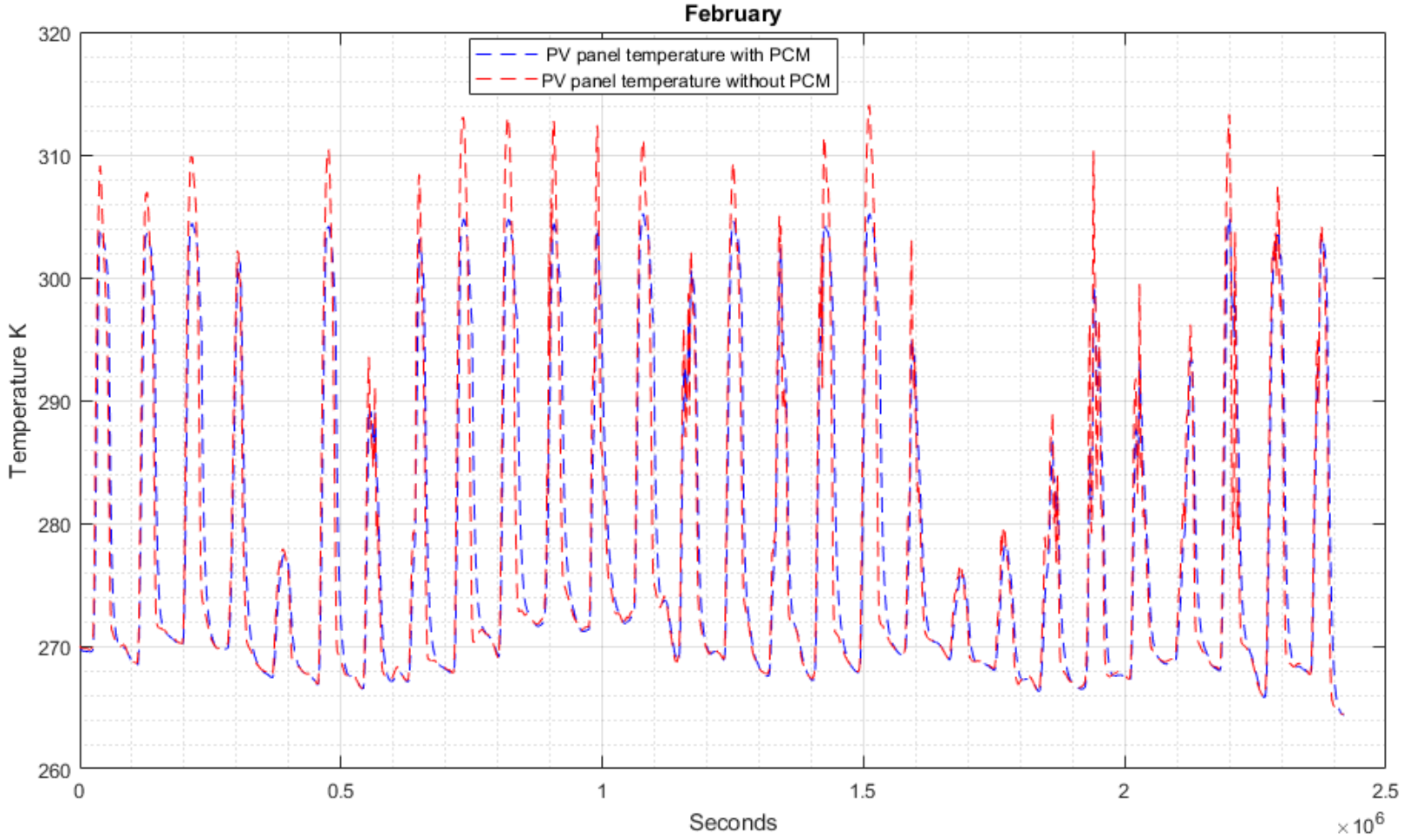

Append figure 2: Temperature trends for the PV-PCM & stand-alone PV panel Baghdad, February.

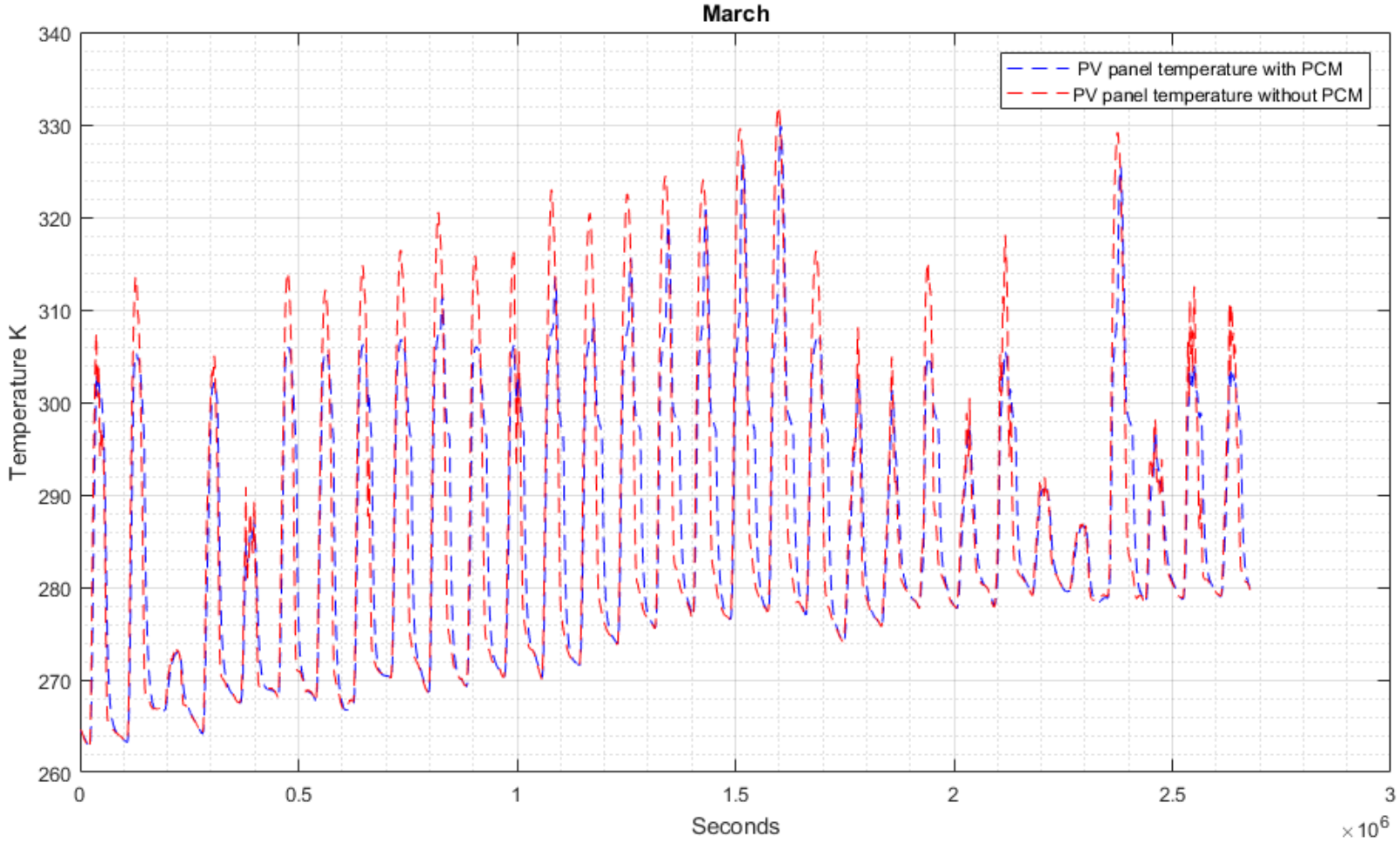

Appendix figure 3: Temperature trends for the PV-PCM & stand-alone PV panel Baghdad, March.

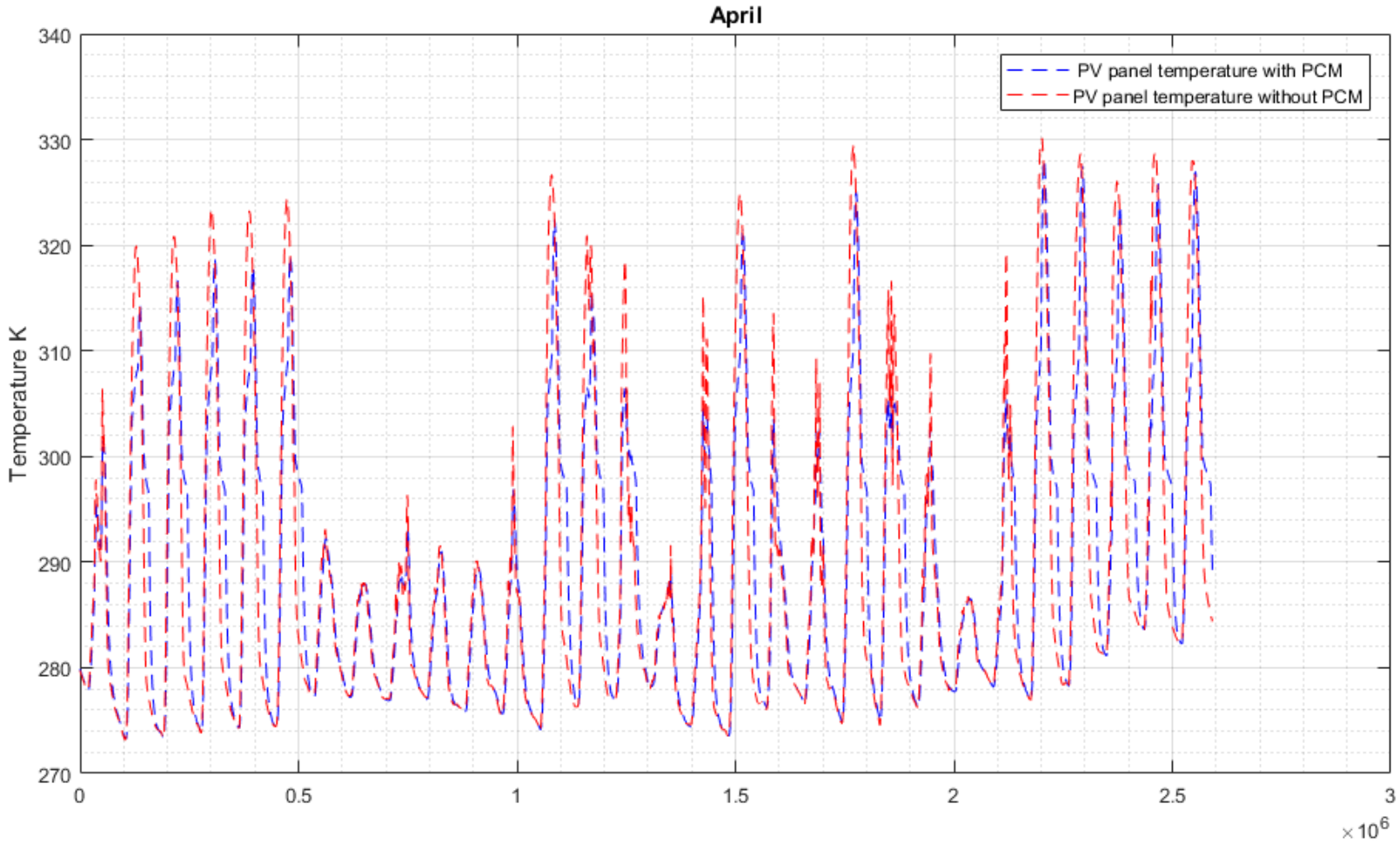

Appendix figure 4: Temperature trends for the PV-PCM & stand-alone PV panel Baghdad, April.

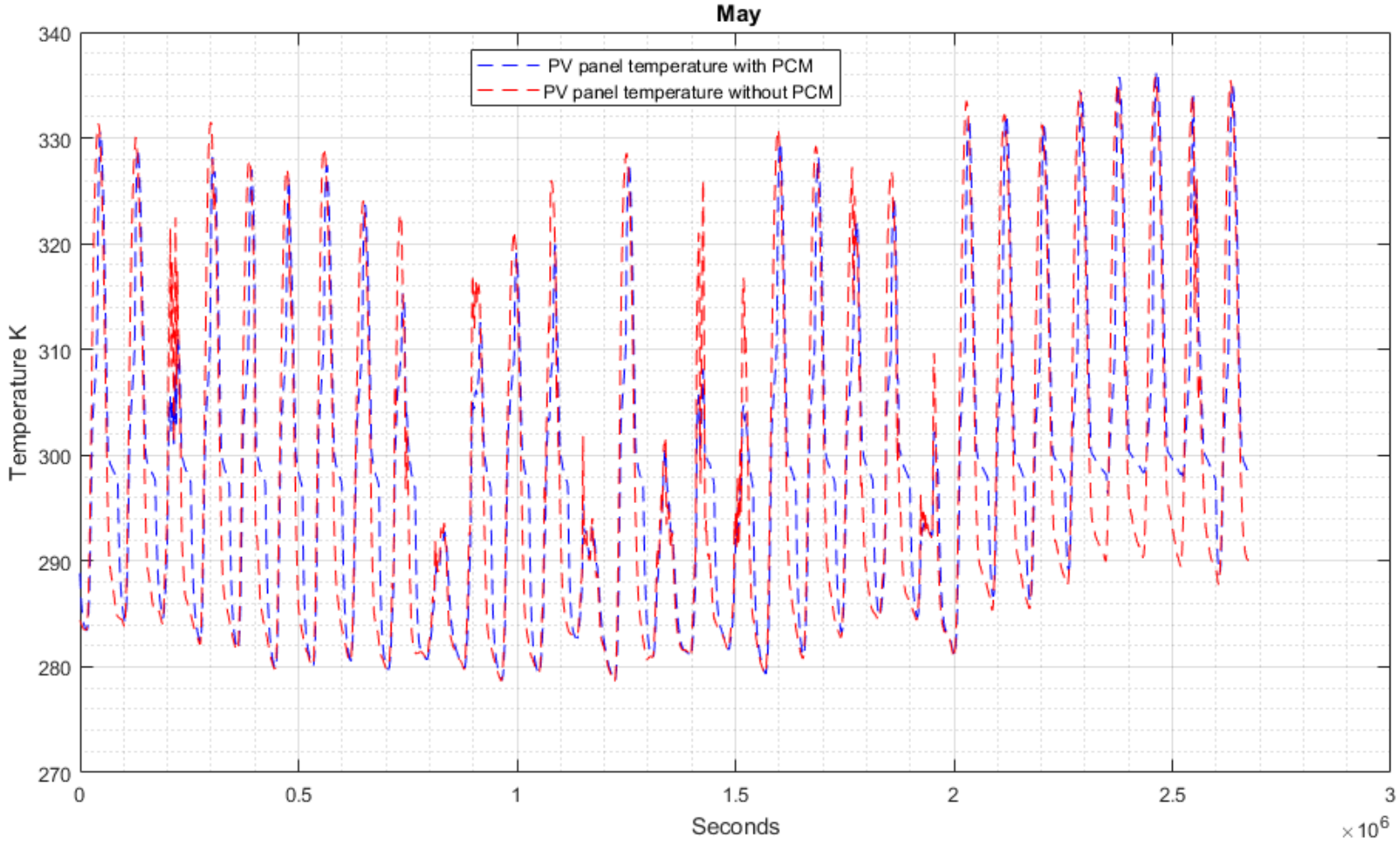

Appendix figure 5: Temperature trends for the PV-PCM & stand-alone PV panel Baghdad, May.

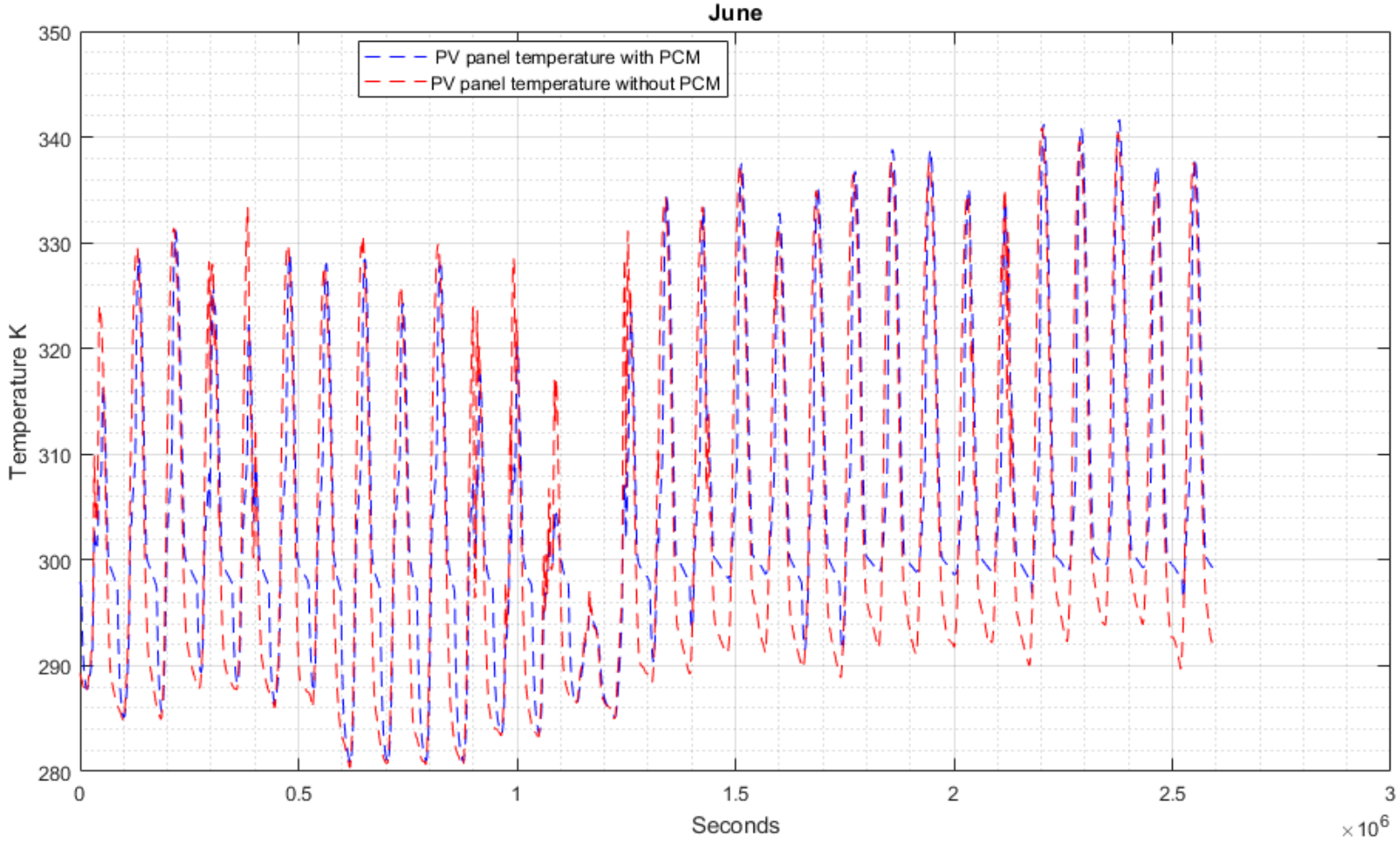

Appendix figure 6: Temperature trends for the PV-PCM & stand-alone PV panel Baghdad, June.

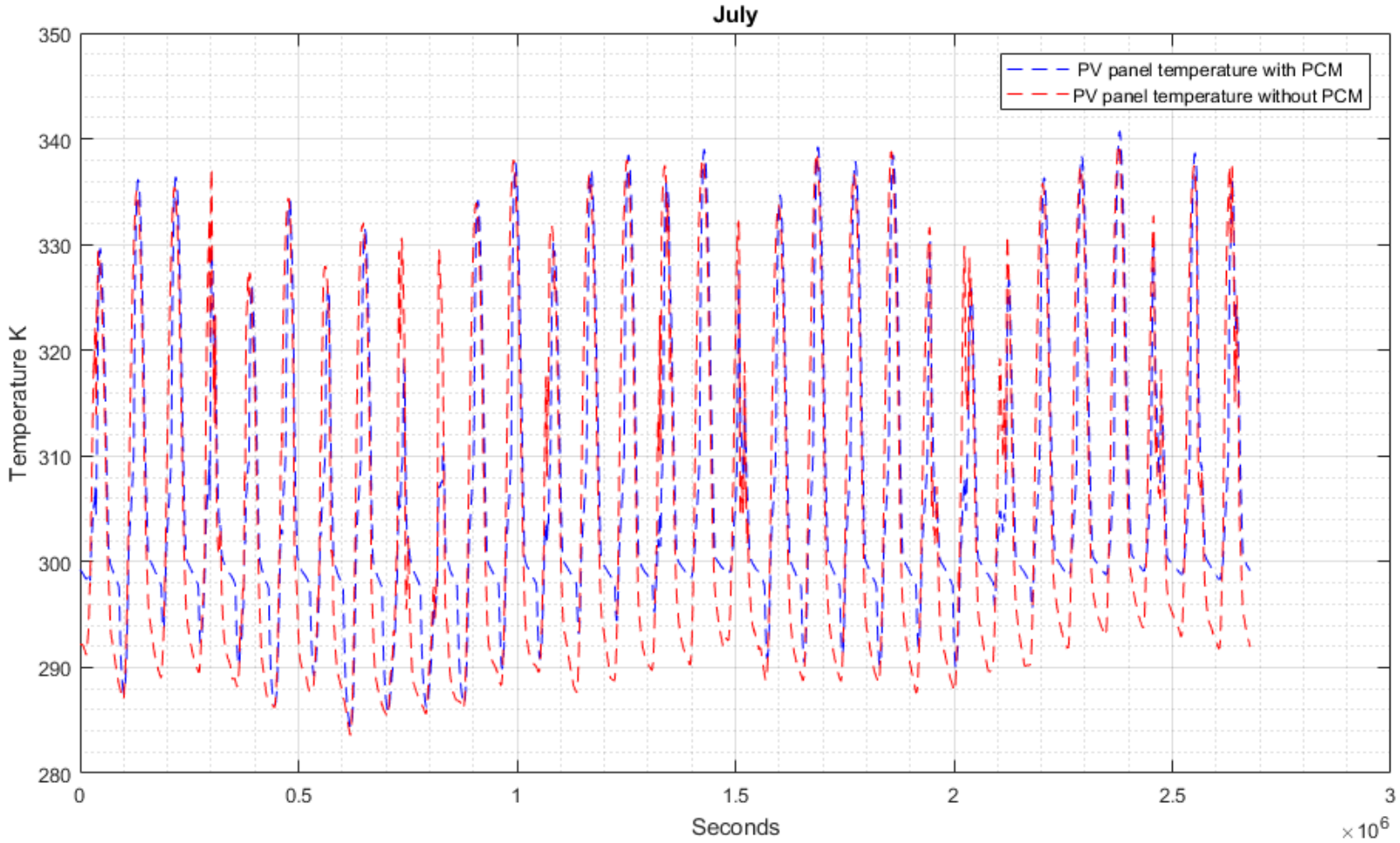

Appendix figure 7: Temperature trends for the PV-PCM & stand-alone PV panel Baghdad, July.

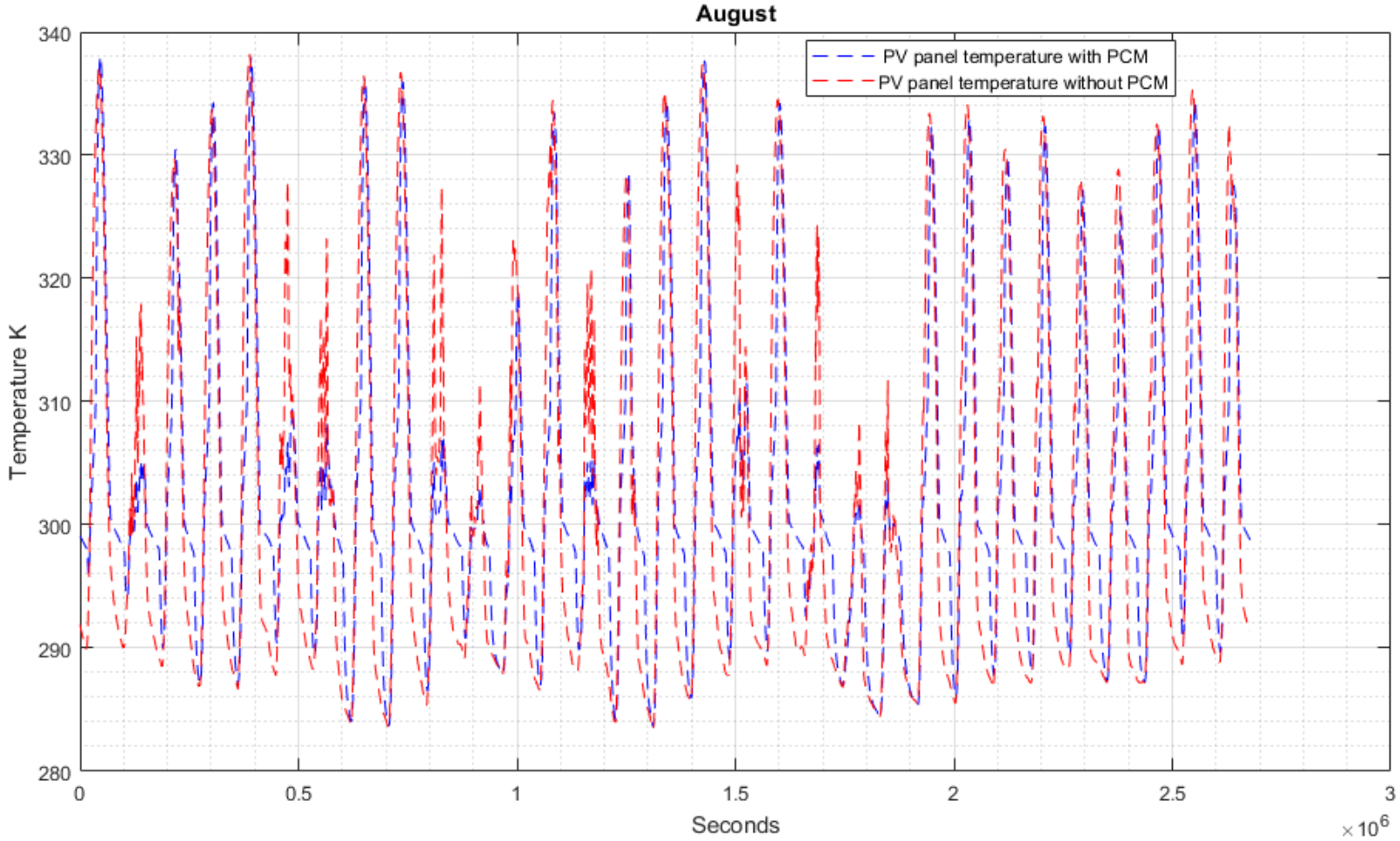

Appendix figure 8: Temperature trends for the PV-PCM & stand-alone PV panel Baghdad, August.

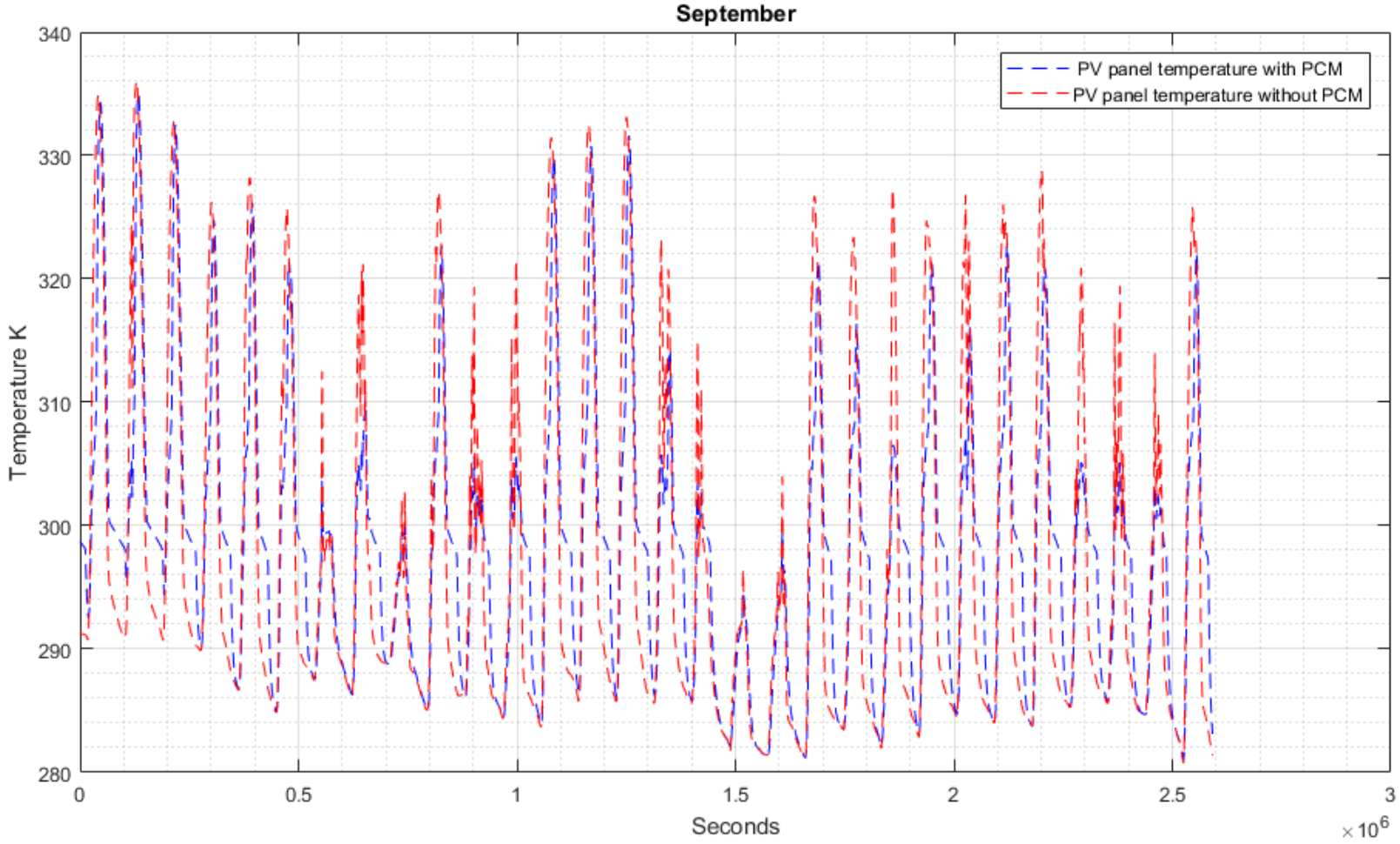

Appendix figure 9: Temperature trends for the PV-PCM & stand-alone PV panel Baghdad, September.

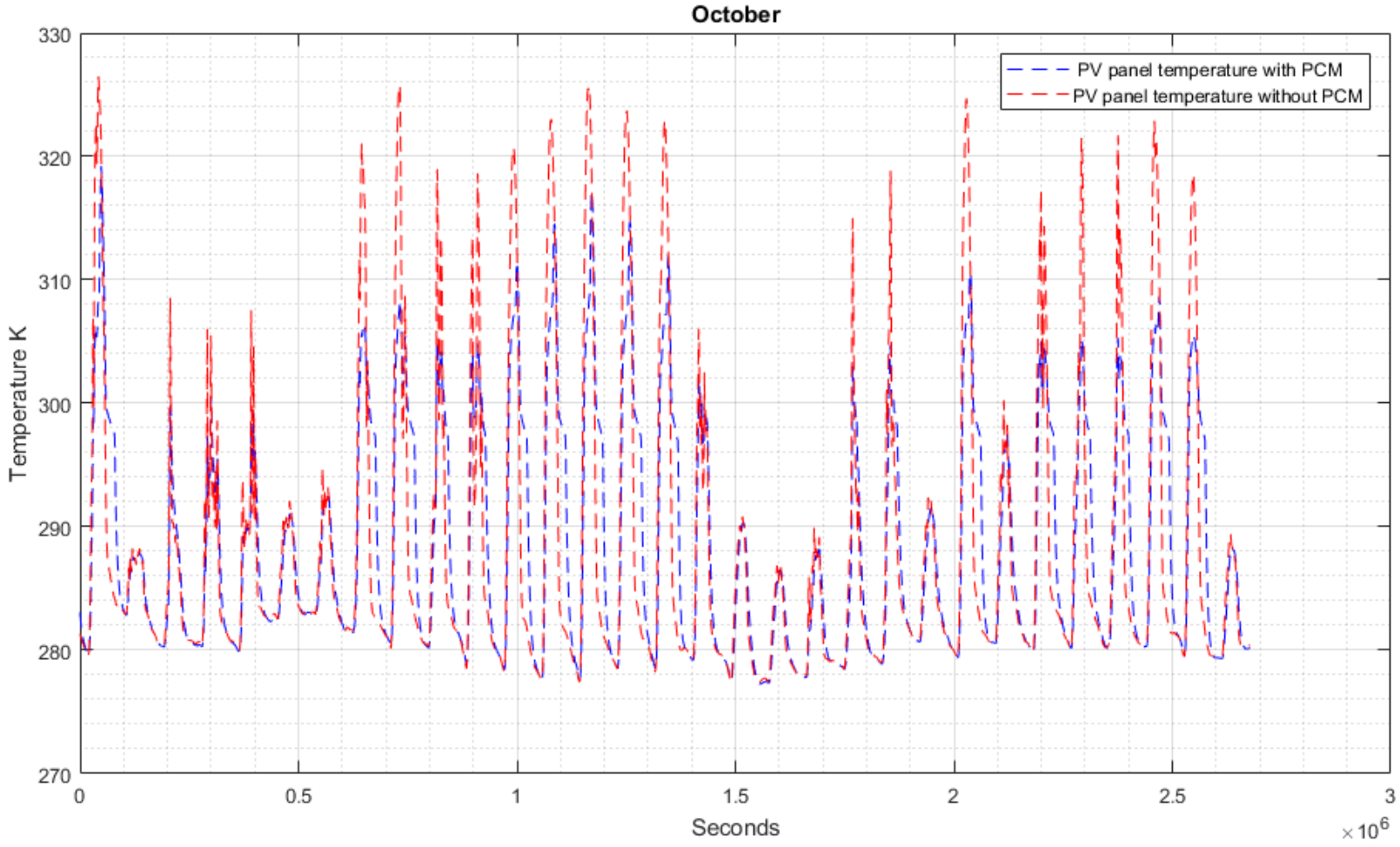

Appendix figure 10: Temperature trends for the PV-PCM & stand-alone PV panel Baghdad, October.

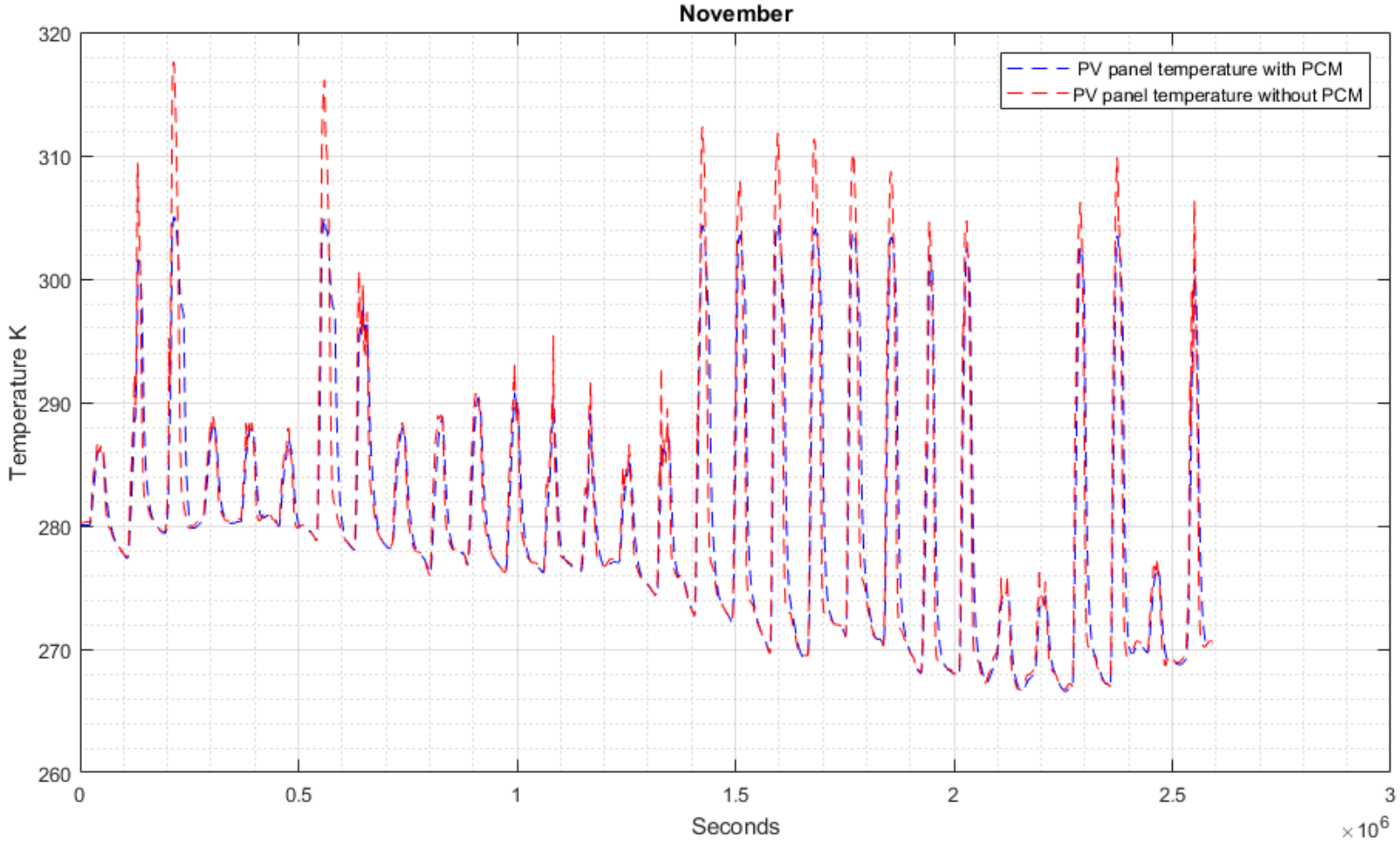

Appendix figure 11: Temperature trends for the PV-PCM & stand-alone PV panel Baghdad, November.

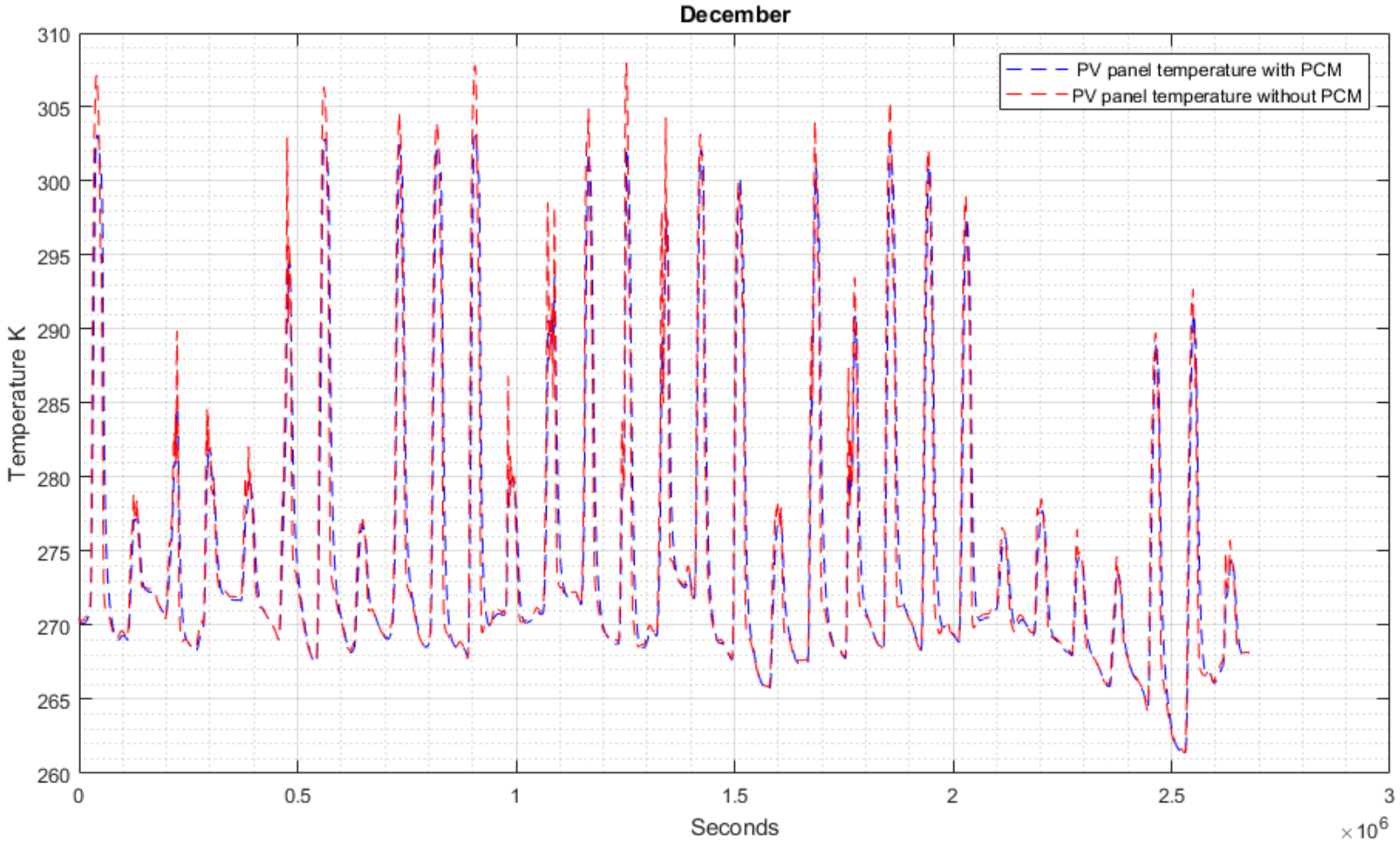

Appendix figure 12: Temperature trends for the PV-PCM & stand-alone PV panel Baghdad, December.

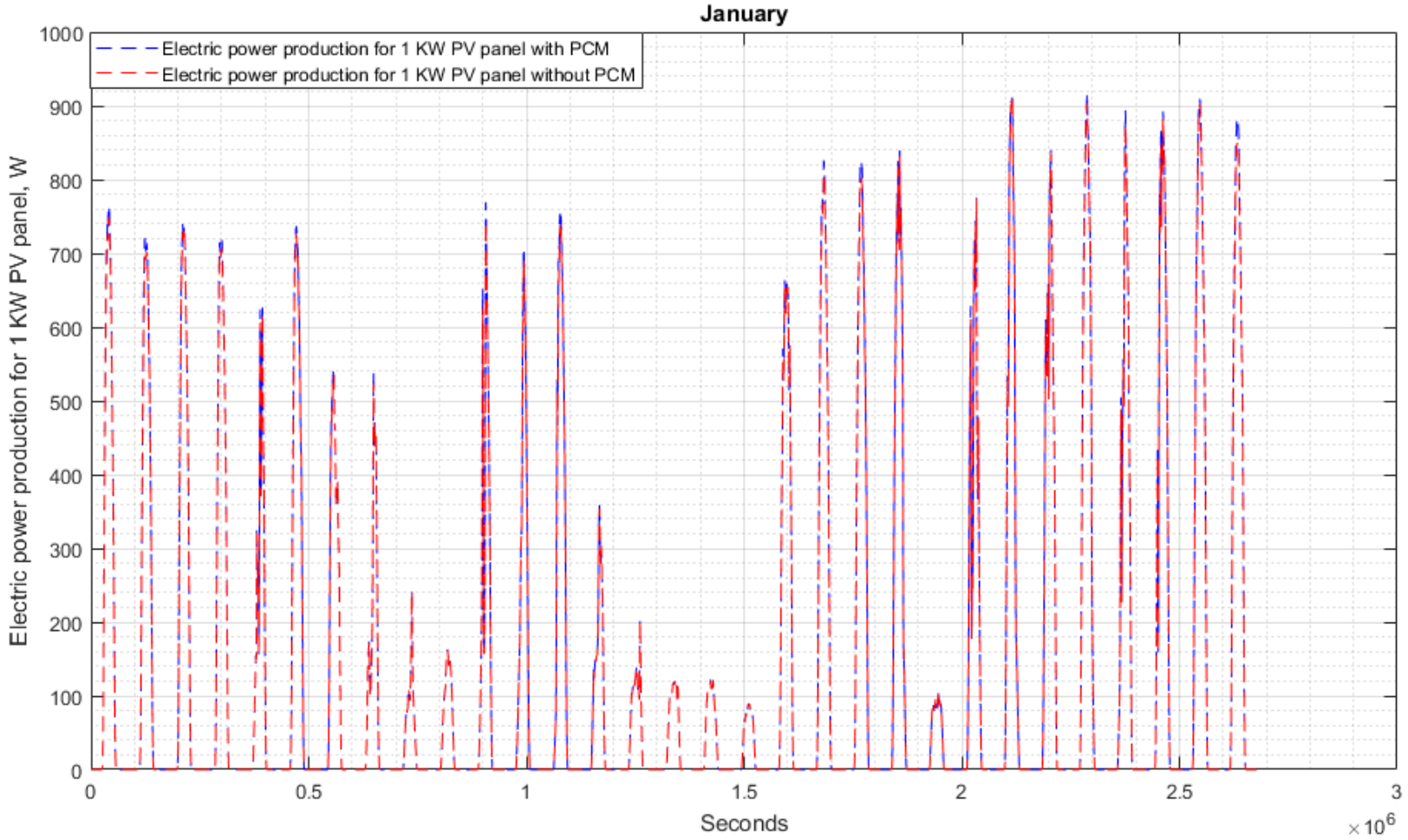

Appendix figure 13: The electrical power production for 1 kw of the PV-PCM and 1 kw of stand-alone PV panel, Baghdad, January.

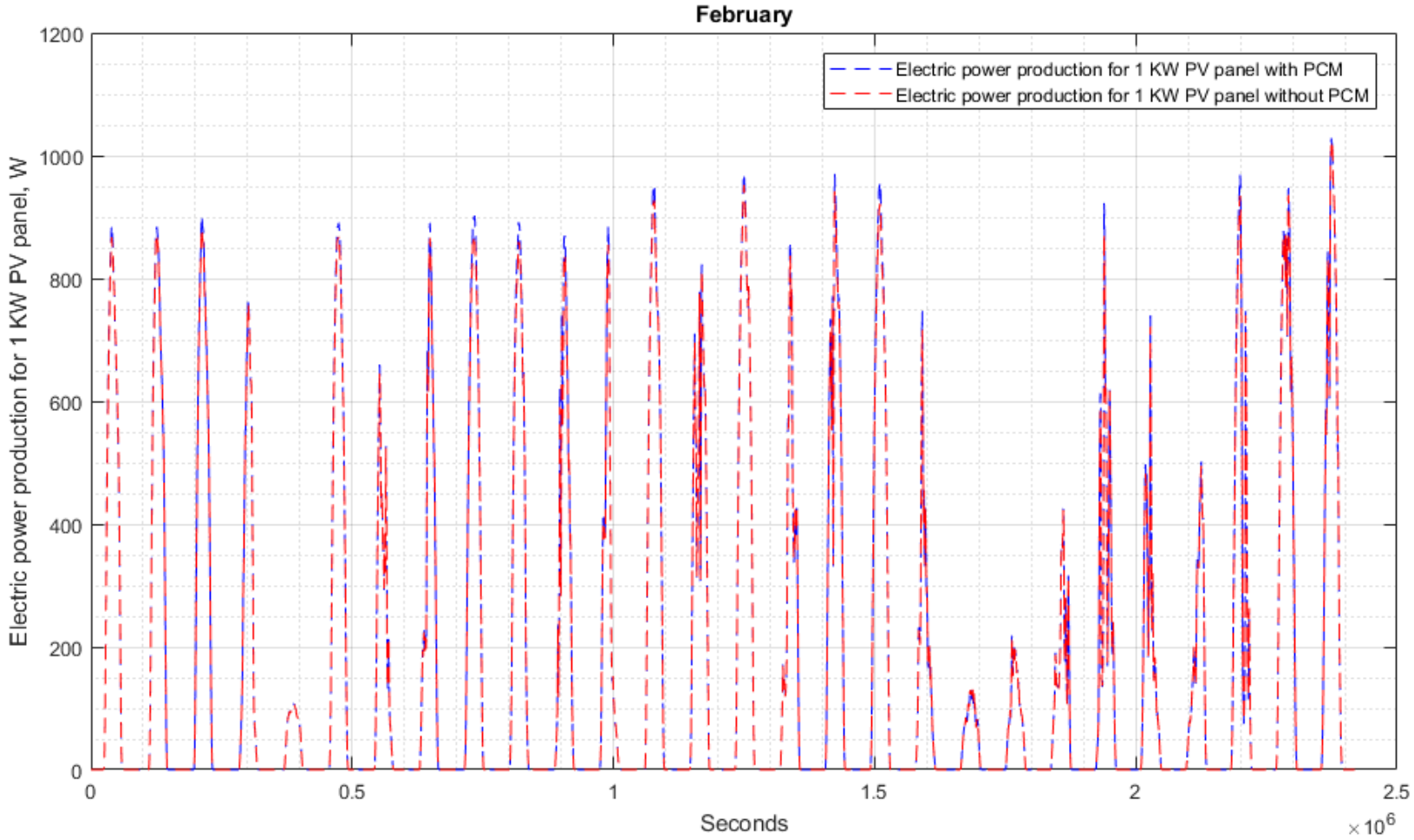

Appendix figure 14: The electrical power production for 1 kW of the PV-PCM and 1 kW of stand-alone PV panel, Baghdad, February.

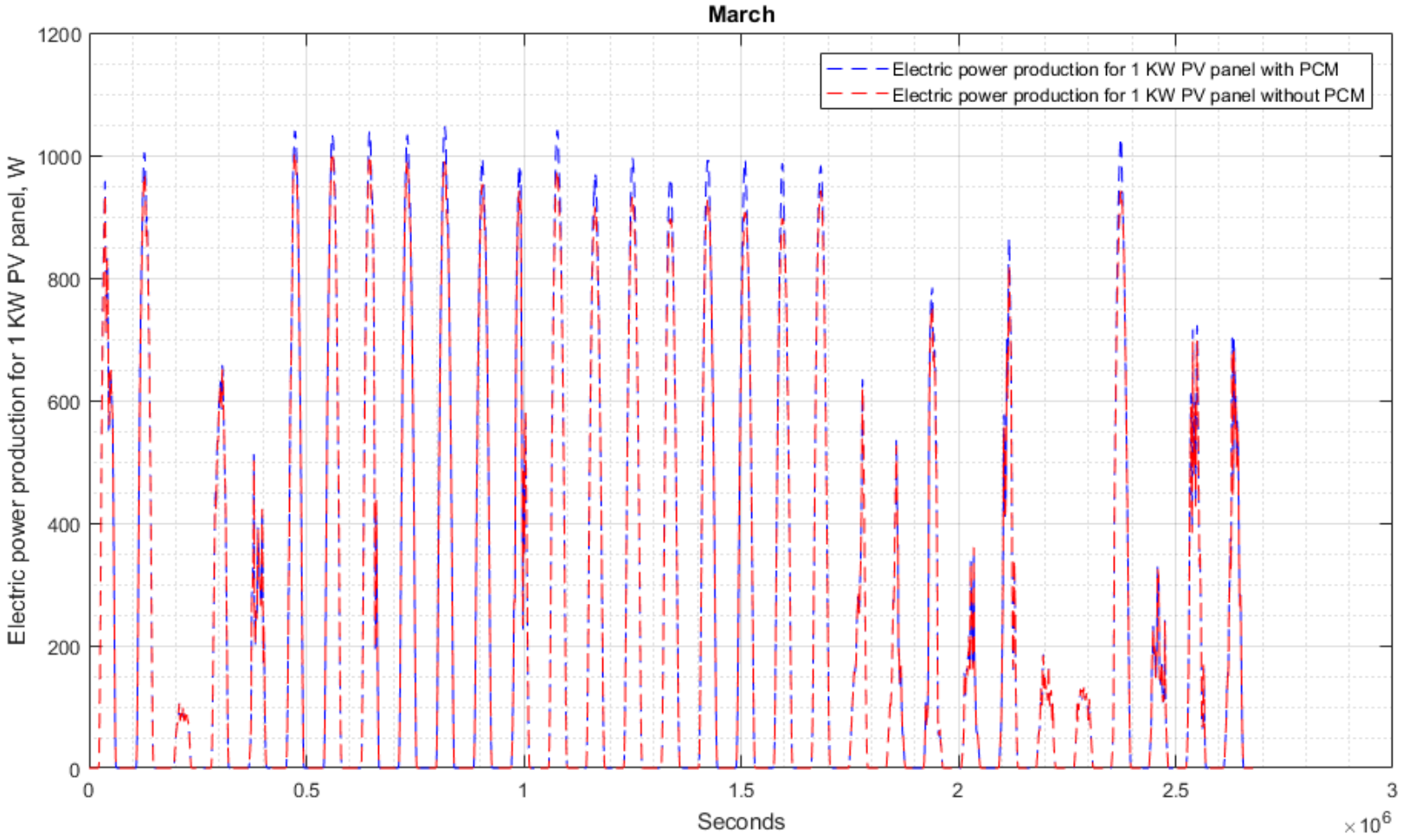

Appendix figure 15: The electrical power production for 1 kW of the PV-PCM and 1 kW of stand-alone PV panel, Baghdad, March.

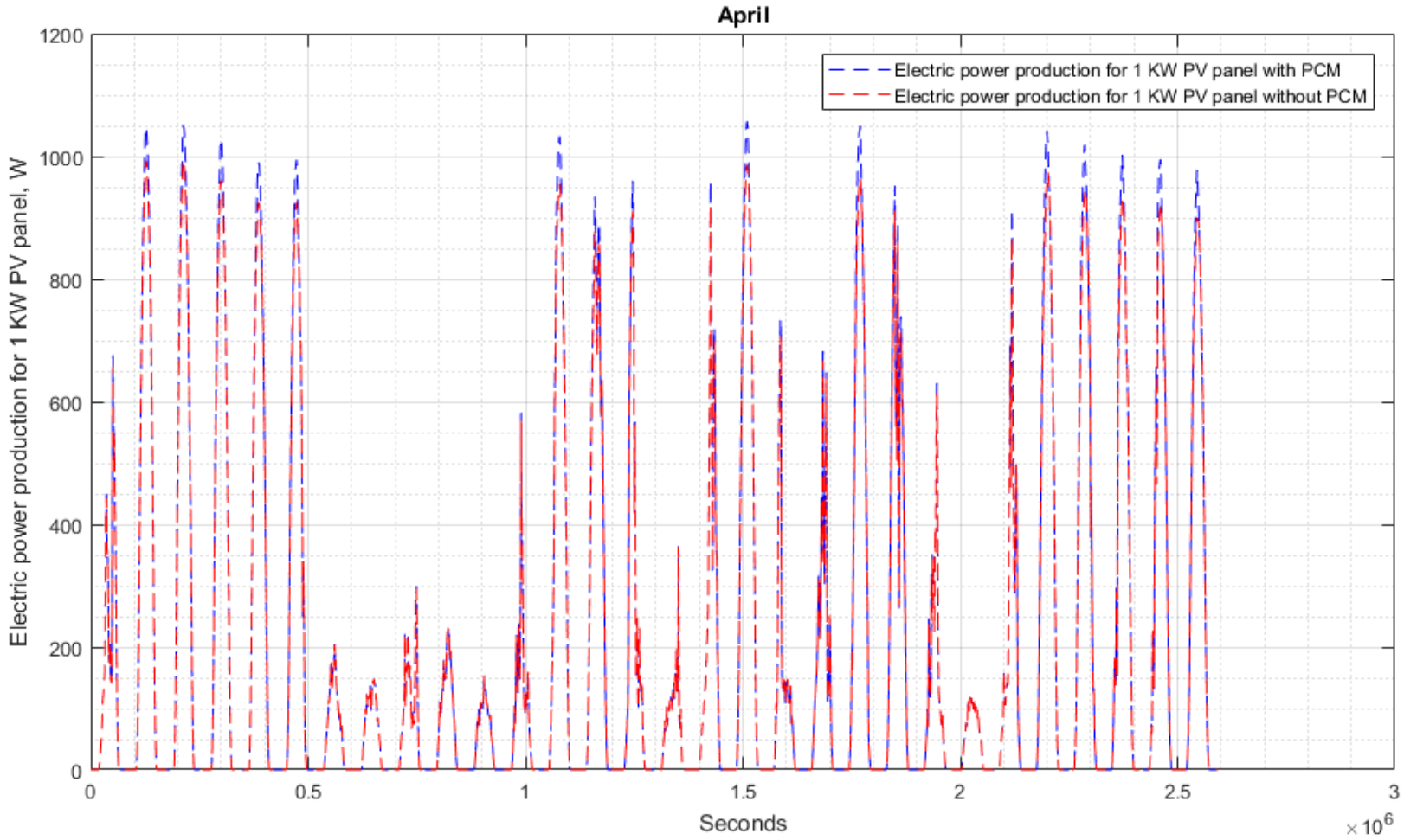

Appendix figure 16: The electrical power production for 1 kW of the PV-PCM and 1 kW of stand-alone PV panel, Baghdad, April.

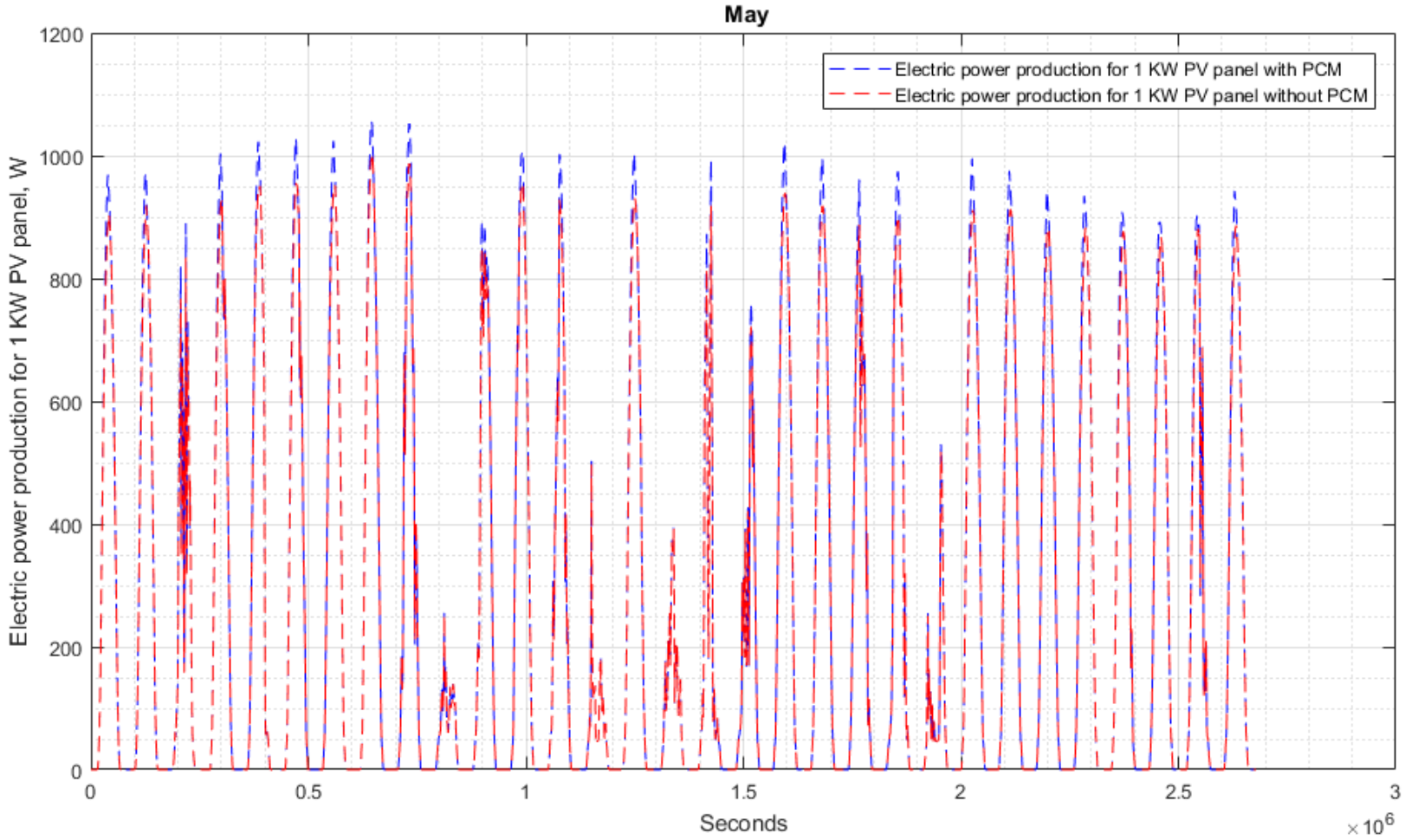

Appendix figure 17: The electrical power production for 1 kW of the PV-PCM and 1 kW of stand-alone PV panel, Baghdad, May.

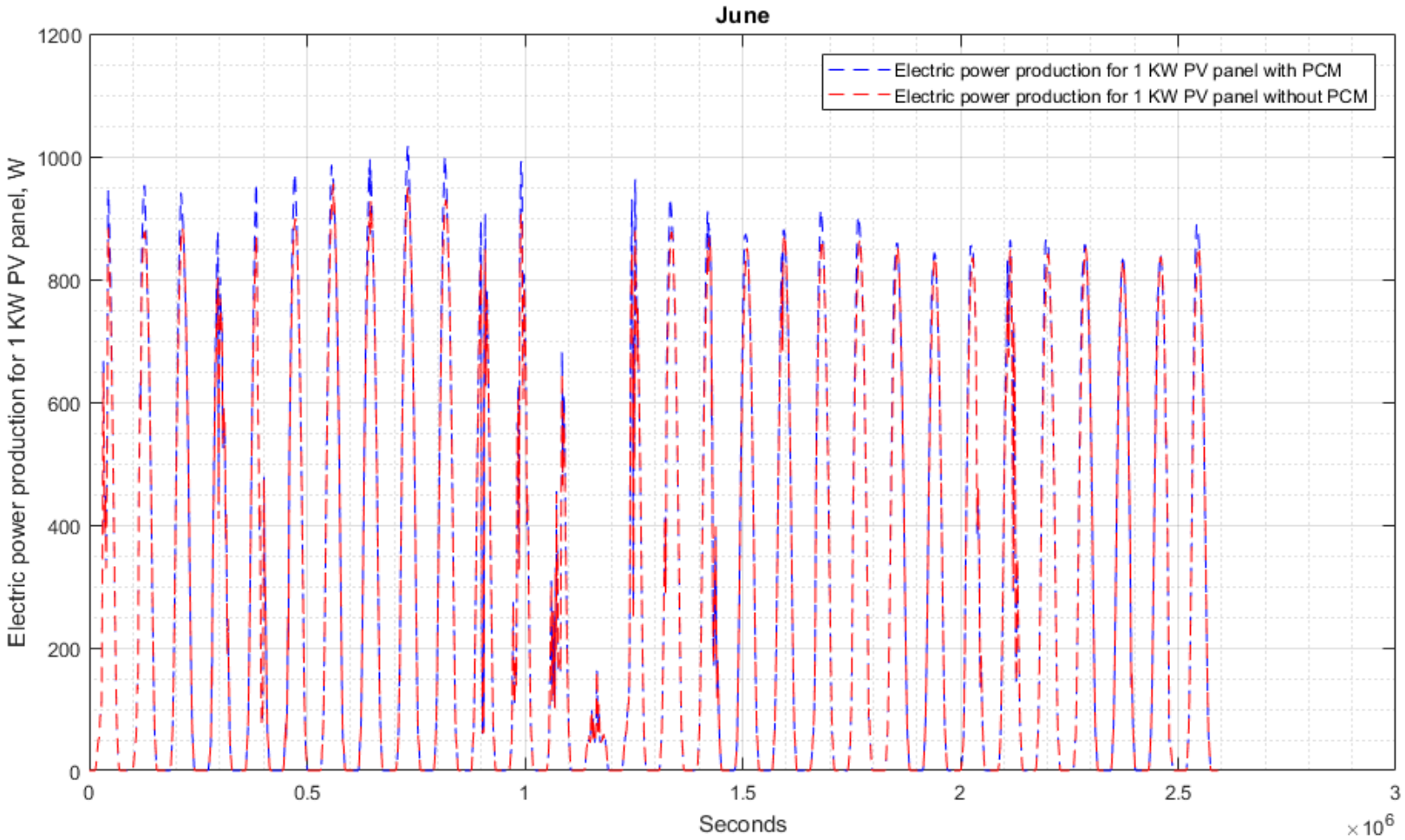

Appendix figure 18: The electrical power production for 1 kW of the PV-PCM and 1 kW of stand-alone PV panel, Baghdad, June.

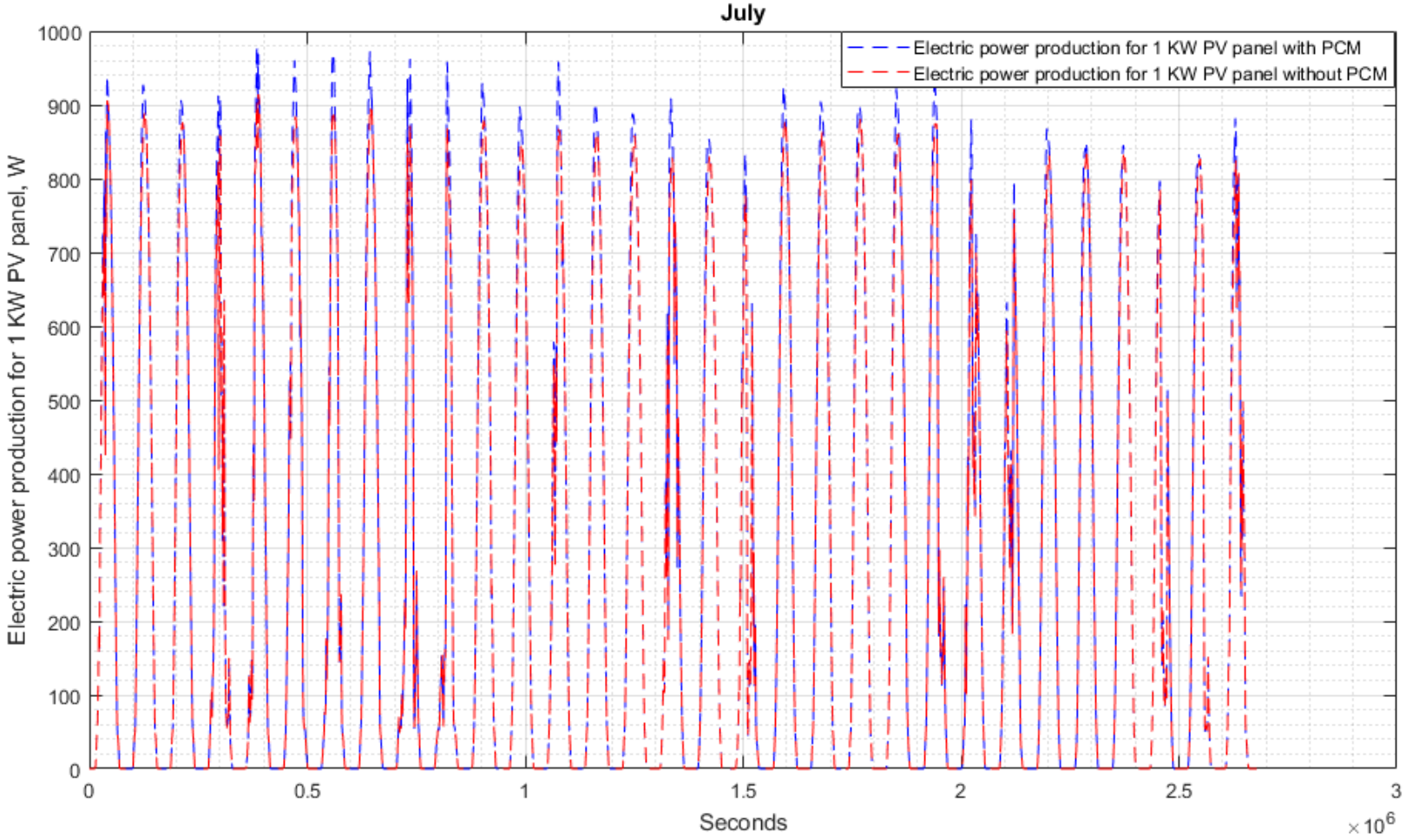

Appendix figure 19: The electrical power production for 1 kW of the PV-PCM and 1 kW of stand-alone PV panel, Baghdad, July.

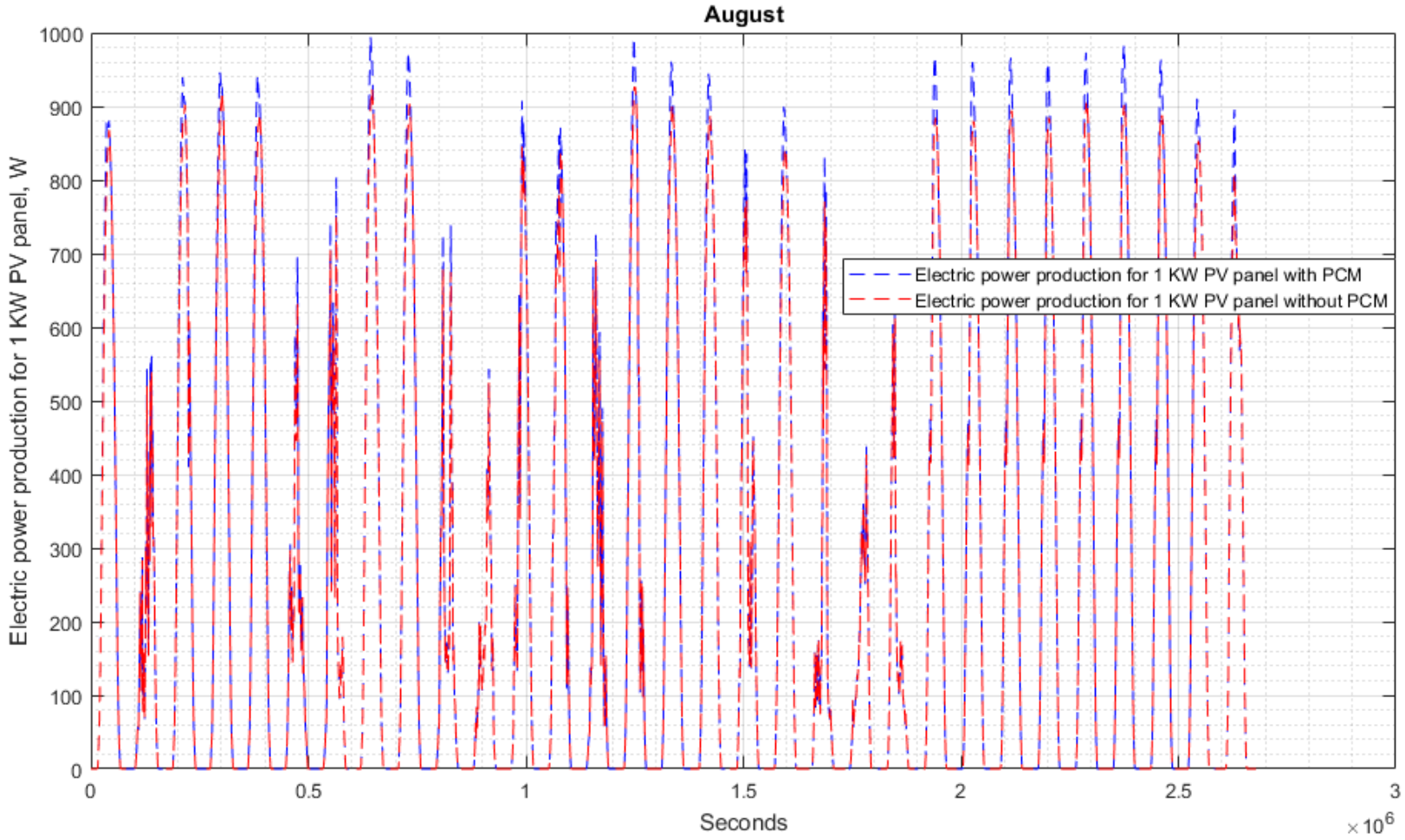

Appendix figure 20: The electrical power production for 1 kW of the PV-PCM and 1 kW of stand-alone PV panel, Baghdad, August.

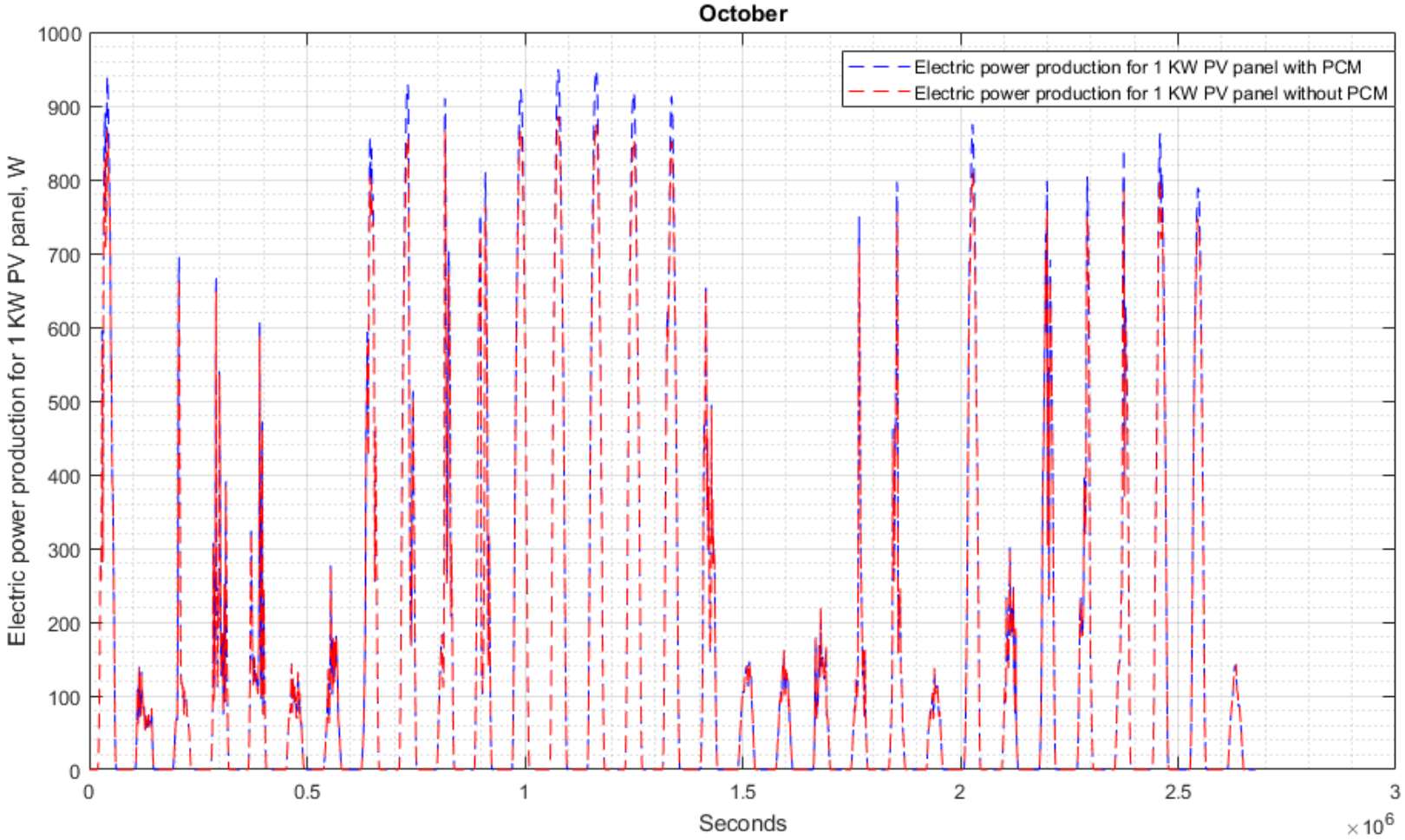

Appendix figure 21: The electrical power production for 1 kW of the PV-PCM and 1 kW of stand-alone PV panel, Baghdad, October.

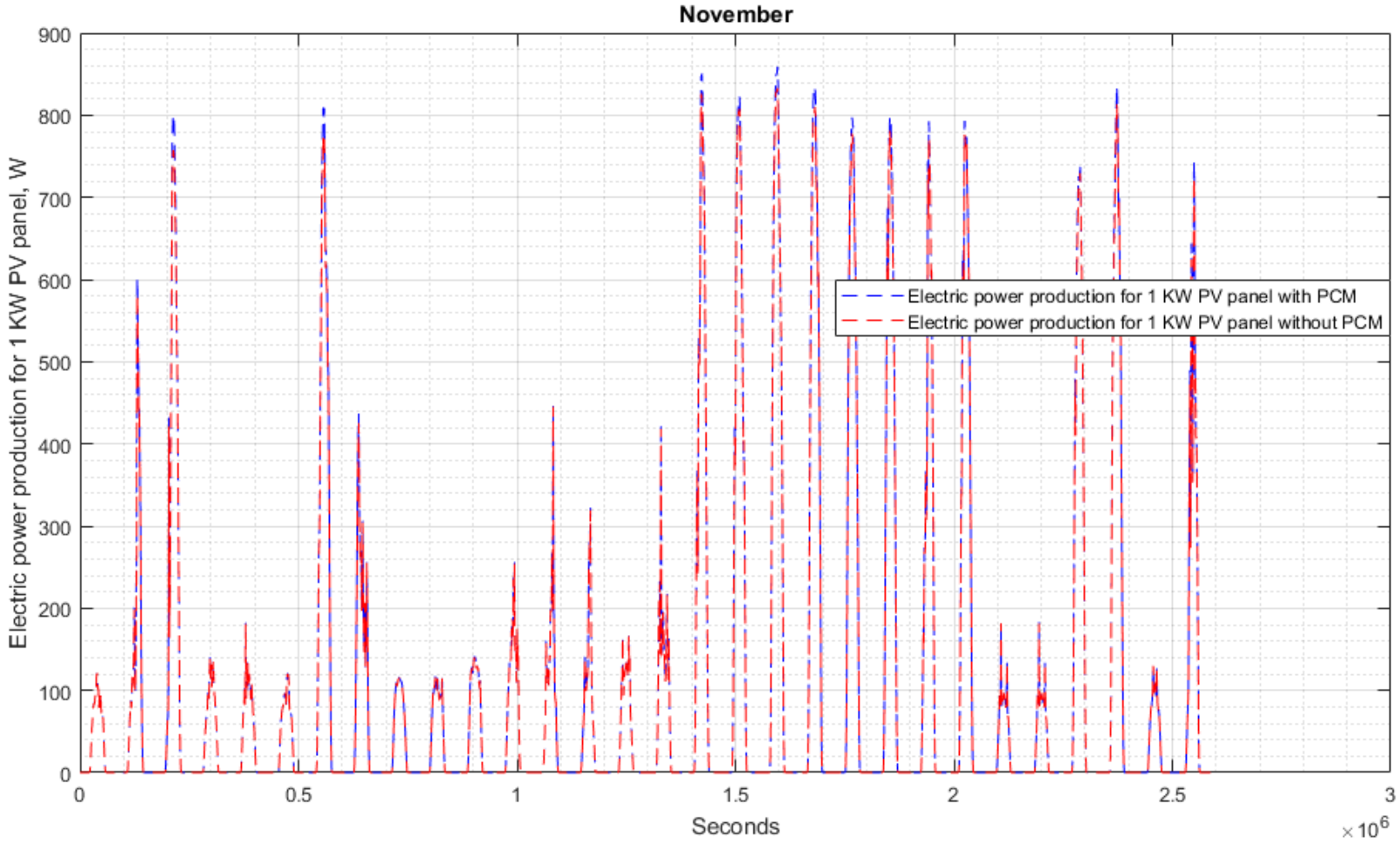

Appendix figure 22: The electrical power production for 1 kW of the PV-PCM and 1 kW of stand-alone PV panel, Baghdad, November.

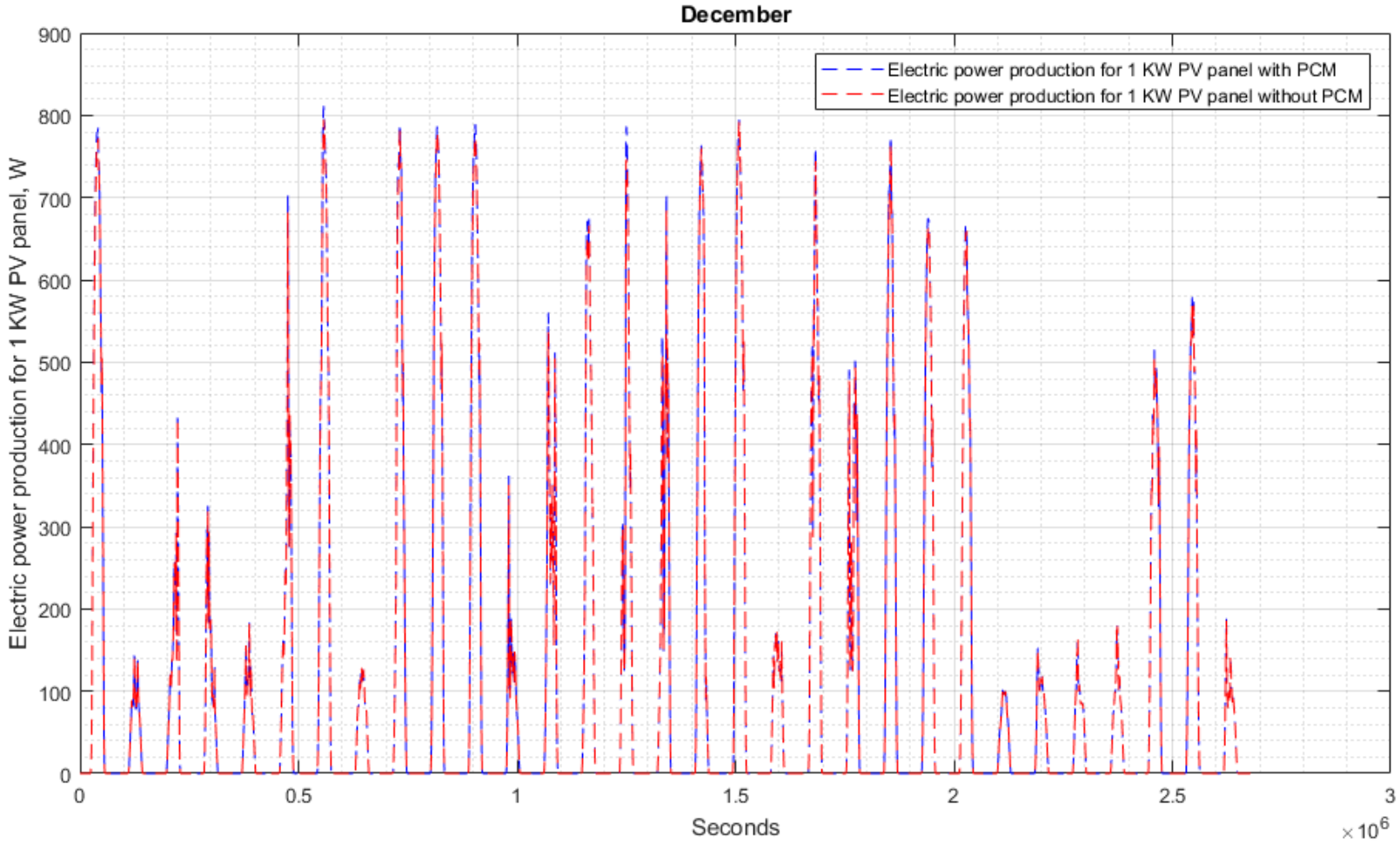

Appendix figure 23: The electrical power production for 1 kW of the PV-PCM and 1 kW of stand-alone PV panel, Baghdad, December.